TESIS DE LA UNIVERSIDAD DE ZARAGOZA

2024 481

Elena Redaelli

Characterizing patient-specific corneal biomechanics. High fidelity modeling and AI techniques

Director/es
Grasa Orús, Jorge

ISSN 2254-7606

Prensas de la Universidad Universidad Zaragoza

Universidad de Zaragoza
Servicio de Publicaciones

ISSN 2254-7606

Universidad Zaragoza
1542

Tesis Doctoral

CHARACTERIZING PATIENT-SPECIFIC CORNEAL BIOMECHANICS. HIGH FIDELITY MODELING AND AI TECHNIQUES

Autor

Elena Redaelli

Director/es

Grasa Orús, Jorge

UNIVERSIDAD DE ZARAGOZA
Escuela de Doctorado

2024

Universidad Zaragoza
1542

Escuela de Ingeniería y Arquitectura Universidad Zaragoza

OBERON

Ph.D Degree in
Biomedical Engineering

CHARACTERIZING PATIENT-SPECIFIC CORNEAL BIOMECHANICS. HIGH FIDELITY MODELING AND AI TECHNIQUES

Elena Redaelli

Faculty Advisor
Prof. Jorge Grasa

Escuela de Ingeniería y Arquitectura (EINA)
Universidad de Zaragoza
Zaragoza, 2021 - 2024

Abstract

The interaction between the optical and biomechanical properties of the cornea governs the way the eye refracts and focuses light onto the retina. The mechanical properties of corneal tissue vary between individuals and can change over time due to various factors such as ocular growth, aging, and possible pathologies like keratoconus. The increase in life expectancy and social demands for high-quality vision lead to increased concern for ocular health.

Estimating the biomechanical properties of ocular tissues is crucial for understanding, diagnosing, and treating some ocular pathologies, such as corneal ectasias, planning refractive surgeries, implanting intrastromal segments, minimally invasive glaucoma surgeries (MIGS), corneal crosslinking treatments, etc. This doctoral thesis aims to estimate the mechanical properties of human corneal tissue in vivo and in real-time through a combination of high-fidelity numerical models that simulate the non-contact tonometry diagnostic test and artificial intelligence techniques.

Non-contact tonometry is a non-invasive clinical test used to characterize corneal biomechanics and estimate intraocular pressure (IOP), deforming the anterior surface of the cornea when stimulated by an air pulse. In the developments of this thesis the tonometer Corvis ST will be considered. During the clinical test, corneal deformation is recorded using a high-speed camera. This deformation depends on the combination of corneal geometry (particularly corneal thickness), IOP, the mechanical properties of corneal tissue, and finally, on the air pulse pressure. In-silico models allow studying the influence of each factor and, through inverse analysis techniques, estimating the mechanical properties of the tissue that cannot be obtained today with any diagnostic equipment.

This thesis develops and validates a numerical methodology that combines fluid-structure interaction (FSI) simulations to reproduce as faithfully as possible the non-contact tonometry for a specific patient, for whom corneal topography and IOP have been recorded. The deformation of the cornea in the numerical model will depend on the properties of the corneal tissue and the IOP, which are not known. However, both the IOP and these properties can be estimated by forcing the numerical deformation to mimic the deformation recorded during the diagnosis with the Corvis ST.

Based on the results of the numerical simulation, an energetic approach to study non-contact tonometry is presented, and a new algorithm to estimate IOP independently of the mechanical properties of the corneal tissue is proposed. The time of maximum apex velocity during the air puff is used to estimate IOP, rather than the first applanation time, as currently used in clinical practice.

The drawback of the proposed numerical simulation is its high computational time (the computational time for each simulation is 24 hours), making it not feasible for real-time estimation. This has been addressed in this thesis by developing a reduced-order model based on the proper orthogonal decomposition technique, which will be used in combination with artificial intelligence techniques to estimate the specific mechanical properties of corneal tissue in real-time. The estimation of the properties

with the surrogate model is on the order of milliseconds. The FSI numerical model will generate virtual results of the non-contact tonometry to train a data-based surrogate model, enabling real-time predictions of the corneal mechanical properties. Having the mechanical response of the tissue will improve the diagnosis of pathologies associated with changes in stiffness and support clinicians' decision-making to establish treatments and assess their effectiveness.

The FSI numerical model developed for the eye has also been used in this thesis to simulate two other clinical problems. The feasibility of the Corvis ST device to detect keratoconus has been studied. Numerically, it has been observed that in patients with keratoconus who have not yet developed evident topographic problems, the corneal deformation along the air jet is different from that of a healthy patient. New biomarkers based on the asymmetry of the deformation are defined, and it is proposed to analyze the section perpendicular to the one currently considered in the Corvis ST. In this way, early detection of keratoconus is possible. Finally, the aqueous humor flow after the implantation of MIGS devices has been simulated, observing that numerically it is necessary to use a fluid-structure interaction simulation because the properties of the eye influence the IOP and viceversa. In the future, the established methodology will allow designing new devices or analyzing the optimal implantation position of the device.

Keywords: Corneal Biomechanics, Intraocular Pressure, Corneal Mechanical Properties, High-Fidelity modeling, Fluid Structure Interaction simulation, Machine Learning, Real-Time estimate, Patient-Specific simulations.

Resumen

La interacción entre las propiedades ópticas y biomecánicas de la córnea gobierna la manera en que el ojo refracta y enfoca la luz en la retina. Las propiedades mecánicas del tejido corneal varían entre individuos y pueden cambiar a lo largo del tiempo debido a diferentes factores como el crecimiento ocular, el envejecimiento y posibles patologías como por ejemplo el queratocono. El aumento en la esperanza de vida y las demandas sociales de una visión de alta calidad conduce a un incremento en la preocupación por la salud ocular.

Estimar las propiedades biomecánicas de los tejidos oculares es crucial para entender, diagnosticar y tratar algunas patologías oculares, como ectasias corneales, planificación de cirugías refractivas, implantación de segmentos intrastromales, cirugías mínimamente invasivas de glaucoma (MIGS), tratamientos como el crosslinking corneal, etc. Esta tesis doctoral tiene como objetivo estimar las propiedades mecánicas del tejido corneal humano in vivo y en tiempo real mediante una combinación de modelos numéricos de alta fidelidad que simulan la prueba de diagnóstico de la tonometría de no contacto y técnicas de inteligencia artificial.

La tonometría de no contacto es una prueba clínica no invasiva utilizada para caracterizar la biomecánica corneal y estimar la presión intraocular (PIO), deformando la superficie anterior de la córnea cuando se solicita mediante un pulso de aire. En los desarrollos de esta tesis se considerará el tonómetro Corvis ST. A lo largo de la prueba clínica se registra la deformación de la córnea mediante una cámara de alta velocidad. Esta deformación depende de la combinación de la geometría corneal (en particular del espesor corneal), la PIO, y las propiedades mecánicas del tejido corneal y por último de la presión del pulso de aire. Los modelos in-silico permiten estudiar la influencia de cada factor, y mediante técnicas de análisis inverso estimar las propiedades mecánicas del tejido que no pueden ser obtenidas a día de hoy con ningún equipo de diagnóstico.

En esta tesis se desarrolla y valida una metodología númerica que combina simulaciones de acoplamiento fluido estructura (FSI) para reproducir lo más fielmente posible la tonométria de no contacto para un paciente concreto, para el cual se ha registrado la topografía corneal y la PIO. La deformada de la córnea, en el modelo numérico, dependerá de las propiedades del tejido corneal y de la PIO, que no son conocidas. Pero la PIO y dichas propiedades se pueden estimar obligando a que la deformada numérica mimetice la deformada registrada a lo largo del diagnóstico con el Corvis ST.

Basado en los resultados de la simulación numérica, se presenta un enfoque energético para estudiar la tonometría de no contacto y se propone un nuevo algoritmo para estimar la PIO que desacopla la dependencia de la respuesta de las propiedades mecánicas del tejido corneal. El tiempo de velocidad máxima del apex durante el soplo de aire se utiliza para estimar la PIO, en lugar del tiempo en que se produce la primera aplanación, como se usa actualmente en la práctica clínica.

El inconveniente de la simulación numérica propuesta es su elevado tiempo computacional (el tiempo computacional de cada simulación es de 24 horas), que no lo hace factible para estimaciones en tiempo real. Esto se ha solventado en esta tesis

desarrollando un modelo de orden reducido basado en la técnica de descomposición ortogonal, que se utilizará en combinación con técnicas de inteligencia artificial para estimar las propiedades mecánicas específicas del tejido corneal en tiempo real. La estimación de las propiedades con el modelo subrogado es del orden de milisegundos. El modelo numérico FSI generará resultados virtuales de la tonometría de no contacto para entrenar un modelo subrrogado basado en datos, lo que permitirá predicciones en tiempo real de las propiedades mecánicas de la córnea. El disponer de la respuesta mecánica del tejido permitirá mejorar el diagnóstico de patología asociadas a cambio de rigidez y apoyará la toma de decisiones por parte de los clínicos para establecer tratamientos y valorar la eficacia de los mismos.

El modelo numérico FSI desarrollado del globo ocular también se ha utilizado en el marco de esta tesis para simular otros dos problemas clínicos. Se ha estudiado la viabilidad del equipo Corvis ST para detectar la patología del queratocono. Numéricamente se ha observado que, en casos de pacientes con queratocono que todavía no han desarrollado problemas evidentes en la topografía, la deformación de la córnea bajo el efecto del chorro de aire es diferente de la de un paciente sano. Se han definido nuevos biomarcadores basados en la asimetría de la deformación y se propone analizar también la sección perpendicular a la que actualmente se considera en el Corvis ST. De esta manera, es posible la detección precoz de la patología del queratocono. Por último, se ha simulado el flujo del humor acuoso tras la implantación de dispositivos MIGS, observando que numéricamente es necesario utilizar una simulación de acoplamiento fluido-estructura porque las propiedades del ojo influyen sobre la PIO y viceversa. En el futuro, la metodología establecida permitirá diseñar nuevos dispositivos o analizar la posición óptima de implantación del dispositivo.

Palabras clave: Biomecánica Corneal, Presión Intraocular; Propiedades Mecánicas de la Córnea, Modelado de Alta Fidelidad, Simulación de Interacción Fluido-Estructura, Aprendizaje Automático, Estimación en Tiempo Real, Simulaciones Paciente Específico.

Contents

List of Figures

List of Tables

CHARACTERIZING PATIENT-SPECIFIC CORNEAL BIOMECHANICS. HIGH FIDELITY MODELING AND AI TECHNIQUES

1

Introduction

1.1 Eyecare impact on society

Societies are built on the ability to see. Towns and cities, economies, education systems, sports, media and many other aspects of contemporary life are organized around sight. Thus, vision contributes towards everyday activities and enables people to prosper at every stage of life. Vision impairment occurs when an eye condition affects the visual system and one or more of its vision functions, encompassing a large and diverse range of morbidities. Everyone, if they live long enough, will experience at least one eye condition in their lifetime [World Health Organization (WHO)].

Data presented in this section are based on the World Report of Vision (WHO, 2019), published by the WHO in 2019. At least 2.2 billion people globally have a vision impairment or blindness; this figure takes into consideration those with near vision impairment due to presbyopia (1.8 billion), and moderate to severe distance vision impairment or blindness due to unaddressed refractive error (123.7 million, e.g. myopia or hypermetropia), cataract (65.2 million), age-related macular degeneration (10.4 million), glaucoma (6.9 million), corneal opacities (4.2 million), diabetic retinopathy (3 million), trachoma (2 million), and other causes (37.1 million), including those causes that were not classified in surveys or do not fit into any of the aforementioned categories. In addition, this figure also takes into consideration 188.5 million people with mild vision impairment in which the causes are unknown. The 2017 Global Burden of Disease (GBD) study ranked vision impairment the third cause among all impairments for years lived with disability.

The origins of eye conditions are multifactorial, with a range of risk factors interact-

ing to increase both the susceptibility to and the progression of a condition. Ageing is the primary risk factor for many eye conditions. The prevalence of presbyopia, cataract, glaucoma and age-related macular degeneration increases with age. Genetics and ethnicity also play a role in the development of some eye conditions including glaucoma, refractive errors and retinal degenerations.

Population growth and ageing, along with behavioural and lifestyle changes, will increase the number of people with eye conditions, vision impairment and blindness in the coming decades. By 2030, the number of people worldwide aged 60 years and over is estimated to increase from 962 million (2017) to 1.4 billion, while numbers of those aged over 80 years will increase from 137 million (2017) to 202 million. These population changes will lead to considerable increases in the number of people with major eye conditions that cause vision impairment. The number of people with glaucoma has been projected to increase 1.3 times between 2020 (76 million) and 2030 (95.4 million); and those with age-related macular degeneration, 1.2 times between 2020 (195.6 million) and 2030 (243.3 million). Similarly, the number of people with presbyopia is projected to increase from 1.8 billion (2019) to 2.1 billion (2030). As most people over the age of 70 usually develop cataract, the number of people with this condition will also increase substantially.

Scientific and technological advances have opened a wide range of clinical and research opportunities in the field of eyecare. The adoption of telehealth solutions has been effective in improving access to a range of eye care services, particularly for those living in rural and remote areas of many countries. Several emerging technologies in the field of eye care, including the use of mobile-based software applications for vision assessment and cataract surgery benchmarking, and artificial intelligence technologies for the detection of a range of eye conditions, offer further hope for enhancing access and quality of healthcare.

However, further research is required especially in the early detection and timely treatment for all eye conditions. Certain conditions that do not initially cause vision impairment could lead to severe consequences if left untreated. Addressing these gaps in research is crucial for preventing avoidable vision impairment and ensuring comprehensive eyecare for all individuals.

This thesis aims to contribute to the research in this field, in particular the focus will be on the corneal tissue. The objective will be the in-vivo characterisation of the mechanical behaviour of corneal tissue by the combination of numerical methods, artificial intelligence techniques and clinical data of the Non Contact Tonometry obtained with the commercial device OCULUS Corvis ST ®(OCULUS, 2019a).

In this chapter, the necessary concepts for following the development of the thesis are introduced, such as the anatomy of the eye, the concept of corneal biomechanics and the mechanical behaviour of eye tissues. The clinical impact of the study of the mechanical properties of the corneal tissue will also be treated. The clinical impact of studying the mechanical properties of corneal tissue will also be addressed. At the end

of the chapter, the project framework in which this thesis was developed, together with the objectives and the outline will be discussed.

1.2 Anatomy of the eye

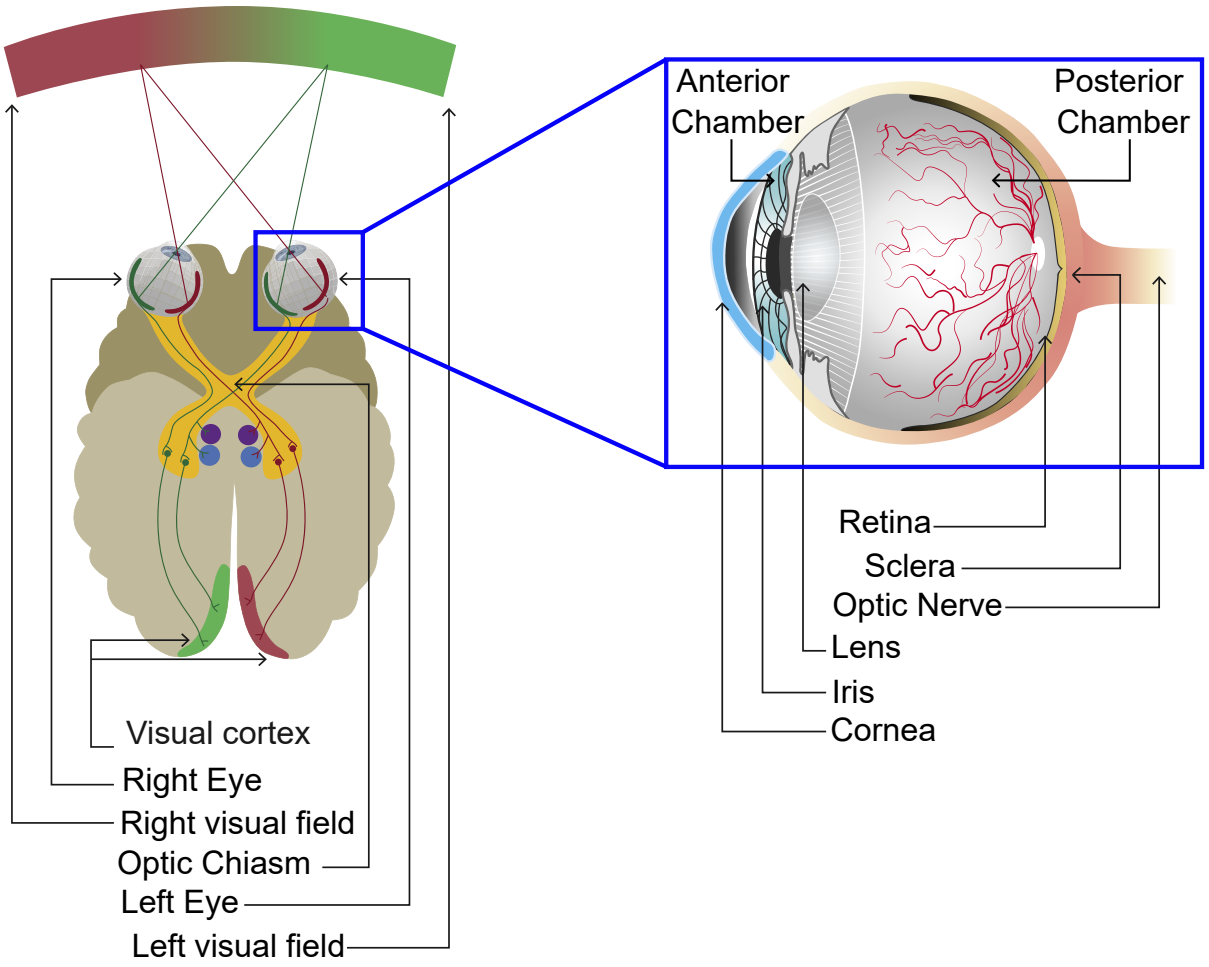

Figure 1.1: Scheme of the structures involved in the vision process (left). The refractive surfaces of the eye focus light onto the retina. In the retina, light is converted into nerve impulses which travel through the optic nerves to the visual cortex. These impulses are then transmitted to other parts of the brain. Principal structures composing the human eye (right) (WHO, 2019).

The visual system comprises the eyes and the optic nerves, as well as the pathways connecting various structures within the brain; figure 1.1 highlights the vision process. The refractive surfaces of the eye, namely the cornea and the lens, focus light onto the retina where light is converted into impulses which travel through the optic nerves to a specific part of the brain known as the visual cortex. These impulses are then transmitted to many other parts of the brain where they integrate with auditory or memory inputs to enable a person to understand the surrounding environment and respond accordingly (LeGrand and ElHage, 2013). The visual field is divided into right and left halves; in the optic chiasm, located at the base of the brain, the optic nerves from each eye partially cross over, allowing information from the left visual field to be

processed by the right hemisphere of the brain and viceversa (LeGrand and ElHage, 2013).

The eye is a complex biological structure composed of different parts and layers (Kels et al., 2015). These layers can be described both in terms of the outermost to the innermost structure and in terms of the anterior and posterior structure. The eye's outermost layer consists of the cornea, the sclera, and the limbus. They provide the eyeball's shape. The middle uveal layer, which is the central vascular layer, is where the iris, ciliary body, and choroid are located. The interior layer is identified with the retina. From the transversal point of view, the anterior section of the eye, which is the space between the cornea and the lens, is made up of the anterior and posterior chambers. The anterior chamber is filled with aqueous humor and is located between the cornea and the iris. The posterior chamber is positioned in between the iris and the lens. On the other hand, the posterior section, which consists of the space between the posterior surface of the lens and the retina, is filled with the vitreous humor (Yadav et al., 2019). A detailed description of the ocular components relevant to the research addressed in this thesis can be found below.

The **cornea** is the transparent outermost layer of the eye, and its dome-shaped structure provides two third of the total refractive power of the eye (Chong and Dupps Jr, 2021). Moreover, it serves as a barrier for the internal parts of the eye from external agents or possible applied loads. Corneal dimensions depend on different factors such as the gender or age of the subject considered (Rüfer et al., 2005). The average corneal diameter ranges from 11 mm to 12 mm, while the average central corneal thickness (CCT) is 500 μm with a gradual increase toward the peripheral area (Rüfer et al., 2005).

As presented in figure 1.2a, the corneal thickness is characterized by the composition of three cellular layers, epithelium, stroma, and endothelium with two a-cellular interfaces, Bowman's layer, and Descemet's membrane (Meeney and Mudhar, 2013). The epithelium represents a barrier to protect the eye from foreign substances and injuries (DelMonte and Kim, 2011). Bowman's layer is made up of collagen and proteoglycans. It is approximately 15μm in thickness (LeGrand and ElHage, 2013) and helps the cornea to maintain its overall shape. The stroma is the middle layer of the cornea, it provides the bulk of its structural framework and comprises roughly 80% to 85% of its thickness (DelMonte and Kim, 2011). Keratocytes represent the main component of the stroma and they are embedded in the Extracellular Matrix (ECM) mainly made up of collagen and glycosaminoglycans. The collagen fibres are arranged in parallel bundles called fibrils, packed in higher structures called lamellae (Meek and Knupp, 2015). The highly organized architecture of collagen lamellae is responsible for the strength of the corneal stroma and the capability of the entire cornea to withstand both internal and external loads. This fibrils organization, with a fixed level of hydration, provides transparency to the structure while keeping stability and mechanical strength. The lamellar organization is variable through the thickness of the cornea and along its surface (Meek et al., 1987). Meek and Knupp (2015) and Daxer and Fratzl (1997) using X-ray scattering, identified two preferential directions for the collagen fibres in the healthy cornea, one orientation in the medial-lateral direction and another in the inferior-superior direction. Moreover,

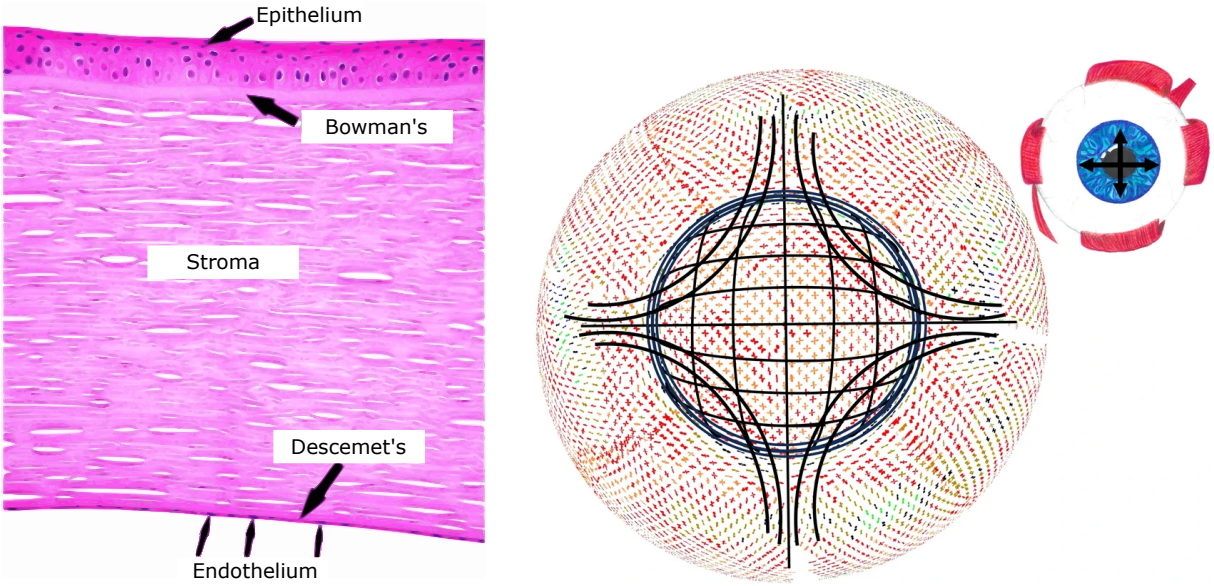

(a) (b)

Figure 1.2: a) Layers composing the corneal depth (Meeney and Mudhar, 2013). b) Organization of the collagen fibres in the corneal stroma (Meek et al., 2024). X-ray scatter data shows the preferred directions of collagen lamellae in different parts of the cornea. Superimposed is a simplified model of the overall preferential directions of lamellae, based on the x-ray data.

they noticed that as the collagen fibrils approach the limbus, they curve to run mainly around the periphery of the cornea. The architecture of the collagen fibres is depicted in figure 1.2b, where X-ray scatter data shows the preferred directions of collagen lamellae in different parts of the cornea and a simplified model proposed in Meek et al. (2024) shows the overall preferential directions of lamellae. Descemet's membrane is a thin layer secreted by the underlying endothelial cells (LeGrand and ElHage, 2013). The endothelium is the innermost layer of the cornea, it is a monolayer of cells essential to provide visual clarity since it is responsible for pumping out excess liquid from the cornea into the anterior chamber of the eye (DelMonte and Kim, 2011).

The **sclera** (figure 1.1) is the white outer rigid shell of the eye which contains numerous blood vessels. It supplies the eye with nourishment and maintains its temperature. The sclera's ability to resist deformations that might otherwise impair vision relies on its biomechanical characteristics given by the regional specialisations of the organisation of its tissue (Boote et al., 2020). The sclera is almost entirely made up of fine collagen fibres that form lamellae (LeGrand and ElHage, 2013). Bundles of parallel-aligned individual collagen fibrils of diameter 25–230 nm, interspersed in places with elastic microfibrils and fibres, form 0.5–6 µm thick lamellae that lie roughly in the plane of the eyeball surface. Scleral lamellae overall demonstrate far more branching and interweaving than those of the neighbouring corneal stroma, and the extent of this varies with both tissue depth and anatomical location. On approaching the limbus, the collagen bundles of the deep scleral stroma form a circumcorneal ring-like structure at the scleral spur (Boote et al., 2020). For this reason, the sclera is approximately ten times stiffer than the cornea. The average scleral diameter and thickness are 22 mm and 1 mm, respectively.

The **limbus** is the portion of the eye between the cornea and the sclera. It is a transitional area where gradually the cornea tissue transitions into the scleral tissue. Like the corneal tissue, it is composed of a network of collagen fibers which tends to assume a circunferential orientation as shown in figure 1.2b. The limbus is the location of the trabecular meshwork, which drains the aqueous humor from the eye and regulate the IOP. The limbus contains a network of blood vessels and nerves that supply the cornea with nutrients and sensory information.

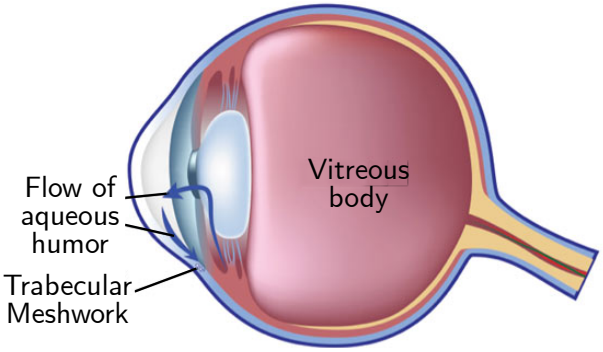

Figure 1.3: Aqueous and vitreous humors in the human eye. The vitreous body fills the posterior chamber of the eye while the aqueous humor is produced by the ciliary body, it flows through the anterior chamber and it is drained by the trabecular meshwork. Both of them contibutes to the value of the IOP.

The **aqueous humor** is a clear fluid that fills the anterior eye chamber as shown in figure 1.3. It is a low-viscosity liquid with a water-like fluidity and is made up of water, carbon dioxide, oxygen, proteins, carbohydrates, glutathione, urea, and organic and inorganic ions (Goel et al., 2010). It is secreted by the ciliary body and drained by the trabecular meshwork and the uveoscleral pathway. Humor's role is to provide nutrition, remove excretory product from metabolism, transport neurotransmitters, stabilize the ocular structure and contribute to the regulation of the homeostasis of the the cornea and the lens. Aqueous humor also permits inflammatory cells and mediators to circulate in the eye in pathological conditions, as well as drugs to be distributed to different ocular structures (Goel et al., 2010). Moreover, aqueous humor contributes to the maintenance of intraocular pressure (IOP) that is the hydrostatic pressure of the eye, which ranges from 8 to 21 mmHg in healthy conditions (Wang et al., 2018). IOP is necessary to both inflate the eye and preserve the globe's proper shape and optical properties.

The **vitreous body** is a transparent gel that maintains the spherical shape of the eye, helps secure the retina to the choroid to prevent retinal detachment, and plays a refractive role due to its transparency, facilitating the transmission of light from the lens to the retina. It is composed by a high water content, ranging from 98 to 99.7% (Jongebloed and Worst, 1987), and comprises approximately 80% of the eye's total volume. Structurally, the vitreous body contains fibrous proteins, predominantly collagen, similar to that found in the cornea. Towards the periphery, collagen fibers align parallel to the surface, forming a membrane like structure known as the vitreous membrane. The anterior and posterior chambers have the same IOP because they

are connected. The corneal response to external loads depends on the pressure in the humors which depends on their production and drainage.

The **crystalline lens** consists of a transparent membrane called the lens capsule, an anterior subcapsular lens epithelium, and lens fiber cells that form the lens nucleus and cortex. The embryonic nucleus remains at the center of the lens throughout life, while the cortex expands progressively around it with new layers of lens fiber cells derived from the lens epithelium (Remington, 2012). The lens is composed of approximately 65% water and 35% protein, along with trace amounts of minerals such as potassium and ascorbic acid (Remington, 2012). Nutrient uptake for the lens occurs via the surrounding aqueous and vitreous humors, as the lens capsule is permeable to water, ions, and proteins necessary for its function and growth. The primary optical role of the lens is to transmit and focus light onto the retina and it is resposible for the process of accomodation.

1.3 Corneal Biomechanics

Corneal biomechanics refers to a collection of features that describes the corneal behavior against different external loads and it is responsible for maintaining the tissue structural integrity and shape. The interaction between the optical and biomechanical properties of the cornea governs how the eye refracts and focuses light onto the retina (Ávila et al., 2021; Meek et al., 2024), therefore understanding corneal mechanical behaviour is crucial for studying some ocular pathologies and predicting eye surgery outcomes (Kling and Hafezi, 2017). Corneal biomechanics depends on three main factors: the IOP, the geometry or shape of the cornea and the intrinsic mechanical properties of the corneal tissue. In this section, the methodologies to characterize these factors are presented.

1.3.1 Methods for measuring the IOP

Ophthalmologists use a variety of techniques to measure IOP, including Goldmann applanation tonometry (GAT) (Goldmann and Schmidt, 1957) and Non Contact Tonometers (NCT) such as Corvis ST ®(Corvis, Oculus Optikgeräte GmbH, Wetzlar, Germany) (Hong et al., 2013) and Ocular Response Analyzer (ORA, Reichert Ophthalmic Instruments, Buffalo, NY) (Luce, 2005). The gold standard is GAT, it involves the use of a probe that is gently pressed against the cornea to flatten a small area, creating a uniform surface of known size. A calibrated force is then applied to the probe, and the amount of force required to flatten the cornea is measured. The estimation of IOP in GAT is based on the Imbert-Fick law (Imbert, 1885), it is a modification of the Maklakoff law (Maklakoff, 1885), and states that an external force against a sphere equals the pressure in the sphere multiplied by the area applanated by the external force. The validity of the law requires that the sphere should be perfectly spherical, dry, perfectly flexible and infinitely thin (Sharma et al., 2020), conditions that are not fulfilled in the cornea (Brusini et al., 2021; Wu et al., 2020). Other methods to measure the IOP are the ORA

and the Corvis ST, which are NCTs. Their purpose is to obtain IOP measurements with minimal invasion of the eye (Silva and Lira, 2022). The idea is the same as GAT but the deformation of the cornea is obtained by a high-velocity air jet, without the need of contact. The difference between ORA and Corvis ST is that in the former, the air pressure at the outlet of the device varies among patients, while in the latter it is always the same; however, both of them provide an estimation of the IOP based on the first applanation time of the cornea during the air jet. In addition, Corvis ST is equipped with a Scheimpflug camera which gives 140 images of the central section of the cornea over the 30 ms of the air jet. In this thesis we will use these images to characterise the corneal tissue response in-vivo.

1.3.2 Methods for characterizing corneal topography

Corneal topography is the mapping of the surface curvature of the cornea in order to characterize its shape. The most used techniques to measure the corneal topography are Placido disc-based topography, Scheimpflug imaging, and Optical Coherence Tomography (OCT). Among these, the Placido disc-based topography employs a Placido disc, which consists of a series of concentric, alternating black and white rings that are projected onto the corneal surface. The reflection of these rings is captured by a camera, and the spacing and deformation of the reflected rings is analyzed to determine the corneal curvature and topographic features (Sridhar and Tripathy, 2022). This technique does not provide information about the posterior cornea or corneal thickness. The OCULUS Pentacam ®(OCULUS, 2019b) utilizes a rotating Scheimpflug camera to capture volumetric data of the anterior and posterior segment of the cornea. The Pentacam provides maps of both the anterior and posterior corneal surfaces, corneal thickness (pachymetry), and anterior chamber depth. Moreover, it computes the map of the corneal curvatures. OCT images employs low-coherence interferometry to capture ultra-high resolution cross-sectional images of the cornea and assess corneal thickness and structural integrity (Kling and Hafezi, 2017). In this thesis we will use the point cloud generated by Pentacam to build the geometric model of the patient-specific cornea.

1.3.3 Caracterization of corneal tissue response

1.3.3.1 Ex-vivo techniques

In this section, the ex-vivo methods for characterizing corneal tissue will be explained. In engineering, in order to characterise the mechanical response of materials, standardised tests are used, using samples of the material. Since the focus of this doctoral thesis is on corneal tissue, the methods will be detailed and specialized for the cornea. However, the same ex-vivo experiments can be applied to other ocular tissues such as the limbus, sclera, and lens, whose mechanical properties will be discussed in the following chapters.

The cornea, being a soft tissue, has mechanical properties dependent not only on its main constituents, but also on their intrinsic organization. Corneal tissue can be defined

as a viscoelastic material (Glass et al., 2008), with the elastic response attributed to the collagen architecture, while the viscous component is related to the ECM components and the water content in the tissue.

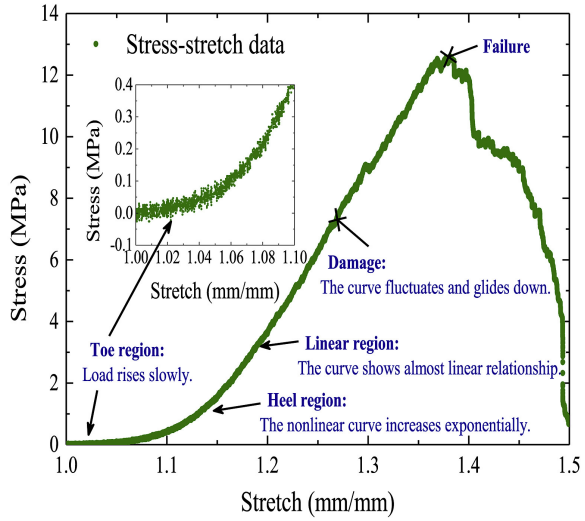

(a) Experimental results from Liu et al. (2020).

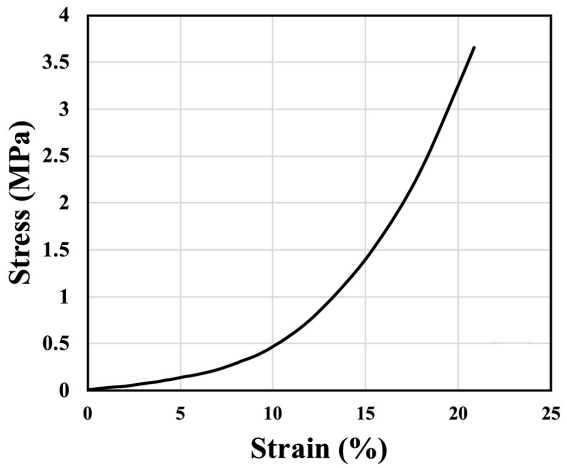

(b) Experimental results from Mahdian et al. (2021).

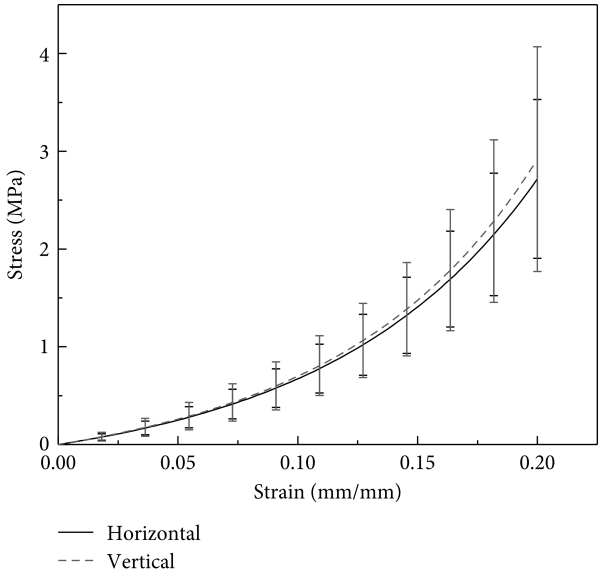

(c) Experimental results from Xue et al. (2018).

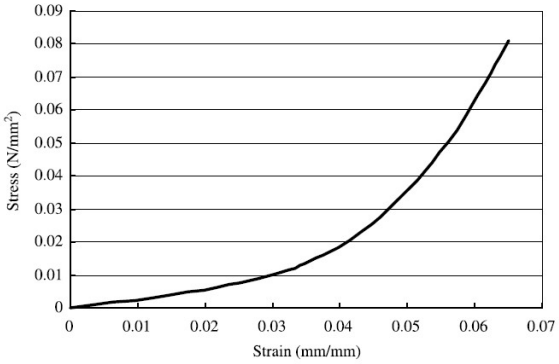

(d) Experimental results from Elsheikh and Wang (2007).

Figure 1.4: Stress strain response of sample of the human corneal tissue obtained from uniaxial tensile tests in different studies.

The plots in figure 1.4 depict the relationship between stress and strain obtained from uniaxial tensile tests on human corneas in different studies (Liu et al., 2020; Mahdian et al., 2021; Xue et al., 2018). The stress-strain behaviour of the tissue is highly non-linear exhibiting stiffening behaviour with increasing strain. For low levels of strain (< 5%), the corneal material response is linear, while for increasing strains, the elastic modulus increases exponentially. This can be explained by the recruitment phenomenon (Jan and Sigal, 2018) describing the alignment and stretch of the network of collagen fibres along

the applied load direction inducing a stiffer material behaviour for increasing values of load. For lower values of strain, instead, the response of the material is controlled by the ECM. Collagen fibres are the primary load-bearing component of the corneal structure and the orthogonal organization of the fibres in the stroma induces a space-dependent tissue response. For this reason, mathematically, the mechanical response of the cornea should be described as an anisotropic tissue with two preferential directions that coincide with the perpendicular directions of the fibres described in figure 1.2b.

The mechanical properties of the corneal tissue can be evaluated by ex-vivo techniques, in which speciments of human cornea are analysed under different loading conditions such as uniaxial (Mahdian et al., 2021; Nambiar et al., 2023; Wollensak et al., 2003), biaxial (Chen et al., 2023), or inflation tests (Bao et al., 2012; Whitford et al., 2016). Strip extensometry (uniaxial and biaxial tests) is the simplest and most commonly used ex-vivo testing method to determine the stress-strain behavior of corneal tissue (Ashofteh Yazdi et al., 2020). In this technique, rectangular samples excised from donor corneal tissue are clamped to a loading machine, and the obtained values of strain are tracked and related to the known values of stress applied. The main limitations of ex-vivo techniques is related to the loss of the natural curvature of the cornea and the difficulties in investigating the properties of pathological areas. The specimens tested and clamped to the machine are flat rectangular-shaped samples obtained from the natural dome-shaped structure of the cornea. The loss in the natural curvature of the tissue can induce an unphysiological strain distribution in the tissue (Elsheikh and Anderson, 2005). Moreover, these techniques do not provide patient-specific assessments and corneal tissue extraction may introduce distortions in mechanical properties due to dehydration issues (Wang et al., 2021) and to due the fact that the cutting breaks the collagen structure of the tissue. It should be noted that the uniaxial tests do not reproduce the working conditions of the cornea, which is instead loaded under a biaxial state. These limitations in ex-vivo analysis, led to the need of using in-vivo devices to investigate corneal biomechanical parameters in physiological conditions and thus be able to diagnose or apply treatment on the basis of the patient's properties.

1.3.3.2 In-vivo techniques

Several approaches have been developed to estimate the mechanical properties of corneal tissue in-vivo based on the devices initially intended to measure the IOP. NCT intends to measure the IOP and characterize the corneal response with minimal invasion of the eye (Silva and Lira, 2022) since the cornea is deformed by a high-velocity air-puff. During the test, the cornea deforms inward and then recovers to its original shape, hence it goes through three main phases: first applanation point, highest concavity point and second applanation point. In the Corvis ST tonometer, the dynamic deformation of the equatorial plane of the cornea is recorded through a high-speed Scheimpflug camera: 141 horizontal 8 mm frames are taken over a period of 33 ms (Esporcatte et al., 2020). From these images, some deformation parameters - or biomarkers - are calculated in order to describe the corneal response to the applied load. A detailed description of Corvis ST biomarkers is included in Appendix A.

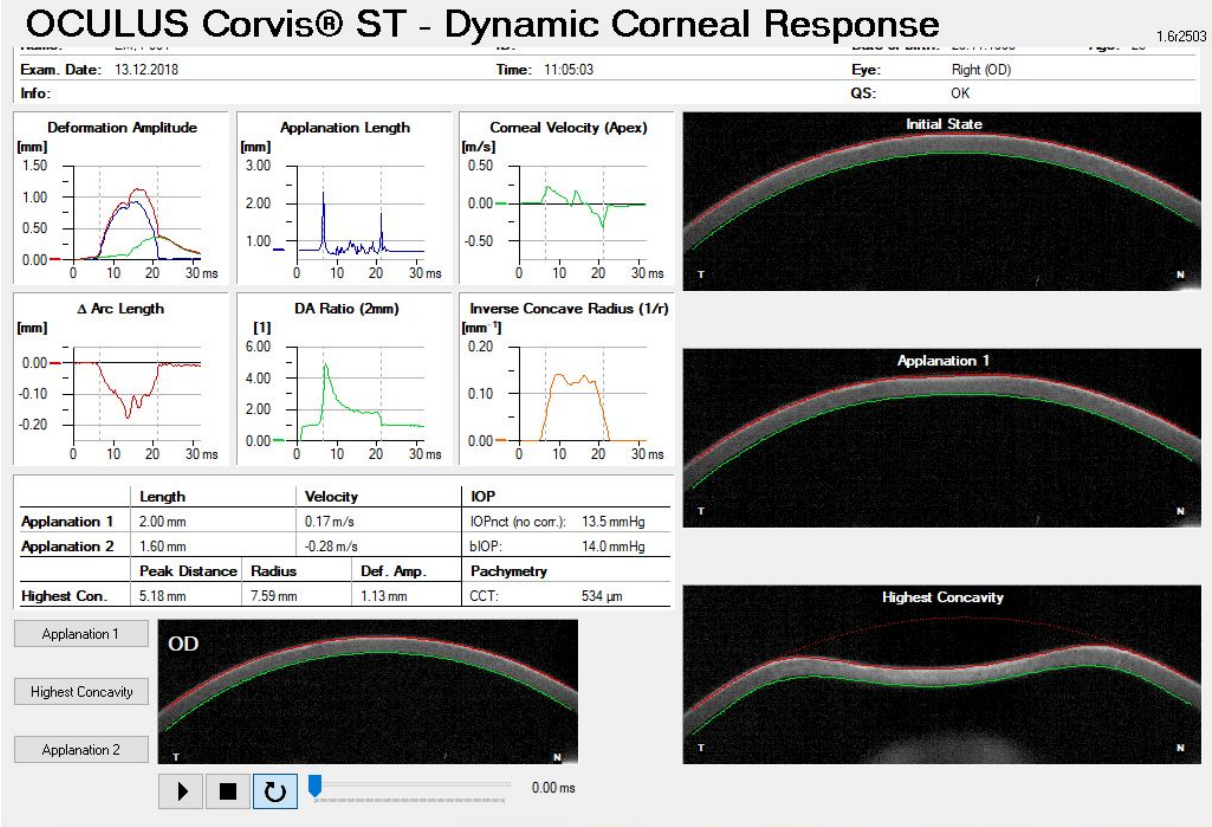

Figure 1.5: Example of clinical results provided by Corvis ST.

An example of clinical results provided by Corvis ST is presented in figure 1.5. In the bottom-left part of the screen, a video with the 141 frames of the corneal deformation can be found. Three significant frames are shown in the right part of the screen: the initial state of the cornea, the first applanation and the highest concavity. On the left, there are six plots showing the temporal evolution of selected biomarkers and a table with parameters describing the applanations and the highest concavity point, the measured IOP and pachymetry. This test gives as output the deformation of the cornea, but it does not isolate the mechanical behaviour of the corneal tissue. These clinical data will be used in combination with numerical simulations to estimate the mechanical properties of the corneal tissue. This topic will be in-depth analyzed in the following sections of the thesis.

1.4 Clinical impact of corneal biomechanics

Corneal biomechanics has emerged as a significant area of research in ophthalmology due to its potential clinical impact across a wide range of ophthalmic conditions. Estimating the mechanical properties of the corneal tissue and the IOP is crucial for understanding various ocular pathologies like ectatic diseases and diagnosing conditions such as glaucoma. It is also essential for improving the predictability of surgeries including corneal crosslinking (Frigelli et al., 2023), intrastromal ring segment implantation (Ariza-Gracia et al., 2020), refractive surgeries (Montanino et al., 2023) and minimally

invasive glaucoma surgeries (MIGS). In this section, the clinical significance of studying the mechanical properties of the cornea in combination with the IOP will be explored.

(a) Early keratoconus detection.

(b) Glaucoma risk factors and treatments.

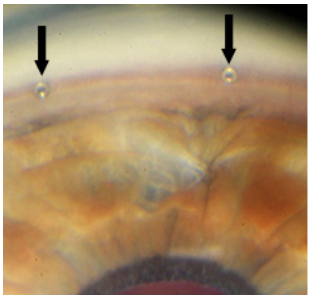

(c) Prediction of minimally invasive glaucoma surgeries (MIGS) outcomes.

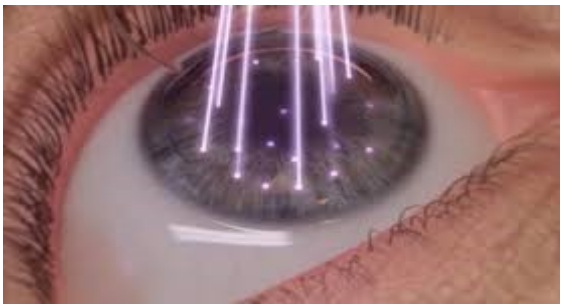

(d) Prediction of refractive surgeries outcomes.

Figure 1.6: Clinical impact of corneal biomechanics.

1.4.1 Keratoconus

Keratoconus is an ocular disorder involving corneal tissue and it is classified as an ectatic corneal disease. Generally, the pathology has its onset at puberty and it develops until the third to fourth decade of life (Santodomingo-Rubido et al., 2022). It is characterized by progressive thinning and subsequent bulging of the outer structure, which can lead to irregular astigmatism of the corneal tissue in combination with decreased visual acuity. The altered external structure causes light to be scattered as enters the eye resulting in a low capability of focusing light and visual distortion. Treatment options for the disease vary depending on the stage of the condition. For mild cases, eyeglasses or contact lenses may be sufficient, however as the condition worsens, surgery such as a corneal transplant may be necessary to restore proper vision (Tan et al., 2012). The aetiology at the date is not fully understood (Blackburn et al., 2019). In literature, reviews evidence the dependency on both genetic and environmental factors (Romero-Jiménez et al., 2010), resulting in keratoconus being classified as a multifactorial disease. Keratoconus can be also caused by a laser based refractive surgery, provided that some hidden corneal disease existed previously. The regular orthogonal arrangement of the collagen fibrils in the corneal stroma is altered in keratoconic patients (Daxer and Fratzl, 1997) (Meek et al., 2005) and a gross rearrangement of vertical and horizontal collagen lamellae can be perceived. Analysis performed with confocal microscopy on excised pathological corneal buttons (Hollingsworth et al., 2005) highlighted the reduction in the density of the keratocytes in the stroma while second harmonic generated imaging

proved the decrease of the number of collagen lamellae (Morishige et al., 2007). The significant importance of keratocytes in maintaining the homeostasis of the cornea can explain the altered organization of the collagen lamellae while their reduction can be due to the increasing density of non-keratocytes that could be involved in the degradation of the collagen matrix (Ferrari and Rama, 2020). The orientation of the fibril layers is an important factor determining the mechanical properties of the cornea (Daxer and Fratzl, 1997) and the loss in the orthogonally arranged pattern of collagen fibres is responsible for the weakening of the tissue (Meek and Boote, 2009). In pathological cases, the structure is less able to withstand the load and it becomes thinner under the IOP. For this reason, in progressive stages of keratoconus, the structure bulges leading to a non-uniform curvature of the outer-most surface. Figure 1.6a shows the difference in shape between a normal eye and a keratoconus eye at late stage. Keratoconus approximately affects 1 person over 2000 people (Ambekar et al., 2011) but data can underestimate the spread of the pathology. This is for the different criteria and modalities used and the limited capability of in vivo diagnosis tools to detect keratoconus, particularly during the first stages of the disease when the outer appearance of the tissue does not mark clear signs of degradation. Estimating the mechanical properties of the corneal tissue can help in the early diagnosis of keratoconus as mechanical degradation precedes changes in corneal tomography.

1.4.2 Glaucoma

The equilibrium between the production and drainage of aqueous humor governs the IOP, which, when elevated, poses a substantial risk factor for the development of glaucoma, a collective term for a group of eye disorders that can lead to irreversible vision loss (Jordanova et al., 2022). Figure 1.6c shows the treatment of a glaucomatous eye. Glaucoma is the leading cause of blindness worldwide, after cataracts in underdeveloped countries and after senile degeneration of the macula in developed countries (Jordanova et al., 2022). In 2020, the disease affected about 80 million people globally, and this figure is projected to rise to 111 million by 2040 (Brusini et al., 2022). Glaucoma leads to peripheral visual loss, firstly in the lateral, superior and inferior visual fields and in a non linear way progressively to the center. The vision impairment associated with glaucoma is primarily attributed to the degeneration of the optic nerve; as a matter of fact, when the IOP exceeds 20 mmHg, the optic nerve can be damaged irreversiblely (Morrison et al., 2005). An increment in the IOP level is usually caused by the blockage of liquid drainage pathways from which the aqueous humour flows into blood vessels. Moreover, certain medications may impact the production or drainage rate of the aqueous humor, for instance, following LASIK surgery, the use of steroid eye drops could potentially elevate IOP (Hamilton et al., 2002). Because glaucoma has a gradual onset and lacks noticeable symptoms until late stages, it is often referred to as a "silent disease" (Brusini et al., 2022). In this context, reducing IOP is the primary option available for managing the pathology and preventing blindness (Eliasy et al., 2022; Sharma et al., 2020). Accuracy and precision in measuring IOP are important requirements to predict and monitor glaucoma progression. Since currently available methods to estimate the IOP in-vivo are indirect -they involve the deformation of the corneal tissue- the managment of glaucoma requires a precise knowledge of the mechanical

properties of the corneal tissue.

1.4.3 Minimally Invasive Glaucoma Surgeries (MIGS)

In order to prevent further damage to the optic nerve caused by glaucoma, the aim of glaucoma treatments is to reduce IOP to a specific target level. Research has shown a correlation between a 1 mmHg drop in IOP and a 10% reduction in the risk of glaucomatous progression (Popovic et al., 2018). Minimally invasive glaucoma surgeries (MIGS) involve the implantation of micro stents in order to develop an alternative path for aqueous humor drainage as shown in figure 1.6b. There are several stents available in clinics, usually classified according to the aqueous humor drainage site (Lee et al., 2020). Among these, the most recent and widely used stent is the iStent inject (Glaukos Corporation, Laguna Hills, CA) (Shalaby et al., 2021). It is a heparin-coated titanium stent which is designed with a thorax aimed to be implanted within the trabecular meshwork, and a head containing four outlets to allow fluid passage. The effectiveness of treating mild to moderate glaucoma with an iStent Inject compared to a treatment without stent implantation was demonstrated by a two-year clinical trial conducted from 2017 to 2019. A reduction of more than 20% in IOP was attained in 24 months in 75.8% of treated eyes compared to 61.9% of untreated eyes. 63.2% of the treated eyes, as opposed to 50% of the untreated eyes, successfully reduced their IOP to values below 18 mmHg (Sng and Barton, 2021). For most patients, maintaining an IOP below 18 mmHg can slow the disease's progression and preserve their visual field (Cantor et al., 2023). MIGS have shown promise in addressing glaucoma pathology, but there is still not enough investigation into their complex biomechanics and their interaction with ocular tissues. Long-term results are not available from current MIGS studies. Long-term data is required to identify changes in the visual field and the state of the cornea following surgery. In order to support clinical use, understanding the mechanical properties of the eye tissues, in particular of the cornea in the region of stent implantation, could help with a long-term investigation of the devices and a thorough examination of MIGS's mechanism of action.

1.4.4 Refractive Surgeries

Refractive errors are one of the leading causes of reversible visual impairment worldwide, with corrective refractive surgery standing as one of the most commonly performed ocular procedures globally (del Barrio et al., 2019). These surgeries aim to change the curvature of the corneal surface in order to adjust its optical power. The most commonly used refractive surgeries are laser-assisted in-situ keratomileusis (LASIK), photorefractive keratectomy (PRK) and small-incision lenticule extraction (SMILE). LASIK involves creating a flap in the cornea, followed by precise reshaping of its curvature using a laser. PRK, on the other hand, is a surface ablation technique that removes the epithelium, followed by the ablation of the Bowman's layer and the anterior corneal stromal tissue. SMILE, meanwhile, is a refractive lenticule extraction procedure where a lenticule of the desired correction is shaped within the cornea and then extracted through a small corneal incision (del Barrio et al., 2019). Laser refractive corneal surgery

is a common procedure with a low complication rate. However, the unpredictability of the surgical outcomes remain. This unpredictability can manifest in side effects such as flap-related complications in LASIK (e.g., flap displacement, diffuse lamellar keratitis, and epithelial ingrowth) and potential weakening of corneal biomechanical strength, which can lead to corneal ectasia. Unlike LASIK, surface ablation in PRK does not create a flap, potentially resulting in a biomechanically stronger cornea due to a thicker post-procedural stromal bed. However, PRK's ablation of Bowman's layer and the keratocyte-rich anterior corneal stroma triggers a wound healing process that may affect refractive correction, induce scarring, and lead to permanent haze formation. Understanding the mechanical properties of the corneal tissue before surgery, can assist surgeons in selecting the most appropriate technique, minimizing damage to the cornea, and reducing post-operative complications.

1.5 Project Framework

Figure 1.7: European institutions involved in the Oberon project and in this thesis project.

The present thesis has been developed within the framework of the OBERON (Opto-Biomechanical Eye Research Network) research project funded by the European Union's Horizon 2020 research and innovation programme under the Marie Skłodowska-Curie

grant agreement No 956720. OBERON project had a total duration of 48 months starting from January 2021 and has been training 15 Early Stage Researchers (ESR) with research topics ranging from ocular refraction and biomechanics, optical modelling, and various applications in both the diagnosis and treatment of various pathologies. The project relies on network-wide collaboration and secondments between 8 beneficiaries, 7 university groups and 1 fully integrated industry, and 4 partners (2 academic hospitals, 2 industry), spanning 8 European countries (United Kingdom, Belgium, Portugal, Switzerland, Spain, Poland, the Netherlands, and France) as depicted in figure 1.7. The consortium was coordinated by University of Minho (Minho, Portugal). OBERON main objective was to create a unique, biologically viable and physiologically relevant modelling platform describing the interactions between ocular mechanical properties, optics and geometry in a way adaptable to a wide range of ocular conditions.

In brief, the project focused on the following objectives:

- **Ocular biomechanics**: Fill in the most important knowledge gaps on the relationship between material stiffness and geometry of the eye structures that need to be addressed to assist in the development of the opto-biomechanical eye model.
- **Crystaline lens optics**: Study the lens' optical properties in great detail using new measurement techniques and calculation methods.
- **Eye modelling**: Develop new optical and opto-biomechanical eye models for virtual clinical testing of novel clinical and industrial applications.
- **Application development**: Develop new clinical devices.

Our research group, Applied Mechanics and Bioengineering group of the University of Zaragoza, led by professor Begoña Calvo Calzada, took part with two PhD projects. The first project, which will be presented in the current thesis, intends to improve on the existing algorithms used to estimate the IOP and the mechanical properties of the cornea by using a combination of finite element models and machine learning.

The doctoral candidate, completed two research stays (secondments) of two months inside the OBERON consortium:

- November-December 2022, at Wroclaw University of Science and Technology (Wroclaw, Poland) under the supervision of Dr. Damian Siedlecki.
- September-October 2023, at University of Bern (Bern, Switzerland) under the supervision of Dr. Sabine Kling and Dr. Philippe Büchler.

This thesis has been conducted in collaboration with the department of Chemistry, Materials and Chemical Engineering "Giulio Natta" of Politecnico di Milano, (Milan, Italy) under the supervision of Dr. José Félix Rodríguez Matas and Dr. Giulia Luraghi.

1.6 Motivation and Objectives

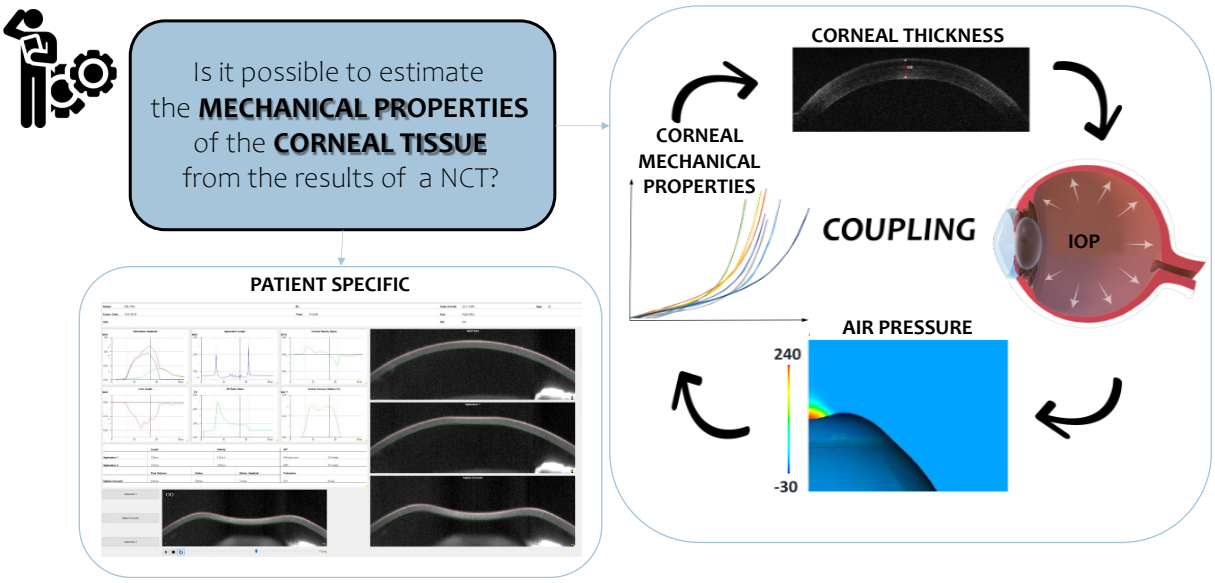

Figure 1.8: Motivation and objective of the thesis project.

This doctoral thesis aims at estimating the mechanical properties of the human corneal tissue in-vivo and in real time by developing a high fidelity modeling of the NCT procedure of Corvis ST. As it has already been mentioned in pararaph 1.3, the interaction between the optical and biomechanical properties of the cornea governs the way the eye refracts and focuses light onto the retina (Meek et al., 2024) . The mechanical properties of the corneal tissue vary between individuals and can change over time due to factors such as eye growth (Liu et al., 2021), ageing (Elsheikh et al., 2007) and pathologies such as keratoconus (Redaelli et al., 2024). Given the increase in life expectancy and in societal demands for high-quality vision, there is a need to estimate the patient-specific mechanical properties of eye tissues, in particular of the cornea (WHO, 2019). Estimating the mechanical properties of the corneal tissue is crucial for understanding various ocular pathologies like ectatic diseases and diagnosing conditions such as glaucoma. It is also essential for improving the predictability of surgeries including corneal crosslinking (Frigelli et al., 2023), intrastromal ring segment implantation (Ariza-Gracia et al., 2020), refractive surgeries (Montanino et al., 2023) and MIGS.

In-silico models can contribute to medicine in several ways. First, if models are patient-specific, they could help to predict the progression of a disease or predict the outcome of a treatment. Such predictions could then play a role in decision support scenarios and could be used in clinical trials. They could then predict the performance of a new device or a new drug, and as such contribute in designing better and more targeted clinical trials, or help in reducing the use of laboratory animals in first screening of devices. A 3D patient-specific in-silico FSI model of a NCT is presented. The development of a in-silico high-fidelity model of the NCT allows to study the interactions between the patient-specific eye geometry, the mechanical properties of the corneal tissue, the IOP and the air pressure of the jet over the corneal surface, with a level of detail not

possible to achieve in clinical studies on real patients. Indeed, it has been demonstrated (Ariza-Gracia et al., 2015) that the response of the cornea to the air-puff depends on the combination of four factors: the geometry of the cornea, in particular its thickness, the IOP, the mechanical behavior of the corneal tissue and the pressure of the air-jet. Only in-silico models give the possibility to study the influence of each factor. To this purpose, a high-fidelity simulation framework is developed and validated to reproduce a clinical NCT procedure. To achieve a high-fidelity simulation, a 3D patient-specific FSI modeling of Corvis ST is developed. In the FSI, the coupling is between the air-jet, represented as a fluid, and the eye, the structural part. The humors inside the eyeball are modelled as incompressible fluids, and the eye tissues with a non linear material response, in particular, the cornea and the limbus are modelled as anisotropic materials to account for the influence of the network of collagen fibers.

Although the main objective of the thesis is to estimate the properties of the corneal tissue, other partial objectives have been established. The NCT simulation framework is used to decouple the contribution of the IOP and the mechanical properties of the corneal tissue in order to estimate the IOP. Although NCT is the most widely used instrument to estimate the IOP (Silva and Lira, 2022), its accuracy is significantly affected by the thickness of the cornea and the mechanical properties of corneal tissue (Ariza-Gracia et al., 2015; Asaoka et al., 2015; Greene et al., 2016). For this reason, after the development of the high-fidelity model, the second objective of the thesis is to estimate the IOP in a way not dependent on the mechanical properties of the corneal tissue and the thickness.

Once the IOP is estimated, the third objective of the thesis is to create a surrogate model of the NCT procedure to estimate in real time the patient-specific mechanical properties of the corneal tissue in-vivo using a combination of model order reduction and artificial intelligence techniques. A surrogate model is a computationally inexpensive model trained to learn the relationship between a set of inputs and outputs, which are realizations of a complex and/or computationally expensive model. The high-fidelity NCT model, which can be defined as a knowledge-driven model, is computationally-expensive, with a calculation time not compatible with the clinical scenario in which the NCT is performed. Therefore, the high-fidelity model is used to produce populations of virtual NCT results for training the surrogate data-driven model, which can provide real-time predictions of the parameters describing the mechanical properties of the corneal tissue and can be potentially used to support the clinical decision-making.

The ability of the validated 3D FSI simulation to study two clinical problems is also investigated. The computational model of the NCT procedure is used in an application to study the keratoconus pathology and a similar framework is used to model the implantation of a MIGS device and to study the aqueous humor flow after the implant.

In summary, this doctoral thesis explores the computational modeling of the NCT with different scopes and methodologies, with the aim of characterizing the corneal biomechanics, in particular of estimating the corneal tissue mechanical properties and

the IOP with a combination of high fidelity simulations and artificial intelligence.

1.7 Thesis outline

The present doctoral thesis is organized in two main parts.

Part I is named *Methodology* and focuses on the development and validation of a framework for high fidelity in silico simulations of the NCT procedure, and its use to decouple the estimation of the IOP and the mechanical properties of the corneal tissue.

- **Chapter 2** presents a detailed methodology to model the NCT. A Fluid Structure Interaction (FSI) simulation of Corvis ST is outlined where the structure is represented by the eyeball and the fluid by the air surrounding and inside the eye. In this chapter, an eye model with averaged dimensions is used. Some sensitivity analyses are conducted to test the mesh of the structural model, the influence of the corneal and scleral material properties, the influence of the IOP and the contribution of the internal structure of the eye (i.e. the cristalline lens and the ciliary muscles) on the deformation results.

- **Chapter 3** aims at demonstrating the capability of the simulation framework to reproduce a patient-specific clinical NCT procedure. In collaboration with the Antwerp University Hospital (Antwerp, Belgium), 21 patients with healthy eye geometries were selected. After the creation of the patient-specific corneal geometries from OCULUS Pentacam ®(OCULUS, 2019b) elevation data, the NCT procedure is virtually replicated with different material properties and IOP. The deformation results of the simulation are compared with the patient-specific OCULUS Corvis ST ®(OCULUS, 2019a) data to validate the procedure.

- **Chapter 4** proposes a methodology to estimate the IOP from the results of the NCT procedure. An energetic approach to study the internal and external mechanical work acting on the corneal surface is presented based on the FSI simulations results. The numerical methodology allowed us to carry out an important number of simulations testing the influence of the geometry, the mechanical properties of the corneal tissue and the IOP, proving that the resulting approach to estimate the IOP is not influenced by the mechanical properties of the corneal tissue and by the corneal thickness.

- **Chapter 5** designs a methodology to estimate in-vivo and in real time the mechanical properties of the corneal tissue. After creating a large dataset of high fidelity FSI solutions based on the numerical framework of the previous chapters, a Reduced Order Model (ROM) is constructed. To create the ROM, a Proper Orthogonal Decomposition (POD) of the simulations results is conducted to find the principal modes of variation of the model. The coefficients mapping the input parameters of the simulations to the reduced basis are then calculated for the entire dataset. These coefficients, together with the IOP and the geometry of the

cornea are used as input to train an Artificial Neural Network (ANN) with outputs the parameters describing the mechanical properties of the corneal tissue.

Part II is named *Applications* and uses the methodologies proposed in the previous part to study two different applications with the aim of providing tools to analyse an ocular pathology, keratoconus, and a MIGS surgery.

- **Chapter 6** uses the FSI model proposed to simulate the development of keratoconus in order to be able to detect the pathology before it is detectable by topographic data. Three sensitivity analyses are conducted to study the influence of the material properties, size and location of the damaged zone on the results of the NCT procedure. New biomarkers based on the asymmetry of the deformation are proposed.
- **Chapter 7** presents a new FSI simulation to simulate the implant of a micro stent for the MIGS procedure and to study the aqueous humor flow after the implant. Structural simulations are conducted to simulate the implant of the device and a FSI simulation reproducing the interaction between the aqueous humor flow and the eyeball structure is run.

Finally, **Chapter 8** provides the main conclusions, original contributions and future lines of the research carried out; and **Chapter 9** the same conclusions in Spanish as requested by the doctoral program.

Part I

Methodology

2

A detailed methodology to model the Non Contact Tonometry

Part of the content of this chapter has been previously published in Frontiers in Bioengineering and Biotechnology: *E. Redaelli, J. Grasa, B. Calvo, J. F. Rodríguez Matas, and G. Luraghi, A detailed methodology to model the non contact tonometry: a fluid structure interaction study. Frontiers in Bioengineering and Biotechnology, 10 (2022), 981665.*

2.1 State of the Art

The approaches to model the Non Contact Tonometry of Corvis ST, in particular the interaction between the air puff and the structure of the eye, can be classified according to the numerical analysis adopted, which are schematized in figure 2.1. Initial studies assumed a structural FEA technique. In Eliasy et al. (2019) and Rahmati et al. (2021) the eye is the structural part with proper mechanical properties, while the action of the air puff test is simulated by a time-dependent pressure. Montanino et al. (2018) and Montanino et al. (2019) employing FEA underlined the need of modelling the filling fluid of the humors, to avoid a wrong estimate of the material properties of the eye tissues. The limitation of FEA modeling is the lack of correlation between the external load and the corneal geometry and mechanical properties. For this reason, other works (Muench et al., 2019; Nguyen et al., 2019; Huang et al., 2020) conducted a computational fluid dynamic (CFD) analysis to find the correct pressure profile to be applied to the corneal surface. The air was modelled as a fluid and the eye as a rigid body. Then, the deformable eye was loaded with the pressure profile obtained from the CFD. In these simulations, the pressure profile depends on the initial geometry of the eye, and

is not modulated by the corneal mechanical properties as happens in reality. Hence, the adoption of FSI analysis, where the structural domain is combined with the fluid domain, has become of great interest. Ariza-Gracia et al. (2018), Maklad et al. (2020b) and Issarti et al. (2021) demonstrated that the best numerical approach to reproduce the NCT is the FSI simulation. Ariza-Gracia et al. (2018) considered a 2D model, which limits the study to an isotropic cornea, Maklad et al. (2020b) and Issarti et al. (2021) used a limited fluid domain. Even though the cornea contains multi-scale structures with distinct patterns of fiber organization (Blackburn et al., 2019), to the best of authors knowledge, current FSI solutions (Ariza-Gracia et al., 2018; Issarti et al., 2021; Maklad et al., 2020b) do not account for the anisotropy of the cornea in the simulation. This chapter presents a high-fidelity fluid-structure finite-element model of an idealized 3D eye to virtually reproduce the NCT.

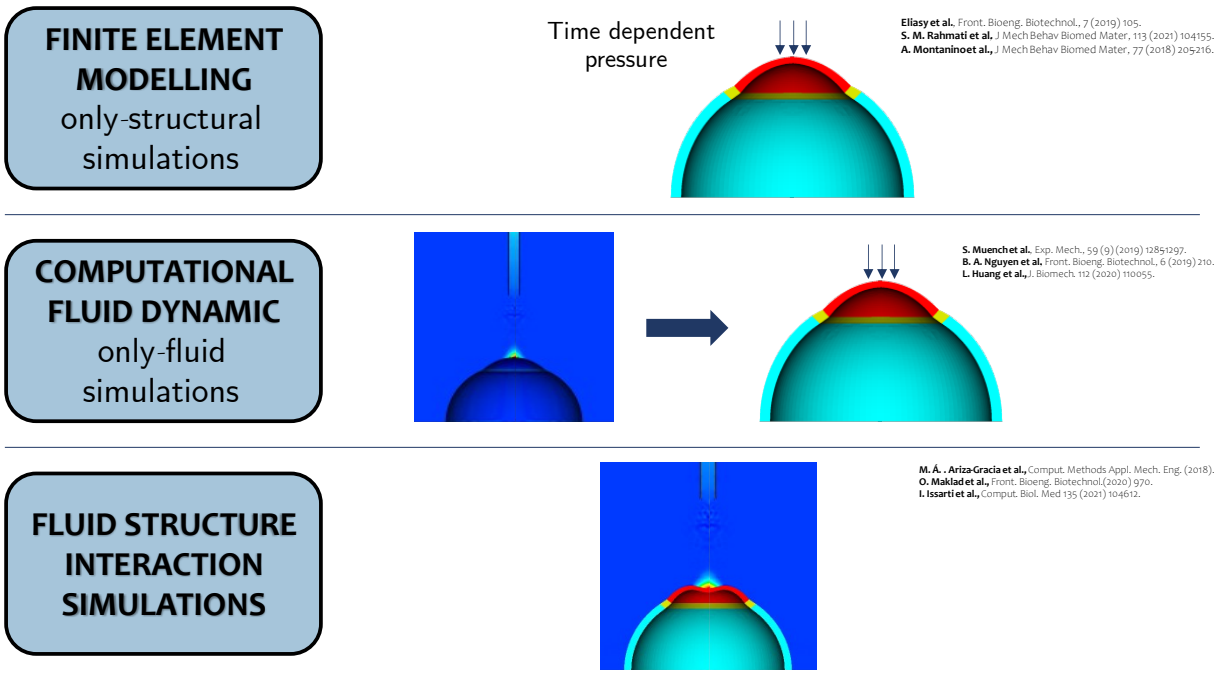

Figure 2.1: Computational methods to model the NCT. The Finite Element Modeling technique, using only structural simulations, apply a time dependent pressure on the corneal apex to simulate the NCT. With Computational Fluid Dynamic (CFD) simulations it is possible to compute the air pressure over the corneal surface to be then applied to the corneal surface. The best numerical approach is the Fluid Structure Interaction (FSI) simulation in which the structure and the fluid are coupled. In this thesis, the FSI approach will be adopted.

2.2 Materials and Methods

2.2.1 Structural model of the eye

A 3D model of an eye (figure 2.2a) is constructed based on averaged anatomic measures taken from literature (Ariza-Gracia et al., 2018; Cabeza-Gil et al., 2021). It contains cornea, limbus, sclera, crystalline lens differentiated in cortex and nucleus, aqueous and vitreous humors separated by the vitreous membrane, and ciliary zonule

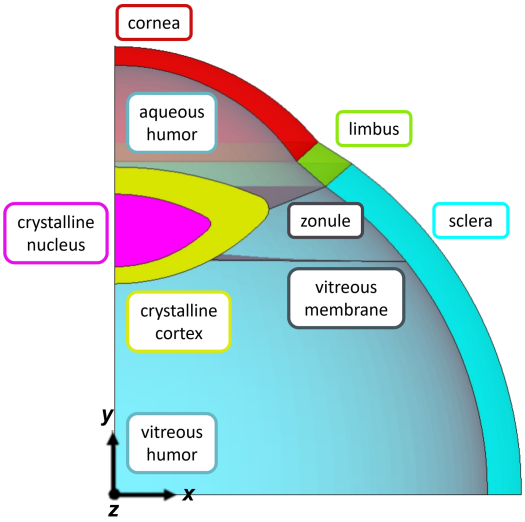

(a) Section of the 3D structural parts: cornea, limbus, sclera, crystalline lens nucleus and cortex, zonule, vitreous membrane, vitreous and aqueous humors.

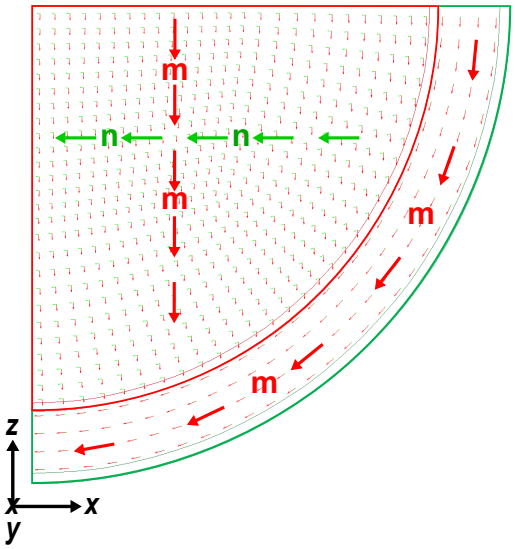

(b) Local reference systems defined in each element of the cornea and limbus to model two family of collagen fibres (**m** and **n** in the corneal plane and one family of fibres (**m**) in the tangential direction of the limbus.

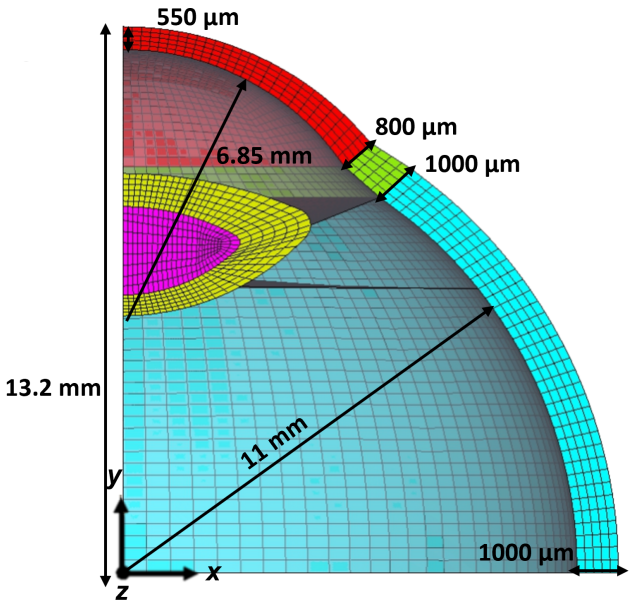

(c) Hexahedral mesh with five elements in the thickness and principal dimension of the structural model.

Figure 2.2: Structural eye model.

modelled as a thin membrane. Due to the double symmetry, only a quarter of a middle eye has been considered and symmetric boundary conditions are imposed, rigid body motions are prevented in the bottom and lateral surfaces. The eye is meshed with hexahedral solid elements (figure 2.2c) with full integration except for the vitreous membrane and the ciliary zonule meshed with quadratic shell elements with full integration (further discretization details are in the following section). The mesh is

realized through the commercially available software ANSA Pre Processor v22.01 (BETA CAE Systems, Switzerland).

The cornea and the limbus are modelled as anisotropic nearly-incompressible hyperelastic materials to account for the influence of the collagen fibres present in the tissues. In the cornea, two families of mutually perpendicular collagen fibres tangent to the corneal surface (Meek and Knupp, 2015) have been considered: i) a nasal-temporal direction coincident with the global x-axis, and ii) a superior-inferior direction coincident with the global z-axis, whereas the limbus is composed of one circumferential family of fibres as shown in figure 2.2b. The Holzapfel Gasser Ogden strain energy function (Holzapfel et al., 2000) is adopted for the cornea and the limbus

$$\Psi = C_{10}(\bar{I}_1 - 3) + \frac{k_1}{2k_2} \sum_{i=4,6} e^{k_2(\bar{I}_i - 1)^2} + \frac{1}{k}(J-1)^2, \tag{2.1}$$

where C_{10} is the material constant associated with the extracellular matrix behaviour, k_1 is the material constant associated with the fibres stiffness and k_2 with the fibres non linearity. k is the bulk modulus, in case of nearly incompressibility the parameter can be thought of as a penalty factor enforcing the incompressibility constraint. $\bar{I}_1$ is the first invariant, $\bar{I}_4$, $\bar{I}_6$ are respectively the fourth and sixth pseudo-invariants of the modified right Cauchy Green deformation tensor ($\bar{\mathbf{C}}$) and J is the determinant of the deformation gradient ($\mathbf{F}$).

$$\mathbf{C} = \mathbf{F}^T \cdot \mathbf{F} \qquad \bar{\mathbf{C}} = \mathbf{J}^{-2/3} \cdot \mathbf{C}, \tag{2.2}$$

$$\bar{I}_1 = tr(\bar{\mathbf{C}}) \qquad \bar{I}_4 = \mathbf{m} \cdot \mathbf{m}^T \qquad \bar{I}_6 = \mathbf{n} \cdot \mathbf{n}^T, \tag{2.3}$$

$\mathbf{m}$ and $\mathbf{n}$ are the vectors defining the direction of the fibres.

In this first study, the mechanical parameters of cornea and limbus are estimated fitting experimental stress strain data reported in the literature (Huang et al., 2020). The same mechanical properties have been assumed for all families of fibres. To simplify the subsequent sensitivity analysis, the sclera is modelled as an isotropic hyperelastic material with a Neo Hookean strain energy density function in which the stiffness is only defined by one parameter.

$$\Psi = C_{10}(\bar{I}_1 - 3) + \frac{1}{k}(J-1)^2, \tag{2.4}$$

C_{10} of the sclera is estimated fitting experimental stress strain data reported in the literature (Eilaghi et al., 2010). Since the deformations of the internal tissues are not large, the crystalline lens, ciliary zonule and vitreous membrane are modelled as linear elastic materials (Kim et al., 2019; Wilde et al., 2012; Krag and Andreassen, 2003). Note that, since the capsule is not included in the model, the Young modulus of the crystalline cortex is arbitrarily selected as the average of the Young modulus of the crystalline cortex reported in Wilde et al. (2012) and the Young modulus of the capsule reported in Krag and Andreassen (2003). All the material constants used in the model are reported in table 2.1.

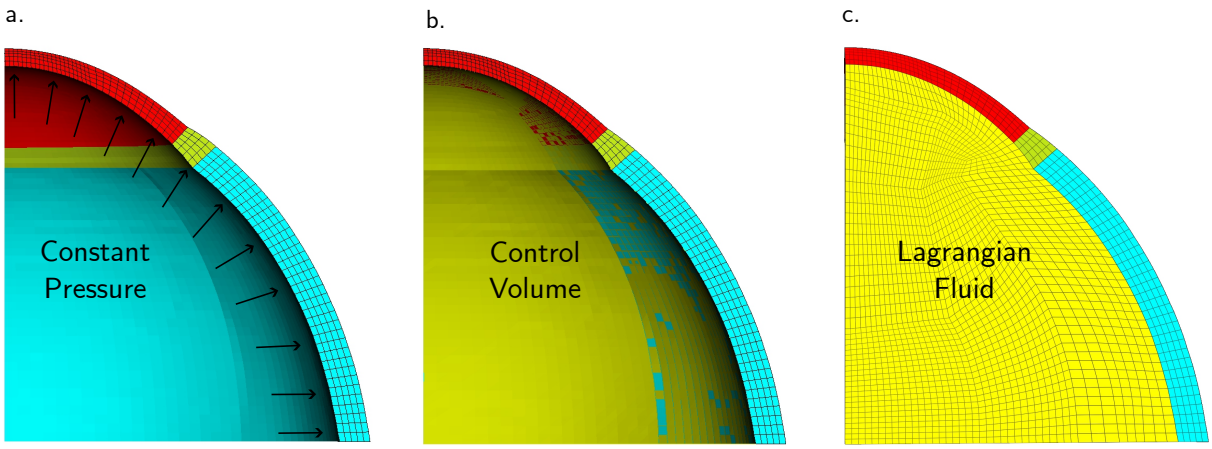

Figure 2.3: Humors formulations tested. (a) Constant pressure; (b) Control volume; (c) Lagrangian fluid.

Considerable attention must be paid to the formulation of the **humors** which are incompressible fluids pressurized at a spatially homogenous intraocular pressure (IOP). Three methodologies to model the humors are tested:

- Constant pressure approach (figure 2.3a). The internal elements of the eyeball are loaded with a constant and uniform pressure during the whole duration of the simulation.

- Control volume approach (figure 2.3b). The humors are modelled as a fluid cavity, in which the relationship between pressure and volume is controlled. Since the initial pressure of the cavity is zero, a positive input flow rate is imposed until the target IOP of 15 mmHg is reached. Then, the volume is closed, no flow is allowed to go in or out, and the humors behave as incompressible fluids.

- Lagrangian approach (figure 2.3c). The humors are modelled as a lagrangian part with mass, through a proper 3D mesh and material with the same properties of the water. The constants used in both the material and the equation of state are taken from Ariza-Gracia et al. (2018).

Since the average dimensions of the eye (figure 2.2c) corresponds to the pressurized configuration, in a first step of the simulation, the zero-pressure configuration of the eye is found through the iterative algorithm described in Ariza-Gracia et al. (2016) and implemented in Python. The algorithm used to find the zero pressure configuration is reported in Appendix B.

In addition, since a dynamic analysis is used for the structural solver, a mass weighted damping has been adopted for all the parts with a damping constant of 0.1 $m \cdot s^{-1}$. The mass weighted damping has the role of damping the oscillations associated with inertial effects.

Material properties					
Part	C_{10} [MPa]	k_1 [MPa]	k_2 [-]	ρ [g/mm^3]	Ref.
Cornea	0.05	0.010	100	0.0011	Huang et al. (2020)
Limbo	0.05	0.010	100	0.0011	Huang et al. (2020)
Sclera	0.8	–	–	0.0011	Eilaghi et al. (2010)
Part	E [MPa]			ρ [g/mm^3]	
Crystalline Lens Nucleus	0.0003			0.0011	Wilde et al. (2012)
Crystalline Lens Cortex	0.35			0.0011	Wilde et al. (2012) Krag and Andreassen (2003)
Ciliary Zonule	0.35			0.0011	Kim et al. (2019)
Vitreous Membrane	0.35			0.0011	Kim et al. (2019)

Table 2.1: Material parameters of the different eye tissues incorporated in the finite element model.

2.2.2 Mesh sensitivity analysis

A sensitivity analysis is conducted to determine the optimal mesh density of the structural model. Four different hexahedral grids are constructed by increasing the number of elements in the thickness of the eye, thus decreasing the size of the elements. Mesh data are reported in table 2.2. For each mesh, the zero-pressure configuration is computed, then the humors are pressurized at 15 mmHg. Finally, a static pressure is applied to the apex of the eye to study the apical deformation. In each case, the displacement of the apex at the instant of highest concavity is recorded as representative primary variable of the model. The error between two consecutive mesh sizes is calculated as:

$$error\ [\%] = \frac{u_{current\text{-}configuration} - u_{previous\text{-}configuration}}{u_{previous\text{-}configuration}} \cdot 100. \tag{2.5}$$

2.2.3 Fluid analysis and air puff simulation

The air domain (figure 2.4) of the NCT test was set in 50 mm (3 times the radius of the eyeball) as it was observed to minimize boundary effects on the flow over the cornea. It presents two symmetric planes and a nozzle with an inlet Gaussian air-puff velocity (with a maximum of 120 $\frac{\mathrm{m}}{\mathrm{s}}$ during a period of 20 ms) at 11 mm from the corneal apex, that is the distance between the device and the eye as reported by the manufacturers (OCULUS, 2019a). Zero pressure is imposed as an outlet boundary condition. The

Mesh Analysis		
Element in the thickness	Total number of elements	Total number of nodes
3	30236	20994
4	31991	22831
5	33746	24668
6	35501	26505

Table 2.2: Mesh data adopted in the mesh sensitivity analysis.

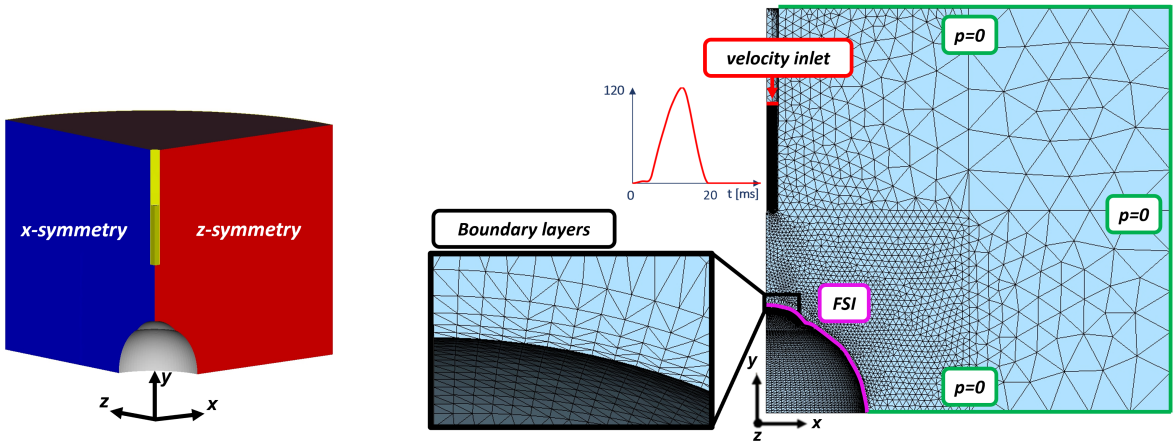

(a) 3D air domain with two symmetric planes.

(b) Surface mesh of the fluid domain with a zoom of the mesh on the 5 boundary layers at the FSI interface. Air velocity inlet in m/s (in red), pressure outlets (in green) and the FSI interface (in purple) are drawn.

Figure 2.4: 3D air domain.

automatic volume mesher of the ICFD solver fills with 212,678 tetrahedral elements the input meshed surfaces. 5 boundary layers are set at the FSI interface. The air domain is solved with an Arbitrary Lagrangian-Eulerian (ALE) kinematic approach. The air is modelled as an incompressible fluid whose density and dynamic viscosity are $\rho = 1.25\frac{kg}{m^3}$, $\nu = 1.8 \cdot 10^{-2} cP$ respectively. A turbulence model based on a variational multiscale approach is assumed. The fluid parameters are tested comparing the results of the computational fluid dynamic simulation (CFD) with the experimental results presented in Roberts et al. (2017). At the interface between the structure and the fluid a no-slip condition is adopted. NCT is simulated by a strongly coupled, 2-way and boundary fitted FSI. The NCT simulation consisted in a single step comprising the inflation of the eye at a 15 mmHg IOP in the first 30 ms, followed by 10 ms of rest, to then apply the air puff between 40 and 60 ms.

2.2.4 Material sensitivity analysis

A sensitivity analysis is performed to identify the influence of the IOP and the material constants parameters. Five parameters governing the mechanical response of the eye are analysed: the IOP; the matrix stiffness parameter C_{10-c}, the fibres stiffness parameter k_1 and the fibres non-linearity parameter k_2 of the cornea; and regarding the sclera the matrix stiffness parameter C_{10-s}. A 2^5 full factorial design which takes into account five different variables at two different levels (low and high) for a total of 32 different analysis is used. Data adopted in the analysis are reported in table 2.3. The IOP and the material parameters are considered within a 50% of variation relative to the reference value. For each case, the air-puff FSI analysis as described in section 2.2.3 is carried out and three biomarkers of the Corvis clinical test are examined:

- the deflection amplitude that is the displacement of the corneal apex at the instant of highest concavity and it gives information about the amplitude of the deformation of the cornea (Lopes et al., 2021) (appendix A).
- the peak distance i.e., the distance between the two bending peaks on the cornea's anterior surface at the instant of highest concavity. This markers gives information about the shape of the deformed cornea (Lopes et al., 2021) (appendix A).
- the air pressure at the apex of the cornea at the instant of highest concavity.

To study the main effects and the interaction effects of the input parameters on the responses, an ANOVA analysis is conducted by means of R-studio (RStudio Team, 2020).

Material sensitivity analysis				
Cornea			Sclera	IOP
C_{10-c} [MPa]	k_1 [MPa]	k_2 [-]	C_{10-s} [MPa]	IOP [mmHg]
0.25-0.75	0.005-0.015	50-150	0.4-1.2	8-22

Table 2.3: Low and high parameters tested in the material sensitivity analysis.

2.2.5 Influence of the internal structures

A FSI analysis of the NCT without the internal structures of the eye (lens, zonule and vitreous membrane) is also conducted to evaluate their influence on three selected biomarkers. The variation of the IOP during the simulation, the deflection amplitude and the peak distance are compared with the same parameters of the simulation including the internal structures.

All the simulations described were performed using an Intel i9-10940X (3.30GHz) with the finite-element solver LS-Dyna R 13.0 (LSTC, Livermore CA, USA)(Corp, 2021). The structural part is solved through a dynamic implicit structural solver, whereas the air is modelled as an incompressible fluid and solved using the implicit ICFD solver.

2.3 Results

2.3.1 Humors analysis

When the air jet deforms the corneal surface, the IOP increases due to the incompressibility of the internal fluids. The second and third approach tested, considering the humors as fluid cavity or as fluid with mass (lagrangian approach), exhibit an IOP increment close to 2-3 times the physiological IOP, consistent with Ariza-Gracia et al. (2018). The results in terms of corneal deformation reveal distinct patterns. Modeling the humors as a load leads to a higher deflection amplitude of the eye, as the internal pressure remains constant. Conversely, using a control volume or a Lagrangian approach shows a reduction of the deflection amplitude during the air puff. This implies that neglecting the incompressibility of the humors affects the maximum displacement of the cornea. Consequently, overlooking the incompressibility of the humors would result in an overestimation of corneal stiffness. For this reason, assuming a uniform pressure during the simulation of the NCT test is inaccurate. On the other hand, the lagrangian approach has a significantly higher computational cost if compared to the control volume. Since the results in terms of corneal deformation are similar, the control volume approach is used for all the simulations presented in the following sections.

2.3.2 Mesh sensitivity analysis

The results for the mesh sensitivity analysis are reported in figure 2.5. As expected, the simulation time increases with the number of degrees of freedom in the model. The maximum apical displacement in the four cases ranges between 1.08 and 1.10 mm with the maximum error of 1.1% between the coarsest mesh and the mesh with four elements in the thickness. Based on the mesh convergence study, the mesh with five elements in the thickness is chosen for all the FSI simulations, which shows an error below 1%.

2.3.3 Fluid analysis

In order to test the imposed boundary condition of the air-puff, a simulation of the air-puff with the fluid domain defined as described in paragraph 2.2.3 but without the eye has been carried out, to reproduce the results in Roberts et al. (2017). The fluid velocity during the air-puff at different distances from the nozzle along the centerline is recorded and reported in figure 2.6.

The range of the peak velocity (from 130.55 m/s at 2 mm to 119.9 m/s at 10 mm)

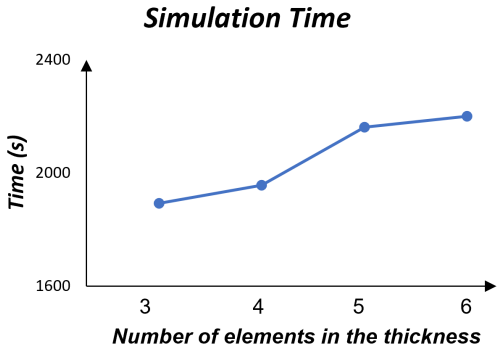

(a) Simulation time.

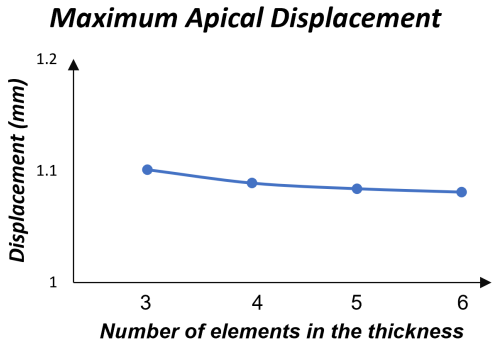

(b) Displacement of the apex at the instant of maximum concavity.

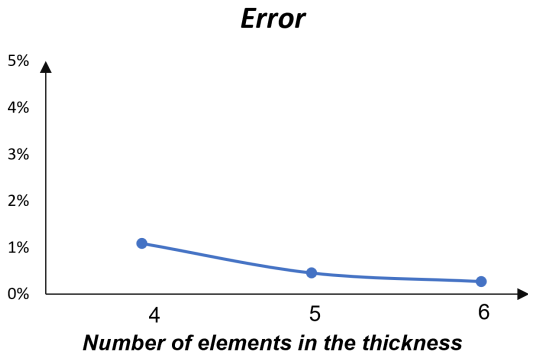

(c) Percentage error between consecutive mesh.

Figure 2.5: Mesh sensitivity analysis. The plots are functions of the number of elements in the thickness.

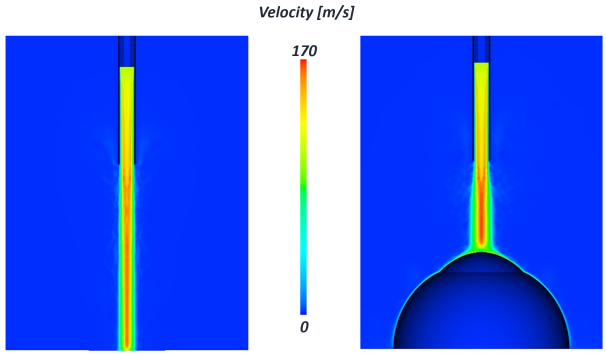

(a) Contour of the air peak velocity in the CFD simulation without the eye shape and with the eye shape.

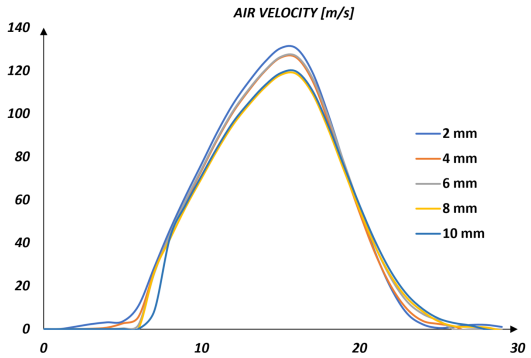

(b) Centerline velocity distribution as a function of the distance from the nozzle used to test the fluid parameters in the case without the eye shape.

Figure 2.6: Fluid Analysis.

from the numerical simulation was within the range reported in the experiments (from 133.57 m/s at 2 mm to 127.43 m/s at 10 mm) indicating that the time velocity profile

used as boundary condition was appropriate to describe the air-puff.

2.3.4 FSI analysis

One of the main objectives of the NCT is the evaluation of the IOP based on the Imbert-Fick principle, which states that in a flattened spherical body with an infinitely thin, dry, and elastic membrane wall, the internal pressure equals the force applied on the body divided by the applanation surface. Knowing the pressure exerted by the air puff and the applanation area derived from the images of Corvis ST Scheimpflug camera, the IOP is derived (Gonzalez Castro et al., 2016). Our simulation shows that the IOP varies during the NCT (figure 2.7a). Since the eye is a closed volume filled with incompressible fluids, when the air jet deforms the corneal surface, the IOP increases reaching 22.5 mmHg (+50%).

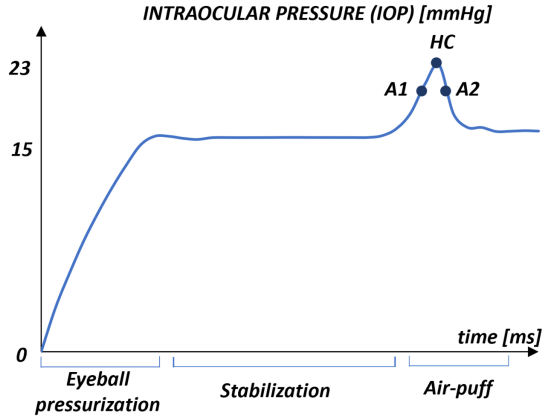

(a) Variation of the intraocular pressure (IOP) during the NCT simulation. The first applanation point (A1), highest concavity point (HC) and second applanation point (A2) are highlighted.

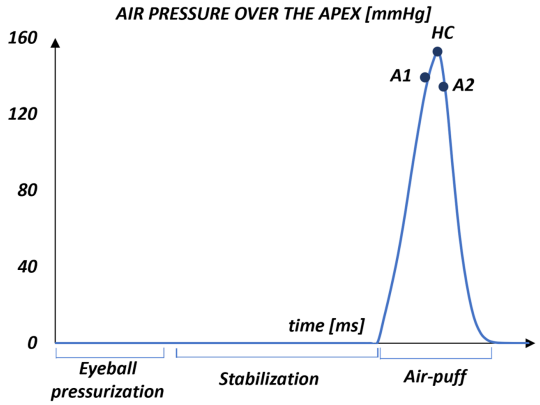

(b) Air pressure over the corneal anterior surface during the NCT simulation.

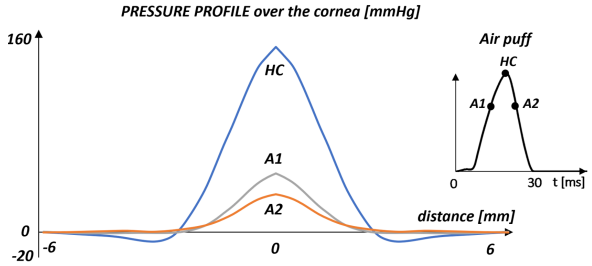

(c) Pressure profile over the cornea in three significant instants of the simulation as a function of the distance from the apex.

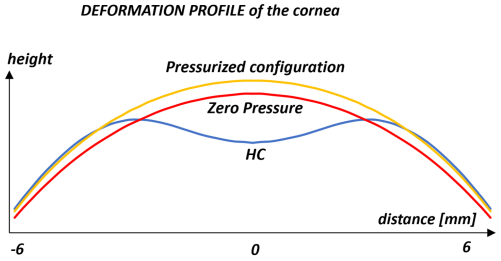

(d) Corneal profile in the zero pressure configuration, with an intraocular pressure of 15 mmHg and at the instant of highest concavity (HC).

Figure 2.7: Results of the FSI simulation.

On the air side, the pressure-time variation at the corneal apex during the air-puff is shown in figure 2.7b. The maximum pressure in the apex, 152 mmHg, corresponds with the instant of maximum concavity of the cornea ($t = 55$ ms). The air pressure exerted over the corneal surface is reported in figure 2.7c for A1, A2 and HC as a function of

the distance from the apex. As expected, the maximum pressure is located at the apex of the cornea to then decrease. In the three cases, the pressure is zero for a distance from the apex higher than 5.5 mm, meaning that from this position, the eye does not perceive directly the air jet, the pressure component is negligible, and the flow follows the eye shape. In the instant of HC, there is a region where the air pressure is negative lending support to previous findings in the literature (Muench et al., 2019)(Ariza-Gracia et al., 2018)(Maklad et al., 2020a). Negative pressure occurs if the fluid reflects from the corneal surface in the opposite direction to the flow, causing the change of concavity of the cornea in the deformed state (figure 2.7d, curve HC). The maximum pressure at A1 is higher than the maximum pressure at A2, due to the energy loss caused by the damping of the cornea and the deceleration of the air-jet during this phase of the test.

The deformation profile of the cornea is reported in figure 2.7d where it is possible to appreciate the difference between the undeformed shape of the cornea's central section in the zero-pressure configuration, in the pressurized configuration, and in the instant of highest concavity (HC). In the instant of HC, the deflection amplitude of the apex is 1.14 mm found to be within the range of clinical data (1.09 ± 0.10) (Roberts et al., 2017). The contours of the air velocity in three significant points of the simulation are reported in figure 2.8. In the instant of highest concavity the velocity (172m/s) is higher than the inlet velocity due to an acceleration caused by the turbulent flow and the obstacle that the air meets, the eye structure.

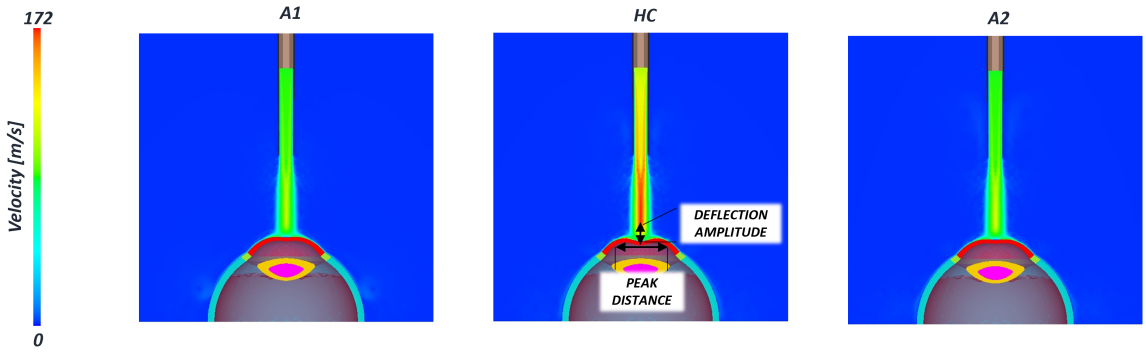

Figure 2.8: Air velocity contour in three-time points (A1, HC and A2) during the air-puff. In the instant of highest concavity two biomarkers (peak distance and deflection amplitude) are highlighted.

Physiologically, the cornea works in tension because of the IOP. However, during the air-puff, the cornea undergoes bending, therefore its anterior surface changes its state of tension to a compression state, whereas the posterior surface carries on working under tension as shown in the contour of the stress at the instant of HC (figure 2.9). This means that the collagen fibres in the anterior surface do not contribute to load bearing during most of the duration of the air-puff, relying in this case on the mechanical properties of the matrix under compression. The evolution of the normal stress and strain values of two points of the apex (anterior and posterior surfaces) is plotted in figure 2.9. As anticipated, the plot demonstrates the contribution of the collagen fibres

when the cornea is subjected to tension because, after a first response of the matrix, a stiffer behaviour is reported. In compression (blue values), only the matrix contribution is present resulting in a more compliant response.

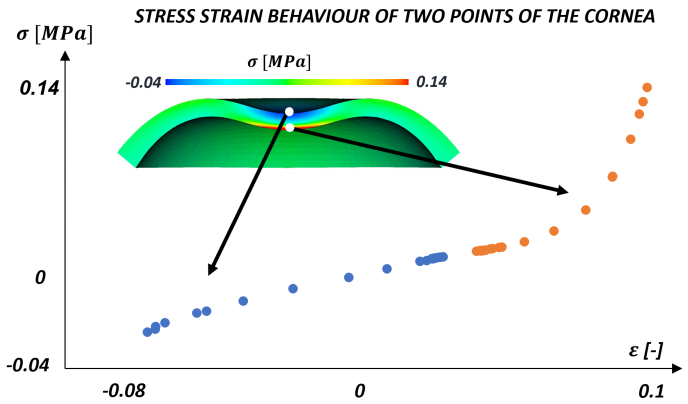

Figure 2.9: Evolution of normal stresses and strains at two locations (anterior and posterior) during the air puff. At the beginning of the air-puff both points are at a tension state due to the IOP. Then, during the air-puff, the anterior surface works in compression (blue) and the posterior in tension (red) with the contribution of the collagen fibres.

2.3.5 Material and IOP sensitivity analysis

The results of the ANOVA analysis for the biomarkers are reported in table 2.4 and table 2.5. For both the deflection amplitude and the peak distance, the IOP is the most important parameter followed by the matrix stiffness of the cornea, C_{10-c}, with the other material parameters having little effect on the response. However, the effect size of the IOP is more than tenfold the size effect of C_{10-c}. However, this could be associated with the relatively large range of IOP considered in the design of experiments. The results from the ANOVA also indicate a little interaction between the effects, being the $C_{10-c}\cdot$ IOP interaction and the $C_{10-s}\cdot$ IOP the most important, though very low with respect the effect of the singles (see table 2.4).

The Pearson correlation matrix in figure 2.10 reports the results for the statistical analysis conducted. The dimension of each circle is related to the correlation between the factors of the design of experiment (C_{10-c}, k_1, k_2, C_{10-s}, IOP) and the dependent variables considered (deflection amplitude, peak distance, and air pressure over the apex). The colour of each circle tells whether the linear correlation is direct (blue) or inverse (red). The most important result that emerges from the data is the inverse correlation between the IOP and the deflection amplitude and the peak distance. As the IOP increases, the air pressure encounters a higher mechanical resistance, the deformation of the cornea is lower and, as a consequence, the deflection amplitude and the peak distance are lower. The figure also shows that the maximum air-pressure at the corneal apex is little influenced by the IOP and the material properties of the cornea and sclera.

ANOVA for the Deflection Amplitude		
Source	DF	Effect
Linear	5	
C_{10-c}	1	0.27
k_1	1	0.03
k_2	1	0.14
C_{10-s}	1	0.14
IOP	1	4.01
2-way interactions	2	
C_{10-c}· IOP	1	0.03
C_{10-s}· IOP	1	0.03

Table 2.4: Analysis of variance (ANOVA) results on the deflection amplitude. Degrees of freedom (DF) and Effect size.

ANOVA for the Peak Distance		
Source	DF	Effect
Linear	5	
C_{10-c}	1	0.86
k_1	1	0.17
k_2	1	0.37
C_{10-s}	1	0.15
IOP	1	17.05

Table 2.5: Analysis of variance (ANOVA) results on the peak distance biomarker. Degrees of freedom (DF) and Effect size.

Given that these findings are based on two IOP levels of 8 and 22 mmHg, (values reached when the intraocular pressure is very low and when the patient presents glaucoma), a further analysis is conducted with the IOP ranging between 12 and 15 mmHg (the physiological range) and all the other parameters as described in section

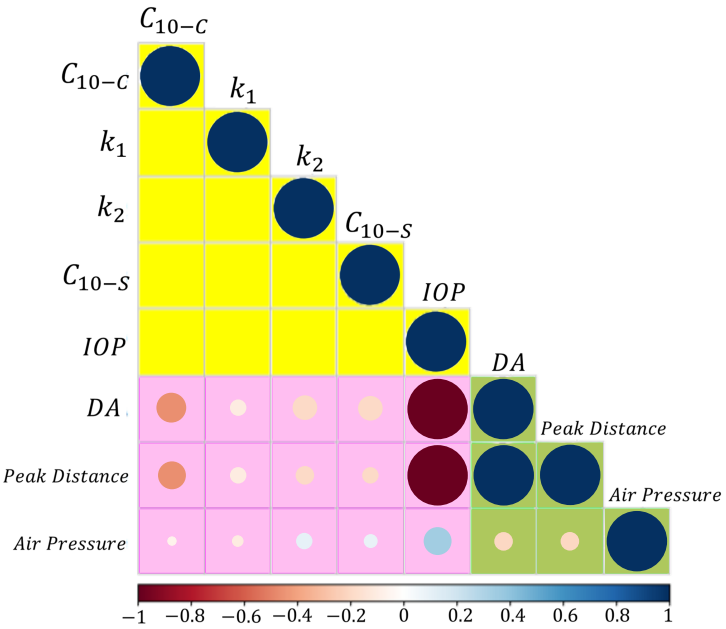

Figure 2.10: Pearson correlation matrix (full-level factorial design, $2^5 = 32$). Factors: matrix stiffness of the cornea (C_{10-C}), fibres stiffness of the cornea (k_1), fibres non linearity of the cornea (k_2), matrix stiffness of the sclera (C_{10-s}), intraocular pressure (IOP). Output parameters: deflection amplitude (DA), peak distance and air pressure over the cornea at the instant of maximum concavity. The colour of each circle depicts whether the linear correlation is direct (positive) or inverse (negative) (blueish palette, direct; reddish palette, inverse). The larger the circle diameter, the higher the correlation.

2.2.3. The main effect of the parameters on the deformation amplitude and the peak distance is shown in figure 2.11. Each line depicts the difference in the mean response between the two levels of a factor, as long as each point represents the mean result for one level of a factor. The horizontal line indicate the average for all runs.

The results obtained for this reduced range of IOP are consistent with those shown in figure 2.10, i.e., an inverse relationship with the corneal displacement and peak distance. However, within the physiological range of the IOP, the mechanical properties of the sclera have the same influence as the corneal matrix stiffness, whereas the anisotropic component of the cornea appears to plays a more important role on the corneal deformation against an air-puff.

2.3.6 Influence of the internal structures

The results for the analysis of the influence of the internal structures of the eye is reported in table 2.6. The influence of the crystalline lens, the ciliary zonule and the vitreous membrane on the biomarkers was found to be always below 5%, meaning that they could be removed from the model improving the computational efficiency.

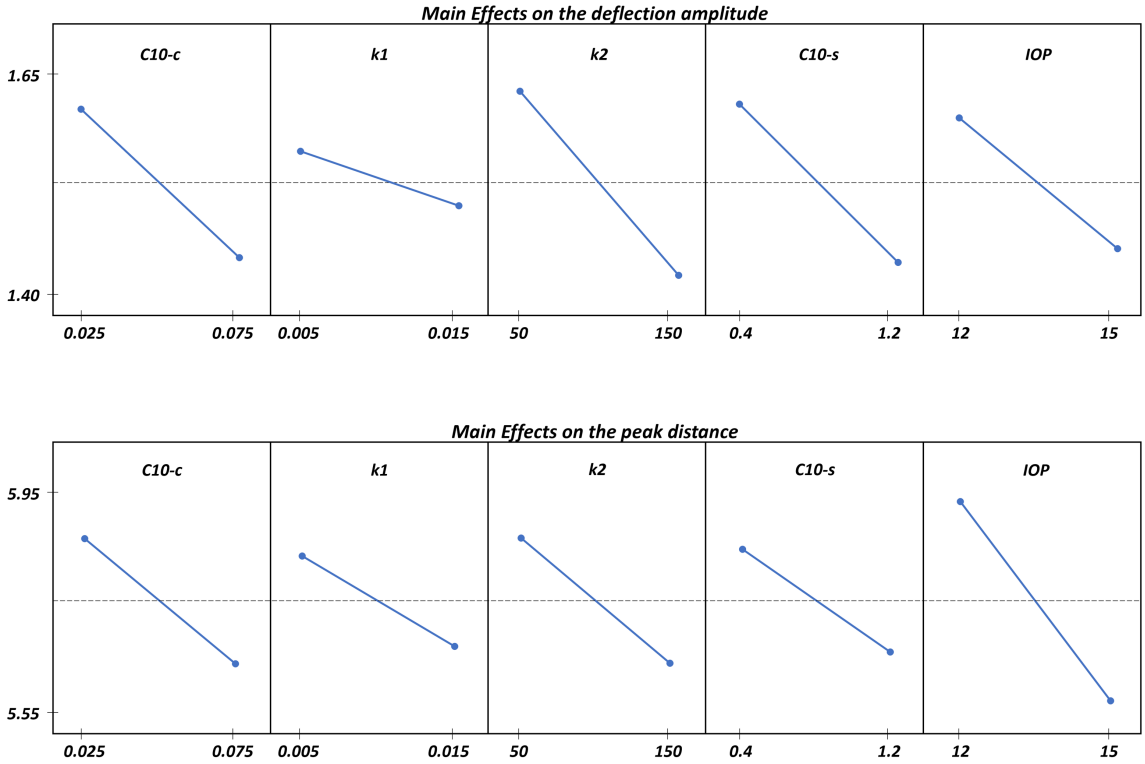

Figure 2.11: Main Effects plot of the analysed factors on the deflection amplitude and on the peak distance. All the parameters show an inverse influence on the results.

Influence of the internal structures of the eye			
Biomarker	With internal structures	Without internal structures	Error
IOP max	22.40 mmHg	23.25 mmHg	3.7%
Deflection amplitude	1.402 mm	1.445 mm	3%
Peak distance	5.54 mm	5.60 mm	1.16%

Table 2.6: Influence of the internal structures of the eye on the biomarkers.

2.4 Discussion

The deformation of the cornea during the NCT stems from the combination of different biomechanical factors; hence, to identify the influence of each factor, an in-silico study is necessary. To the best of the authors knowledge, this is the first complete methodology capable to model the NCT using FSI considering an anisotropic formulation for the cornea and a complete fluid domain for the air. The results confirm the need of using FSI for the correct simulation of NTC as stated in Ariza-Gracia et al.

(2018). The use of FSI, instead of only structural FEA, is key to capture the correct air pressure distribution over the cornea during the air-puff. The simulations show that the interaction of the air-puff with the deformable cornea causes a confinement of the flow in the proximity of the cornea (about 3.5 mm from the corneal apex) that increases the velocity of the jet-stream near the centerline with respect to what is seen in a free-flow condition (without obstacles) shown in figure 2.6. This increment in the kinetic energy of the flow causes that the maximum pressure in the cornea reaches values of 152 mmHg, coincident with the moment when the air-puff reaches the maximum speed. Previous works estimated the pressure profile in the cornea as the dynamic pressure associated with the air-puff velocity profile (Ariza-Gracia et al., 2015; Nguyen et al., 2019). However, doing so, the maximum pressure on the cornea maybe greatly underestimated as demonstrated in this study where the dynamic pressure associated with a velocity of 120 m/s results in 67 mmHg, almost half of the pressure obtained with the FSI analysis. The FSI proposed is 2-way and strongly coupled, thus iteratively the solid mechanics solver transfers the displacements of the eyeball to the fluid solver while the fluid solver transfers the air pressure to the solid mechanics solver. Thanks to this interaction, it is possible to appreciate the negative pressure in correspondence to the corneal peaks at the instant of maximum concavity, thus the dependence of the pressure on the biomechanical behaviour of the eyeball tissues.

The sensitivity analysis demonstrates the important role of the IOP on the corneal biomarkers during NTC. This effect has been found to be comparable to the effect of the material properties of the cornea and the sclera as reported in previous studies based on structural analysis (Ariza-Gracia et al., 2016, 2017b). These results demonstrate the interplay between the mechanical properties of the eye and the IOP and the importance of taking into account this interaction when interpreting the results from a NTC test. Regarding the influence of the material properties, the sensitivity analysis confirms the results from (Ariza-Gracia et al., 2016, 2017b) about the importance that corneal anisotropy has on the corneal biomarkers extracted during a NCT test, in particular for values of the IOP within the physiological range. This demonstrates the need of accounting for the anisotropic behaviour of the cornea in the models of the eye. At the instant of maximum concavity, the anterior surface of the corneal section works under compression, whereas the posterior surface works under tension. During tension, the collagen fibres are recruited which increases the corneal stiffness, and the load bearing capacity of the tissue. In fact, the material sensitivity analysis shows a contribution of the fibres parameters on the deformation amplitude and on the peak distance comparable to the extracellular matrix of the cornea.

Another remarkable result emerging from the material sensitivity analysis is the importance of the sclera: the stiffer the sclera, the lower the corneal deformation to the air-puff. Nguyen et al. (2019) reported a similar trend in a computational-experimental work with ex-vivo human donor eyes. This indicates that an accurate model of the eyeball to simulate the response to an air-puff should incorporate the sclera since otherwise the corneal displacements will be understimated. On the contrary, the sensitivity analysis shows a negligible effect of the remaining internal structures of the eye i.e., crystalline lens, ciliary zonule and vitreous membrane. This occurs in great part because

of the lower stiffness of the components as happens with the zonule and the vitreous membrane which cause the crystalline lens to show a rigid body like motion during the NTC test. Hence, depending on the aim of the simulation, the internal structure could be neglected. Last but not least, the simulation corroborates the findings from Montanino et al. (2018, 2019); Ariza-Gracia et al. (2018) that the humors need to be modelled as a fluid-like material with a specific density when simulating a NCT test. Since the eye-ball is a closed system and the humors behave as an incompressible fluid, the deformation of the cornea during the air-puff causes an increase in the IOP up to a 50% of the nominal value. Most experimental works regarding indentation (Ariza-Gracia et al., 2017a; Ortillés et al., 2017) or NTC (Nguyen et al., 2019) tests, impose a constant pressure in the eye-ball during the test by means of a column of water, which makes the humor to behave as an open system, contrary to what really happens during the actual test. The important influence that IOP has on the deformation of the cornea during the air-puff, makes that considering it as constant in the simulation causes an understimation of the corneal deformation, and therefore to overstimate the corneal stiffenss as a consequence.

3

Validation of the methodology

3.1 Introduction

The achieved work described in chapter 2 was to design a methodology to develop a 3D FSI simulation of the NCT. The study was based on an idealized geometry and the carried out sensitivity analysis did not consider the variability in the geometry which may significantly affect corneal deformation as shown in Ariza-Gracia et al. (2015, 2016, 2017b). In this context, this chapter objective is to consider patient-specific geometries in order to quantify the variability in corneal biomarkers associated with the intrinsic geometric variability of the eye-ball and validate the methodology against clinical data. To achieve the objective, the following tasks are presented.

- Generate an extensive dataset using Montecarlo simulations based on models with patient-specific geometric features that simulate the NCT test.
- Demonstrate that during the NCT, the mechanical properties of the corneal tissue and the IOP are coupled.
- Validate the FSI simulation proposed in chapter 2 against clinical OCULUS Corvis ST ®(OCULUS, 2019a) data.

3.2 Materials and Methods

An extensive dataset of corneal deformations during NCT was generated through Monte Carlo simulations, following the Fluid Structure Interaction (FSI) model devel-

oped previously. To apply the methodology to the simulation of a large number of patients, an algorithm in Python has been developed that fully automates the simulation of the Corvis ST with different input parameters (IOP, mechanical properties, and corneal geometry). The process is depicted in figure 3.1 and it will be detailed in the following sections. The process of building the input file and randomly selecting parameters is fully automated and takes a few seconds.

3.2.1 Patient Specific Geometries

21 healthy patient-specific corneal geometries with thickness ranging from 484 to 588 μm were constructed based on Pentacam data. The data used were randomly selected from a previous study conducted at Antwerp University Hospital (reference number of the Antwerp University Hospital Ethical Committee: 17/12/136). That study was conducted following the principles of the Declaration of Helsinki, and participants provided signed informed consent before measurement. Pentacam is a tomographer which creates an elevation map and a pachymetry map (corneal thickness measured in microns) of the cornea. The elevation map is composed of a point cloud of the anterior surface of the cornea. By subtracting point to point the pachymetry data from the elevation data, the posterior point cloud data was achieved. The available topographic data are limited to a corneal area between 8 and 9 mm in diameter. However, a corneal diameter of 12 mm is needed to build the 3D Finite Element model to be incorporated in the FSI simulation. To achieve a 6 mm radius cornea, the point cloud of each patient, was adjusted by Zernike Polynomials of sixth order (Wang et al., 2022; Wei et al., 2021). The patients analysed were healthy, without corneal geometry complications. Once the anterior and posterior surfaces were extended to 12 mm diameter, the models were meshed with hexahedral solid elements by the Pre processor ANSA (Beta CAE). The patient specific cornea was then linked to a model of limbus and sclera with the dimensions presented in chapter 2 to construct the input file of the FSI simulation. The fluid model and the relative boundary conditions are the same as chapter 2.

3.2.2 Material parameters and IOP

300 FSI simulations were executed, varying the mechanical properties of corneal tissue within a range found in literature (Ariza-Gracia et al., 2017b), coupled with IOP values ranging from 8 to 30 mmHg. A uniform distribution of input variables was assumed since there is no a priori data on the dispersion of the mechanical parameters in the human cornea, and therefore a total ignorance about the population is assumed. 100 simulations were performed on one single corneal geometry, to study the influence of IOP and mechanical properties of the corneal tissue on the results of the NCT. Then, for each of the remaining 20 patients, 10 simulations were performed. The same materials formulations presented in chapter 2 was used. The range of parameters adopted in the Montecarlo simulation are the following:

- C_{10} [MPa] $\in$ (0.010; 0.071)

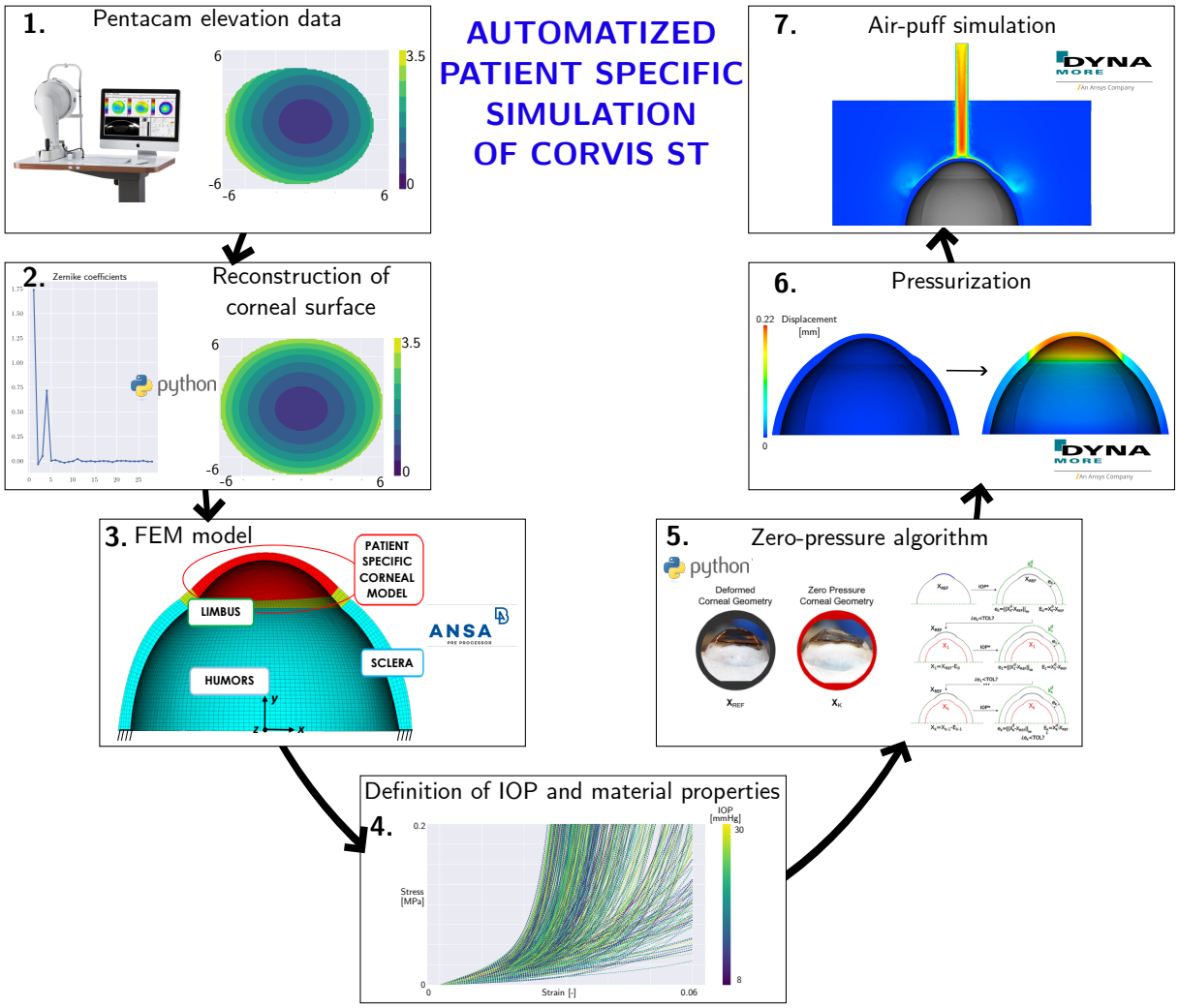

Figure 3.1: Automatized process to run the patient-specific simulations. Corneal elevation data obtained from the Pentacam topographer (1.) are extended using the Zernike polynomial approximation (2.), and the geometric and finite element model is constructed based on this data (3.). Each patient-specific cornea model is combined with average-sized limbus, sclera, and humors models. Different mechanical properties of the corneal tissue and IOP are defined in each simulation (4.). Then, after finding the zero-pressure configuration of the eye (5.), the simulation is run involving two steps: the pressurization of the eye (6.) and the air-puff simulation (7.).

- k_1 [MPa] $\in (0.015; 0.130)$
- k_2 [MPa] $\in (10; 997.5)$

The range considered comprises the mechanical response of the cornea found experimentally in literature (Nambiar et al., 2023; Xue et al., 2018; Maklad, 2019).

The result of one FSI simulation is depicted in figure 3.2. For each simulation, the anterior and posterior surfaces of the Nasal Temporal (NT) section of the cornea were recorded at each 0.21428 ms, the same output frequency of Corvis ST. The deformation

of the NT section of the cornea during the air puff was therefore obtained. From these results, the Corvis ST biomarkers were calculated for each simulation and the air pressure over the apex of the cornea was recorded.

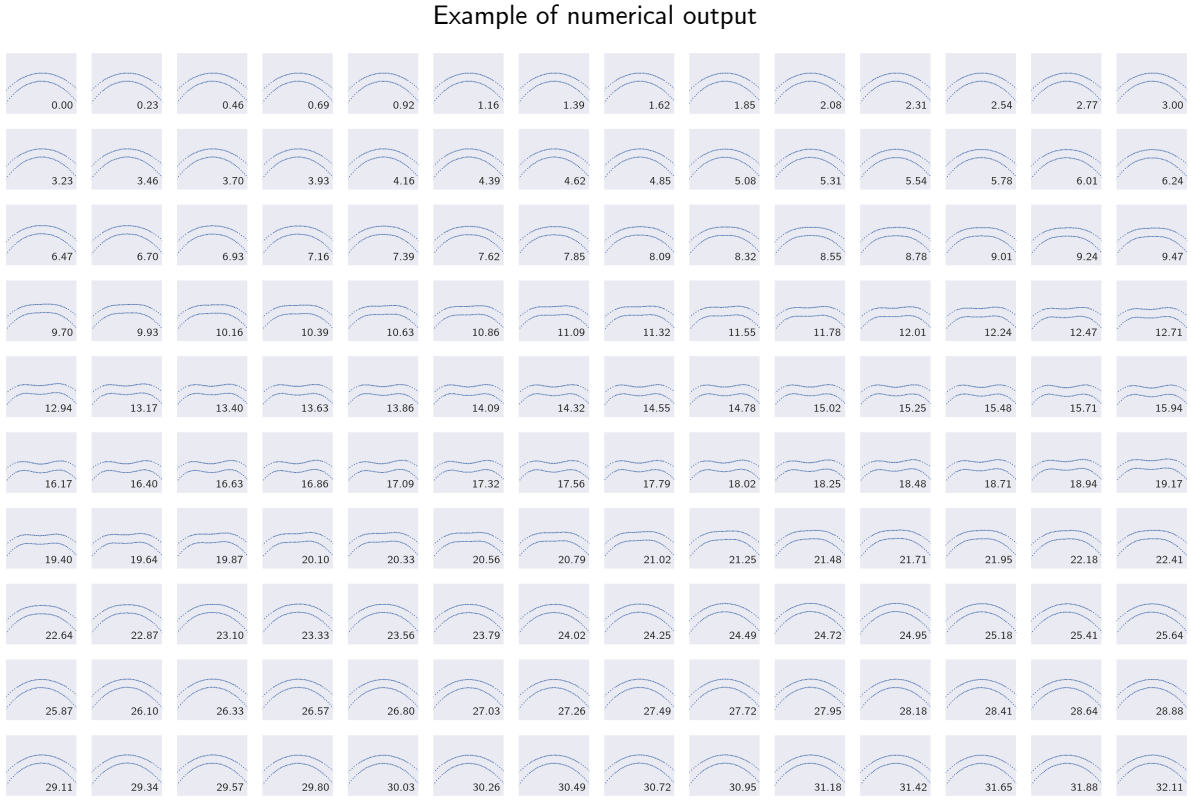

Figure 3.2: Example of FSI results. Deformation of the NT section of the cornea for different times during the simulation. The numbers reported indicate the time of the air-jet in ms.

3.3 Results

3.3.1 Coupling between mechanical properties and IOP

For patient ID 181, an extensive analysis was conducted through 100 simulations, wherein the mechanical properties of the corneal tissue and IOP were systematically altered. The outcomes of these simulations are presented in figure 3.3, illustrating the deformation results obtained in the instant of highest concavity. The deformation of the cornea is different in each simulation depending on the mechanical properties of the corneal tissue and on the IOP.

The analysis delved into computing several biomarkers given as clinical output of the device. Specifically, the deflection amplitude, peak distance, and apex velocity were analysed. In figure 3.4a, the deflection amplitude for the entire dataset of simulations is depicted, with the clinical result for the specific patient highlighted in red. Remarkably, the clinical result falls within the range of the numerical results, affirming the capability of the tested parameters to accurately characterize the real behaviour of a human cornea.

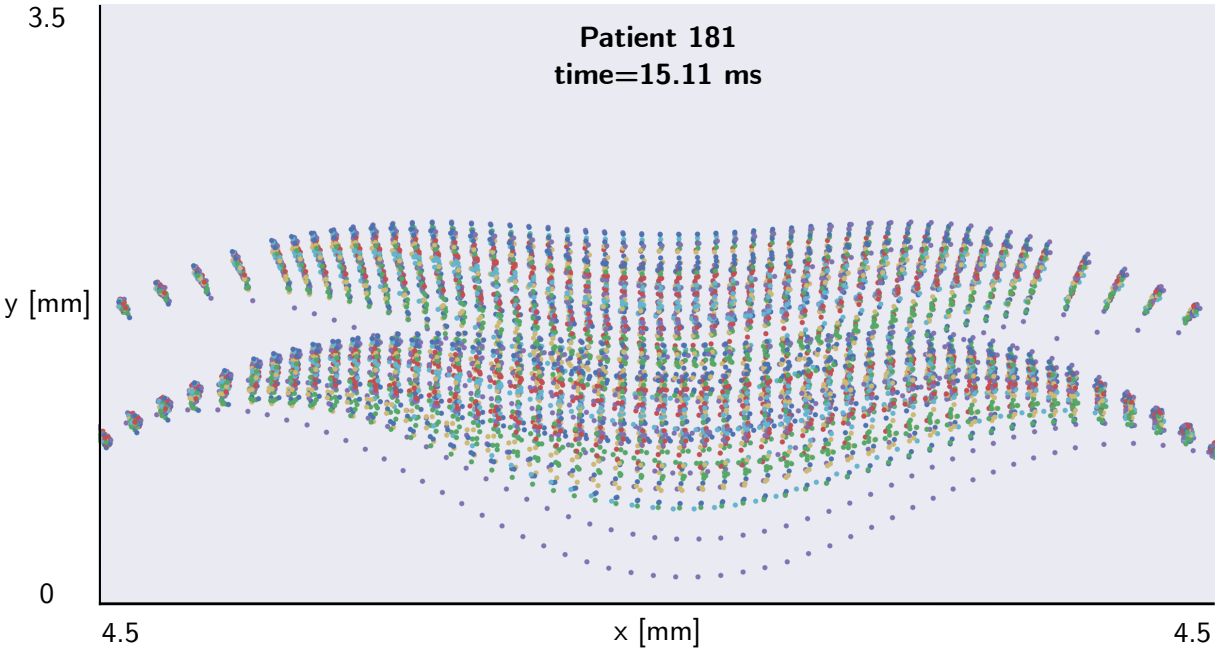

Figure 3.3: Deformation of the NT section of the cornea for the 100 simulations of patient 181 in the instant of maximum concavity. The difference in the deformation is caused by the different material properties and IOP.

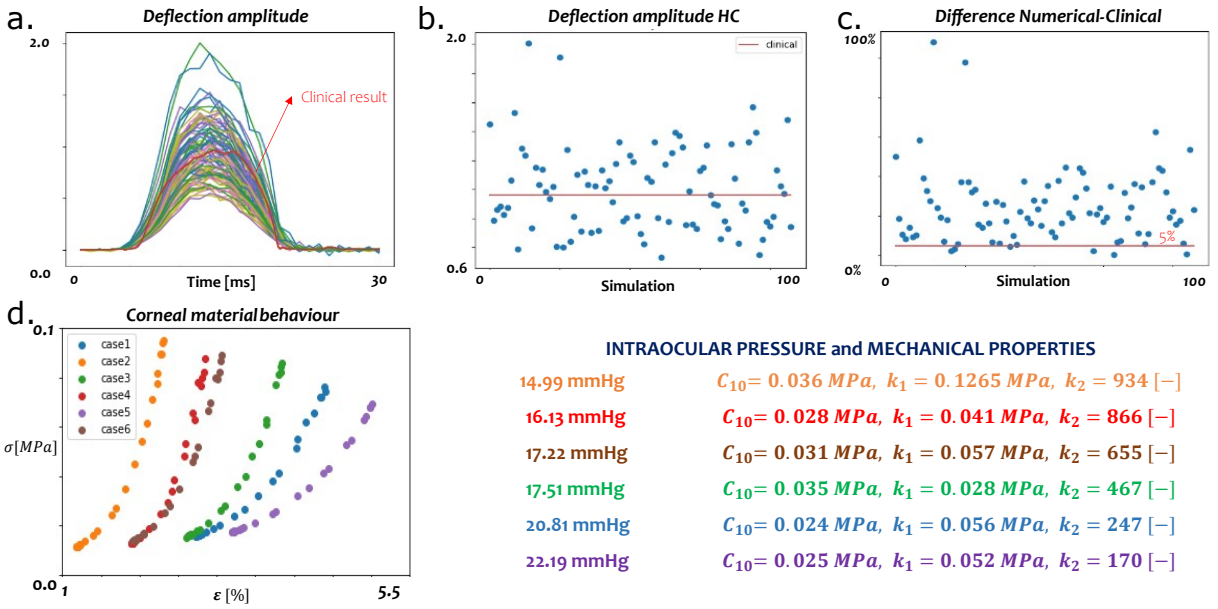

Figure 3.4: Analysis of the biomarkers of patient 181. (a) Evolution of deflection amplitude in time. (b) Deflection amplitude at the highest concavity point, (c) Difference between numerical and clinical maximum deflection amplitude. (d) Stress strain curves of the corneal tissues in the case where a difference less than 5% was recorded.

Examining the deflection amplitude at the highest concavity (HC) in figure 3.4b, values ranging between 0.6 and 2 mm were observed, aligning with the physiological range of Corvis. For the patient under consideration, the deflection amplitude at HC was measured at 0.964 mm. Six numerical cases exhibited a difference of less

than 5% compared to the deflection amplitude at HC measured in clinical settings. In-depth analysis of these cases involved an analysis of the mechanical properties of the corneal tissue. In figure 3.4d, the stress-strain behaviour of selected elements of the cornea during the air puff is graphically represented for those cases. Notably, to achieve an identical deflection amplitude at HC, the stiffer mechanical behaviour of the tissue was associated with a lower IOP, and vice versa. This relationship between mechanical properties and IOP underscores the intricacies of corneal biomechanics. Further exploration of computed biomarkers for these six cases did not reveal significant differences. Moreover, a comparative analysis of the deformed shape of the cornea in each simulation demonstrated uniformity across those cases. This comprehensive examination highlights the coupling between the mechanical properties of the corneal tissue and IOP in the context of a NCT. The findings not only enhance our understanding of corneal biomechanics but also emphasize the importance of considering these interdependencies in clinical assessments.

3.3.2 Validation of the methodology

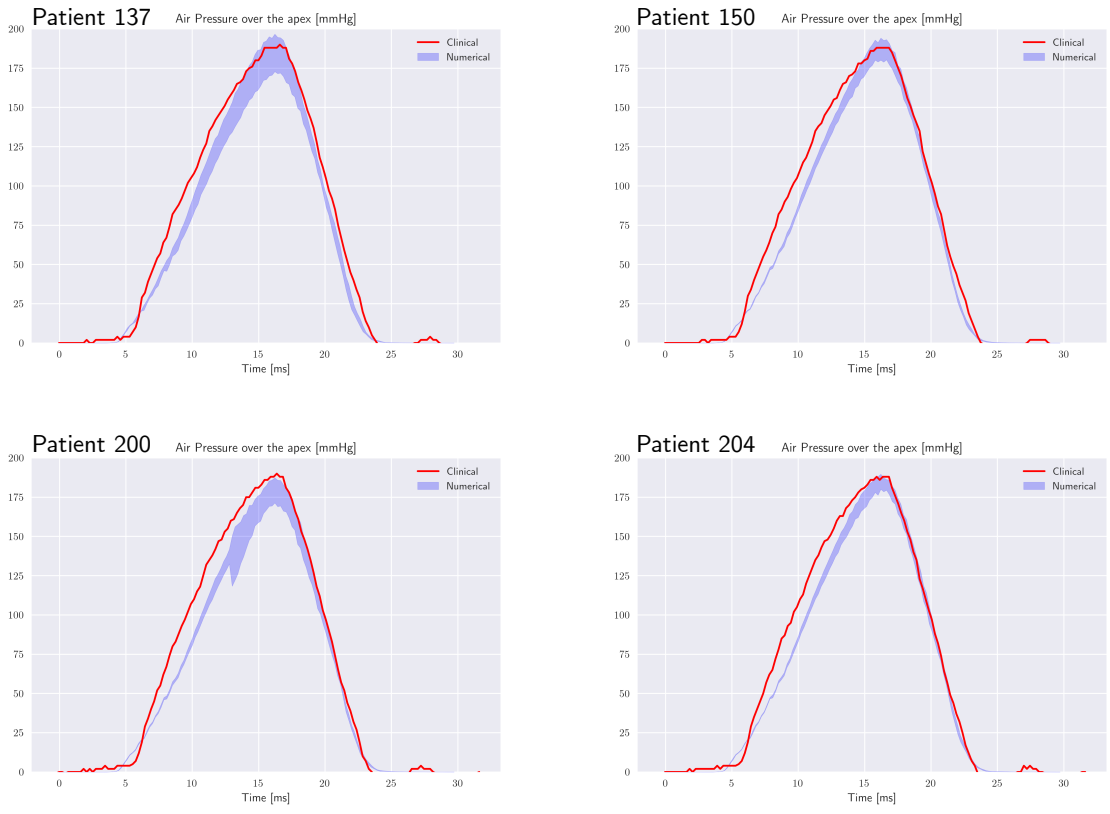

Figure 3.5: Air pressure over the apex for 4 selected patients. Clinical result (red) against average and standard deviation results for the 10 numerical simulations computed for that patient.

In this section, the validation of our FSI simulation model is presented. To validate the model, two parameters were studied: the air pressure over the apex and the deflection amplitude. These parameters, fundamental to understanding corneal biomechanics, are pivotal in ascertaining the fidelity and accuracy of our simulation

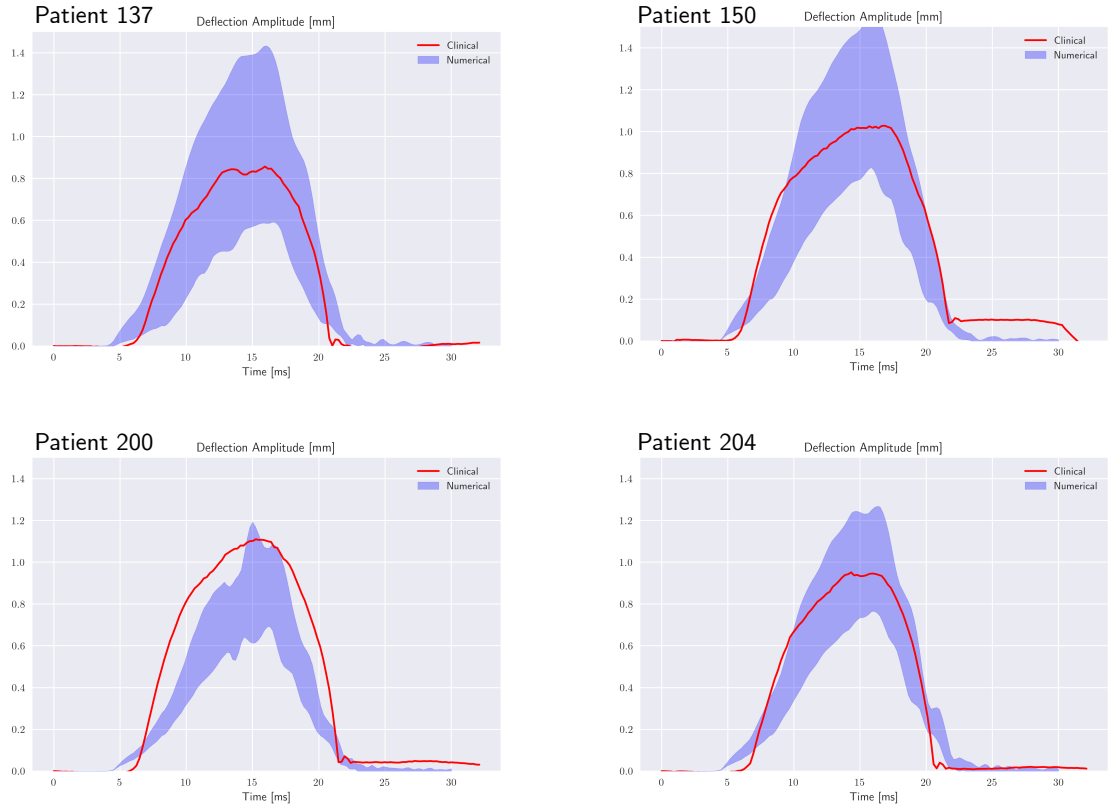

Figure 3.6: Deflection amplitude in time for 4 selected patients. Clinical result (red) against average and standard deviation results for the 10 numerical simulations computed for that patient.

model in replicating real-world scenarios. Figure 3.5 graphically depict the temporal evolution of the air pressure over the apex for four selected patients of the Montecarlo simulation which serves as representative cases. The clinical result is represented in red, while regarding the numerical results, the area covered by the whole dataset of simulations is plotted. The same is presented for the deflection amplitude in figure 3.6. Analysing the temporal variations in air pressure and deflection amplitude we can notice that the model is able to reproduce the biomechanical responses exhibited by patients with distinct ocular characteristics. The model is therefore able to reproduce the clinical scenario of different patients, mechanical properties and IOP.

3.4 Discussion

The cornea's anisotropic biomechanical properties play a crucial role in maintaining ocular health. Estimating the biomechanical properties of the corneal tissue has significant clinical implications, impacting the understanding, diagnosis, and treatment of various ocular pathologies. Recent studies have highlighted the importance of analyzing corneal biomechanics in the context of diseases such as keratoconus and glaucoma, where alterations in the mechanical properties of the cornea can serve as early indicators

of disease progression (Ambrósio Jr et al., 2017).

To this end, we developed a 3D patient-specific FSI simulation of NCT that has been clinically validated. This simulation involved generating an extensive dataset of simulations, constructing patient-specific corneal geometries, and exploring the coupling between mechanical properties and IOP in a completely automatized manner.

The use of patient-specific models is essential, as it accounts for individual variations in corneal geometry, which are critical for accurate biomechanical assessment (Ariza-Gracia et al., 2016). The output of the large dataset of numerical simulations run demonstrate the reliability of the methodology, as the results in terms of deflection amplitude and air pressure over the apex fall within the range of clinical data.

The simulations explored the coupling between mechanical properties and the IOP. As it was already demonstrated by Ariza-Gracia et al. (2015), the corneal response during an air-puff is the result of the interaction between four factors: the mechanical properties of the corneal tissue, the IOP, the geometry of the cornea and the air pressure over the cornea. We demonstrated numerically that the same corneal deformation can be caused by a stiff cornea with low IOP and viceversa, by a less stiff cornea and an high IOP. For this reason, in order to estimate the mechanical properties of the corneal tissue in-vivo from the results of a NCT, it is first necessary to find a methodology to decouple the four contributions. Since the information about the corneal thickness is known from topographic data and the air pressure over the apex can be determined using a FSI simulation, the objective of the following chapters will be decoupling the contribution of IOP and mechanical properties of the corneal tissue.

Moreover, the high computational time makes the FSI model unsuitable for estimating the mechanical properties of the corneal tissue in real-time. This limitation is a common challenge in computational biomechanics, where the trade-off between model accuracy and computational efficiency often restricts real-time applications. To address this issue, in the following chapters we will create a reduced order model for the simulation of the NCT.

4

Intraocular pressure estimation

Part of the content of this chapter has been previously published in Frontiers in Bioengineering and Biotechnology: *E. Redaelli, B. Calvo, J. F. Rodríguez Matas, G. Luraghi, and J. Grasa, Non-Contact Tonometry: Predicting Intraocular Pressure Using a Material - Corneal Thickness - Independent Methodology. Frontiers in Bioengineering and Biotechnology, 12 (2024), 1406870.*

4.1 State of the Art

We demonstrated in chapter 2 that the IOP is the factor which influences the most the corneal deformation during a NCT and in chapter 3 that the mechanical properties of the corneal tissue are coupled with the IOP. For this reason, to estimate accurately the mechanical properties of the corneal tissue from the results of a NCT, it is important to evaluate the IOP.

Moreover, accurate and repeatable IOP measurements are the key to diagnose the glaucoma in time and to provide for effective treatment strategies. However, currently available methods are indirect, they only provide an estimation of IOP (Brusini et al., 2021, 2022; Silva and Lira, 2022), and the evaluation of their precision and accuracy is a critical field of research.

Although GAT and NCT are the most widely used instruments to estimate the IOP (Silva and Lira, 2022), their accuracy is significantly affected by the thickness of the cornea and the mechanical properties of corneal tissue (Ariza-Gracia et al., 2015; Asaoka et al., 2015; Greene et al., 2016). It has been proved (Ajazaj et al., 2018), for

instance, that IOP measurements following LASIK refractive surgeries for the correction of myopia may be unreliable due to changes in central corneal thickness (CCT) and due to the applanation of the corneal surface after surgery. To mitigate the risk of obtaining falsely low IOP applanation readings after LASIK, adjustments should be made to the measured IOP, as highlighted in studies such as Ajazaj et al. (2018); Helmy and Hashem (2020); Kohlhaas et al. (2006). Other studies demonstrated that the biomechanical properties of the eye affect the measurement of IOP (Aoki et al., 2023; Kaushik et al., 2012; Liu and Roberts, 2005). The first applanation time used to estimate the IOP in NCT, could be different in patients with the same IOP because those patients can have different corneal mechanical properties or different corneal geometries.

Corvis ST provides a corneal-corrected IOP measurement, the bIOP, designed to exclude the influence of central corneal thickness and age (Joda et al., 2016; Eliasy et al., 2022). There is still a need to reduce its dependence on corneal mechanical properties. bIOP derives from an algorithm correlating various dynamic corneal response parameters obtained through structural numerical simulations of Corvis ST (Eliasy et al., 2022). However, the simulations assume a constant air pressure over the corneal apex which does not depend on corneal deformation like in the real scenario. Furthermore, the numerical model assumes the mechanical properties of the corneal tissue solely age-dependent. While age is a factor, individuals of the same age may exhibit different mechanical properties in their corneal tissue (Ariza-Gracia et al., 2015). As a consequence of this simplification, the algorithm proposed can be improved. A methodology to reliably estimate the IOP not influenced by the mechanical properties and geometry of the cornea is still missing.

This chapter aims to propose a new methodology to estimate the IOP. The methodology is based on the analysis of the internal and external energies impacting the anterior corneal surface during the first 10 ms of the corneal deformation during the air puff in order to obtain the equilibrium point of the system which corresponds to the point of maximum apex velocity. Numerically, it will be verified that the equilibrium point does not depend on the mechanical properties of the corneal tissue and on the corneal thickness.

The chapter is organized as follows. In the materials and methods section, the numerical model of the eye is presented. Two different loading conditions are proposed: a simplified model of a mass falling under the gravity effect - which allows for a easier examination of the external energy exerted on the eye - and the FSI simulation presented in the previous chapters. In the same section, the energetic analysis is outlined highlighting the region of interest (the anterior corneal surface) and the energies playing a role in the deformation of the eye. In the following section, the results of the energetic analysis are presented for both the loading cases. Then, the new methodology to estimate the IOP is proposed. The chapter concludes with a discussion of the obtained results.

4.2 Materials and Methods

4.2.1 Numerical model

The structural model of the eye used in the simulations is depicted in figure 4.1a. It comprises cornea, limbus, sclera and humors. The humors are modelled as an incompressible fluid pressurized at IOP. More details on the geometry and materials functions used in the structural model can be found in chapter 2. The geometry is meshed using software ANSA Pre Processor v23.01 (BETA CAE Systems, Switzerland) with hexahedral solid elements. The structural eye model presented corresponds to a pressurized configuration, therefore, in the first step of each simulation, the zero pressure configuration of the eye is computed following the iterative algorithm presented previously (Ariza-Gracia et al., 2016). Once the zero-pressure configuration is found, the incompressible fluid of the humors is pressurized to obtain the reference configuration of the eye.

To study the energetic balance of the eye during NCT, we preliminary investigated the behaviour of a mass falling under the effect of gravity as presented in figure 4.1b. A mass of 2.02 g modelled as a rigid cube with a side length of 1.5 mm, falls onto the cornea from a height of 8mm with respect to the apex of the cornea. This simplified model is useful to comprehend the energetic balance of the eye when subjected to an external load. In this case, the total mechanical energy of the mass transmitted to the cornea during the impact is easy to calculate (corresponding to the sum of potential and kinetic energy of the mass).

Once the simplified model was analyzed, 3D FSI simulations were run to reproduce in silico the NCT. The fluid domain of the FSI, along with the boundary conditions are depicted in figure 4.1c.

In both cases, after the pressurization, a deformation of the eye occurs caused by the action of an external agent. In the first phase of the impact, small deformations occurs, then, after the corneal applanation, the cornea continues to deform through bending, resulting in larger deformations.

The simulations were implemented in the finite-element solver LS-Dyna R14.0 (ANSYS, 71 Inc., Canonsburg, PA, United States) (Corp, 2021) and performed using an Intel i9-10940X (3.30 GHz) on 14 CPUs. The average computational time of the falling mass simulation was 10 minutes; while the average computational time of the FSI simulation was 48 hours.

4.2.2 Energetic analysis

All mechanical motion is the result of some form of energy transformation. Work is a measure of the energy transfer that occurs when an object is moved over a distance by an external force. The sign of the work done on an object determines if energy is

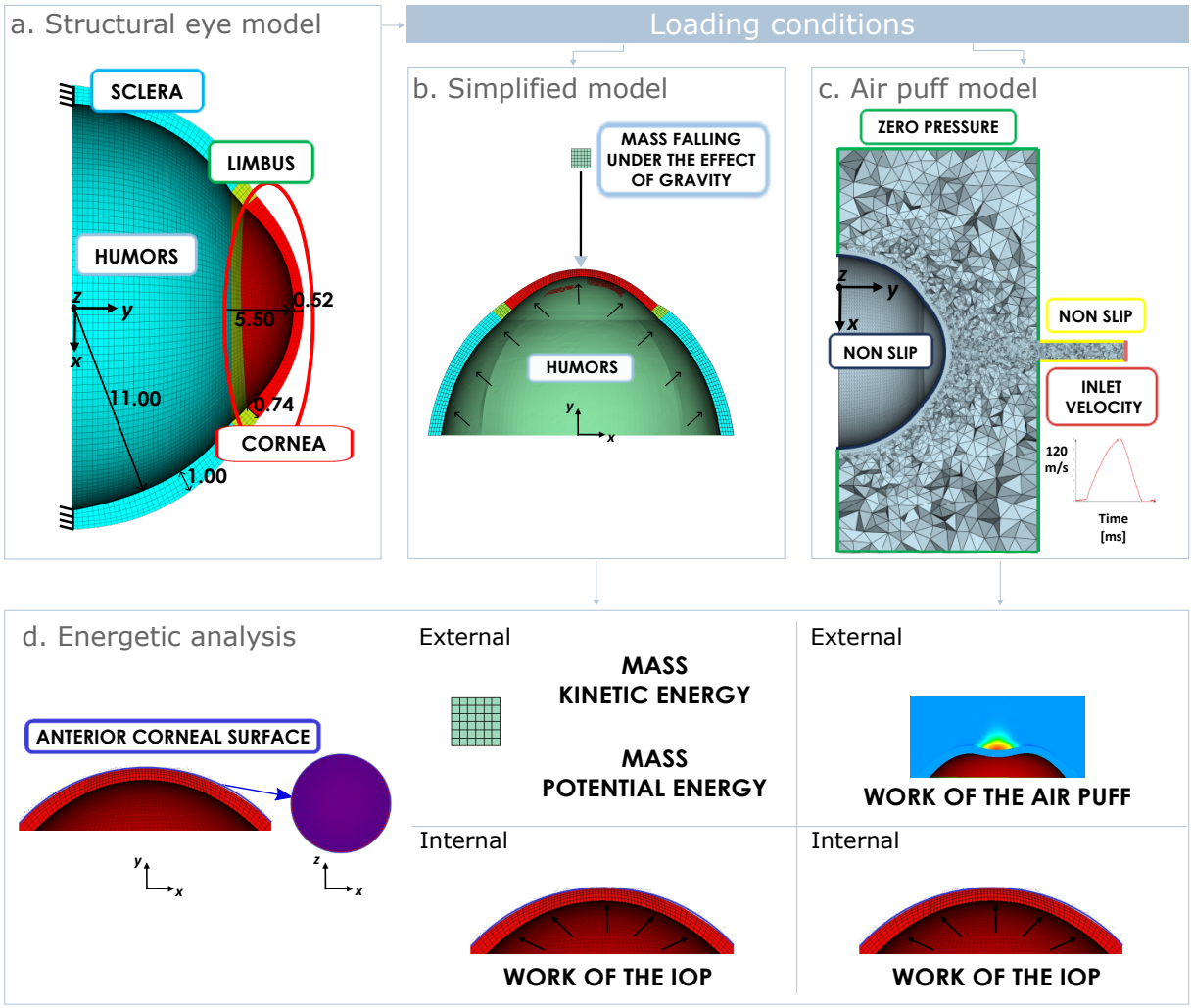

Figure 4.1: (a) Structural eye domain with some dimension in mm and boundary conditions. Loading conditions of the eye: (b) Mass falling under the gravity effect. (c) Fluid domain simulating the air puff and boundary conditions. (d) Energetic analysis performed on the anterior corneal surface in both cases. In case of a falling mass, the anterior corneal surface is loaded externally by the mass kinetic energy and the mass potential energy. In case of an air puff, the anterior corneal surface is loaded externally by the work of the air puff. Internally in both cases the cornea is loaded by the work of the IOP.

transferred in or out of the object. A force applied to an object in the opposite direction to its motion will tend to slow it down, and thus it would drew kinetic energy off the object. With energy leaving the object, the work done should be negative and vice versa.

In this study, we conducted an analysis of the mechanical work exchange occurring on the anterior corneal surface, as illustrated in figure 4.1d, under the loading conditions detailed in section **??**. As explained earlier in chapter 1, Corvis ST records by means of a Scheimpflug camera 140 images of the central section of the cornea over the 30 ms of the air jet. While the anterior corneal surface is visible at all times, the posterior corneal surface may experience distortion during corneal deformation, and cannot be acurately identified. Results of previous studies indicated statistically significant

differences among the thickness values obtained from Pentacam and Corvis ST (Rajabi et al., 2022). Consequently, to make our energetic analysis more reliable, we focused on the anterior corneal surface rather than the posterior surface.

The work of external forces is computed in the y-direction (figure 4.1d) due to the axi-symmetric nature of the eye model, rendering the total work along the x and z axes zero.
In both the simulations, the cornea is loaded internally by the IOP. The work of the IOP in direction y on the anterior corneal surface can be calculated with Equation 4.1.

$$\begin{aligned} \text{Work}_{\text{IOP}} &= \sum_{j=1}^{\text{increments}} \text{Work}^{j}_{\text{IOP}}, \\ \text{Work}^{j}_{\text{IOP}} &= \sum_{i=1}^{\text{nodes}} \frac{(F^{j}_{\text{IOP}_i} + F^{j\text{-}1}_{\text{IOP}_i}) \cdot (u^{j}_{i} - u^{j\text{-}1}_{i})}{2}, \\ F^{j}_{\text{IOP}_i} &= \text{IOP}\left(\Delta t^{j}\right) \cdot \text{area}_i(\Delta t^{j}), \end{aligned} \tag{4.1}$$

where at increment j of the simulation: $\text{area}_i(\Delta t^j)$ is the area associated to the node i and u^j_i is its displacement in direction y. Since the IOP exerted by the humors is modelled as homogenous in space, it has the same interpolated value over the nodes.

On the external side of the anterior surface, the region of interest is loaded by different conditions in the two problems. In case of the mass falling under the effect of gravity, the external work transmitted to the cornea corresponds to the total mechanical energy of the mass, which is the sum of its kinetic and potential energies.

$$\begin{aligned} \text{Kinetic energy} &= \frac{1}{2} \cdot m \cdot v^2, \\ \text{Potential energy} &= m \cdot g \cdot h, \end{aligned} \tag{4.2}$$

where m is the mass of the cube, v its velocity, h its height and g the gravity acceleration. In case of the air puff, the external work due to the air is given by:

$$\begin{aligned} \text{Work}_{\text{AIR}} &= \sum_{j=1}^{\text{increments}} \text{Work}^{j}_{\text{AIR}}, \\ \text{Work}^{j}_{\text{AIR}} &= \sum_{i=1}^{\text{nodes}} \frac{(F^{j}_{\text{AIR}_i} + F^{j\text{-}1}_{\text{AIR}_i}) \cdot (u^{j}_{i} - u^{j\text{-}1}_{i})}{2}, \\ F^{j}_{\text{AIR}_i} &= P_{\text{AIR}_i}\left(\Delta t^{j}\right) \cdot \text{area}_i(\Delta t^{j}), \end{aligned} \tag{4.3}$$

where at increment j of the simulation: $P_{\text{AIR}_i}\left(\Delta t^j\right)$ is the equivalent air pressure on the node i on the corneal anterior surface obtained by the software; $\text{area}_i(\Delta t^j)$ is the area associated to that node and u^j_i is its displacement in direction y. The air pressure is

calculated by the software on the center of the cell and then projected to the nodes of the mesh. The air pressure over the corneal anterior surface is not constant neither homogeneous; it depends on the corneal deformation as depicted in figure 4.1d.

4.3 Results

4.3.1 Energetic analysis of the deformation of the eye under the effect of a falling mass

In this section, the results of the energy analysis of the mass falling onto the eye are presented.

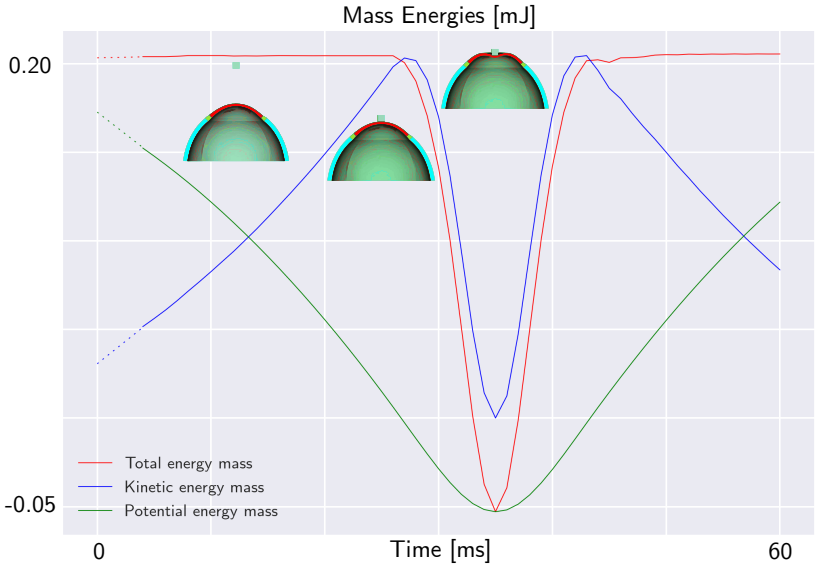

Figure 4.2: Total mechanical energy of a mass falling under the effect of gravity on the eye. The potential energy is in green, the kinetic energy in blue and the total mechanical energy in red. In the first 25 ms, the mass is falling without impacting the eyeball. Until the impact, the total mechanical energy of the mass is constant. When the mass impacts the eye, its mechanical energy decreases. At 35 ms, the maximum deformation of the eye occurs, then the structure returns to its original configuration.

Initially, the mass is at a certain height with respect to the eye and starts falling under the force of gravity. As it falls, its kinetic energy increases due to its increasing speed while its potential energy decreases. In the initial part of the plot in figure 4.2, the curves are depicted with dashed lines, because numerically it is not possible to impose to the mass a sudden acceleration equal to the gravitational acceleration. Numerically, the mass begins with zero acceleration, and in the initial instants, it dynamically reaches the gravitational acceleration. For this reason, when the gravitational acceleration is

reached (at 4 ms), the velocity (and therefore the kinetic energy of the mass) is not zero. When the system stabilizes, the sum of the potential and kinetic energies is constant as depicted with the red line in figure 4.2.

When the mass contacts the external surface of the eye-globe, it starts to deform the object. For this reason, the total energy of the mass decreases. The total mechanical energy of the mass along with its potential and kinetic energy during the impact are depicted in figure 4.2. At the point of impact, the energy of the mass is transmitted to the eye where it is stored in the form of elastic energy. Figure 4.3.a. plots both the total energy of the mass and the total internal energy of the eye. The total internal energy of the eye increases in the first 5 ms corresponding to the eye pressurization. Then, it remains constant before experiencing an important increase during the impact. Since there is no energy dissipation, the absolute decrease of the energy of the mass is equal to the increase of the internal energy of the eye as shown in figure 4.3.b.

Meanwhile, as the mass falls onto eye-ball, the pressure inside the chamber of the eye increases uniformly in all directions, following the principles of hydrostatic pressure (figure 4.3.c). This pressure acts on the surrounding walls of the container, causing it to expand to accommodate the increased pressure. The pressure in the fluid exerts a mechanical work on the anterior surface of the cornea calculated with equation 4.1. The work of the IOP increases as the pressure rises during the pressurization phase. In the pressurization phase, the work is positive because it is done by the fluid expanding the surrounding walls. After the impact with the mass, the work done by the fluid starts to decrease (figure 4.3.d). This decrease occurs because the displacement of the cornea is in the opposite direction to the IOP force.

On the other hand, during the impact of the mass with the eye, the internal energy of the cornea increases. Since the cornea is much more compliant than the sclera, the variation in the internal energy of the cornea during the impact is very close to the work exerted by the IOP as shown in figure 4.3.e. In the first phase of the impact, all the corneal deformation is converted into an increase of IOP. Moreover, even if the variation in the elastic energy of the cornea during the impact generally is an unknown fraction of the variation of the elastic energy of the eye-ball, depending on the compliance of the sclera and on the diameter of the cornea relative to the diameter of the sclera, in the first phase of the simulation this fraction is close to 1. For this reason, since the corneal deformation energy fully transmits energy to the internal fluid, we can analyze the energy balance only by considering the work done by the IOP and the external energy.

When the work of the IOP becomes equal to the total mechanical energy acting on the mass, the net force on the mass becomes zero and the mass stops accelerating. We will concentrate our analysis on the time at which the works acting on the corneal anterior surface are equal. The intersection point between the work of the IOP and the decrease in the total energy of the mass is the point of maximum kinetic energy and, therefore the point of maximum velocity of the mass as depicted in figure 4.3.f. The maximum velocity of the mass is equal to the maximum velocity of the corneal apex because the mass falls over the corneal apex; therefore when the works acting on the

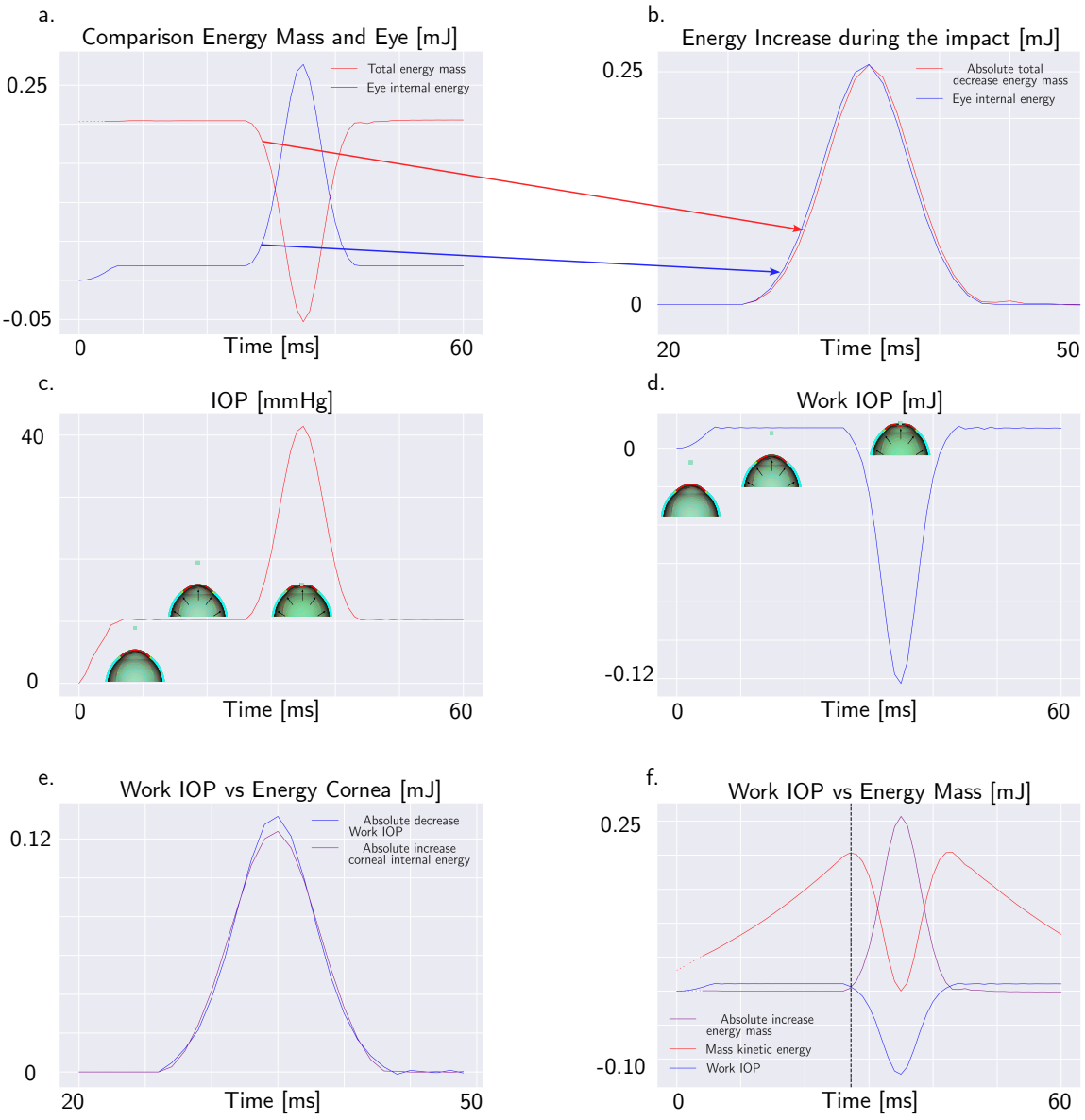

Figure 4.3: Mass falling under the effect of gravity on the eye: (a) Total energy of the mass and total internal energy of the eye. (b) Increase of the internal energy of the eye and absolute value of the decrease of the total energy of the mass during the impact. (c) Pressure of the fluid cavity during the impact. (d) Work of the internal fluid on the anterior corneal surface. (e) Internal energy of the cornea and work of the internal fluid (with opposite sign). (f) Work of the internal fluid, total energy of the mass and kinetic energy of the mass. In the intersection point between the total energy of the mass and work of the internal fluid, the kinetic energy is maximum.

anterior corneal surface are equal, the apex velocity is maximum.

Remark 1. *The mechanical energy of the mass (kinetic and potential) is converted in deformation of the eyeball, in particular, in the first phase of the deformation it is converted in deformation energy of the cornea.*

Remark 2. *The deformation of the cornea during the impact is converted in increase of IOP.*

Remark 3. *The time when the works acting on the anterior corneal surface are equal occurs when the velocity of the apex is maximum.*

4.3.2 Energetic analysis of the deformation of the eye under the effect of an air jet of Corvis ST

According to the results obtained by the mass falling model, we propose to study the cornea subjected to the air puff of Corvis ST at the time when the works acting on the anterior corneal surface are equal. Based on those previous results, all the external energy is converted in increasing the IOP, therefore during the first part of the deformation, the energy transfer only depends on the IOP. In this section, the balance between the work of the air puff and the work of the IOP on the corneal anterior surface is calculated, to verify that the air puff effect on the eye is the same as the mass. To achieve this aim, the outline of the FSI simulation described in section **??** is used with multiple combinations of mechanical properties of corneal tissue, IOP and thickness as presented in table 4.1. Actually, the displacement field, strain and stress states of the FSI depend on the IOP, the mechanical properties of the corneal tissue and corneal geometry as demonstrated in our previous work (Redaelli et al., 2022) because it is a strongly coupled problem. In the simple problem with the mass, the energy of the mass does not depend on the eye deformation, while in this case, the air pressure over the corneal apex depends on the corneal deformation as presented in figure 4.1d. We performed the same FSI simulation sixteen times, with each repetition involving a variation in one parameter in order to reproduce the NCT test for different patients. In the first thirteen simulations, the corneal geometry was the same with a Central Corneal Thickness (CCT) of 558 µm, the varying parameters of these simulations were the parameters describing the mechanical properties of the corneal tissue and the IOP. In the last three simulations, also the corneal geometry changed, with different corneal thickness. The parameters used in the simulations are listed in table 4.1. For each simulation, the air pressure over the corneal anterior surface, the corneal displacement and the IOP were measured as output during the air puff. These quantities were used to calculate the work of the IOP and the work of the air pressure over the corneal anterior surface with equations 4.1 and 4.3.

4.3.2.1 Pressurization phase

Initially, we analyzed the first five simulations characterized by the same CCT and mechanical properties and different IOP (ranging between 10 and 30 mmHg). The zero-pressure configuration of the eye varies in each simulation since we started from the same pressurized configuration. For this reason, the displacement of the anterior surface of the cornea from the zero pressure configuration to the end of pressurization is different in each case. The displacement contour at the end of the pressurization (starting from the zero-pressure configuration) is depicted in figure 4.4.

The deformation state of the cornea at the end of pressurization is different in each case since the displacement at the end of pressurization depends on the IOP. In

Parameters of the mechanical model of the corneal tissue, IOP and CCT for each simulation.

simulation	C_{10} [MPa]	k_1 [MPa]	k_2 [-]	IOP [mmHg]	CCT [μm]
1	0.045	0.027	180	10	558
2	0.045	0.027	180	15	558
3	0.045	0.027	180	20	558
4	0.045	0.027	180	25	558
5	0.045	0.027	180	30	558
6	0.0675	0.027	180	15	558
7	0.0225	0.027	180	15	558
8	0.045	0.0405	180	15	558
9	0.045	0.0135	180	15	558
10	0.045	0.027	270	15	558
11	0.045	0.027	90	15	558
12	0.035	0.13	1000	15	558
13	0.01	0.015	100	15	558
14	0.045	0.027	180	15	484
15	0.045	0.027	180	15	525
16	0.045	0.027	180	15	600

Table 4.1: Parameters of the mechanical model of the corneal tissue, intraocular pressure (IOP) and central corneal thickness (CCT) for each simulation. C_{10} represents the collagen matrix stiffness in MPa, k_1 the fibers stiffness in MPa and k_2 the fibers non linearity [-].

particular, the maximum displacement in each case has a linear relationship with the IOP as depicted in figure 4.4. The work of the IOP at the end of pressurization depends on the IOP of the patient and on the displacement of the anterior surface of the cornea. For this reason, the IOP has a quadratic relationship with the work of the IOP at the end of pressurization as depicted in figure 4.5.a and 4.5.b.

In particular, under the mechanical properties of the corneal tissue analysed, the relationship between the IOP and the work of the IOP at the end of pressurization is defined by equation 4.4:

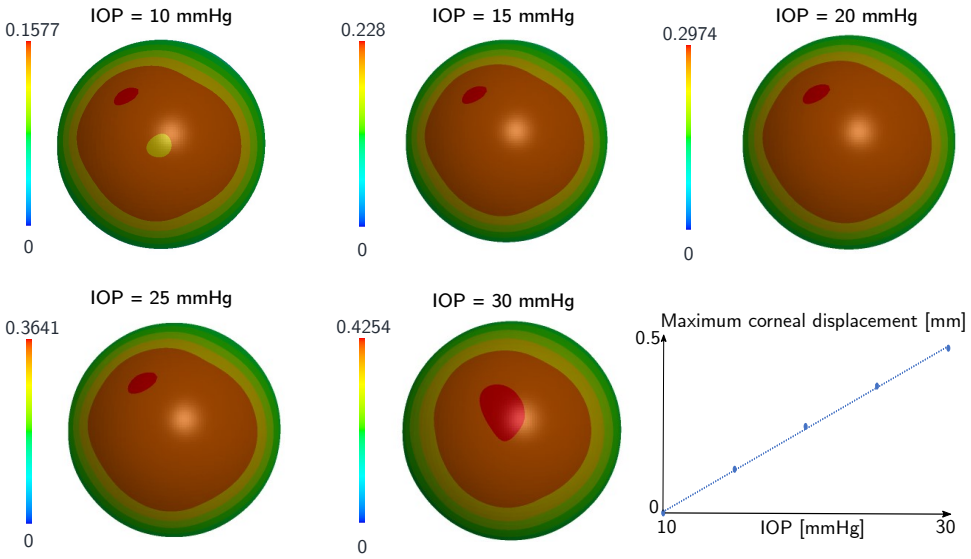

Figure 4.4: Displacement in mm of the anterior corneal surface at the end of pressurization for the first five cases of the sensitivity analysis. The mechanical properties and the geometry of the cornea are the same in each case, the IOP varies. The corneal displacement at the end of pressurization had a linear relationship with the IOP.

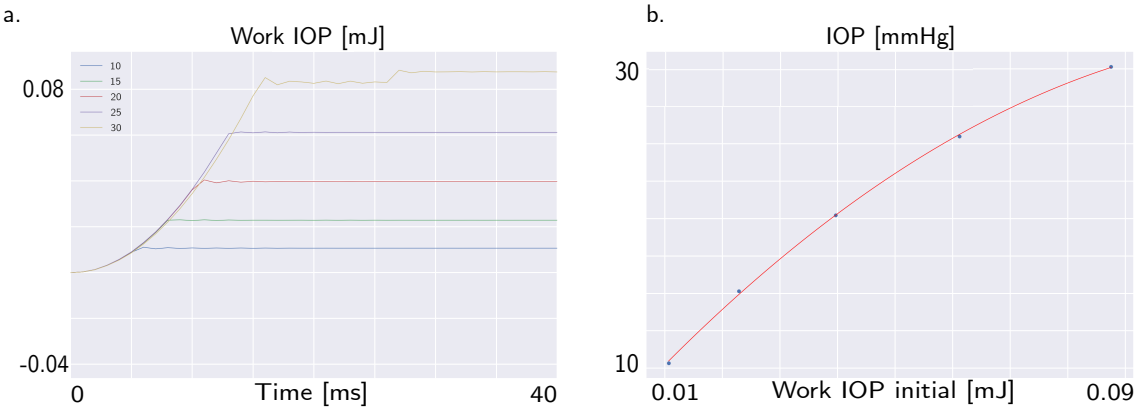

Figure 4.5: (a) Work of the IOP during the pressurization phase for different IOP. (b) Relationship between the work of the IOP at the end of pressurization and the IOP.

$$\text{IOP} = (-1.69 \cdot 10^3) \cdot \text{Initial work IOP}^2 + (4.21 \cdot 10^2) \cdot \text{Initial work IOP} + 6.18 \quad R^2 = 0.98. \tag{4.4}$$

4.3.2.2 Air jet phase

In figure 4.6 the evolution of the work of the air puff and the work of the IOP during the impact are represented for one of the sixteen cases from the sensitivity analysis (table 4.1).

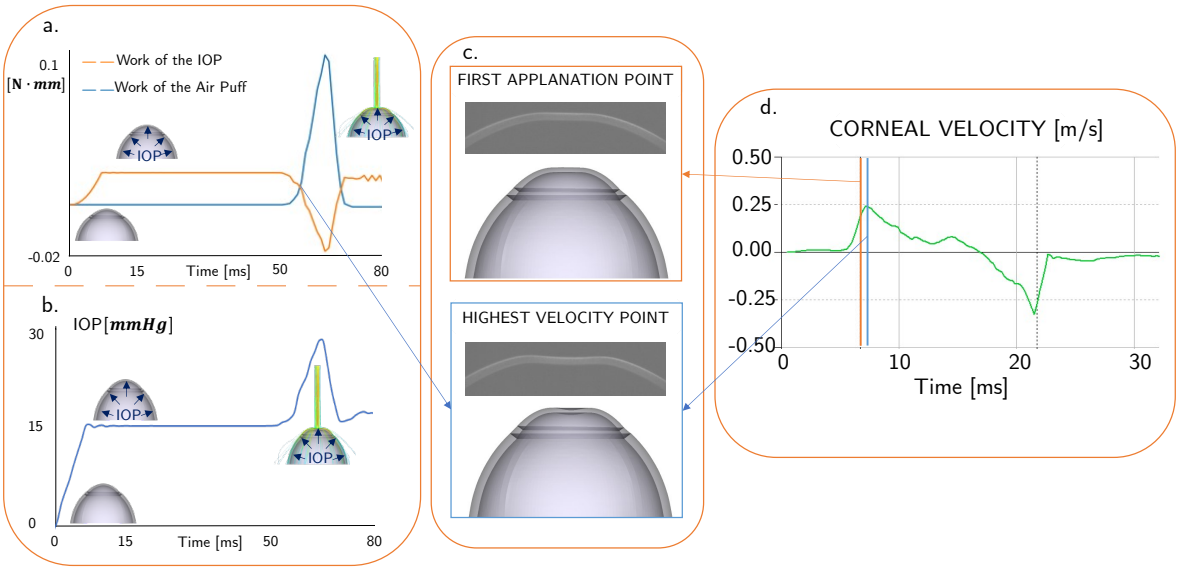

Figure 4.6: (a) Work of the air puff (in blue) and work of the IOP (in orange) calculated from the FSI simulation: the intersection point of the curves is the interest of this analysis. (b) Evolution of the IOP during the simulation: when the air puff impact the eye, the IOP increases. (c) Clinical and numerical comparison between the first applanation point and the highest velocity point. (d) Clinical result: apex velocity as output of Corvis ST: the first applanation time (orange line) does not coincide with the highest velocity time (blue line).

As illustrated in figure 4.6.a, the IOP's work increases in the first 10 ms as the eye undergoes pressurization from its initial zero-pressure state. In the subsequent stabilization step, both the work of the air puff and the work of the IOP remain constant. At 50 ms, the corneal surface is impacted by the air puff, resulting in deformation in the direction opposite to that of the IOP but in the same direction as the air puff pressure. Additionally, the IOP increases during the air puff, as depicted in figure 4.6.b and reported in our previous work (Redaelli et al., 2022) because the fluid is incompressible. Conversely, the work of the air puff increases during the impact (figure 4.6.a), while the work of the IOP decreases. There are two intersection points of the curves, which correspond to the time of maximum velocity of the apex. This time is different from the time of the first applanation, as shown in figures 4.6.c and 4.6.d. The time difference is not always the same since it depends on the corneal structural properties, the range of difference is between 1 and 5 ms.

Analyzing the first five simulations characterized by the same central corneal thickness (CCT) and mechanical properties but different IOP, we observe that the work of the IOP and the work of the air puff during the impact differ in each simulation, as shown in figure 4.7.a. Figure 4.7.b demonstrates that, for the considered mechanical properties and thickness, the relationship between the initial work of the IOP and the work at the intersection is linear. Specifically, the work at the intersection is approximately half of the initial work. In particular, a quadratic relationship exists between the time of maximum velocity and the initial work of the IOP, as shown in figure 4.7.c and reported in equation (4.5).

$$\text{Initial work IOP [mJ]} = (1.09 \cdot 10^{-3}) \cdot \text{time}_{\text{max-vel}}{}^2 + (-8.28 \cdot 10^{-3}) \cdot \text{time}_{\text{max-vel}} + 1.19 \cdot 10^{-2} \quad R^2 = 0.98. \tag{4.5}$$

But what happens when we change the mechanical properties of the corneal tissue and the thickness of the cornea? (simulations 6-16 in table 4.1). Changing both the mechanical properties of the corneal tissue and the thickness of the eye, the time of intersection between the work of the air puff and the work of the IOP does not change as demonstrated by the plots in figure 4.7.d and 4.7.e. Therefore, this point does not depend on the geometry and mechanical proprierties of the cornea. The work of the air puff and the work of the IOP during the air puff for each simulation are reported in figure 4.8.

Remark 4. *There exist a relationship between the maximum velocity time of the corneal apex during the deformation and the initial IOP.*

Remark 5. *The mechanical properties of the corneal tissue and the corneal thickness does not influence the energetic balance at the beginning of the deformation.*

4.4 IOP estimation with Corvis ST

4.4.1 Clinical analysis of the first applanation time and highest velocity time

We presented in the previous sections, the results of numerical simulations of the Corvis ST test, to analyse the energy balance of the system. The outcomes of these simulations can be extrapolated to the clinical scenario, as the equipment captures the temporal evolution of apex velocity for each patient. In this section, we will delve into a detailed analysis of the apex velocity. The Corvis ST results of six healthy and six keratoconic corneas are presented in this section as an example. These data were used to evaluate if the first applanation time of the cornea and the point of maximum velocity are coincident. The data used were randomly selected from a previous study conducted at Antwerp University Hospital. The study was conducted according to the tenets of the Declaration of Helsinki and participants gave signed informed consent prior to measurement (reference number of the Antwerp University Hospital Ethical Committee: 17/12/136). The analysis of the apex velocity during Corvis ST examination from both healthy and keratoconic patients, revealed that the first applanation point, typically used as reference to measure the IOP in-vivo, does not correspond to the instant of highest velocity of the corneal apex as shown in figure 4.9. Additionally, the time difference between the maximum velocity instant and the first applanation time varies among patients. After the first applanation point, the corneal velocity continues to increase, revealing that the cornea is subjected to a positive acceleration and force. The corneal velocity reaches its maximum value when the corneal acceleration is zero,

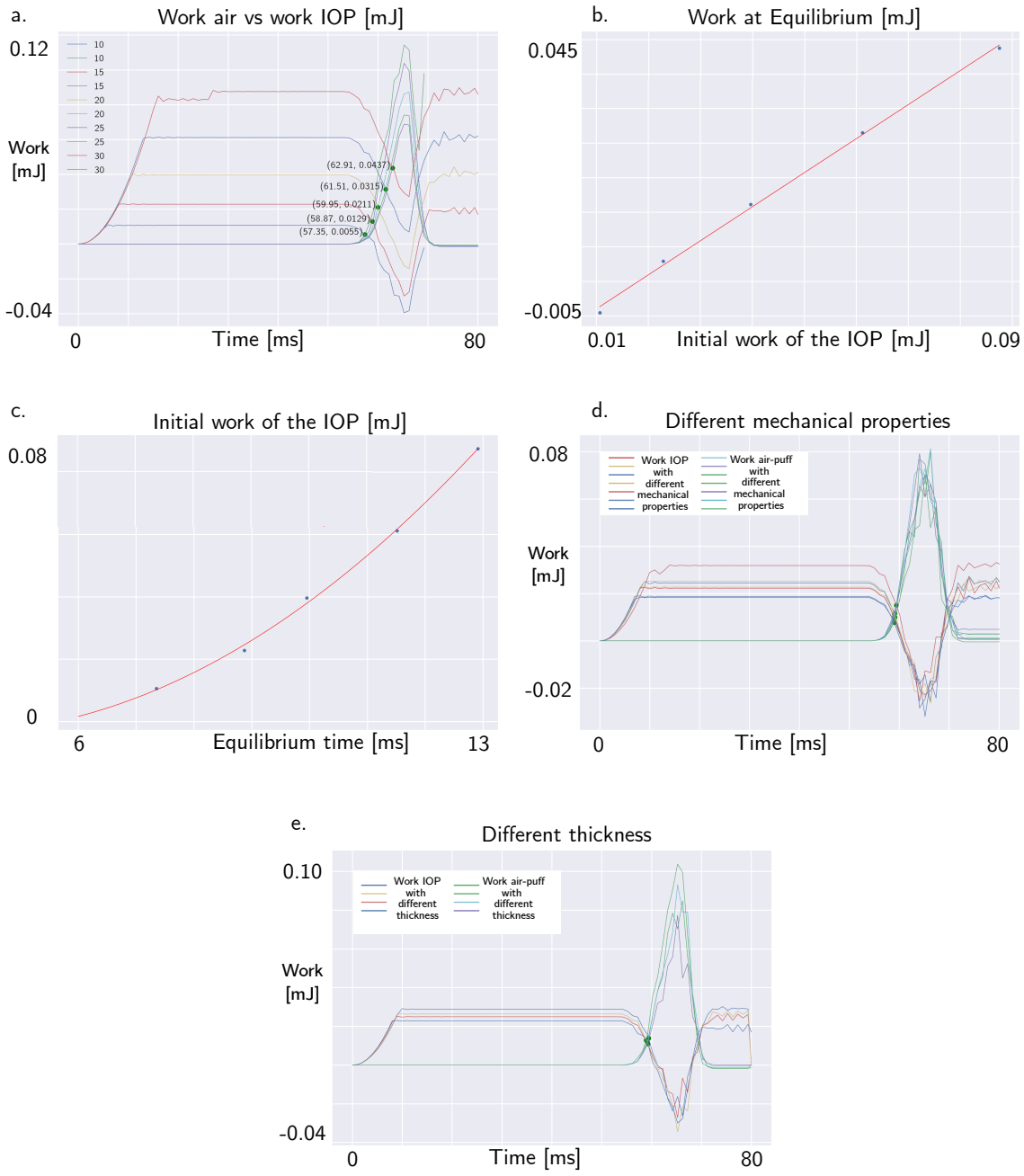

Figure 4.7: (a) Intersection points between internal and external work in the simulations with different IOP. (b) Linear relationship between the initial work of the IOP and the work at intersection (both in mJ). (c) Quadratic relationship between the time of maximum velocity (in ms) and the initial work of the IOP (in mJ). (d) Intersection points between internal and external work in the simulations with different mechanical properties of the corneal tissue. (e) Intersection points between internal and external work in the simulations with different thickness.

therefore the force acting on the cornea is zero. After that, the corneal velocity decreases, reaching zero velocity at the highest concavity.

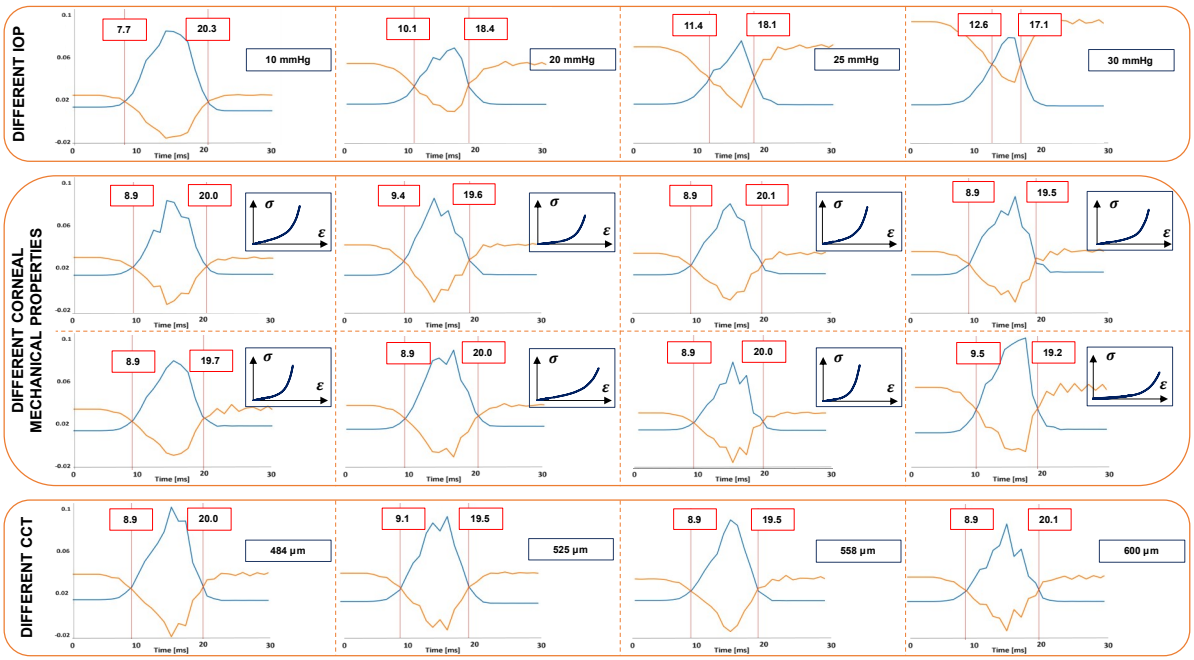

Figure 4.8: Time of intersection between the work of the air puff (in blue) and the work of the IOP (in orange) in different FSI simulations (table 4.1). This point of the cornea changes when the IOP changes. However, it does not depend on the mechanical properties of the corneal tissue and the central corneal thickness.

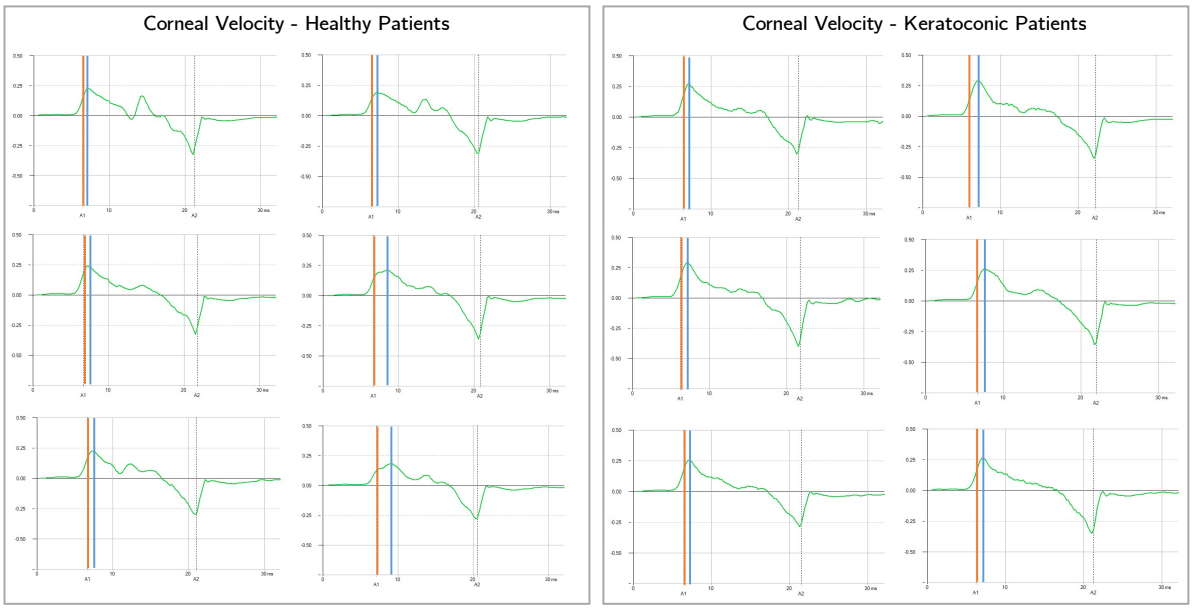

Figure 4.9: Apex velocity in time for 6 healthy and 6 keratoconic patients during Corvis ST. The first applanation time is highlighted with the orange vertical line while the highest velocity time is highlighted with the blue vertical line.

4.4.2 Methodology proposal

Given the results of section 4.3, it is possible to propose a new procedure to estimate the IOP of a patient based on the time of maximum velocity ($\text{time}_{\text{max-vel}}$) of the corneal apex provided by Corvis ST. The new IOP will be called wIOP because it is based on the analysis of the works acting on the corneal anterior surface. Since the time at which the works acting on the corneal surface are equal does not depend on the mechanical properties of the corneal tissue and on the corneal thickness, this time can be used to estimate the wIOP. From the output data of Corvis ST, the velocity of the apex is known. The time of maximum velocity of the apex ($\text{time}_{\text{max-vel}}$) corresponds to the intersection time of the works and it is used to calculate the wIOP by means of equation 4.6 which is given by the combination of equations 4.4 and 4.5.

$$\begin{aligned}\text{wIOP [mmHg]} = (-2.01 \cdot 10^{-3}) \cdot {\text{time}_{\text{max-vel}}}^4 + (3.05 \cdot 10^{-2}) \cdot {\text{time}_{\text{max-vel}}}^3 \\ +(2.99 \cdot 10^{-1}) \cdot {\text{time}_{\text{max-vel}}}^2 - 3.15 \cdot \text{time}_{\text{max-vel}} + 10.95.\end{aligned} \tag{4.6}$$

4.5 Discussion

The point in which the external and internal forces are equal in NCT of Corvis ST was previously believed to be the first applanation point of the cornea (Sharma et al., 2020; Silva and Lira, 2022; Brusini et al., 2021). However, the point in which the external and internal forces are in equilibrium is the point of maximum velocity of the corneal apex. Actually, at this point the acceleration of the system is zero because the forces are balanced. A closer inspection of the clinical results revealed that the first applanation point does not coincide with the point of highest velocity. The cornea's deformation depends on the coupled effect of the IOP, the corneal thickness, the mechanical properties of the corneal tissue and the air pressure on the cornea (Ariza-Gracia et al., 2015; Redaelli et al., 2022). Consequently, the equilibrium point may not necessarily coincide with an applanated cornea. The FSI simulation presented in our previous work (Redaelli et al., 2022) predicts the the air pressure on the corneal surface during the puff; in contrast with the output of the Corvis ST, which only provides the air pressure at the outlet of the device nozzle's (Simonini and Pandolfi, 2016). Previous numerical works attempted to estimate the IOP removing the influence of corneal structural parameters. Joda et al. (2016) and more recently Eliasy et al. (2022) proposed an algorithm to correct the IOP estimated by Corvis ST trying to exclude the influence of CCT and age. However, their algorithm is based on structural numerical simulations in which the air pressure on the cornea does not vary depending on the mechanical properties and thickness of the patient. Simonini and Pandolfi (2016) studied the influence of a varying air jet pressure on the output of the NCT, revealing that different air pressures on the cornea can lead to changes in the estimation of IOP. That work considered different pressure values on the cornea as a defined function of a structural simulation, independent on the corneal deformation. The Corvis ST tonometer nozzle consists of a tube with an inner diameter

of 1 to 2 mm, and a distance of 11 mm between the nozzle and the eye is required, which affects the cross-sectional profile of the pressure applied to the eye. Due to the nozzle to eye distance and subsequent change in the pressure profile, the spatial and temporal profile of the airflow pressure on the cornea differs significantly from that of the internal device pressure (Oehring et al., 2021). Oehring et al. (2021) investigated the spatial distribution of the Corvis ST airflow pressure using mapping grids. However, the pressure on the corneal surface was supposed to be only dependent on the distance, not on the corneal deformation. The novelty of our FSI is the evaluation of the air pressure on the corneal surface in each case with the possibility to calculate the work of the air puff in different scenarios. To the best of our knowledge, only Zhang et al. (2021) have investigated the NCT by means of an energetic approach but they considered a constant pressure on the corneal surface. The work of the air puff in Zhang et al. (2021) is assumed to be equal to the corneal internal energy. Our energetic analysis considers the energy balance of the anterior corneal surface at the intersection point between the work of the air puff and the work of the IOP. Both works are calculated on the anterior corneal surface, so the thickness of the eye is not considered and does not influence the results, as supported by the analysis of different CCT shown in section 4.3.2. We conducted an analysis of the energy balance in the anterior-posterior direction, since the thickness of the structure is negligible with respect to its surface, the mechanical properties of the cornea do not play a role in the results. Our analysis of various mechanical properties in section 4.3.2 supports this non-dependency. Figure 4.10 depicts the stress-strain curves of the corneal materials we tested which are consistent with other previous experimental studies (Elsheikh et al., 2008; Xiang et al., 2018; Liu et al., 2020). Xue et al. (2018) found that under physiological IOP, the corneal stress is about 0.02 MPa, which is consistent with the stress strain curves we tested in our simulations.

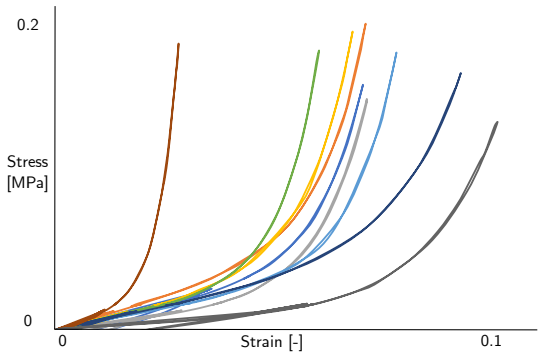

Figure 4.10: Stress-strain curves of the corneal material tested in our simulations.

In conclusion, the significance of our novel pressure estimation lies in two key aspects. Firstly, the method provides a more realistic and real-time assessment of a patient's IOP based on the results of Corvis ST, decoupling it from the mechanical properties of the cornea. This real-time capability enhances the dynamic monitoring of IOP, allowing for prompt and responsive adjustments in clinical interventions.

Secondly, once an accurate estimate of IOP is obtained, it can serve as a foundational

parameter for further investigations. Specifically, this IOP data can be leveraged in conjunction with other methodologies to estimate the mechanical properties of the cornea. This dual-pronged approach addresses an emerging challenge in ophthalmology, offering a comprehensive understanding of both IOP and corneal biomechanics.

5

Reduced order model of the NCT: mechanical properties estimation.

Part of the content of this chapter has been submitted for publication in Computer Methods in Applied Mechanics and Engineering: *E. Redaelli, B. Calvo, J. F. Rodríguez Matas, G. Luraghi, and J. Grasa, A POD-NN model of the eye deformation during a Non Contact Tonometry to determine the mechanical properties of the corneal tissue. Computer Methods in Applied Mechanics and Engineering, submitted*

5.1 State of the art

Some authors made use of numerical simulations to investigate the mechanical properties of the corneal tissue. Jannesari et al. (2018), employed an inverse finite element method (FEM) (which is a combination of FEM and an optimization algorithm) to evaluate the corneal biomechanical properties. In particular, the initial estimated material properties were given as input to a FEM model which simulated Corvis ST tonometry test. The FEM solution was compared with the corneal deformation obtained from clinics and an optimization algorithm was set to reduce their differences by modifying the estimated material properties. The optimization process continued until the FEM solution converged to the corneal deformation obtained from Corvis ST by considering a reasonable error tolerance. However, this methodology employed a FEM with a 2D axysimmetric model considering an isotropic hyperelastic material model for the cornea. Moreover, IOP was applied to the posterior surface of cornea as a constant uniform pressure and the air puff was applied on the anterior surface of cornea as a variable pressure with time and position. These limitations led Huang et al. (2020),

to construct a more detailed simulation employing a combination of computational fluid dynamic (CFD) and structural analyses with a fluid descriptions of the humors and an anisotropic material model for the cornea. They used an inverse FEM to match the deflection amplitude between the simulated and experimental results. Since they were adjusting only one parameter - the deflection amplitude - the material parameter estimated could be only one, otherwise multiple solutions would be possible. With that work, they demonstrated that corneal nonlinearity and anisotropy have significant effects on the corneal deformation rate.

Ariza-Gracia et al. (2017b) employed a different approach with respect to the inverse-FEM to estimate the mechanical properties of the corneal tissue. They generated a large dataset of simulations of Corvis ST, and then, created predictors for the mechanical properties using both the *"response surface approach"* and the *"nearest neighbor approach"*. Also in this case, the used database was obtained from CFD simulations to determine the air pressure over the corneal surface. Later, they demonstrated (Ariza-Gracia et al., 2018) that the best numerical approach to simulate the NCT is the FSI to couple the air pressure over the corneal surface with the corneal deformation. To the best of our knowledge there are no previous studies in the literature estimating the mechanical properties of the corneal tissue based on FSI simulations.

In chapter 2, we proposed a high fidelity FSI methodology to simulate the NCT of Corvis ST. The main problem of that FSI simulation is the high computational cost. Only the running time of one simulation takes 24 hours on 14 CPUs (EPYC 7662 64-Core Processor 154, 2.0 GHz), making it prohibitive to implement an optimization process to detect the mechanical properties of the corneal tissue in real time. Recently, a non-intrusive reduced basis method has been proposed by Hesthaven and Ubbiali (2018) and Wang et al. (2019) in order to obtain in real time the results of computationally costly numerical simulations and this methodology will be followed in the present chapter to obtain a Reduced Order Model (ROM) of the NCT. This technique was successfully applied both to simple problems (for example in reducing the dimensionality of a simulation of a viscous flow within a parallelogram-shaped cavity (Hesthaven and Ubbiali, 2018)) and in more complex problems such as the modeling of cardiac electrophysiology (Fresca et al., 2020).

This chapter aims to construct a data-driven ROM for real-time estimation of the mechanical properties of the corneal tissue based on model reduction of knowledge-driven FSI simulations using Proper Orthogonal Decomposition (POD) and Artificial Neural Network (ANN). The work is divided in an offline and online phase. In the former, (I) FSI simulations of the NCT are used to build a large dataset. The generated dataset is a collection of parameters describing the geometry and material properties of the cornea, the IOP and the deformation of the cornea. (II) POD is used to reduce the dimensionalty of the inputs and (III) an ANN is trained to predict the patient-specific mechanical properties of the corneal tissue that best reproduce the deformation of the cornea during the NCT. In the online phase, the mechanical properties of the corneal tissue of one patient are determined based on the results of Corvis ST.

5.2 Materials and Methods

A ROM of a FSI model is developed to train a neural network to then predict the mechanical properties of the corneal tissue in-vivo. The construction of the algorithm is entirely implemented in Python 3.11 mainly using the libraries NumPy (Harris et al., 2020), SciPy (Virtanen et al., 2020) and keras of TensorFlow (Abadi et al., 2015). It involves three primary steps: (I) the construction of a large dataset of high fidelity simulations, (II) the POD of the simulation data and (III) the training of an ANN to estimate the mechanical properties of the corneal tissue that best reproduce the deformation of the patient's cornea during the NTC. The methodology followed is schematically represented in figure 5.1, the steps are detailed in the following sections.

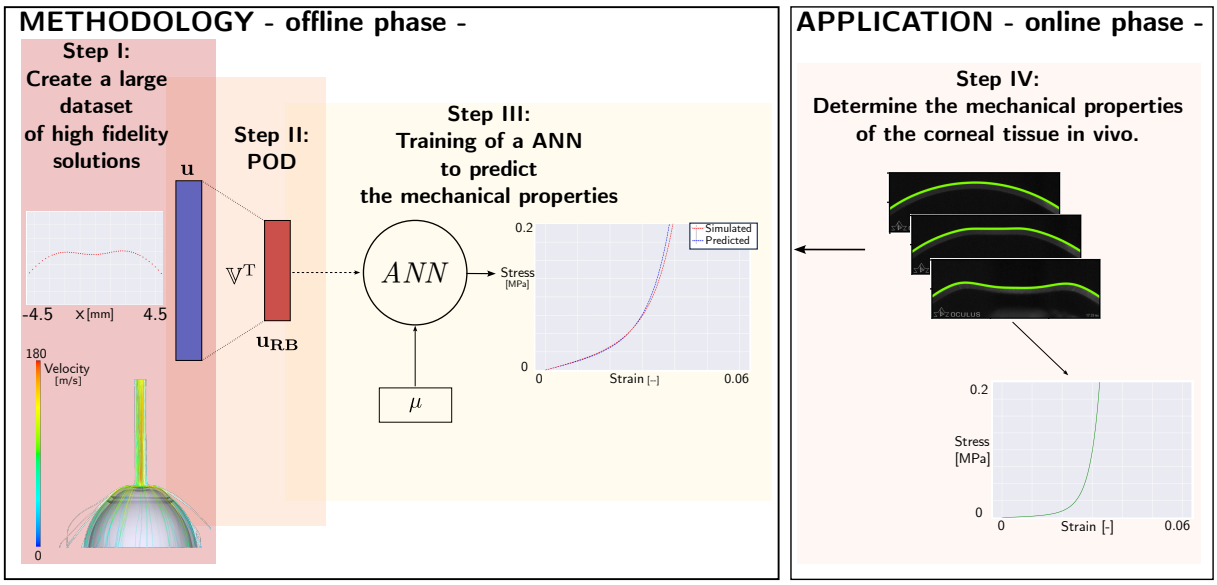

Figure 5.1: Schematic representation of the steps for the construction of the model to predict the mechanical properties of the corneal tissue. The methodology is divided in an offline and online phase. In the former, as a first step (I), a large dataset of high fidelity solutions for the corneal deformation during an air puff is created. Then, (II) a POD is conducted on the numerical output to find the principal modes of variation of corneal deformation. Finally, (III) an ANN is trained to approximate the mechanical properties of the corneal tissue. During the online phase (IV), given a new patient, the deformation of the cornea is used as input to the ANN model to determine in-vivo the mechanical properties of the corneal tissue.

5.2.1 Creation of a large dataset of high fidelity solutions

5.2.1.1 FSI model of the NCT

The NCT of Corvis ST is modelled through high fidelity FSI simulations implemented in the finite-element solver LS-Dyna R14.0 (ANSYS, Inc., Canonsburg, PA, United States). The FSI model comprises both a solid and a fluid component to couple the downward displacement of the eye with the pressure exerted by the incoming air-jet.

The 3D structure of the eye used in the simulations includes the cornea, limbus, sclera, and humors. The geometry of the cornea is patient-specific and constructed based on Pentacam data following the methodology explained in chapter 3. The point cloud of Pentacam is adjusted by Zernike polynomials (Wang et al., 2022). The significance of employing Zernike polynomials lies in the ability to effectively parameterize the corneal geometry. We fit the corneal surface with Zernike polynomials of fifth order (Wei et al., 2021; Wang et al., 2022), resulting in 21 Zernike coefficients both for the anterior and for the posterior corneal surfaces. The information about corneal thickness is intrinsic to the Zernike parametrization since the corneal thickness depends on the combination of anterior and posterior coefficients.

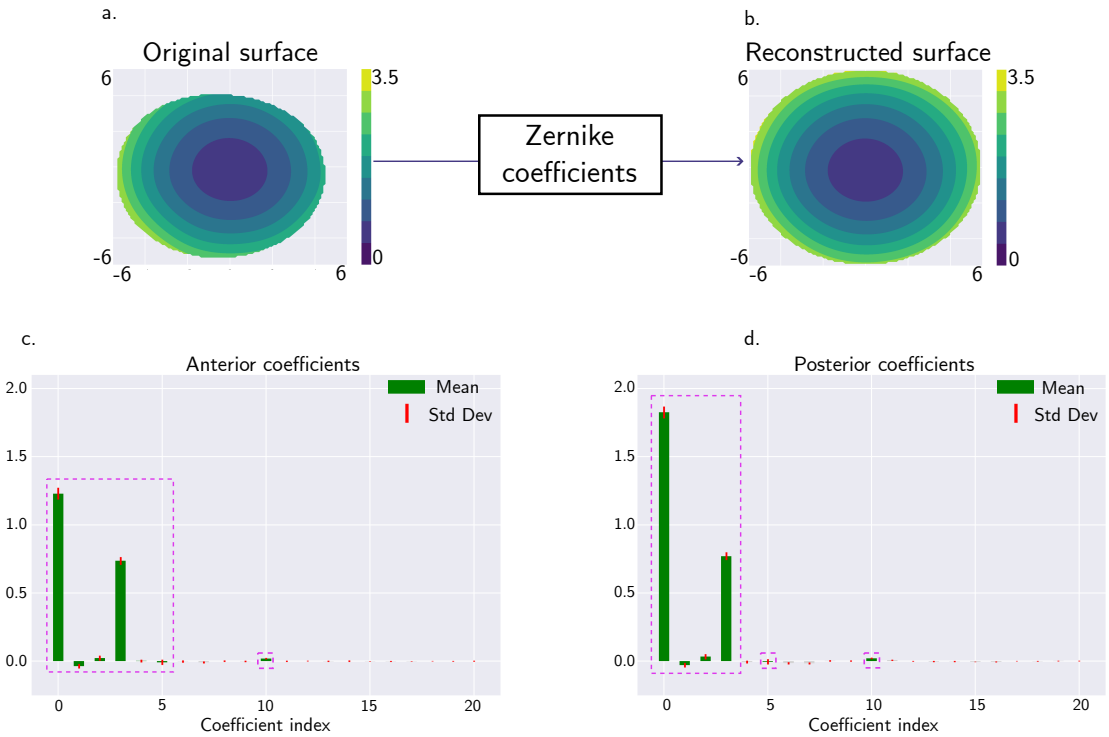

Figure 5.2: Analysis of the reconstruction of the corneal surface with Zernike polynomials. a) Example of original anterior corneal surface from the elevation data of Pentacam, b) reconstructed with Zernike polynomials. c) Mean and standard deviation of the Zernike coefficients obtained for the anterior corneal surface for all the patients analyzed. The coefficients with mean or standard deviation higher than 0.01 are highlighted. d) Mean and standard deviation of the Zernike coefficients obtained for the posterior corneal surface for all the patients analyzed. The coefficients with mean or standard deviation higher than 0.01 are highlighted.

Figure 5.2a depicts an example of the original Pentacam elevation map for the anterior corneal surface and figure 5.2.b the reconstructed corneal elevation map reaching a 6 mm radius cornea. Once the anterior and posterior surfaces are extended to 12 mm diameter, the corneal models are linked to a model of limbus and sclera with averaged dimensions and meshed with hexahedral solid elements with an average element size of 0.2 mm with the Pre processor ANSA (Beta CAE Systems, USA, Farmington Hills, Michigan). More details about the model can be found in chapter 3.

5.2.1.2 Design of experiment (DoE)

Twenty patient-specific corneal geometries with thickness ranging from 484μm to 588μm are constructed based on Pentacam data. The data used were randomly selected from a previous study conducted at Antwerp University Hospital (reference number of the Antwerp University Hospital Ethical Committee: 17/12/136). That study was conducted following the principles of the Declaration of Helsinki, and participants provided signed informed consent before measurement.

The patients under analysis are healthy, without corneal geometry complications caused by keratoconus or refractive errors, for this reason, Zernike coefficients describing the asymmetries are nearly zero in all the patients. In particular, analyzing the mean and the standard deviation of the coefficients for both the anterior and posterior corneal surface, we identify 7 coefficients for the anterior surface and 6 for the posterior surface with mean or standard deviation higher than 0.01 (figures 5.2c and 5.2d). We therefore adjusted the anterior and posterior surfaces with the coefficients with a mean or a standard deviation higher than 0.01 to keep the input parameters to a minimum.

Each FSI of the database is parametrized with n_f=17 relevant features:

- 7 Zernike coefficients describing the anterior corneal surface;
- 6 Zernike coefficients describing the posterior corneal surface;
- the intraocular pressure: IOP;
- 3 parameters describing the mechanical response of the corneal tissue: C_{10}, k_1, k_2.

A Montecarlo simulation of a total of 584 FSI simulations is executed, varying the mechanical properties of corneal tissue and the IOP within ranges found in literature (Ariza-Gracia et al., 2017b) listed in table 5.1 using a Latin Hypercube sampling method. To simplify the model, the mechanical properties of the sclera are kept the same in the whole dataset of simulations (Redaelli et al., 2022). A uniform distribution of input variables is assumed since there is no a priori data on the dispersion of the mechanical parameters in the human cornea, and therefore a total ignorance about the population is assumed.

The set of input parameters is collected in a matrix $\boldsymbol{\mu} = [\boldsymbol{\mu}_1, \boldsymbol{\mu}_2, ..., \boldsymbol{\mu}_N]^T$. Each vector $\boldsymbol{\mu}_i$ represents one simulation i and it contains the set of n_f=17 parameters. N is the total number of simulation run. A total of 394 simulations are performed on the first corneal geometry, then, for each of the remaining 19 corneal geometries, 10 simulations are carried out. Therefore, the dimension of matrix $\boldsymbol{\mu}$ is [N x n_f]=[584x17].

The stress-strain relationship for each combination of tested parameter is plotted in figure 5.3, with colors indicating the corresponding IOP used in the simulation. The range of mechanical response considered corresponds to the mechanical response of the

Ranges of input parameters			
Parameter	Min Value	Max Value	Unit
C_{10}	0.010	0.142	MPa
k_1	0.015	0.130	MPa
k_2	10	1000	-
IOP	8	30	mmHg

Table 5.1: Ranges of the input parameters regarding the mechanical properties of the cornea and the IOP of the FSI model for the NCT simulation.

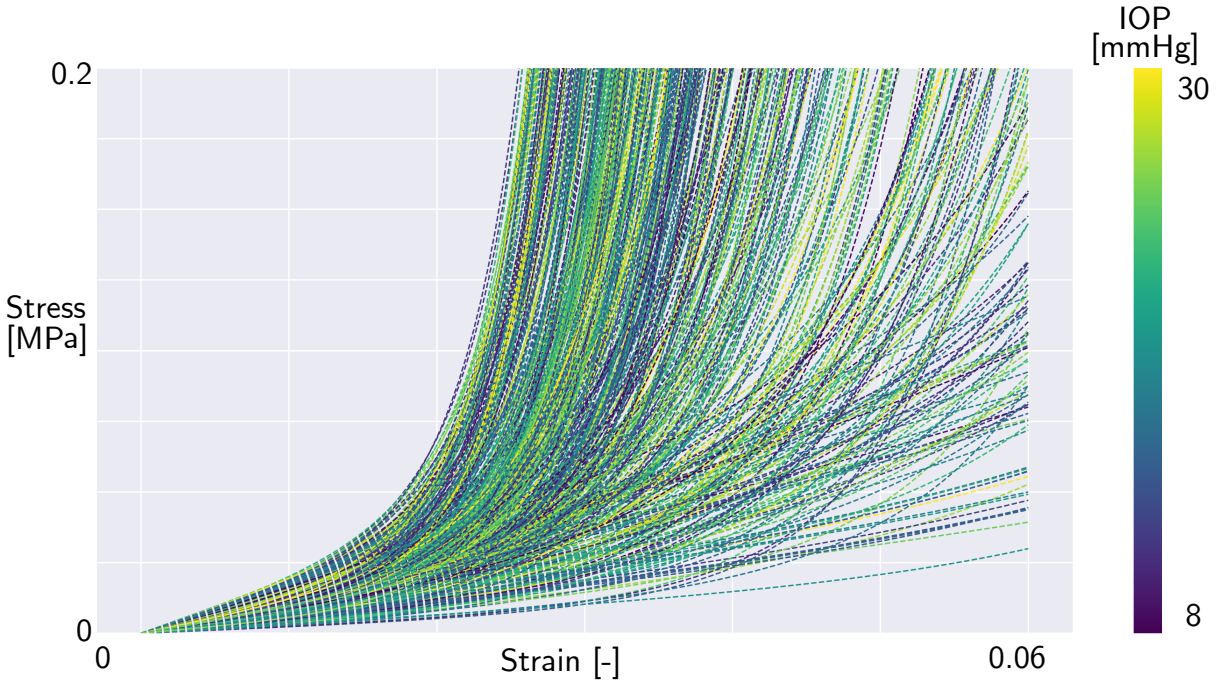

Figure 5.3: Stress-strain relationship of the corneal tissue model and associated IOP for each combination of parameters tested.

cornea found experimentally in literature (Maklad, 2019; Nambiar et al., 2023; Xue et al., 2018).

For each simulation, the x and y coordinates of the anterior surface of the Nasal Temporal (NT) section of the cornea (in the range $-4.5\text{mm} < x < 4.5\text{mm}$) are recorded at each $\Delta t = 0.21428\text{ms}$ - the same output frequency of Corvis ST (Boszczyk et al., 2019). Since the total duration of each simulation is 30 ms, the x and y coordinates of each point of the central section of the eye model are recorded 141 times per simulation.

All the simulations described are performed on 14 CPUs using a EPYC 7662 64-Core

Processor (2.0 GHz). The average computational time of each simulation is 24 hours.

5.2.2 Proper Orthogonal Decomposition (POD) of the displacement

The second step consisted in the reduction of the dimensionality of the collection of high fidelity solutions of the FSI simulations obtained running the model with different parameter values. POD is a dimensionality reduction technique often used in fluid dynamics, structural mechanics, and data analysis which analyzes and extracts dominant modes of variation in data. In POD, a singular value decomposition (SVD) is applied to a snapshot data (time-series data) to identify the most important spatial modes, which represent the primary patterns of variation in the data. The high-fidelity solutions dataset consists of a matrix $\mathbb{S}$ containing the x and y coordinates of the anterior central section of the cornea during the air-puff. In particular, $\mathbb{S} \in \mathbb{R}^{N_h \times N_{snap}}$ where $N_{snap} = N_t \cdot N$ (with N_t the number of time-steps in each simulation, N the total number of simulations run) and $N_h = 2 \cdot n$ are the x and y coordinates of the n points of the NT section of the corneal anterior surface.

POD is based on SVD, which is a mathematical technique that decomposes the matrix $\mathbb{S}$ into three matrices:

$$\mathbb{S} = \mathbb{U}\Sigma\mathbb{Z}^T, \tag{5.1}$$

where the matrix $\mathbb{U} \in \mathbb{R}^{N_h \times N_h}$, the matrix $\mathbb{Z}^T \in \mathbb{R}^{N_t \cdot N \times N_t \cdot N}$ and the matrix $\Sigma \in \mathbb{R}^{N_h \times N_t \cdot N}$ is a diagonal matrix. The values on the diagonal of Σ represent the singular values of the matrix $\mathbb{S}$. The singular values in Σ appear in descending order: the first singular value is the one explaining the highest amount of variance. The principal components contained in $\mathbb{U}$ and obtained through POD are orthogonal to each other and capture the most significant directions of variation in the data.

Our goal is to approximate the matrix $\mathbb{S}$ by means of a reduced number L of orthonormal vectors in $\mathbb{U}$ and L singular values in Σ. In order to choose the number L of orthonormal vectors sufficient to explain the full order model, an analysis based on the explained variance is conducted. The individual variance of each basis is a measure of the contribution of that basis to the total variance of the dataset. Each POD basis captures a certain amount of variability in the data, and the individual variance indicates how much of the overall variance is explained by each mode. The individual variance of the i-th POD mode is calculated as the ratio of the i-th singular value to the total sum of singular values. If we denote the singular values of $\mathbb{S}$ as σ_1, σ_2, ..., σ_m, where m is the total number of modes (m= $N_h = 2 \cdot n$), then the individual variance (IV) for the i-th mode is given by:

$$IV_i = \frac{\sigma_i}{\sum_{j=1}^{n} \sigma_j}, \tag{5.2}$$

and the cumulative variance:

$$\mathrm{CV}_i = \sum_{j=1}^{i} \mathrm{IV_j}. \tag{5.3}$$

The cumulative variance of equation 5.3 describe the variance explained by the basis considered and all the previous bases. According to this value, we decided to choose the number of bases explaining the 99% of the full order model. In this way, the dimensionality of the system is reduced to L, and the first singular values explaining the 99% of the model are stored in the matrix $\mathbb{V}$. The reduced basis solution $\mathbf{u}_L$ for a given set of input parameters $(\boldsymbol{\mu}, t)$ is an approximation of the full order solution $\mathbf{u}_h(\boldsymbol{\mu}, t)$ and is given by the product of a set of reduced coefficients $\mathbf{u}_{RB}(\boldsymbol{\mu}, t)$ with the reduced basis $\mathbb{V}$.

$$\mathbf{u}_L(\boldsymbol{\mu}, t) = \mathbb{V}\mathbf{u}_{RB}(\boldsymbol{\mu}, t), \tag{5.4}$$

where $\mathbf{u}_L(\boldsymbol{\mu}, t) \in \mathbb{R}^{\mathrm{N_h}\times 1}$, $\mathbb{V} \in \mathbb{R}^{\mathrm{N_h}\times \mathrm{L}}$ and $\mathbf{u}_{RB}(\boldsymbol{\mu}, t) \in \mathbb{R}^{\mathrm{L}\times 1}$. The coefficients $\mathbb{V}^{\mathrm{T}}\mathbf{u}_{\mathrm{h}}(\boldsymbol{\mu}, t)$ projects the full order model solution $\mathbf{u}_{\mathrm{h}}(\boldsymbol{\mu}, t)$ into the reduced basis $\mathbb{V}$ (equation 5.5).

$$\mathbf{u}_{\mathrm{RB}} = \mathbb{V}^{\mathrm{T}}\mathbf{u}_{\mathrm{h}}(\boldsymbol{\mu}, t). \tag{5.5}$$

These coefficients are calculated for each of the high fidelity solution in the dataset.

To evaluate the predictions of the ROM we calculated the POD projection error:

$$\mathrm{E_{POD}} = \frac{\|\mathrm{u}(\boldsymbol{\mu}, t) - \mathbb{V}\mathbb{V}^{\mathrm{T}}\mathrm{u}(\boldsymbol{\mu}, t)\|}{\|\mathrm{u}(\boldsymbol{\mu}, t)\|}, \tag{5.6}$$

and considered the maximum projection error over the set of snapshot. We denoted $\mathrm{E}_{1-\mathrm{POD}}$, $\mathrm{E}_{2-\mathrm{POD}}$, and $\mathrm{E}_{\infty-\mathrm{POD}}$ the 1-norm, the 2-norm and the infinity-norm of $\mathrm{E_{POD}}$ respectively.

5.2.3 Training of an Artificial Neural Network

Once the reduced bases $\mathbb{V}$ are constructed via POD of the snapshot matrix, the next step is to estimate the mechanical properties of the corneal tissue in each simulation based on the reduced coefficients in time, the IOP and the Zernike coefficients for anterior and posterior surfaces.

For the regression of the mechanical properties of the corneal tissue we adopt a feedforward artificial neural network as depicted in figure 5.4. Neurons are arranged into layers: one input layer composed of M_1 source neurons; K hidden layers, each one constituted of H_k computing neurons and one output layer of M_0 computing neurons. The output shape is the shape of the output layer. A feedforward network establishes a

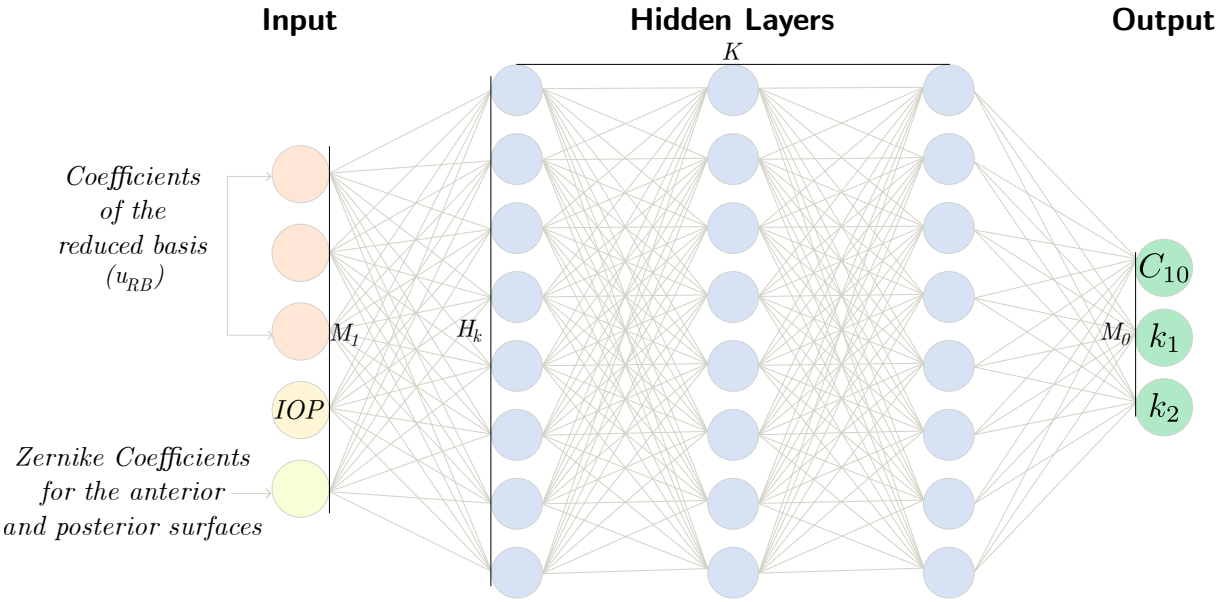

Figure 5.4: ANN architecture adopted for the regression of the mechanical properties of the corneal tissue. The network consists of one input layer containing the set of reduced coefficients in time ($\mathbb{V}^{\mathrm{T}}\mathbf{u}_{\mathrm{h}}(\boldsymbol{\mu}, t)$), the intraocular pressure (IOP) and the selected Zernike coefficients for the anterior and posterior surfaces; K hidden layers composed of $\mathrm{H_k}$ neurons and an output layer containing three parameters describing the mechanical properties of the corneal tissue (C_{10}, k_1 and k_2).

map between the input space and the output space. The inputs of the regression model are the coefficients of the reduced basis $\mathbb{V}^{\mathrm{T}}\mathbf{u}_{\mathrm{h}}(\boldsymbol{\mu}, t)$, the selected Zernike coefficients for the anterior and posterior corneal surface ($\mu_{Zernike}$) and the IOP. On the other hand, the output are the parameters describing the mechanical behaviour of the corneal tissue: C_{10}, k_1 and k_2.

We use a supervised learning paradigm, training the perceptron via exposition to a collection of known input-output pairs. To develop the model, the first step is the split of the available dataset into distinct subsets for training and testing purposes. In this study, we allocated 90% of the data for training and reserved the remaining 10% for testing. The training dataset serves to the ANN model to learn; whereas the test dataset, which remains unseen during the training phase, is utilized to assess the generalization performance of the trained ANN model.

Each component of the input pattern is called *feature*. Initially, a feature scaling technique in which all the features are scaled to the same range, is applied to the dataset. Given a feature x, the min-max normalization presented in equation 5.7 is applied.

$$\mathrm{x}_{\mathrm{scaled}} = \frac{\mathrm{x} - \mathrm{x}_{\mathrm{min}}}{\mathrm{x}_{\mathrm{max}} - \mathrm{x}_{\mathrm{min}}}. \tag{5.7}$$

The outputs are normalized as well with a min-max normalization to accelerate

the training of the network. The Leaky Rectified Linear Unit (Leaky ReLU) function (Ramachandran et al., 2017) is selected as activation function and the Adam stochastic optimizer (Kingma and Ba, 2014) as optimization method. The loss function used is the Mean Squared Error (MSE):

$$\mathrm{MSE} = \mathrm{mean}((t_{\mathbf{p}} - q_{\mathbf{p}})^2), \tag{5.8}$$

where for each input vector $\mathbf{p}$ belonging to the training set, $t_{\mathbf{p}}$ and $q_{\mathbf{p}}$ denote respectively the predicted and actual output. An optimization process to tune the NN hyperparameters is conducted to define the simplest neural network possible to best predict the results. The hyperparameters tuned are the batch size (number of samples processed at once during training), the learning rate (the pace at which the NN learns the values of a parameter estimate; it indicates how often the neural network refreshes the notions it has learned), the number of epochs (one complete pass of the entire training dataset through the learning algorithm) and the number of neurons in each layer. To achieve this, the kerastuner Hypermodel class (Gulli and Pal, 2017) is used.

To evaluate the predictions of the neural network we calculated for each of the three output parameters the error presented in equation 5.9.

$$E_{X-C_{10}} = \frac{\|C_{10-\mathrm{real}} - C_{10-\mathrm{predicted}}\|_X}{\|C_{10-\mathrm{real}}\|_X}, \tag{5.9}$$

where $C_{10-\mathrm{real}}$ and $C_{10-\mathrm{predicted}}$ are the actual and predicted material parameter respectively, and $X = 1, 2, \infty$.

5.2.4 Corneal mechanical properties estimation

The model constructed is used to estimate in real-time the mechanical properties of the corneal tissue in-vivo when the patient undergoes the Corvis ST test.

Given the 141 frames describing the corneal deformation, output of Corvis ST, a segmentation algorithm is applied. From the segmentation of the first frame, the Zernike coefficients for the anterior and posterior surfaces are calculated. The IOP directly given by Corvis ST can be used; however, since this IOP estimation depends on the mechanical properties of the corneal tissue, we proposed in chapter 4 a new methodology to estimate the IOP. Both the options can be used. The reduced basis coefficients are calculated projecting the corneal deformation obtained from the segmentation to the reduced basis with equation 5.5. The coefficients of the reduced basis, the Zernike coefficients and the IOP are given as input to the ANN model constructed and the mechanical properties of the corneal tissue are estimated in real time.

5.3 Results

This section begins by verifying the approximation of the geometry with the selected Zernike coefficients, then proceeds to the creation of the ANN to estimate the material properties for a single patient, and for 20 patients. Finally the methodology is applied to a clinical case.

5.3.1 Geometry parametrization evaluation

The choice of using only 7 coefficients for the anterior corneal surface and 6 coefficients for the posterior corneal surface does not compromise the accuracy of surface approximations compared to employing 21 coefficients. Figure 5.5 refers to the worst case scenario among all the patients. Figure 5.5a shows the elevation map of the anterior corneal surface when approximated with 21 Zernike coefficients wherease figure 5.5b shows the elevation map for the anterior corneal surface when approximated only with the 7 coefficients with mean and standard deviation higher than 0.01. The discrepancy between these two cases is demonstrated in figure 5.5c, showing a maximum difference of 0.17 mm at the corneal border (at a radius of 6 mm), which falls outside the scope of this study. Within the region of interest, specifically at a 4.5 mm radius, the difference is negligible. Since Corvis ST records only the NT section of the cornea, comprised between -4.5 mm and 4.5 mm, we conducted the analysis considering only this region. The cornea is the structure deforming the most during a NCT, therefore neglecting the other structures should not alter the results. Similar comparisons for the posterior surface are presented in Figures 5.5d and 5.5e.

5.3.2 Case 1: Corneal material prediction for one patient

We first considered the results corresponding to one patient - the geometrical parameters (the 13 zernike coefficients) were the same in each simulation. We had N=394 simulations, each with N_t=141 time steps. The x and y coordinates of 57 nodes of the anterior central section of the cornea were recorded, leading to N_h=114. Therefore, the snapshot matrix $\mathbb{S} \in \mathbb{R}^{114\times55554}$.

5.3.2.1 Dimensionality reduction

After centering the data by subtracting the mean within each row, the basis $\mathbb{V} \in \mathbb{R}^{114\times114}$ and 114 singular values were obtained. The distribution of the first 100 POD normalized singular values is depicted in figure 5.6a. The individual and cumulative explained variance in figure 5.6b shows that 11 principal components are sufficient to explain 99% of the model. With 11 basis, the maximum projection errors are: $E_{1-\text{proj}}$=0.78%, $E_{2-\text{proj}}$=0.16% and $E_{\infty-\text{proj}}$=0.25% (figure 5.6c). In terms of displacement, the maximum difference between the simulated and projected result over all the snapshots is 0.0195 mm, which is an acceptable result given that such a difference correspond to the dimension of only one pixel of the Corvis ST images (Redaelli et al., 2024). The section

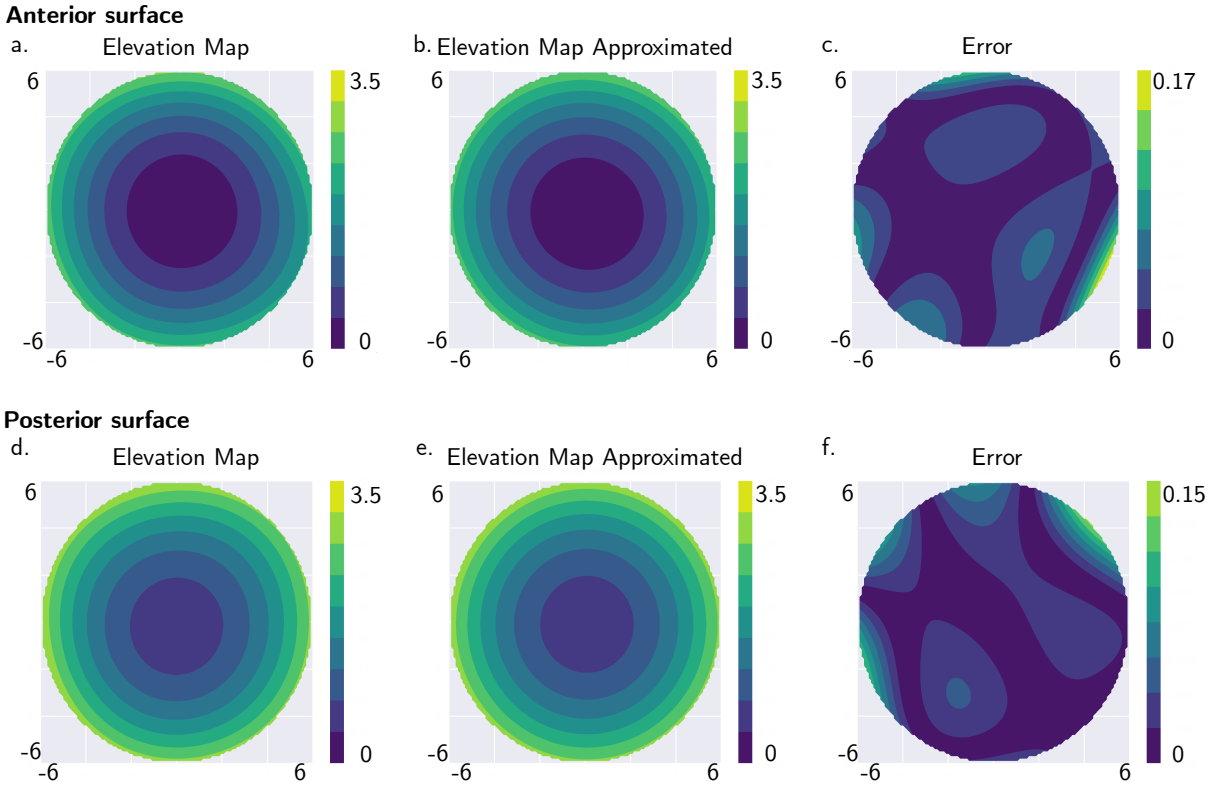

Figure 5.5: Anterior and posterior corneal surface. (a,d) Elevation map with 21 Zernike coefficients; (b,e) Elevation map only with coefficients with mean and standard deviation higher than 0.01; (c,f) difference in mm (corresponging to the absolute error) between the first two cases. The patient with maximum difference between the original and approximated map is presented.

corresponding to the snapshot with the highest difference between the simulated (in red) and projected (in blue) displacement is depicted in figure 5.6d.

5.3.2.2 Neural Network predictions

The ANN comprises an input layer with 12 input variables. Each input variable vary in time, therefore the inputs are organized in a matrix (141, 12) where 141 denotes the time steps considered for each simulation and 12 includes the 11 coefficients of the reduced basis and the IOP. 354 simulations were used in the training phase and 40 simulations in the testing phase. In this first case, since only one geometry is considered, the Zernike coefficients are not included as input. After tuning, the ANN architecture was configured with 2 hidden layers each containing 128 neurons and a *flatten layer* (Abadi et al., 2015) to reduce the dimension of the output. Notably, the parameters describing the mechanical properties of the corneal tissue does not vary during the period of the air-puff, thus the predicted parameters should not be dependent on time. For this reason, the dimension of the output will be (1,3) instead of (141,3). The learning rate is set to $10e^{-5}$ s and the number of epochs to 2000. An early stopping technique is also implemented to prevent overfitting, if the loss function does not decrease at an established rate during 40 epochs, the training stops without reaching the total number

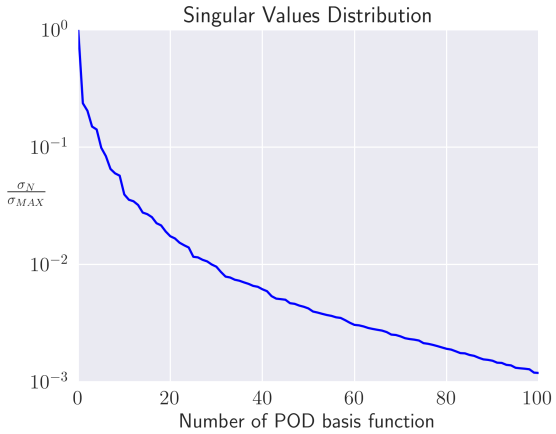

(a) Distribution of the first 100 normalized POD singular values in logarithmic scale.

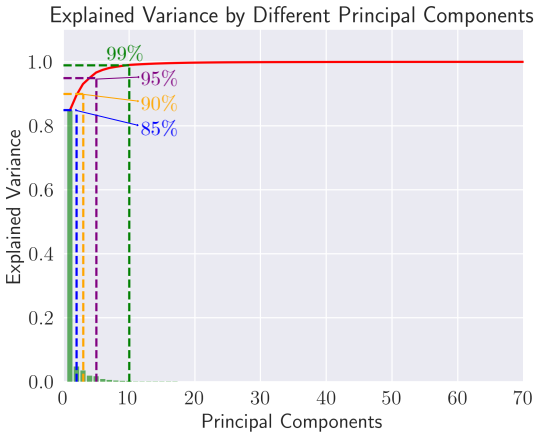

(b) Individual and cumulative explained variance. 11 principal components are required to account for 99% of the model's explanatory power.

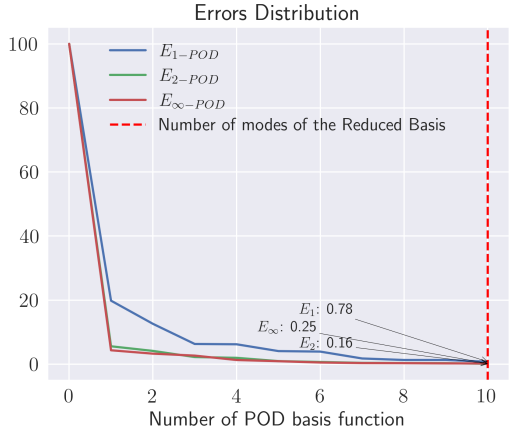

(c) POD projection errors with respect to the number of POD basis functions. L_1=0.78%, L_2=0.16%, L_∞=0.25%.

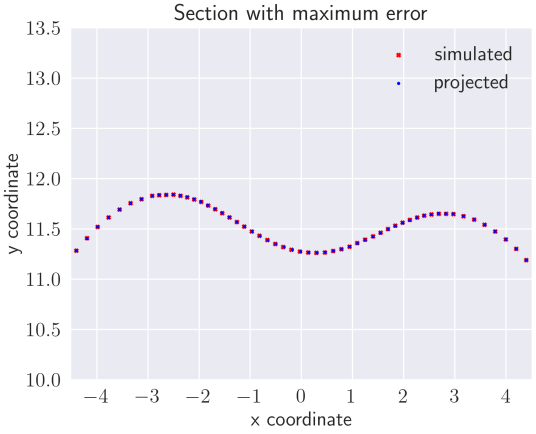

(d) Over the whole dataset of snapshots, the section with the maximum error between the FEM solution (in red) and the projected solution (in blue) is depicted.

Figure 5.6: Case 1: dimensionality reduction results for one patient.

of epochs initially determined. During each epoch, 10% of the training data is reserved for validation, with the split between training and validation data changing dynamically. The validation loss function decreases by two order of magnitude within 500 epochs before reaching a plateau. ANN training resulted in an average training time of 20 min using a commercially available Intel(R) Core(TM) i7-7700 CPU (3.60GHz).

The parameters describing the mechanical properties of the corneal tissue using the matematical model defined by the eqution 6.1 were estimated. The test data were not used during the training phase. Table 5.2a provides a comprehensive breakdown of the errors between the predicted and original parameters based on error equation 5.9. The prediction of C_{10} is the most accurate because it is the parameter influencing the most the corneal deformation (Redaelli et al., 2022).

Prediction errors one patient			
Parameter	E_1	E_2	E_∞
C_{10}	6.96%	7.19%	10.77%
k_1	16.53%	19.93%	45.12%
k_2	10.94%	12.48%	21.64%

(a) Errors in the prediction of the mechanical parameters when considering only one patient.

Prediction errors twenty patients			
Parameter	E_1	E_2	E_∞
C_{10}	5.85%	7.02%	9.77%
k_1	16.60%	21.38%	42.21%
k_2	9.64%	11.61%	20.42%

(b) Errors in the prediction of the mechanical parameters when considering 20 patients.

Table 5.2: Errors in the prediction of the mechanical parameters.

5.3.3 Case 2: Corneal material prediction for 20 patients

We then considered the displacement of the corneal nodes over the whole set of simulations comprising different geometical features. To the 394 simulations of the first patient, other 187 simulations were added leading to N=581, each with N_t=141 time steps. The x and y coordinates of 57 nodes of the anterior central section of the cornea were recorded, hence N_h=114. The snapshot matrix $\mathbb{S} \in \mathbb{R}^{114\times 81921}$.

5.3.3.1 Dimensionality reduction

From the POD, we obtained the basis $\mathbb{V} \in \mathbb{R}^{114\times 114}$ and 114 singular values. The distribution of the first 100 POD singular values is depicted in figure 5.7a. The individual and cumulative explained variance in figure 5.7b shows that 18 principal components expalins 99% of the model. With 18 basis, the maximum projection errors are: $E_{1-\text{proj}}$=0.53%, $E_{2-\text{proj}}$=0.11% and $E_{\infty-\text{proj}}$=0.21% (figure 5.7c). The section corresponding to the snapshot with the highest difference between the simulated (in red) and projected (in blue) displacement is depicted in figure 5.7d.

5.3.3.2 Neural Network predictions

The ANN comprises an input layer with a size of 32 varying in 141 time steps. The 32 coefficients include the 18 coefficients of the reduced basis, the IOP and 13 Zernike coefficients describing the anterior and posterior corneal surface. 523 simulations were used in the training phase and 58 simulations in the testing phase. The same ANN architecture described in section 5.3.2.2, is used.

The validation loss function decreases by two order of magnitude within 700 epochs before reaching a plateau. ANN training resulted in an average training time of 30 min using the same CPUs previously detailed.

The parameters describing the mechanical properties of the corneal tissue for the test

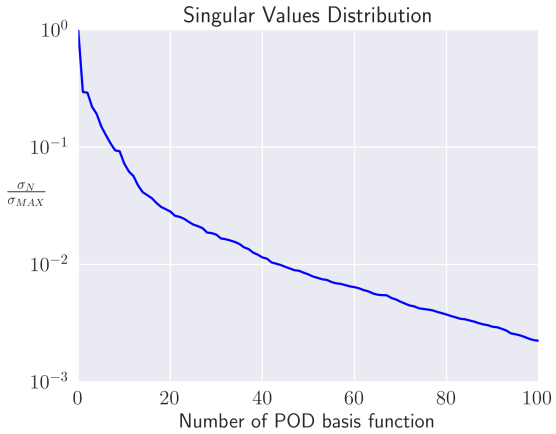

(a) Distribution of the first 100 normalized POD singular values in logarithmic scale.

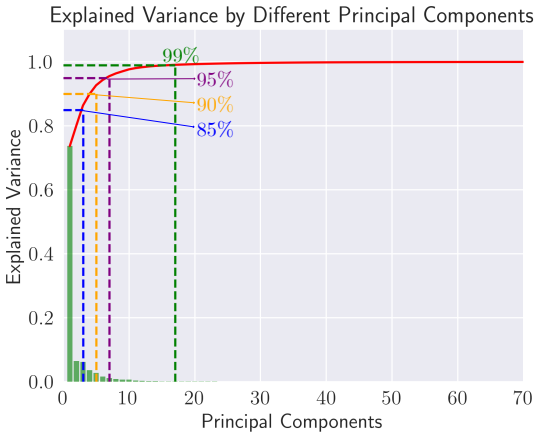

(b) Individual and cumulative explained variance. 18 principal components are required to account for 99% of the model's explanatory power.

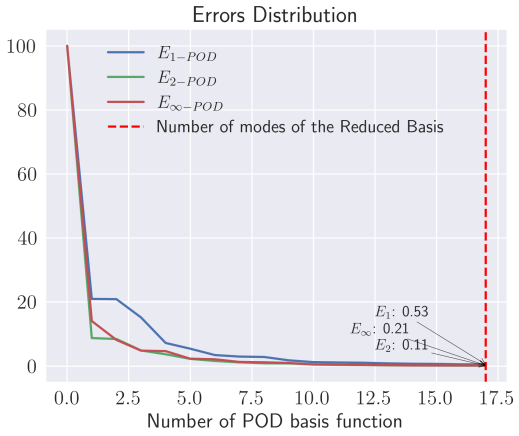

(c) POD projection errors with respect to the number of POD basis functions. L_1=0.53%, L_2=0.11%, L_∞=0.21%.

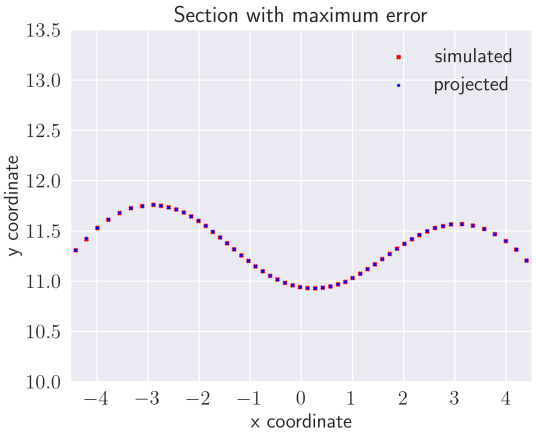

(d) Over the whole dataset of snapshots, the section with the maximum error between the FEM solution (in red) and the projected solution (in blue) is depicted.

Figure 5.7: Case 2: dimensionality reduction results for 20 patients.

data were estimated. Table 5.2b provides a detailed breakdown of the errors between the predicted and original parameters, calculated using equation 5.9. Also in this case, the prediction of C_{10} is the most accurate because it is the parameter influencing the most the corneal deformation (Redaelli et al., 2022). Figure 5.8 illustrates the stress-strain relationship for the parameters describing the mechanical behaviour of the corneal tissue for both the input parameters (in red) and the predicted parameters (in blue) across various test cases. The curves, representing different ranges, show acceptable differences between the actual and predicted relationships. At low strain levels (0-2% of deformation), when the fibers are not yet recruited, the mechanical response of the cornea is primarily governed by the parameter C_{10} and the prediction of the mechanical response is always coincident with the real response. On the other hand, at high strain levels, when the fibres are recruited, the slope of the curve is accurately predicted due to the low errors in predicting k_2. There are instead some discrepances in the strain

level at which the fibres are recruited, given by the parameter k_1.

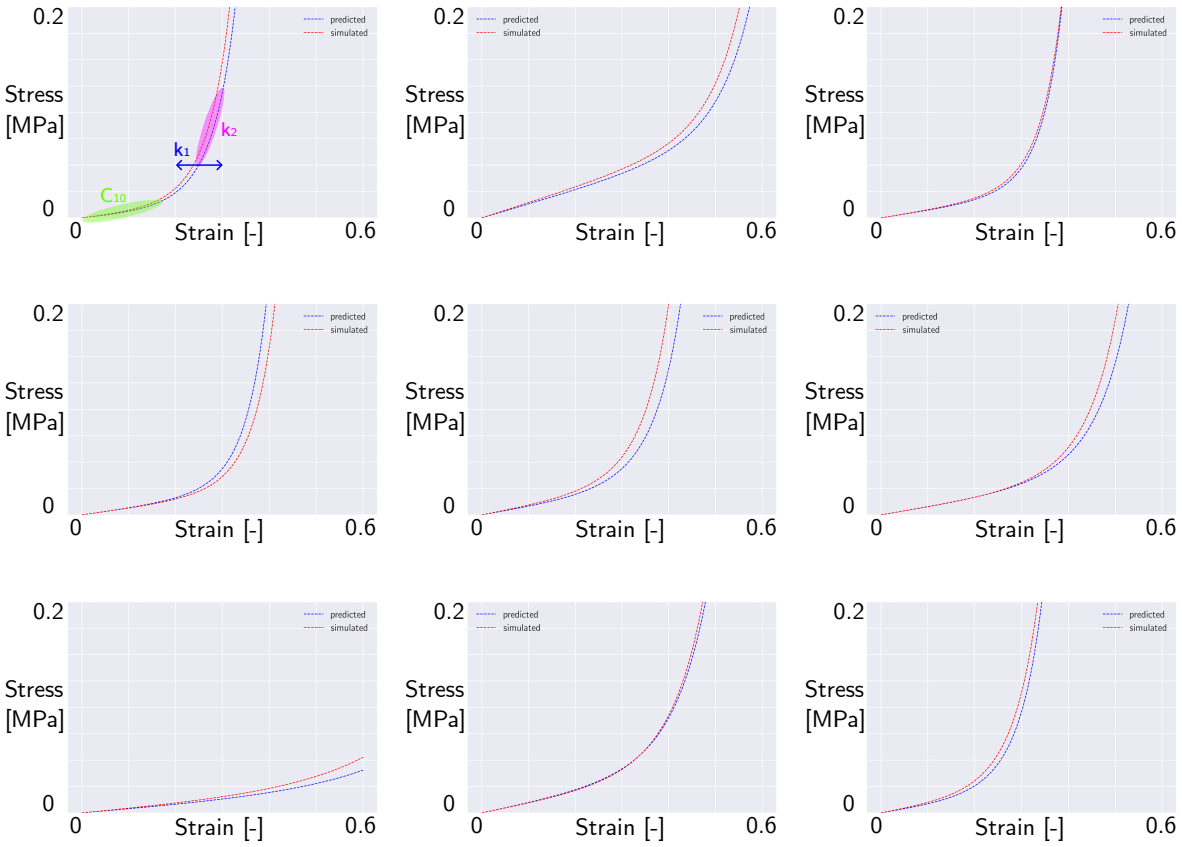

Figure 5.8: Mechanical response of the corneal tissue with the input parameters of the simulations (in red) and predicted by the artificial neural network (in blue).

5.3.4 Clinical application

To analyze the efficiency of the constructed methodology, the ANN trained in this study is used for real-time estimation of the mechanical properties of corneal tissue for one patient. Clinical data used in this section were randomly selected from a previous study conducted at Antwerp University Hospital (reference number of the Antwerp University Hospital Ethical Committee: 17/12/136). Initially, a set of 141 images obtained from Corvis ST undergo automated segmentation using a custom Python code. This segmentation process enables the extraction of the x and y coordinates of the anterior corneal surface which are subsequently utilized to compute the coefficients of the reduced basis, computed in section 5.3.3.1. The time corresponding to the maximum apex velocity, identified from the Corvis ST data, is used to estimate the intraocular pressure (IOP) using the methodology proposed in our recent work (*under review*). Elevation data from Pentacam scans are employed to calculate Zernike polynomials, providing an approximation of the anterior corneal surface. Once all necessary inputs are obtained, they are fed into the ANN model developed in Section 5.3.3.2 for real-time prediction of the mechanical properties of the corneal tissue in-vivo.

5.4 Discussion

Recently, the advancement in the development of new techniques based on artificial intelligence has revolutionized various sectors, including ophthalmology. One of the prominent applications of artificial intelligence in ophthalmology lies in the screening of pathologies (Ting et al., 2019). By training neural networks with images obtained from OCT or other imaging modalities, these models can identify characteristic patterns associated with pathologies such as diabetic retinopathy (Abràmoff et al., 2016), age-related macular degeneration (Ting et al., 2017), and retinopathy of prematurity (Brown et al., 2018). Lopes et al. (2019) reviewed the current applications of artificial intelligence techniques in corneal pathologies and few examples are reported. The Pentacam random forest index (Lopes et al., 2018) utilizes a random forest model for early keratoconus detection, using data from preoperative Pentacam exams of patients who developed ectasia after refractive surgery. In the field of the early detection of keratoconus, Arbelaez et al. (2012) introduced a new classification method based on corneal measurements obtained from Scheimpflug camera combined with Placido corneal topography (Sirius, CSO, Florence, Italy). Moreover, artificial intelligence models have enhanced the evaluation of in-vivo corneal morphology, for instance, to automatically identify healthy corneal layers in confocal microscopy exams (Ruggeri and Pajaro, 2002). The in-vivo assessment of corneal biomechanics is an open field of research. Ambrósio Jr et al. (2017) defined a tomography and biomechanical index (TBI) which integrates logistic regression analysis of Corvis ST data with artificial intelligence-driven tomographic data analysis.

To the best of our knowledge, there are no studies in literature which estimate the mechanical properties of the corneal tissue in-vivo. We developed an ANN model based on FSI numerical simulations to estimate the mechanical properties of the corneal tissue in-vivo and in real time. This work presents both a proof of concept, describing the methodology used to create the ANN model and a clinical application. For what regards the proof of concept, we first parametrized the geometry of the cornea (derived from elevation data of Pentacam) by means of Zernike polynomials and selected the most significant one demonstrating that they are sufficient to accurately describe the corneal surface. We run a large dataset of numerical FSI simulations of Corvis ST with different mechanical properties and IOP. Once a large dataset of corneal deformation was obtained, a POD technique was applied to find the principal modes of variation of the model and therefore to reduce the dimensionality. Hsu et al. (2023) used a similar approach to investigate the influence of IOP on corneal biomechanics. They segmented the Corvis ST images and identified temporal changes in the corneal behavior under the air-puff by applying a "modal analysis" with Legendre polynomials. Their study demonstrated that the corneal deformation during the air puff could be accurately captured by an orthogonal basis comprising a limited number of vectors. Actually, while the magnitude of corneal deformation may vary among patients, the underlying shape remains consistent across individuals. Consequently, in both cases analyzed in this work, a small number of basis vectors are sufficient to explain the variability of the model. In particular, when considering a single patient, only 11 basis vectors are needed to explain 99% of the model's variance. When adding the geometric variability, 18 basis

vectors are required to account for the same amount of variance. The reduced basis was used to calculate the reduced coefficients for each set of input parameters. These coefficients, together with the IOP and the Zernike coefficients, were given as input to train a feedforward ANN with as output the parameters describing the mechanical properties of the corneal tissue. The model constructed in the proof of concept is applied to a clinical case to estimates in real time the parameters describing the mechanical properties of the corneal tissue. One of the greatest advantages of this model is that it is a completely “data-driven" code, eliminating the need for running numerical simulations as required in previous works employing inverse analysis.

Concerning the architecture of the ANN, typically deeper networks provide a better fit to the data. In our study, we maintained the same architecture in both cases to facilitate comparison of the results. Even when incorporating geometric variability by considering 21 patients, thus necessitating more basis vectors, the training of the network yielded comparable results to the first case. The errors observed were similar, slightly lower in the case involving 21 patients. This could be attributed to the larger input dataset available in the latter scenario. In a future work, an even larger dataset could be considered to train the ANN in order to test the accuracy of the results.

The range of mechanical properties employed in this work is based on a previous study that combined findings from both inflation and uniaxial tests. Due to limited knowledge of the variation range of these properties, we opted to utilize the same broad range. A future work could be the application of the present methodology to a large cohort of clinical data to establish the human range of variation.

Part II

Applications

6

Early detection of Keratoconus

Part of the content of this chapter have been previously published in Journal of the Mechanical Behavior of Biomedical Materials: *E. Redaelli, M. Nana, B. Calvo, J. F. Rodríguez Matas, G. Luraghi, J. Rozema, and J. Grasa, Improving early detection of keratoconus by non contact tonometry. a computational study and new biomarkers proposal. Journal of the Mechanical Behavior of Biomedical Materials, 152 (2024), 106413.*

6.1 Introduction

Despite the evidence in the architectural organization of keratoconic tissue, data from ex-vivo testing of biomechanical properties of keratoconic corneas are limited and it is unclear how their results relate to true mechanical properties in-vivo. Andreassen et al. (1980) showed that the mechanical strength of the cornea is reduced in keratoconus using uniaxial tensile tests. On the other hand, Nash et al. (1982) did not encounter a significant difference in the elastic behaviour of normal corneas with respect to keratoconus corneas for physiologically relevant stress levels. They instead highlighted that keratoconic corneas were weaker for high levels of strain. A number of studies (Blackburn et al., 2019; Ambekar et al., 2011; Vellara and Patel, 2015) reported that keratoconic corneas are weaker compared to normal corneas, however, none of them provide reliable information about their mechanical properties in-vivo. Several techniques have been developed to investigate the mechanical behaviour of the corneal tissue in-vivo. To detect the presence of keratoconus from the results of Corvis ST, different indexes have been proposed. Vinciguerra et al. (2016) (Vinciguerra et al., 2017) introduced the Corvis Biomechanical Index (CBI) based on various dynamic corneal response parameters obtained from Corvis ST. The index can successfully differentiate between keratoconic

and healthy eyes in 98% of the analysed cases (Vinciguerra et al., 2016). In 2017, Roberts et al. (2017) proposed an index to evaluate the stiffness of the corneal tissue, the stiffness parameter A1 (SP-A1). The SP-A1 is the difference between the adjusted air pressure over the cornea at first applanation time and the biomechanically corrected IOP (bIOP (Eliasy et al., 2023)), divided by the deflection amplitude at first applanation time. Zhao et al. (2019) observed a decrease in SP-A1 in keratoconic patients. Both the CBI and the SP-A1 are only useful to classify healthy from keratoconic patients without giving any information about the mechanical properties of the pathological tissue and they are based only on the analysis of the NT section of the cornea. In a computational simulation, with a 3D model, it is possible to analyse the entire behaviour of the corneal structure, and not only its NT section, highlighting its anisotropic behaviour.

This chapter aims to evaluate the effectiveness of the current clinical biomarkers used in Corvis-ST in detecting early-stage keratoconus and establishing a relationship between these biomarkers and the mechanical properties of the pathological corneal tissue. In the initial stage of keratoconus, the ongoing alterations in the internal structure of the tissue are not reflected in its outer appearance, making it challenging to identify the presence of the pathology only by means of topographic analysis. Besides the computation of the biomarkers currently in use, a double-sectional analysis coupled with an asymmetry-based approach is proposed.

6.2 Materials and Methods

6.2.1 Numerical model of the NCT

The NCT is modelled using the FSI simulation presented in the previous chapters. Figure 6.1.a illustrates the 3D structure of the eye used in the simulations; the geometry comprises cornea, limbus, sclera, and humors. The crystalline lens, the ciliary zonule and the vitreous membrane are not included in the model since we demonstrated in our previous work (Redaelli et al., 2022) that they do not have an important influence on the corneal deformation during the NCT. The humors are represented as a cavity simulating an incompressible fluid, with an initial IOP set at 15 mmHg. The cornea and the limbus are described as anisotropic, nearly incompressible, hyperelastic materials, to account for the influence given by the network of collagen fibres. The cornea is described with two families of mutually orthogonal collagen fibres assumed perfectly aligned with the nasal-temporal (NT) and superior-inferior (SI) direction and the limbus is described with one circumferential family of fibres as shown in figure 6.1.b. In both cases, the Holzapfel-Gasser-Ogden (Holzapfel et al., 2000) constitutive model is used. Equation 6.1 shows the isochoric contribution of this model to the free energy.

$$\bar{\Psi} = C_{10}(\bar{I}_1 - 3) + \frac{k_1}{2k_2} \sum_{i=4,6} e^{k_2(\bar{I}_i - 1)^2} \tag{6.1}$$

where C_{10}[MPa] is a material parameter related to the extracellular matrix behaviour, k_1[MPa] refers to the stiffness of the fibres and k_2[-] models their non-linearity. I_1 is the first invariant of the right isochoric Cauchy-Green stress tensor, while I_4 and I_6 are respectively the fourth and the sixth pseudo-invariants related to the fibres stretch. The sclera is modelled as a nearly incompressible hyperelastic isotropic material with a Neo-Hookean formulation. The material parameters of the healthy eye tissues incorporated in the finite element model are listed in Table 6.1.

Material parameters				
Part	C_{10} [MPa]	k_1 [MPa]	k_2 [-]	Ref
Cornea	1.80×10^{-2}	1.26×10^{-1}	9.34×10^{2}	(Redaelli et al., 2022)
Limbus	2.50×10^{-2}	1.00×10^{-2}	1.00×10^{2}	(Redaelli et al., 2022)
Sclera	8.00×10^{-1}	–	–	(Redaelli et al., 2022)

Table 6.1: Material parameters of the healthy eye tissues incorporated in the finite element model.

The mesh and boundary conditions for the fluid domain are depicted in figure 6.1.c. First, a simulation is run with the healthy values of the corneal tissue. This simulation modelled the physiological scenario is denominated as PHY. Then, simulations corresponding to the pathological cornea are performed.

With reference to Pandolfi and Manganiello (2006), keratoconus is designed as a rounded diseased tissue with a core of 1.5 mm in radius and a transitional area of 1.5 mm in width that is divided into six circular zones as shown in figure 6.1.d and 6.1.e. Hence, the total pathological tissue has a diameter of 3 mm. This size is used for all analysis except for the sensitivity analysis where this dimension is varied. Keratoconus typically arises in the Inferior-Nasal region of the eye during its initial stages (Eliasy et al., 2020), therefore, the pathological area is modelled in the Inferior-Nasal region, corresponding to the negative x-axis ($x = -0.4$ mm) and positive z-axis ($z = 2$ mm) as shown in figure 6.1.d. In the numerical simulation, a left eye is considered. The central region of the rounded diseased tissue is modelled as an isotropic, nearly incompressible hyperelastic material using a Neo-Hookean formulation with the same C_{10} reported for the corneal tissue in Table 6.1. This approach aims to replicate the loss of the architectural organization of the collagen fibres (Meek and Boote, 2009). The six transitional zones are intended to provide a smooth progression from the healthy anisotropic tissue of the cornea to the completely isotropic tissue of the centre of the disease. With this intention, the parameter related to the stiffness of the collagen fibres k_1 is decreased linearly from 0.1265 [MPa] (healthy) to zero (pathological). The stress strain response of the zones considered is shown in figure 6.1.f.

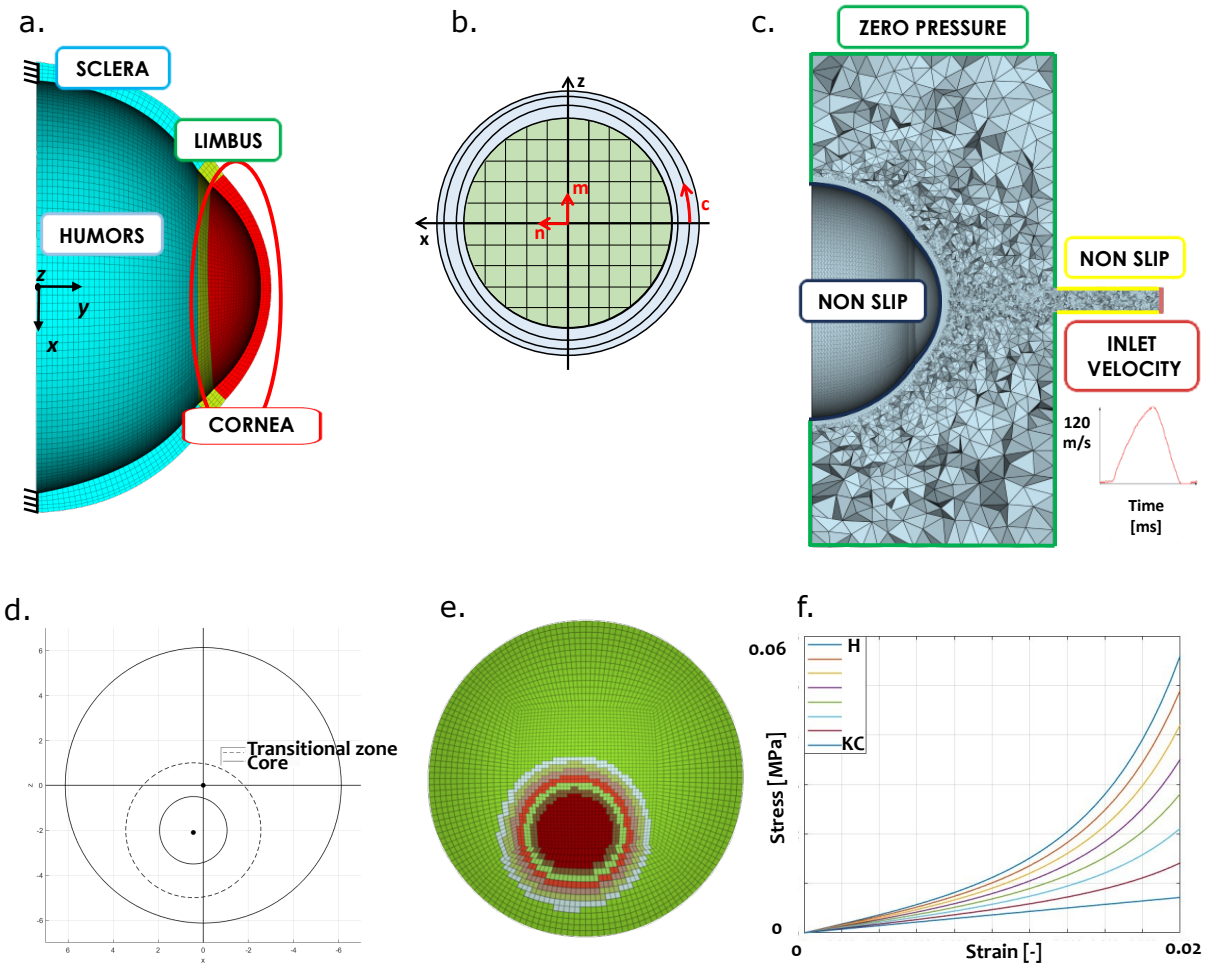

Figure 6.1: Numerical model of the Non Contact Tonometry: (a) structural model and boundary conditions; (b) assumption on collagen fibres distribution on cornea and limbus; (c) Fluid model and boundary conditions; (d) Pathological corneal model where the transitional region and the core of the pathological region are highlighted in the Inferior-Nasal quadrant; (e) Mesh of the pathological corneal model, the transitional zone is composed of six rings of elements. (f) Stress strain response of the pathological (KC), transitional and healthy(H) zones. In the model, a left eye is considered.

6.2.2 Sensitivity Analyses

6.2.2.1 Material sensitivity analysis

The first sensitivity analysis aims to evaluate the influence of the mechanical properties of the pathological area on the NCT results. For this purpose, the size and the location of keratoconus are kept constant, in particular, the centre is in $x = -0.4$ mm and $z = 2$ mm and the radius of the entire pathological area is 3 mm. Three different mechanical properties of the same material model are designed for this analysis. In the three pathological models, the mechanical behaviour of the core of the disease is

kept hyperelastic isotropic but different values of C_{10} are applied, to model different degrees of severity conditions. In the Template material model (TEM), C_{10} describing the response of the pathological area is of the same value as for the healthy tissue, while in the Increased material model (INC) and Decreased material model (DEC) the parameter is respectively increased or decreased by one third to describe a damaged tissue. The values of C_{10} used in the material sensitivity analysis are reported in Table 6.2.

Pathological model	C_{10} [MPa]
TEM	1.80×10^{-2}
INC	2.40×10^{-2}
DEC	1.20×10^{-2}

Table 6.2: Stiffness of the extracellular matrix in the pathological area of the three models of the material sensitivity analysis. TEM: template material model, INC: increased material model, DEC: decreased material model.

6.2.2.2 Size sensitivity analysis

The purpose of the size sensitivity analysis is to simulate the progression of the pathology. To achieve this, the size of the keratoconus (comprising both the core and the transitional area) is reduced to radii of 2 mm and 1.5 mm, as illustrated in figure 6.2.a. Consistent with the previous analyses, the centre of the rounded diseased tissue is kept in $x = -0.4$ mm and $z = 2$ mm, and the material parameters of the TEM model are assigned to each geometry to evaluate the influence of only size and assess the presence of a threshold value below which the pathology cannot be detected by the device.

6.2.2.3 Location sensitivity analysis

The last analysis performed is intended to examine the effect of the location of the pathological area. The TEM is renamed *"centred model"* and the output data obtained are compared with the *"shifted model"* obtained by displacing the initial pathological area on the bisector of the Nasal-Inferior quadrant of the left eye and keeping the same distance to the apex of the cornea (see figure 6.2.b). The positions of the centred and shifted models depicted in figure 6.2.b, corresponds to $x = -0.4$ mm for the initial position and $z = -1.75$ mm and to $x = -1.75$ mm and $z = 2$ mm for the shifted centre position.

6.2.3 Biomarkers

The computational approach provides the possibility to track and register the time evolution of all the nodes of the corneal model. However, to make the simulation

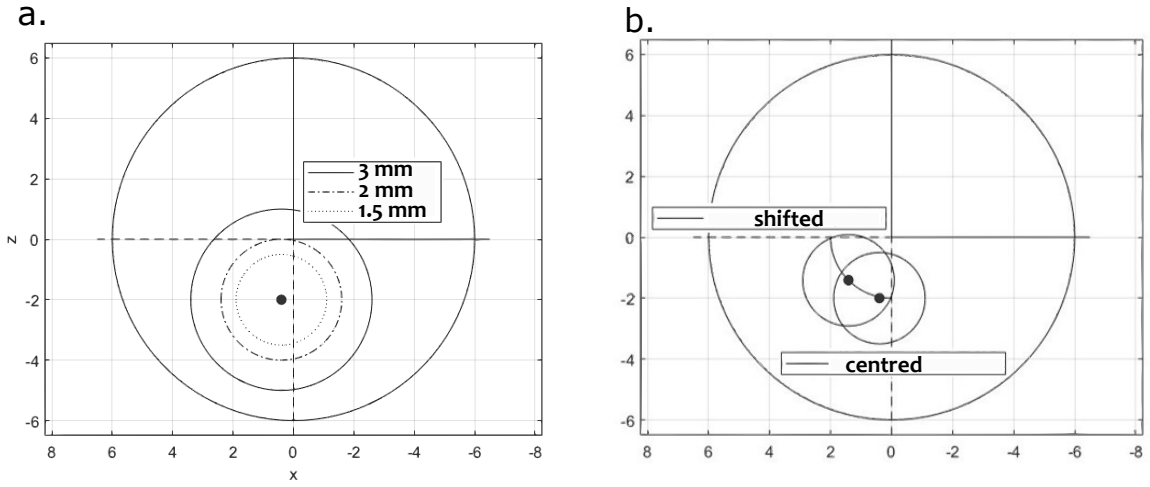

Figure 6.2: (a) Dimension of the pathological areas in the size sensitivity analyses; (b) Position of the pathological areas in the location sensitivity analyses. Keratoconus centre is placed in the Nasal-Inferior quadrant.

results comparable with the clinical results, three Corvis-ST biomarkers are selected and evaluated in the NT plane of each computational model:

- Deflection amplitude, which is the downward displacement of the corneal apex with respect to its initial position (figure 6.3.a).
- Delta arc length, which represents the difference between the length of a meridional section of the anterior surface computed between -3.6 mm and 3.6 mm in the initial configuration and the same length at HC (figure 6.3.b).
- Peak distance, which is the horizontal distance computed between the right and left peaks in the HC configuration (figure 6.3.c).

Among these biomarkers, only the deflection amplitude is tracked over time, and its peak value is used to determine the HC moment during the simulation.

In addition to the NT section captured by the device, from the simulations the SI section is also analysed and the respective biomarkers are computed. The nodes of the NT section coincide with the nodes of the anterior surface of the cornea that belongs to the xy plane of the system, whereas for the SI section corresponds the yz plane (figure 6.1.d). The two configurations are analysed in time during the air jet every 0.2 ms, which coincides with the frequency of the Corvis ST camera. Besides the abovementioned clinical biomarkers, at the HC instant, vertical and horizontal asymmetry indexes are defined with the purpose of better characterizing the influence of the diseased tissue on the corneal response. From an initial in silico analysis of the pathological cornea during the NCT, an evident asymmetry in the deformation has been seen and the need to have indexes to quantify this asymmetry became evident. Along both sections, the horizontal position of the lowest point of the anterior surface is captured and stored in the Sym_h index (figure 6.3.d), while the difference in height between the positive and negative

peaks of the configuration is defined as Sym_v (figure 6.3.e). The results of both the biomarkers and the asymmetry indexes are always compared with the pixel dimension of Corvis ST images (14 μm) to assess if the difference evaluated in the simulation can be observed by analysing the clinical images.

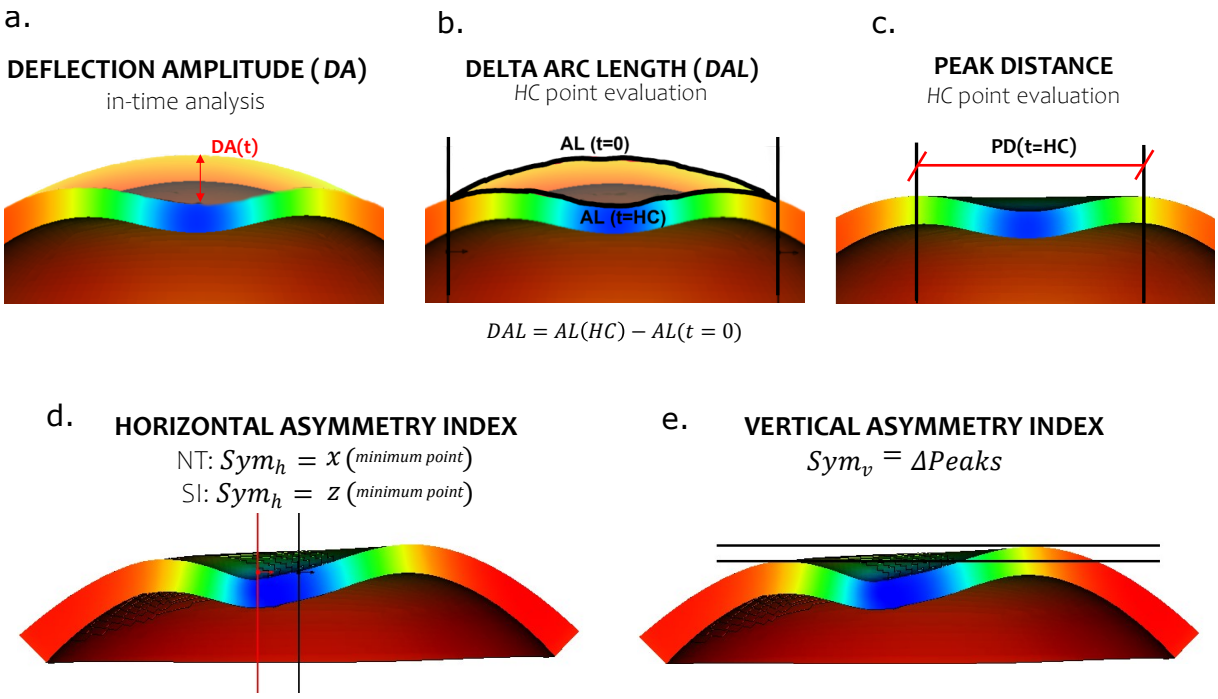

Figure 6.3: Graphical representation of the biomarkers analysed in both the NT and the SI sections: (a) Deflection amplitude, (b) Delta Arc Length, (c) Peak Distance, (d) Horizontal asymmetry index, (e) Vertical asymmetry index.

6.2.4 Clinical analysis

Six clinical cases with pathological corneas are analysed using both the topographic maps of Pentacam (OCULUS, Wetzlar, Germany) (OCULUS, 2019b) and their Corvis ST results. The data used were randomly selected from a previous study conducted at Antwerp University Hospital (reference number of the Antwerp University Hospital Ethical Committee: 17/12/136). That study was conducted following the principles of the Declaration of Helsinki, and participants provided signed informed consent before measurement. The analysed patients present late-stage keratoconic corneas with visible changes in axial curvature within the pathological zone. Two left eyes and four right eyes are considered. In the FEM model, a left eye has been considered. For all patients, the initial corneal profile and the profile at the time of HC are detected to determine if any asymmetries can be observed. The Sym_h and the Sym_v indexes are calculated for each patient at HC, and the relationship between the position of the pathological area and the asymmetry indexes is assessed.

6.3 Results

6.3.1 Material sensitivity analysis

The displacement fields captured at the HC time on the anterior surface of the cornea are depicted in figure 6.4.a for all the designed pathological models, alongside the data obtained for the healthy geometry. A trend of increasing values of downward displacement is evident, and it is consistent with the material weakening. This trend can also be appreciated by analysing the computed values of three biomarkers in figure 6.4.b. The deflection amplitude increases with the weakening of the pathological tissue. The values of the computed peak distance and delta arc length exhibit significant alterations compared to the healthy data, with a remarkable increase in magnitude in the SI section of the analysis. In particular, with the weakening of the tissue, the peak distance increases, and the delta arc length decreases. The anterior surface profiles at HC depicted in figure 6.4.c underline a non-symmetrical downward displacement induced by the degeneration of the tissue. The values of Sym_h reported in Table 6.3 show how the lowest point of each pathological configuration is shifted towards the positive values of x along the NT section and the negative values of z along the SI section, consistent with the position of the centre of the pathological tissue. This leads us to the conclusion that the weaker the mechanical properties of the tissue, the closer the minimum point is to the centre of the pathological area. The analysis of the Sym_v index in Table 6.3 indicates that all the models exhibit a difference in height between the peaks of the HC configuration, with the lowest peak captured in the positive values of x along NT and on the negative value of z along SI. To assess the detectability of the variations computed by the indexes, their magnitude should be compared with the resolution of the clinical images characterized by squared pixels of 14 μm. Since the values of all the indexes are higher than 14 μm, they can also be potentially used in a clinical analysis. We have introduced a progressive color scale ranging from green to red to map the Sym_v index, enabling a rapid visual assessment of the severity of the asymmetry. The scale is depicted in figure 6.5 and it is defined based on the conversion of the index to pixels. This scale is not applied to the Sym_h index because the value of this index is related to the position of the pathological area, not to its gravity.

6.3.2 Size sensitivity analysis

The progressive reduction of the size of the keratoconus (diameter reduced from 3 to 1.5 mm) results in a progressive reduction of corneal deformation as shown in figure 6.6.a (The healthy case and the pathological case with a radius of 1.5 mm are highlighted). From the analysis of the deflection amplitude of the apex of the cornea during the test depicted in figure 6.6.b, evince how halving the size of the damaged area to 1.5 mm leads to a deflection amplitude similar to the healthy case, with differences between the peaks of the curves of less than 2% mostly associated with numerical oscillation due to the numerical simulation. This is strengthened by the almost identical values of the peak distance, with a maximum difference of 0.3% on the SI direction, and the complete symmetrical downward displacement depicted in the asymmetry analysis

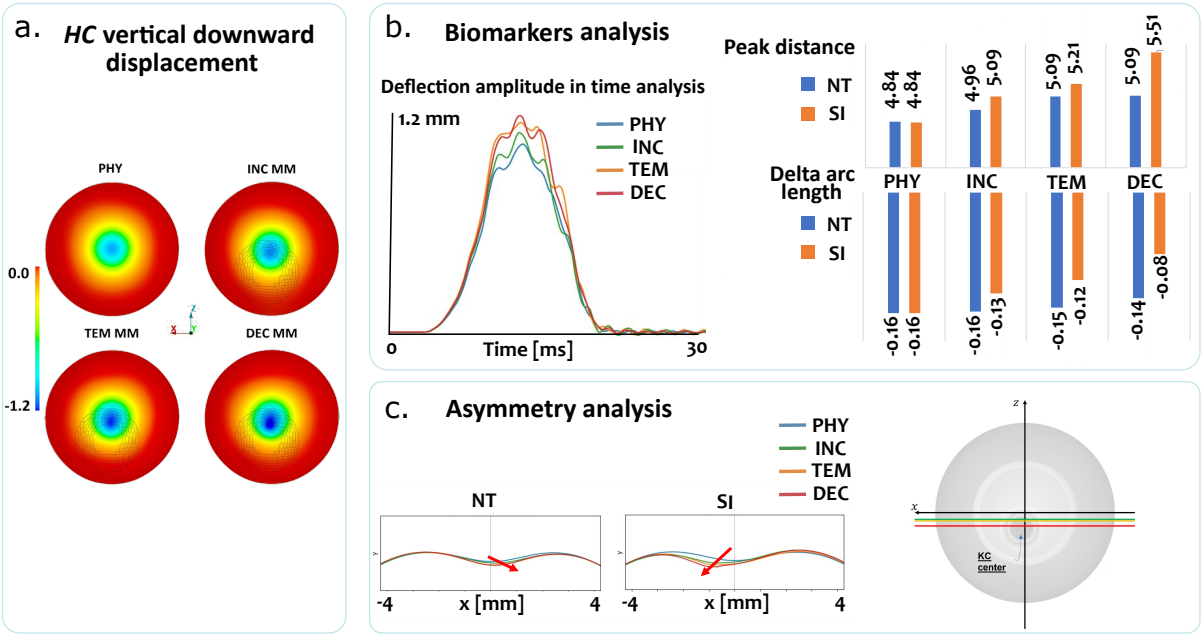

Figure 6.4: Material sensitivity analysis: (a) Contour of vertical displacement [mm] captured at HC time on the anterior surface of the cornea in the healthy case (PHY), in the template material model (TEM), in the increased material model (INC) and the decreased material model (DEC); (b) Corvis ST biomarkers evaluated in the four models; (c) Asymmetry analysis at highest concavity.

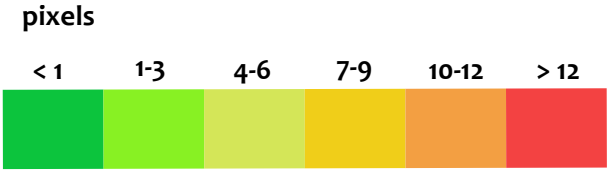

Figure 6.5: Scale colour introduced to visualize in the Sym_v index the severity of the pathological area.

		INC	TEM	DEC
Sym_h [mm]	NT	0.1321	0.1436	0.1513
	SI	−0.6305	−0.6624	−0.9141
Sym_v [mm]	NT	0.0639	0.0711	0.0787
	SI	0.1815	0.1007	0.1742

Table 6.3: Asymmetry indexes of the models evaluated in the material sensitivity analysis. The values of Sym_h of the NT section are positive, while the values of Sym_h of the SI section are negative consistent with the position of the centre of the pathological tissue. The values of Sym_v are filled with colors defined in the severity scale of figure 6.5.

of figure 6.6.c. The alterations due to the size of the keratoconus are of the order of one pixel, resulting undetectable by the segmentation technique used to analyse clinical images. When instead the radius of the pathological area is 2 mm, there are detectable differences both in the biomarkers and in the asymmetry indexes. This result highlights that there is a minimum size below which the NCT is not able to detect the presence of the pathology even using other sections of analysis and the new biomarkers.

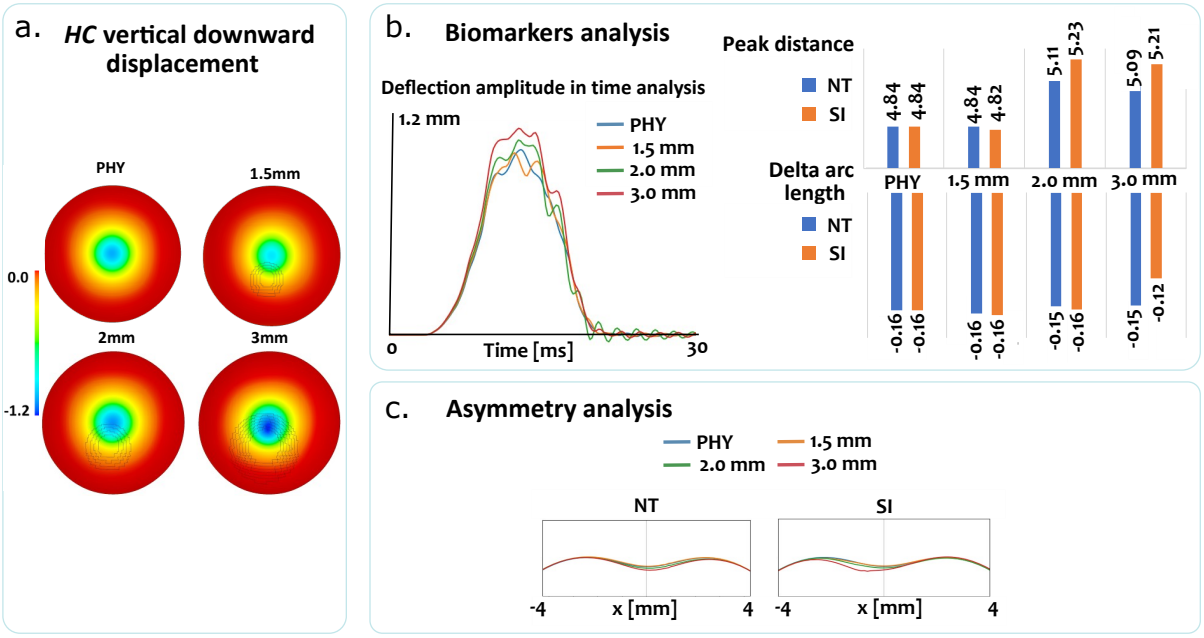

Figure 6.6: Size sensitivity analysis. (a) Contour of vertical displacement [mm] captured at HC time on the anterior surface of the cornea in the healthy case (PHY), and with different radii of the pathological area; (b) Corvis ST biomarkers evaluated in the four models; (c) Asymmetry analysis at highest concavity. The results are highlighted for the healthy case and the pathological case of 1.5 mm diameter to show that there is no difference between them.

6.3.3 Location sensitivity analysis

The displacement of the anterior surface of the cornea at HC (figure 6.7.a) and the biomarkers calculated in the NT section (figure 6.7.b) do not show important differences between the two models. More relevant variations can be appreciated by comparing the biomarkers in the SI section. Moreover, the Sym_h values of the two geometrical models are different. The shifted model registers the lowest point of the HC configuration in $x = -0.375$ mm and $z = 0.551$ mm, showing a remarkable asymmetrical downward displacement along both sections of the analysis. The SI and NT sections at HC configurations are depicted in figure 6.7.c along with vertical lines passing through the lowest points. The centred model exhibits a lower asymmetrical displacement along NT, where the lowest point is in $x = 0.14$ mm, while a higher asymmetrical degree on the perpendicular section can be seen by the Sym_h index equal to -0.663 mm.

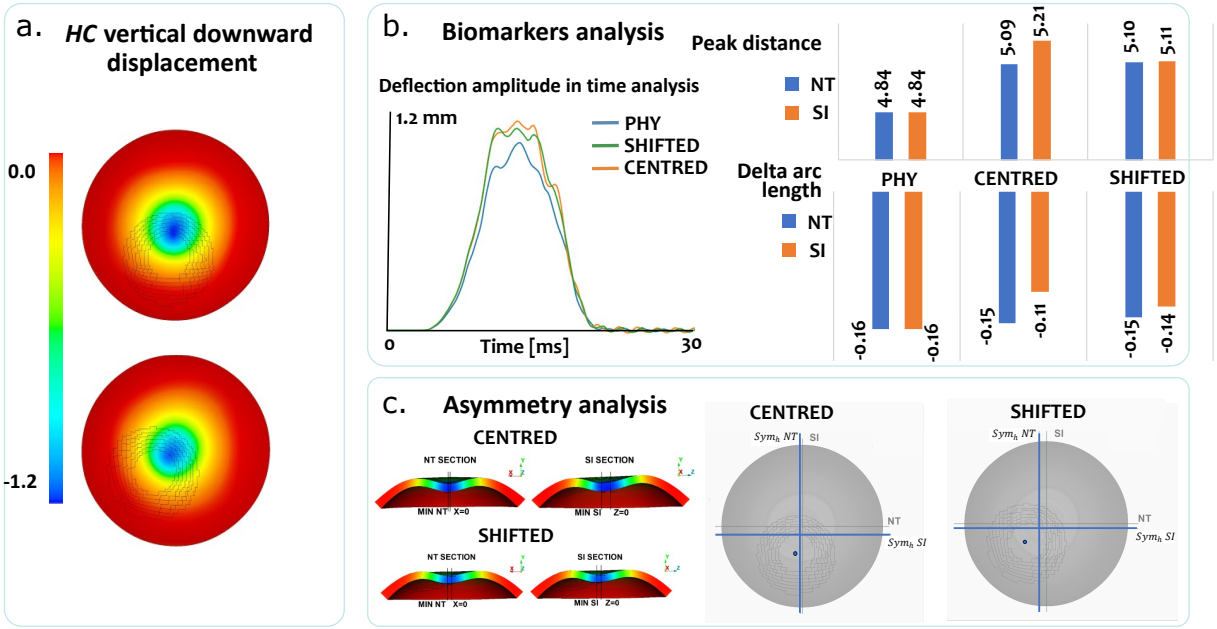

Figure 6.7: Location sensitivity analysis. (a) Contour of vertical displacement[mm] captured at HC time on the anterior surface of the cornea in the centred and shifted models; (b) Corvis ST biomarkers evaluated in the four models; (c) Asymmetry analysis at highest concavity.

6.3.4 Clinical analysis

The Pentacam axial maps of the patients analysed are shown in figure 6.8.a. The prevalence of the pathology in the Nasal-Inferior quadrant of the eye can be highlighted, demonstrating that our model represents the correct location of the disease. Figure 6.8.b shows that the highest deformation amplitude is reported for patients 53 and 92 who also have a steepest pathological area visible in the Pentacam maps. In those two patients, the pathological area covers almost the entire inferior part of the cornea, with an equivalent radius reaching 4 mm, higher than the one used in the simulations. The deformation amplitude is a Corvis ST biomarker defined as deflection amplitude plus whole-eye movement. Our material sensitivity analysis has shown that the deflection amplitude is higher for the weaker pathological tissues. This clinical evidence highlights that the more protruded the cornea, the weaker the underlying pathological tissue. Regarding the asymmetry of the structure, figure 6.8.a shows the corneal profiles at the initial configuration and at HC. Even if all the eyes are initially with a symmetric and centred shape, at HC they present an asymmetry both horizontally and vertically. The green line highlighting the Sym_h index shows that horizontally the asymmetry is not very evident because the position of the centre of keratoconus in the eyes considered is located near the vertical axis. In these cases, an analysis of the SI section of the cornea, as in our numerical analysis, could be useful to differentiate the patients. The Sym_h indexes reported in table 6.4 present both positive and negative values depending on the position of the center of keratoconus but they are close to zero. The Sym_v indexes reported in table 6.4, show an increasing value with the increase of the area affected by the pathology. In particular, patient 110, which presents the largest pathological area has the highest value of Sym_v. In treating clinical data it is worth noting that right and left

eyes are detected in different orientations by Pentacam and Corvis. The Nasal-Inferior region for right eyes (as patients 19, 53, 103, 110) is the fourth quadrant of the screen, while for left eyes Nasal-Inferior region is in the third quadrant of the screen.

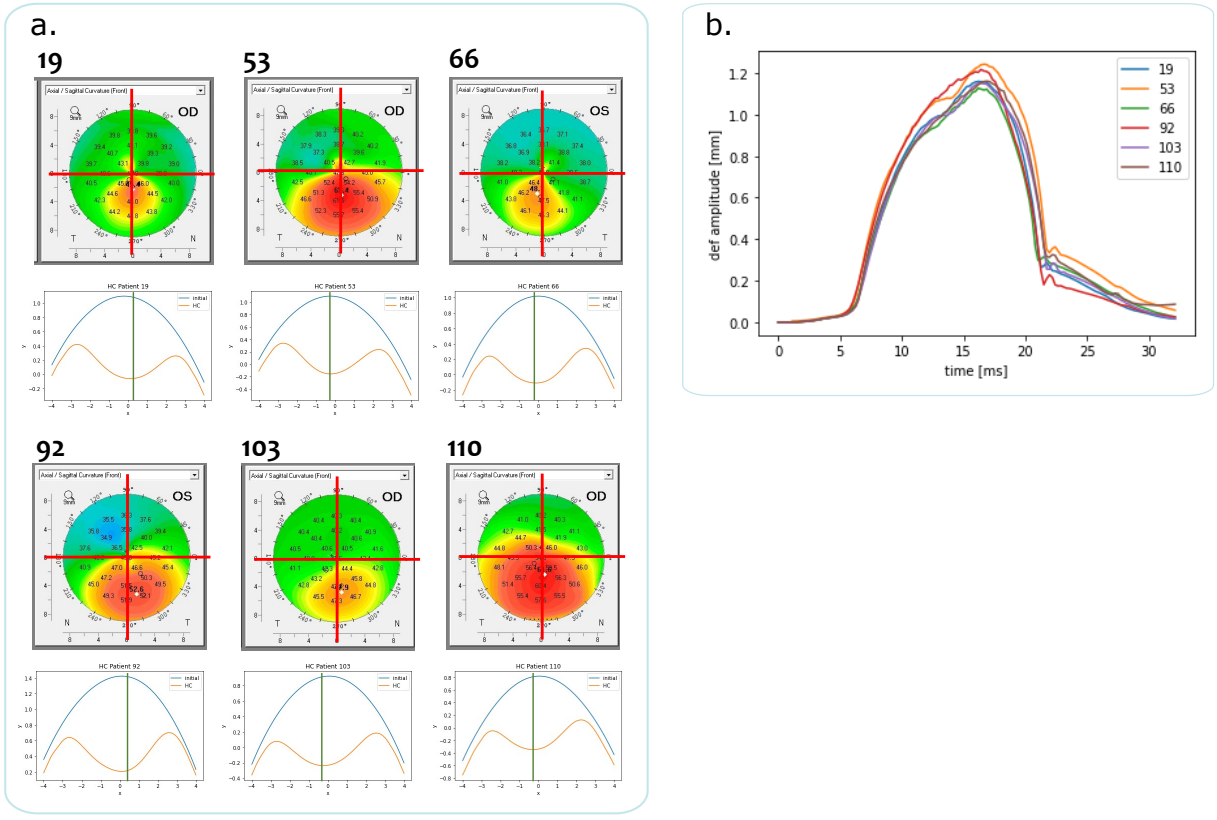

Figure 6.8: (a) Pentacam maps showing the axial curvature of the anterior corneal surface of each patient. The initial and HC configuration of the same corneas during Corvis ST are shown below each map. The green line shows the position of the minimum point. (b) deflection amplitude in time for each patient evaluated by the Corvis ST device.

Patient Number	Sym_h [mm]	Sym_v [mm]
19	0.130	0.162
53	−0.234	0.101
66	−0.136	0.101
92	0.102	0.062
103	−0.248	0.108
110	−0.290	0.173

Table 6.4: Horizontal and vertical asymmetry indexes for the patients analysed. The values of Sym_v are filled with colors defined in the severity scale of figure 6.5.

6.4 Discussion

The increasing incidence of keratoconus and its clinical implications have sparked interest in modelling and characterizing the mechanical properties of pathological corneas through new devices and numerical simulations which are useful for describing the corneal dynamic response. In their work, Anderson et al. (2004) developed a finite element model of a keratoconic cornea, wherein the pathological area was characterized by a gradual loss of thickness. They modelled the corneal behaviour during Goldamann Applanation Tonometry (GAT), founding an increased corneal deformation as a result of the disease and they highlighted that the distribution of the deformation is dependent on the location of the pathological area. Our analysis has shown that the behaviour of the keratoconic cornea during Corvis ST is in line with its behaviour during GAT. However, their modelling of the diseased tissue focused solely on reducing the thickness of the structure without studying the influence of the material properties. Gefen et al. (2009) examined the mechanical behaviour of the keratoconic cornea using a simulated inflation test, modifying the parameters of the healthy orthotropic material model alongside a thickness reduction to represent the pathological tissue. They underlined that the combination of tissue thinning, and degraded material properties is involved in the pathogenesis of keratoconus, leading subsequent works to concentrate the analysis on the pathological mechanical properties. Pandolfi and Manganiello (2006) employed the Holzapfel-Gasser-Ogden equation to model the corneal tissue as a fibre-matrix reinforced material. They proposed to lower the parameters of the healthy model when simulating the keratoconus and they compared the results of their simulations with experimental uniaxial tensile tests and inflations tests, demonstrating that the lowering of the mechanical properties of a region of the cornea could describe in a reliable way the behaviour of keratoconic corneas. For this reason, the same approach has been adopted in this work, together with the approach adopted in Roy and Dupps (2011) in which, to simulate the response of keratoconic corneas to collagen cross-linking patterns, the centre of the pathological area was considered isotropic. In a more recent publication, Giraudet et al. (2022) investigated the origin of keratoconus pathology comparing in a simulation the change in pathological geometry and mechanical properties. They tested the influence of small variations of each mechanical parameter of an anisotropic material model on the corneal deformation during an inflation test, and they observed that the most sensitive parameter is the unfolding stretch, that is the stretch at which the fibrils start to generate force. This result supports our choice of isotropic behaviour of the core of the pathological cornea.

To the best of our knowledge, this is the first study dealing with the numerical simulation of NCT on a keratoconic eye. During the NCT, the cornea undergoes non-physiological deformation, enabling the evaluation of its response at high levels of strain. Since the first stage of keratoconus is characterized by alterations in the fibres organization, which impact the corneal response at high levels of strain, establishing a connection between the mechanical properties of the corneal tissue and the results of the NCT test could be of great interest for early-stage pathology detection (Santodomingo-Rubido et al., 2022). We have presented three sensitivity analyses regarding the influence of mechanical properties, size and location of the pathological area on the outputs of a

commercially available NCT, the Corvis ST. Our analysis goes beyond the typical focus on the NT section of the cornea of Corvis ST. We have proposed a double sectional analysis, which allows for a deeper examination of corneal deformations. This approach is supported by previous research by Curatolo et al. (2020) and Li et al. (2023), which showed that exploring multiple meridians reveals important differences between keratoconic and normal eyes. In particular, Curatolo et al. (2020) proposed a customized OCT system coupled with a collinear air-puff excitation unit, capable of acquiring dynamic corneal deformation on multiple meridians, both in ex-vivo and in-vivo eyes demonstrating that the early-keratoconic eyes show a higher apical displacement, as well as a distinct asymmetry between the vertical and horizontal meridians. On the other hand, Li et al. (2023) explored different meridians showing that the differences between the keratoconic and normal eyes in the SI and SN-IT meridians were increased compared to the NT meridian.

Our study extends the idea of these papers by introducing two new indices, the horizontal asymmetry index (Sym_h) and the vertical asymmetry index (Sym_v), which further enrich our understanding of corneal asymmetry in pathological conditions. In the material sensitivity analysis, the fields of downward displacement captured at HC, reflect the increasing compliance induced by the presence of the keratoconus. The magnitudes of the computed biomarkers are significantly altered when compared with the benchmark results obtained from the healthy geometry on both sections of analysis. These parameters exhibit a persistent increment in SI, resulting from the fixed position of the damaged tissue that crosses the SI section. This higher influence is confirmed by the asymmetry-based analysis. The Sym_h value shows an increase in amplitude with the weakening of the tissue towards the coordinate of the core of the rounded diseased tissue, centred in $z = -2$ mm. In the size sensitivity analysis, we found that Corvis ST in unable to detect pathological areas with a diameter lower than 1.5 mm. The unaltered deformation behaviour of the 1.5 mm model with respect to the healthy behaviour, is given by the combination of two separate factors. The acquired data resulted from both the halving of the initial size of the diseased tissue and the increased distance of the tissue from the area subjected to the applied pressure load. This increased distance is due to the fixed position of the centre of the rounded diseased tissue. The last analysis evaluates the accuracy of the proposed asymmetry indexes to locate the pathological tissue. In both geometries tested, the clinical biomarkers were significantly apart from the healthy ones, emphasizing how these variations could lead to the detection of the pathology but without providing suitable details regarding the location of the affected area. Instead, the data obtained from the asymmetry-based analysis can be integrated for deriving position information on the direction of maximum displacement of the anterior surface of the cornea. In each model, combining the values of the Sym_h parameter computed along the two sections of analysis a point on the outer surface of the tissue can be derived and assumed as a guide to identifying the affected region. The values computed in both models are in fact directed toward the centre of the designed rounded diseased tissue.

Given that our findings are based on a numerical simulation of a left eye, the results from such analyses should be treated with caution. In a left eye, according to our

reference system, the Nasal-Inferior quadrant corresponds to the negative values of the x-axis and positive values of z-axis. In a right eye, instead, the Nasal-Inferior quadrant correspond to positive x-axis and positive z-axis. While the Sym_v index is always positive, we demonstrated that the sign of the Sym_h index gives information about the position of the centre of the pathological area. To avoid misunderstandings about the position, Table 6.5 relates the sign of the horizontal asymmetry index with the position of the pathological area.

Eye	Sym_h in the NT section	Sym_v in the SI section	Keratoconus centre position
Left	-	+	NASAL-INFERIOR
Left	-	-	NASAL-SUPERIOR
Left	+	+	TEMPORAL-INFERIOR
Left	+	-	TEMPORAL-SUPERIOR
Right	-	+	TEMPORAL-INFERIOR
Right	-	-	TEMPORAL-SUPERIOR
Right	+	+	NASAL-INFERIOR
Right	+	-	NASAL-SUPERIOR

Table 6.5: Correspondence between the values of the horizontal asymmetry indexes and the centre of the pathological area.

In conclusion, our study underscores the potential of integrating information from the SI section to enhance the ability to detect pathological corneas. By considering corneal deformations along both meridians and introducing asymmetry-based indices, we offer a more comprehensive understanding of corneal behaviour in keratoconus. As the clinical analysis have revealed, the pathological area usually appears in the Temporal-Inferior quadrant of the eye, affecting more the SI plane with respect to the NT plane. This is the reason why the deformations of the SI plane are higher than the deformation of the NT during the NCT. Considering both the deformations, not only advances our knowledge of the disease but also holds promise for more accurate and early-stage pathology detection in clinical settings.

7

MIGS implant and aqueous humor drainage simulation

7.1 State of the art

The aqueous humor is produced in the posterior chamber of the eye, and it flows across the anterior surface of the lens, passing through the pupil to enter the anterior chamber. At this point, two outflow pathways are available: the conventional pathway, where the aqueous humor flows through the trabecular meshwork, and the uveoscleral pathway, where the aqueous humor leaves the anterior chamber by diffusing through intercellular spaces among the ciliary muscle fibers. Finally, the aqueous humor enters the Schlemm's canal. When the permeability of these channels changes, the aqueous humor is drained less effectively, leading to increased intraocular pressure and causing glaucoma. To prevent optic nerve damage, minimally invasive glaucoma surgeries (MIGS) aim at developing an alternative path for aqueous humor drainage with the implantation of micro stents as detailed in chapter 1. To understand the pathophysiology of glaucoma treatments, limited computational investigations have been conducted on the hydrodynamics of the aqueous humor following the implantation of MIGS devices. To determine aqueous humor flow characteristics under physiological and pathological conditions, Villamarin et al. (2012) implemented a CFD simulation to reproduce the aqueous humor flow and evaluate the effects of various glaucoma surgeries. The 3D domain consisted of the cornea, lens, iris, trabecular meshwork, Schlemm's canal and ciliary body. Trabecular meshwork was modeled as a porous domain, with different permeabilities for healthy and pathological eyes. To simulate aqueous humor production, an inlet flow rate was imposed at the level of the ciliary body, while as outlet boundary condition, a static pressure of 7 mmHg was imposed at the level of the Schlemm's canal.

The initial pressure of the fluid domain was set at 13.5 mmHg for healthy cases, and at 27 mmHg for glaucomatous cases. To simulate the surgery, they created a scleral flap with the same outlet boundary condition as the Schlemm's canal where they inserted a model of a commercial MIGS. The objective was to evaluate the aqueous humor velocity, IOP and wall shear stress both in healthy and glaucomatous eyes and the effects of glaucoma surgeries on the same quantities. Following the same methodology, a CFD simulation was carried out by Mauro et al. (2018) evaluating the aqueous humor flow after the implantation of various glaucoma drainage devices, including the iStent Inject. A velocity inlet boundary condition was imposed to simulate the aqueous humor production and as outlet boundary condition a pressure of 10.5 mmHg was imposed at the outlet of the drainage devices. The objective of the study was to evaluate the thermo-fluid characteristics inside the anterior chamber of the eye model, in order to compare pre-operative and post-operative conditions, in terms of IOP values, velocity, and heat transfer. Trabecular meshwork was represented as a porous tissue, characterized by specific permeability and porosity values. This study demonstrated that the resistances imposed by the MIGS to aqueous humor flux were much lower than the trabecular meshwork resistance in pathological cases, for this reason, the majority of the aqueous humor flux go through the devices. Kudsieh et al. (2020) presented another 3D CFD simulation with the purpose to predict and compare the efficacy and safety of three different MIGS devices. A pressure of 15 mmHg was employed as outlet boundary condition and a constant flow rate of aqueous humor as inlet condition. The flow across the implanted device and through the trabecular meshwork was studied. Authors looked into the role of devices' dimensions and implant's positions. The potential risk of corneal endothelial cell loss was studied by evaluating wall shear stress in order to explore the safety of these devices. A recent numerical study of Basson et al. (2024) investigated the endothelial cell damage associated with the implant of glaucoma drainage devices with a CFD simulation. The same boundary conditions described in the previous studies were adopted.

To the best of our knowledge, there are no studies in literature that simulate the surgical process of MIGS implant; all existing studies consider CFD simulations with the device as part of the geometry. However, the implant itself can induce residual stresses on the eye, potentially impacting the aqueous humor flow. Additionally, since the eye is a deformable structure, the IOP value is influenced by the deformation state of the eye and viceversa. Therefore, a FSI simulation that accounts for the deformability of eye tissues could yield more reliable results in studying the aqueous humor flow post-MIGS implantation. We propose a methodology to simulate the MIGS implant and the consequent aqueous humor flow. The objective is to analyze the mechanical stresses and deformations that the devices induce on the eye and to assess the resultant aqueous humor flow after their implantation. The device considered in this study is the iStent Inject (Glaukos Corp., Aliso Viejo, California, USA) (Shalaby et al., 2021).

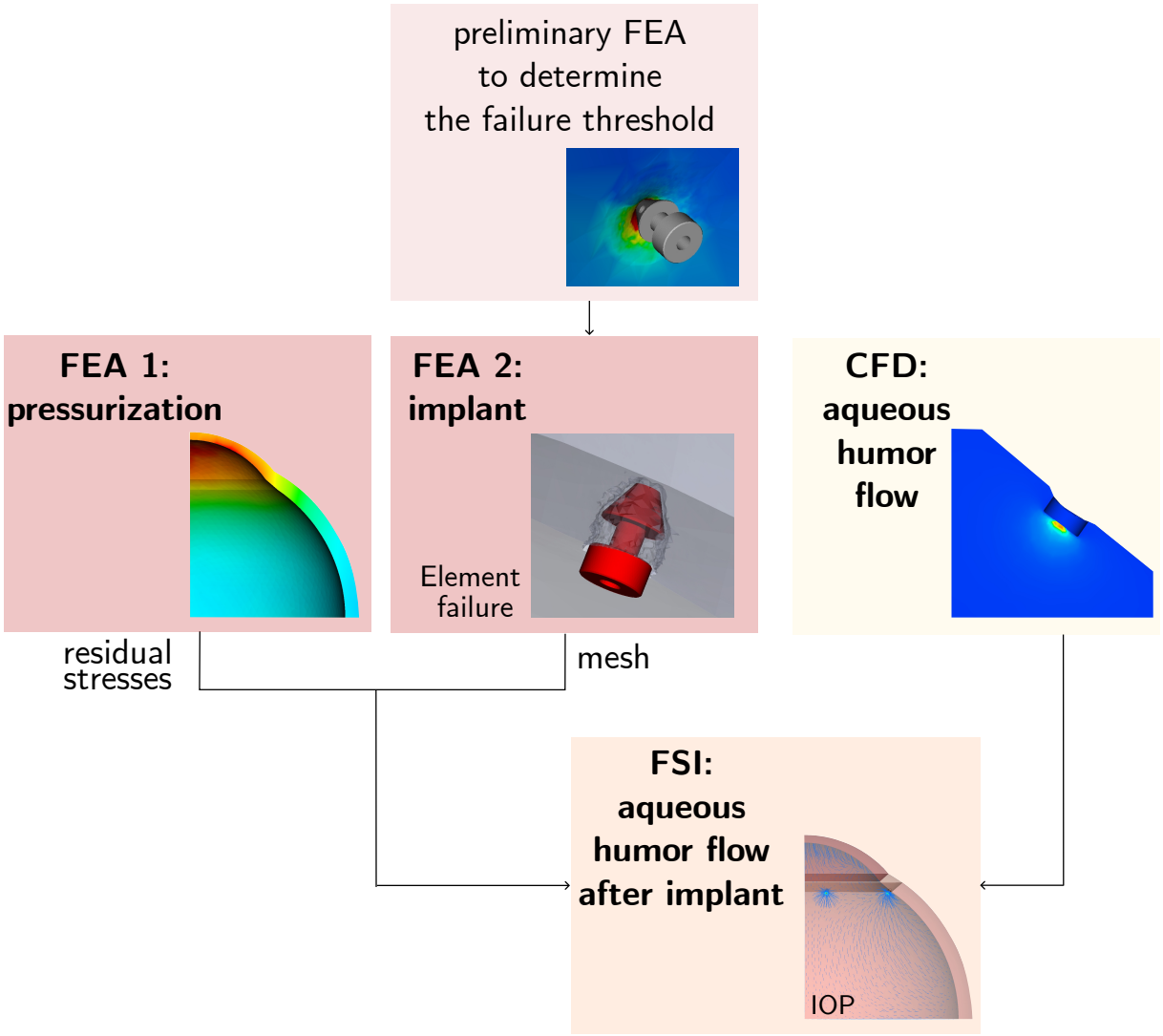

Figure 7.1: Workflow of the methodology to simulate the MIGS implant.

7.2 Materials and Methods

The workflow of the methodology is schematically represented in Figure 7.1. Two structural simulations were conducted to replicate the implantation of the iStent inject. The first structural simulation aimed to reproduce the pressurization of the eye due to the action of the IOP. After determining the zero pressure configuration (with the algorithm in annex C, a constant uniform pressure of 30 mmHg was applied to the internal eye structures. The second structural simulation was designed to replicate the stent implantation by imposing a movement on the stent and inducing element failure on the eyeball. The threshold for element failure was determined based on a preliminary simulation where stent movement and contact with the eye were imposed. CFD simulations were conducted to define the fluid domain of the aqueous humor. Subsequently, the fluid domain was used to construct an FSI simulation in which the structural part was composed by the residual stresses from the first FEA simulation and the final mesh from the second FEA simulation. Details on the simulations set up will

be provided in the following sections. All the simulations presented were implemented in LS-Dyna R14.0 (ANSYS, 71 Inc., Canonsburg, 83 PA,United States) using an Intel i9-10940X (3.30 GHz) on 64 CPUs.

7.2.1 Structural simulations

A CAD file of the Istent inject model was created with the software Rhynoceros 7® based on dimensions found in the literature (Lee et al., 2020) and presented in figure 7.2a. Tetrahedral elements with an edge-length of 0.01 mm were used to mesh the stent using ANSA Pre Processor v24.01 (BETA CAE Systems, Switzerland) as depicted in figure 7.2b.

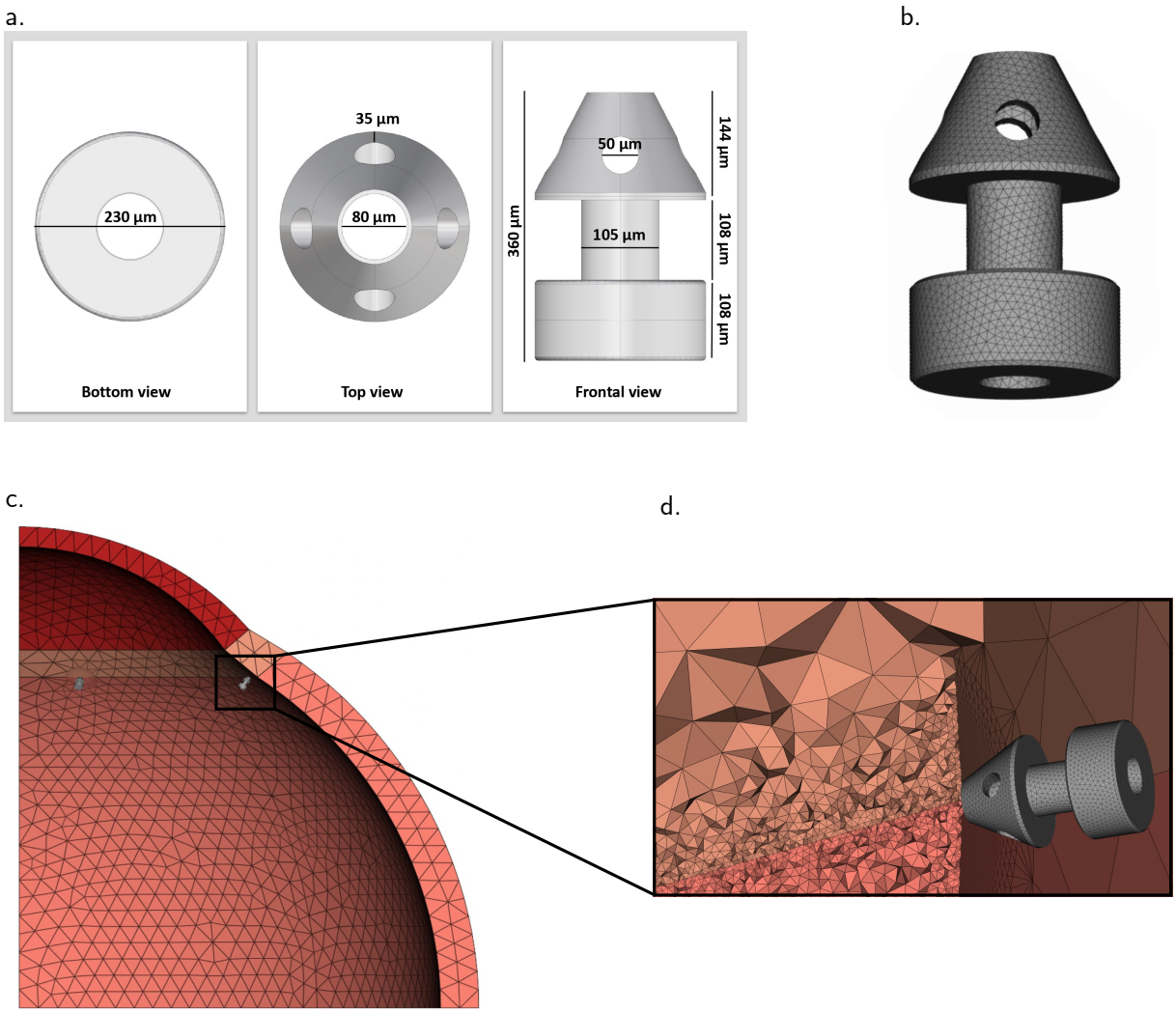

Figure 7.2: a) Dimension of the stent model used to construct the CAD model. b) Tetrahedral mesh of the stent. c) Tetrahedral mesh of the eyeball. d) Detail of the eyeball mesh in the zone of contact with the stent.

The eye model presented in the previous chapters was used for this study. It was meshed with tetrahedral elements, as shown in figure 7.2c, to ensure compatibility with the stent's mesh. All elements, except those in the contact zones, had an average

length of 0.5 mm, a finer mesh was only created in the implantation zones between the limbus and the sclera. Within these zones, a stent-like mesh was constructed using three concentric circles on both the inner and outer surfaces. These circles measured 0.4, 0.6, and 0.8 mm in diameter, with corresponding element sizes of 0.1, 0.02, and 0.01 mm. Figure 7.2d shows a detailed view of the mesh in the implantation zone. Because the healthy eye is symmetrical, we used a quarter model of the eye with symmetry boundary conditions and, since the sclera does not move in the axial direction during stent implantation, translations and rotations were restricted at the base of the sclera. The assumption of symmetry can be used because our hypothesis is that, even if the stent are implanted only in the quarter of the eye we are considering, the depressurization of the eye due to the implant will be the same in the whole eye. The stents are made of titanium which deformation is negligible in this application, therefore we modelled them with a rigid material with a mass density of 0.0045 g/mm^3, a Young's modulus of 2 GPa, and a Poisson ratio of 0.3. Assuming that the eye operates within the isotropic strain ranges, the sclera was represented as an isotropic hyperelastic material with the same material properties presented in chapter 2. The cornea and the limbus were modelled as isotropic hyperelastic materials following the Yeoh strain energy function depending on the parameters C_{10}, C_{20} and C_{30} estimated fitting experimental stress-strain data present in literature (Maklad, 2019). The resultant parameters were $C_{10} = 0.069$MPa $C_{20} = 22.836$MPa $C_{30} = 22.524$MPa.

To replicate the clinical setting, two devices were implanted in the same eye model with an angular separation of 60 degrees between them. The stents were placed at their implant sites, and rotated so that they were perpendicular to the tissue of the eye. Clinically, the stents are implanted through the trabecular meshwork which anatomically cross over between the cornea and sclera, for this reason the stents were inserted in the space between the sclera and the limbus. Two main simulations have been conducted to replicate the implantation of the devices. In the first structural simulation, the stress-free configuration of the eye was determined through the iterative algorithm presented in Ariza-Gracia et al. (2016) implemented in Python. The eye was then pressurized at a glaucomic pressure of 30 mmHg with a pressure load on the interior surface of the eyeball. We obtained the pressurization-related residual stresses which are then included in the FSI simulation.

In the second FEA simulation, to replicate the stent's entry into the eye, we imposed movement on the two stents and defined contact interactions between the stents and the eyeball. The internal surfaces of the limbus and sclera were set to form a two-way automatic mortar contact with the two stents. Additionally, we incorporated material failure through a damage criterion for the limbus and sclera materials. Elements of the limbus and sclera failed once they exceeded a certain von Mises stress value, allowing the stent to pass through upon contact and deformation of the eye. The von Mises stress can be used in this case as threshold because we are considering an isotropic material model. To determine the threshold, a preliminary simulation was conducted without including the failure criteria. In this simulation, we analyzed the stresses caused by the contact between the stent and the eyeball. To achieve the correct implantation position, we imposed a total displacement of 0.302 mm on the devices. By including the damage

criteria in the second FEA simulation, we obtained the mesh of the eyeball with the implanted stents. Incorporating the residual pressurization stresses from the first FEA simulation into the implant model, we created the structural model to be used for the FSI simulation.

7.2.2 FSI simulation

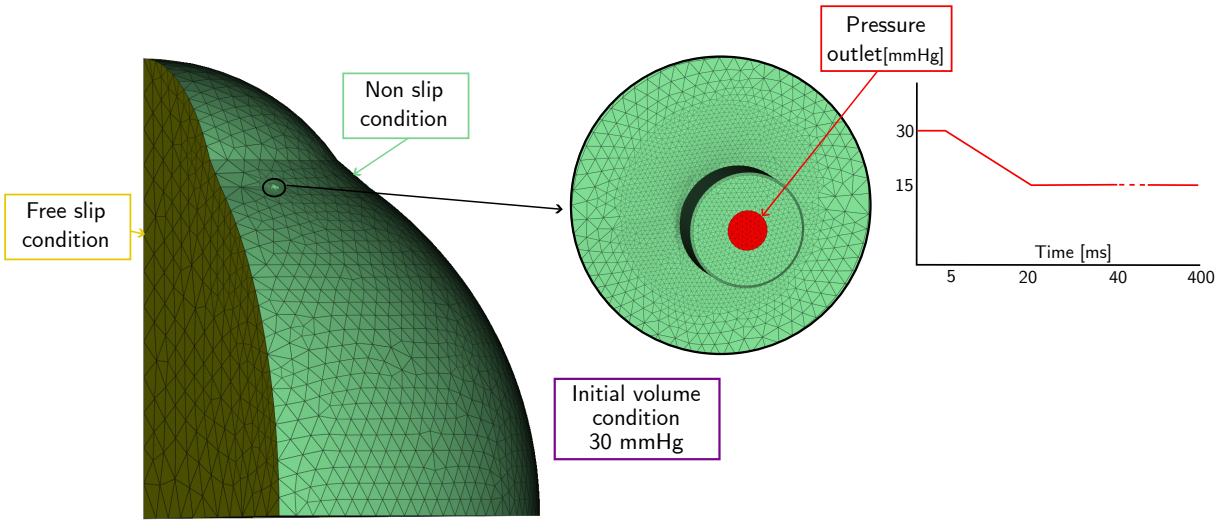

Figure 7.3: Mesh and boundary conditions of the fluid model.

The flow of aqueous humor within the stents was studied using a CFD simulation. To test the fluid parameters, a preliminary CFD simulation was conducted. The CFD mesh and the boundary conditions are displayed in figure 7.3. The fluid domain consisted of three walls simulating the symmetry parts of the humors (shown in yellow in figure 7.3), the base, two fluid outlets (represented by the central inlets of the iStent Injects, shown in red in figure 7.3), and a contact portion (represented by the internal surface of the eye, shown in green in figure 7.3). The contact wall was subjected to a non-slip boundary condition, while the eye walls were subjected to a free-slip condition. The pressure curve depicted in red in figure 7.3 was applied as a boundary condition to the outflow sections of the stents. The outlet pressure was set to 30 mmHg at the beginning of the simulation to allow the system to stabilize, then it dropped to 15 mmHg over 15 ms, corresponding to the episcleral venous pressure. An initial pressure of 30 mmHg was assigned to all the nodes of the fluid volume. The aqueous humor was modeled as an incompressible fluid with a density of 1000 kg/m^3 and a dynamic viscosity of 0.75 cP (Mauro et al., 2018).

In the subsequent FSI analysis, the CFD domain was coupled with the structural domain at the end of the implant. The aqueous humor flow after the MIGS implant was simulated using a strongly coupled, two-way, and boundary-fitted FSI approach. In the initial stages of the simulation, an equilibrium state was established between the pressurized structure and the pressurized fluid domain. This equilibrium resulted from the initialization of the stress tensor in the structural domain and the fluid-structure coupling. When the fluid came into contact with a structure in a tensioned state, its

initial pressure condition of 30 mmHg was maintained. When the pressure inside the stent reached 15 mmHg, a pressure gradient formed, causing the aqueous humor to flow through the stents. Without residual stresses on the eye structure, an instantaneous depressurization of the fluid would occur, preventing the establishment of the required pressure gradient and the subsequent aqueous humor flow. The termination time of the FSI simulation was set to 400 ms, in order to evaluate the aqueous humor flow and pressure after 400 ms.

7.3 Results

7.3.1 Structural results

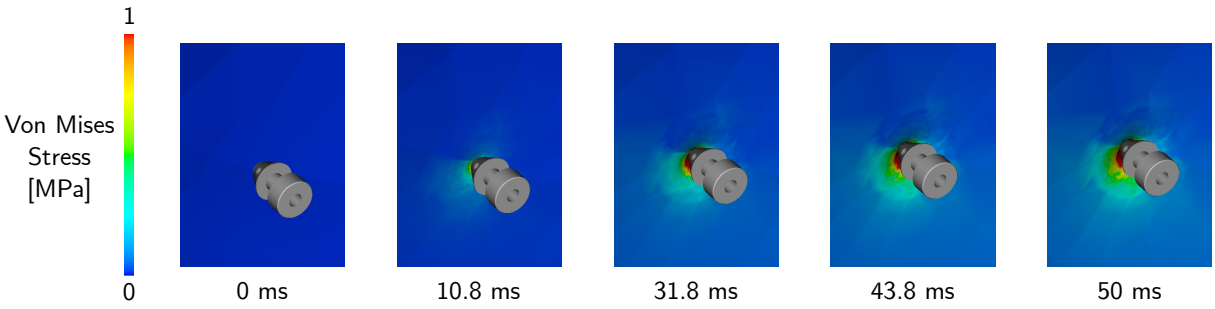

Figure 7.4: Von Mises stress distribution during the preliminar structural simulation without element failure. After this preliminary simulation, a threshold of 1 MPa was chosen for both the limbus and the sclera.

The results of the preliminary simulation to determine the threshold for element failure are depicted in figure 7.4. The movement of the stents caused a stress concentration in the contact zone, which increased progressively with continued movement. A threshold of 1 MPa was used for both the limbus and sclera to prevent excessive element failure while ensuring the stent could enter the eye. Only the red elements in figure 7.4 would be eliminated at a 1 MPa threshold, indicating that the head of the stent should be able to penetrate the eye structure.

In the first FEA simulation, the eye was pressurized to 30 mmHg from its zero-pressure configuration. It experienced a maximum absolute displacement of 0.111 mm on the cornea and a maximum residual stress value of 0.1 MPa. The computational cost for this simulation was 19 minutes and 58 seconds.

The computational cost for the second FEA simulation amounted to 183 hours, 38 minutes, and 15 seconds, due to the necessity of using a very small time step of $1 \cdot 10^{-4}$ ms required by the contact and failure algorithms. By incorporating element failure upon contact with the stents, it became feasible to evaluate the implantation position of the devices and make comparisons with existing literature data. Figure 7.5 shows a comparison between three-dimensional micro-computed tomography data (Bahler et al., 2012) and the final state of the structural simulation, where the stents have reached their ultimate implant positions. Notably, the head and thorax of the devices are embedded

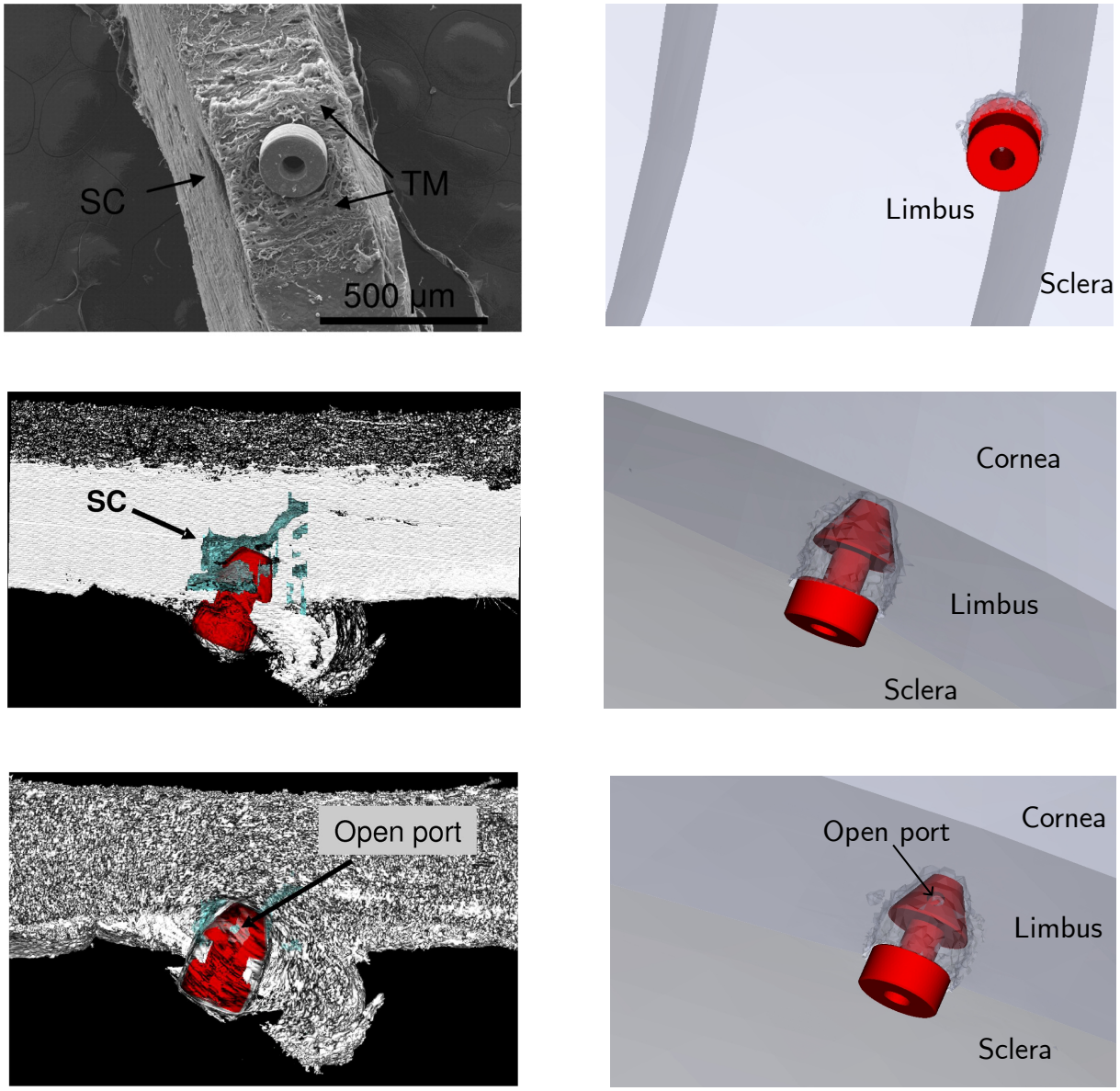

Figure 7.5: Implant of the istent inject. Comparison between three-dimensional micro-computed tomography (3D micro-CT) (Bahler et al., 2012) and numerical simulations.

within the tissues, while the flange remains prominently visible. The correspondence between the clinical images and those obtained through our research is clearly evident, validating our implant simulation.

The residual stresses caused by the IOP in the first FEA analysis were included in the final state of the second FEA analysis. By simulating the implant and incorporating residual IOP stresses, we were able to determine the concentration of residual stresses within the implantation zone. Thus, in addition to the stresses induced by pressurization, the stresses brought on by stent insertion were also present within the eye model. In the future, stent designs that result in lower stress concentrations could be originated based on the results of this simulation.

7.3.2 FSI results

The FSI simulation had a computational cost of 79 h 21 min and 35 s. The time step used simulation is $4 \cdot 10^{-4}$ ms.

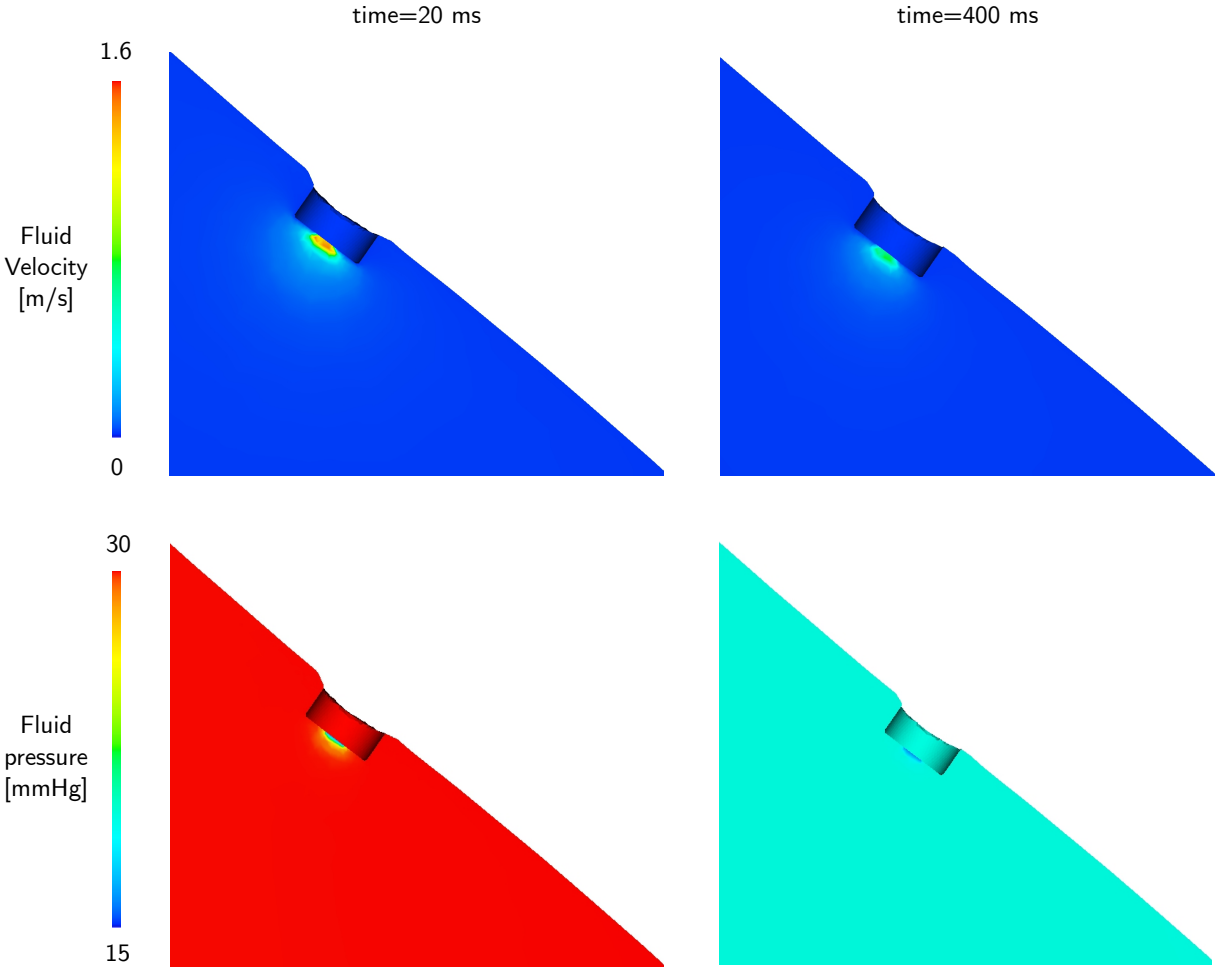

Figure 7.6: Fluid results. Pressure gradient between the aqueous humor and the stents at the beginning (20 ms) and at the end (400 ms) of the simulation. Velocity contour at the beginning (20 ms) and at the end (400 ms) of the simulation.

The initial pressure condition of 30 mmHg in the humor is maintained in the first instants of the simulation thanks to the interaction with the pressurized eyeball. After 20 ms, the stents' pressure drops to 15 mmHg, creating a pressure gradient between the pressure of aqueous humor and the pressure at the stents. The pressure gradient is the driving force that causes aqueous humor flux to form in the stents. The pressure gradients at the beginning and at the end of the simulation are depicted in figure 7.6. At 400 ms, the pressure in the humors achieves the value of 18.78 mmHg. The velocity of aqueous humor is depicted in figure 7.6. At 20 ms, the pressure gradient of 15 mmHg causes a flux of aqueous humor with a maximum velocity of 1.589 m/s; the velocity decreases to 0.788 m/s at 400 ms, due to the drop of the pressure gradient during the simulation.

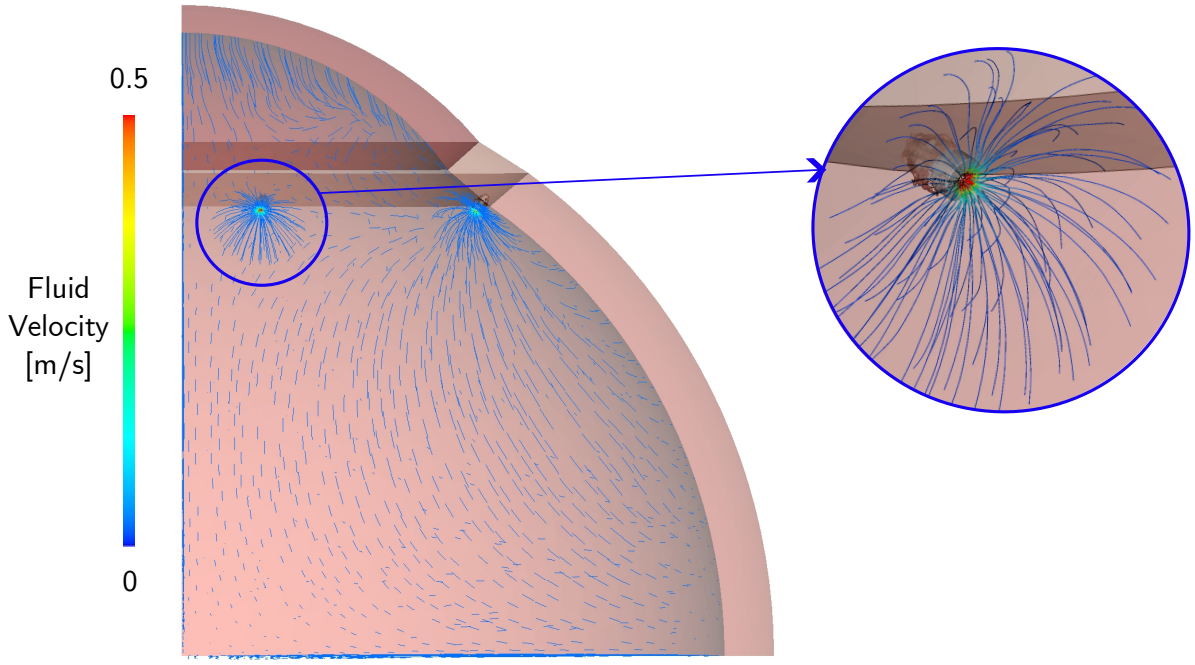

Figure 7.7: Fluid velocity streamlines at t=22ms.

The streamlines depicted in figure 7.7 enable the visualization of aqueous humor flow entering the stents in the instant of maximum velocity.

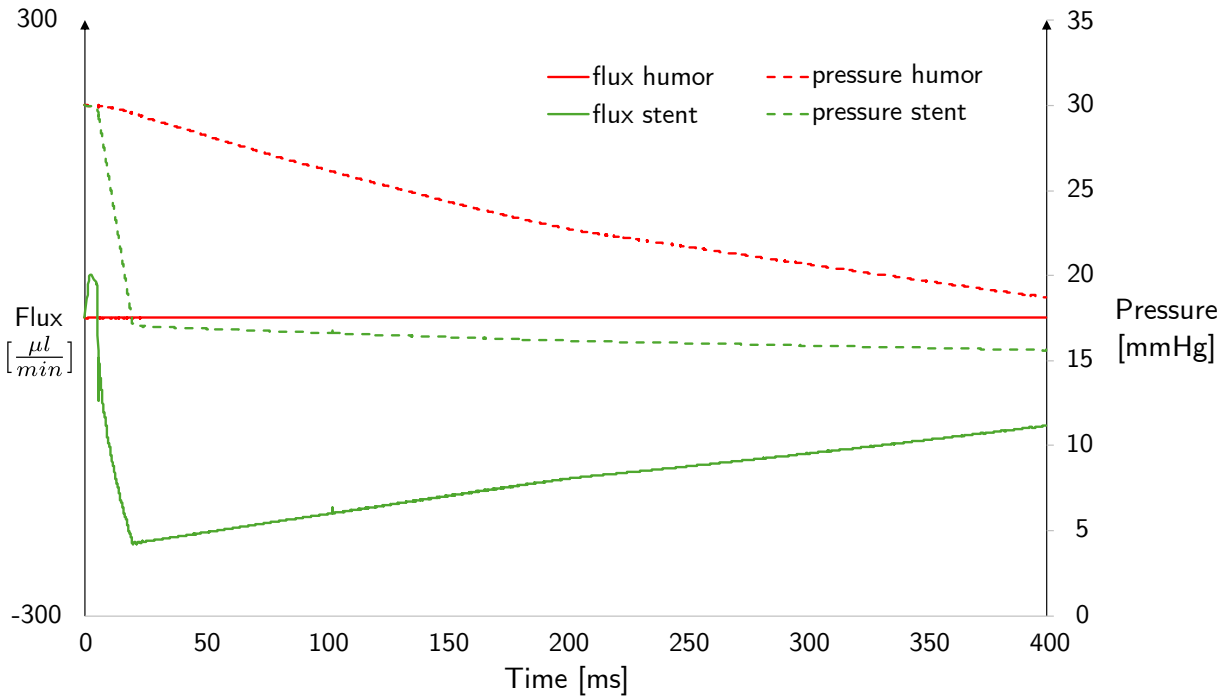

Figure 7.8: Humors (red lines) and stents (green lines) pressure (dashed lines) and flux (solid lines) in time.

The aqueous humor flux in the stents and the volume of the humors is presented

with solid lines in figure 7.8, while the pressure is depicted with dashed lines in the same figure. The flux outflow from the two stents is equal, with the negative sign indicating that the flux is exiting the system. Since the system does not receive any input flow, the flux in the volume of the humors is zero (red solid line). The flux in the stents and the pressure gradient are correlated: the peak stent flux occurs at the time of maximum pressure gradient, at 20 ms. As the pressure gradient diminishes, both the flux and velocity decrease accordingly. The maximum flux through the stents is 228.2$\frac{\mu l}{min}$, while at the end of the simulation, at 399.70 ms, the flux decreases to 108.6$\frac{\mu l}{min}$. The pressure through the stents is imposed as a boundary condition, as detailed in figure 7.3, with the imposed boundary condition corresponding to the green dashed line in figure 7.8. Initially, the pressure in the volume of the humors is 30 mmHg, but it begins to drop as soon as the pressure gradient occurs, tending to reach the pressure value at the stents' outlet.

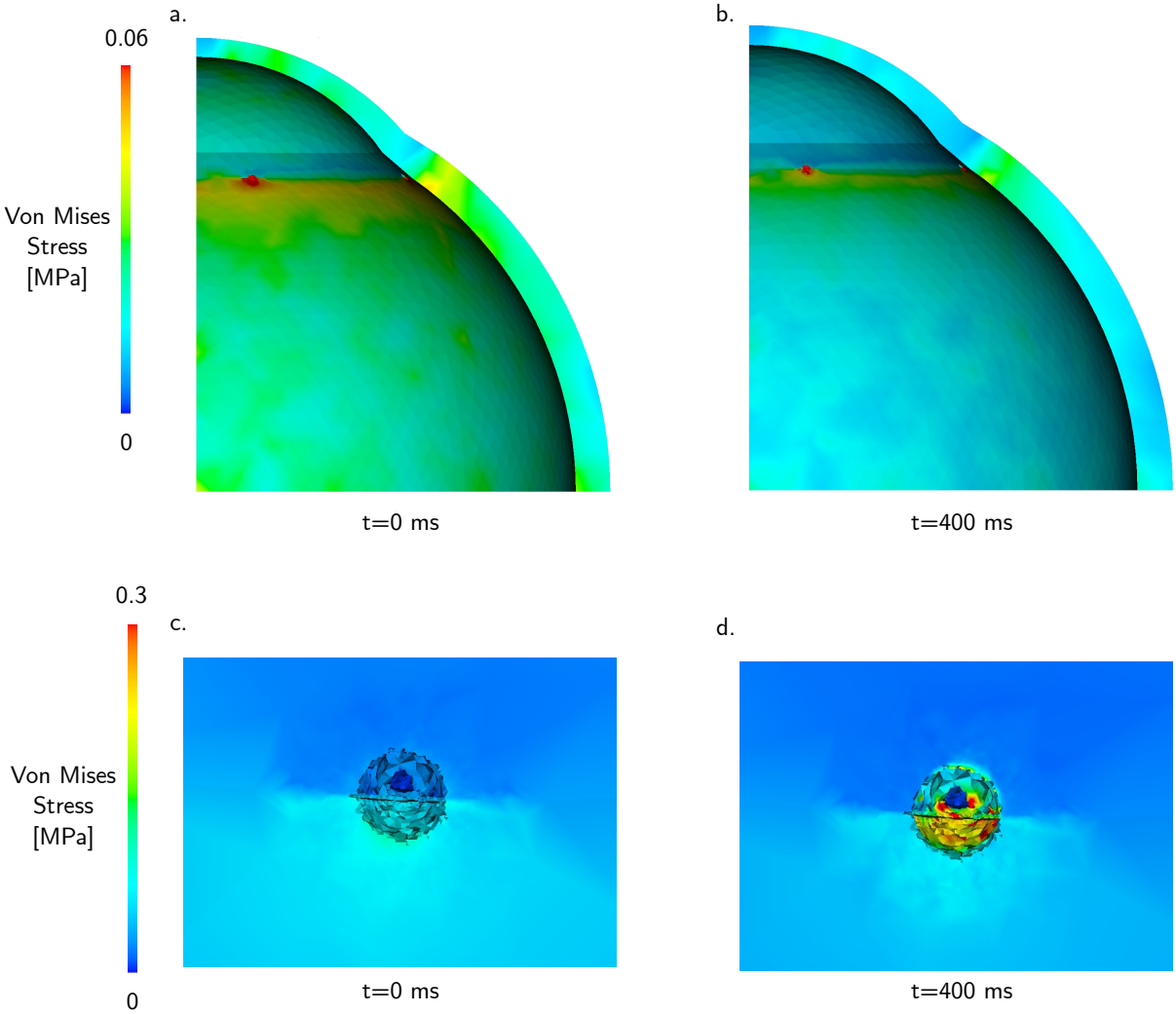

Figure 7.9: Von Mises stress distribution at the beginning and at the end of the FSI simulation.

Figure 7.9 shows the von Mises stress distribution on the eye at the beginning (figures 7.9a and c) and at the end of the FSI simulation (Figures 7.9b and d). Initially, we observe residual stresses in the structure due to the action of the IOP and stent

implantation. At 400 ms, when the simulation is completed, the contour of the von mises stress on the eye changes, attributed to the depressurization effect induced by the outflow of aqueous humor through the stents. Except for the implantation region, where the contact between the tissues and the rigid bodies is maintained, the cornea, limbus, and sclera exhibit decreased von Mises stress values compared to the initial values. As the structure depressurizes and interacts with the stents towards the end of the simulation, von Mises stresses increase in the contact zone, as shown in figure 7.9d.

7.4 Discussion

We developed a methodology for simulating the implantation of a couple of MIGS devices aimed at treating glaucoma. The simulation enables a thorough investigation into the interaction among the ocular structure, the devices and the aqueous humor. Based on the findings regarding pressure, flow, and aqueous humor drainage rate, the efficacy of the iStent inject in reducing IOP is confirmed. Our study evaluated the immediate effects of implantation, revealing a 62.6% reduction in IOP during the stents' implant. The effects of IOP reduction influenced the results obtained in terms of residual stresses within the ocular structure, as well as the outcomes in aqueous humor fluid dynamics. These findings highlight the importance of having conducted a FSI analysis. The stents' action depressurized the eye, causing displacements in the eye tissues as a result of the deflation brought on by the decreased IOP. As the structure depressurizes and interacts with the stents towards the end of the simulation, a concentration of von Mises stresses rise in the contact zone. To the best of our knowledge, only CFD analysis are present in literature, which does not account for the eye's contribution. Neglecting the impact of tissue depressurization leads to underestimate the results in terms of velocity, aqueous humor flux, and IOP. Our findings indicate that the eyeball structure plays an important role in keeping the fluid pressurized.

Structural simulations of the stent implantation encompassed multiple elements that substantially contributed to nonlinearity in our analysis. The eye tissue's hyperelastic nature, the pre-stress caused by IOP pressurization, the requirement for a contact algorithm, and the element failure were among these factors. These non-linearities led to a very high computational time for the simulation of the implant.

The numerical methodology proposed can potentially be used in different applications and future developments. This work could help in determining the optimal implant position of the iStent inject, and in the investigation of alternative MIGS. We made the analysis with an idealized eye geometry but a patient-specific analysis can be carried out by setting patient-specific pressure values and by adjusting the geometry to consider the variability in the eye morphology.

We conducted a dynamic analysis of AH flow response at the time immediately following implantation since the interest was on the effects of the pressure gradient that developed when the iStent inject is implanted. The flow and velocity results obtained are the outcome of lowering the pressure from 30 to 15 mmHg, and they are not comparable

to those from published CFD studies; for instance Villamarin et al. (2012) obtained their results from a static condition, where the system was already in equilibrium. For this reason, in this first analysis we did not take into account the continuous flow of aqueous humor. A future development could be the introduction of an inlet condition of aqueous humor to perform a long-term aqueous humor behavior study. The impact of IOP dynamics on endothelial cell damage around the implant zone is another possible future line. Stresses have been observed rising in the eye tissues in the contact zone with MIGS due to structural depressurization. Further studies may assess the long-term consequences of these stresses.

The validation of the model using in-vitro or ex-vivo data is the most crucial improvement to be put into practice. A possible in-vitro apparatus must allow for the acquisition of parameters that are pertinent to our analysis. Relevant parameters to be evaluated are IOP and aqueous humor flux, which can be estimated through a pressure probe and a flowmeter in an experiment wit an eye plastic model or a porcine eye.

Part III

Conclusion

8

Conclusions and Future lines

8.1 Main conclusions and original contributions

The aim of this doctoral thesis was to construct a methodology based on in-silico high fidelity simulations and artificial intelligence techniques to estimate in real time the intraocular pressure (IOP) and the mechanical properties of the corneal tissue in-vivo starting from the results of a Non-Contact Tonometry (NCT), specifically performed by the Corvis ST device. The NCT evaluates the IOP and the corneal biomechanics by deforming the corneal surface with an air-jet during 30 ms, and recording the deformation with an high-speed camera.

During the development of this methodology, an in-silico Fluid-Structure Interaction (FSI) simulation of the NCT is constructed to address the interaction between the eyeball - the structure - and the air-puff - the fluid. The eyeball incorporates the main tissues of the eye: cornea, sclera, lens, and humors. We first demonstrated that it is essential to use an FSI tool to simulate the NCT. Actually, the mechanical properties of the eye tissues influence corneal deformation, which affects the air pressure on it; and vice versa, corneal deformation depends on air pressure. Therefore, it is crucial to simulate the NCT using a two-way FSI approach. Air pressure is highest at the corneal apex (with peak pressures ranging between 160 and 180 mmHg) and decreases towards the periphery of the eye. However, the cornea deforms creating two peaks of deformation, above which the air pressure becomes negative (up to -20 mmHg) due to changes in flow direction. This negative pressure effect would not be observable without an appropriate FSI simulation.
To the best of our knowledge, this is the first 3D FSI model of the NCT and, for this reason, for the first time, the corneal tissue has been modelled as a quasi-incompressible

anisotropic hyperelastic material. The model constants were initially estimated from ex vivo experimental tests documented in the literature. Through a "Full Factorial" study, it has been shown that the parameters describing fiber stiffness influences significantly both the deflection amplitude of the cornea and the peak distance. During deformation, the anterior surface of the corneal section experiences compression, while the posterior surface experiences tension. Under tension, the collagen fibers activate, increasing the tissue's stiffness and load-carrying capacity. Not considering tissue anisotropy would result in a significantly more compliant cornea and an incorrect estimation of its properties.
It has also been demonstrated that intraocular fluids should be modeled as fluids and not as a homogeneous static pressure acting on the posterior side of the cornea, since during the simulation, the increase in IOP (2/3 times of the initial pressure value) influences corneal deformation. If IOP is kept constant throughout the simulation, it would lead to a stiffer mechanical response of the corneal tissue
Lastly, it has been proved that the influence of the crystalline lens, the ciliary zonule and the vitreous membrane on the corneal deformation is below 5%, meaning that they could be removed from the model improving the computational efficiency.
Summarizing, the first original contribution of the present doctoral thesis is the development of an high-fidelity model of NCT. For the first time, a 3D simulation is considered, intraocular fluids are modeled as fluid, and the cornea material is considered anisotropic.

For the information provided by the simulation to be reliable, the in silico model must replicate the real problem's response as faithfully as possible. The model has been validated using clinical data from 20 patients. To apply this methodology to the simulation of a large number of patients, an algorithm in Python has been developed that fully automates the simulation of the Corvis ST with different input parameters (IOP, mechanical properties, and corneal geometry). The automated algorithm constructs a geometric model of the cornea for each patient from their corneal topography. Corneal elevation data obtained from the Pentacam topographer is extended using the Zernike polynomial approximation, and the geometric and finite element model is constructed based on this data. Each patient-specific cornea model is combined with average-sized limbus, sclera, and humors models, and the Corvis ST simulation is performed by adjusting mechanical properties and IOP as necessary. The process of building the input file and randomly selecting parameters is fully automated and takes a few seconds. The computational time for each simulation is 24 hours on 16 CPUs. By running 100 simulations for each patient, it has been verified that corneal deformation with an average range of corneal tissue properties reproduces the deformations and air pressure recorded by the Corvis ST. For healthy tissues, the maximum displacement of the anterior surface is around 0.9 mm. NCT simulation with different properties and IOP has highlighted the strong coupling between intraocular pressure (IOP), corneal thickness, and tissue mechanical response in corneal biomechanical behaviour. It has been observed that the same corneal deformation can be obtained with both stiff mechanical properties and low IOP, as well as with softer mechanical properties and high IOP.

Once the FSI tool has been successfully developed and validated, it has been used to devise two new methodologies aimed at decoupling IOP measurement from estimating the corneal tissue's mechanical properties. Currently, in clinical practice, IOP is estimated based on the time when the first corneal applanation occurs. However, the point in which the external and internal forces acting on the corneal surface are in equilibrium is the point of maximum veloicty of the corneal apex. Actually, at this point the acceleration of the system is zero because the forces are balanced. By considering the balance between the internal fluid's mechanical work (IOP) and the external fluid's mechanical work (air pulse) in simulations with different geometries, mechanical properties of the corneal tissue and IOP, it has been observed that the point of equilibrium between external and internal work, corresponding to the point of maximum corneal velocity, does not depend on the mechanical properties of the corneal tissue and the thickness, it only depends on the IOP. Actually, during the impact, the mechanical energy of the air-jet is converted in deformation of the eyeball and the deformation of the eyeball is converted in increase of IOP. In this way, the energetic analysis of the NCT problem has allowed us to decouple the effect of corneal tissue response from the IOP. The novelty of this methodology brings a new algorithm, wIOP, to estimate IOP based on the relationship between the maximum velocity time of the apex and the initial IOP.

The proposed FSI model takes 24 hours on 16 CPUs to reproduce the NCT test, making it prohibitive to use for estimating tissue properties using, for example, an optimization process whose objective function would be to determine the tissue properties that match the numerical deformation with that recorded by the Corvis ST for a patient. In this thesis, a reduced model has been proposed to estimate the corneal tissue's mechanical properties. A methodology that integrates NCT simulation results, orthogonal decomposition (POD), and Artificial Neural Networks (ANN) is used to obtain the parameters describing corneal tissue mechanical properties in real-time. A large dataset of simulations (581) was used to train an ANN. This entirely data-driven approach is promising for practical implementation within the device's software, offering the potential for in vivo evaluation of corneal biomechanics during clinical examinations. It is the first time a reduced-order model has been used in combination with ANN models to estimate the corneal tissue's mechanical properties in real-time and in a patient-specific manner.

The FSI numerical model developed for the eyeball in this thesis has also been used to simulate two other clinical problems. The feasibility of the Corvis ST device for detecting keratoconus pathology has been studied. The FSI simulation of NCT was performed with different corneal models simulating various stages of keratoconus. Numerically, it has been observed that in patients with keratoconus who have not yet developed evident topographic problems, corneal deformation along the air jet is different from that of a healthy patient. Data obtained from simulations highlight potential improvements that can be achieved by adjusting the Corvis ST device's operation. A 90-degree rotation of the camera during the clinical procedure can improve the device's ability to detect diseased tissue's presence and relative position when it is in the most typical position in the lower nasal quadrant. Additionally, two new asymmetry indices are proposed. Adding the proposed adjustments to the clinical device can help detect

keratoconus, even in the most challenging cases where topographic analysis does not show indications. By considering corneal deformations along both meridians and introducing indices based on asymmetry, a more comprehensive understanding of corneal behavior in keratoconus is offered. Since the pathological area usually appears in the Temporal-Inferior quadrant of the eye, affecting the Superior-Inferior (SI) plane more than the NT plane, SI plane deformations are greater than NT deformations during NCT.

Finally, for the first time in the literature, the aqueous humor flow has been simulated after the implantation of MIGS devices, observing that it is numerically necessary to use a fluid-structure coupling simulation because the eye's properties influence IOP and vice versa. First, the implantation of a commercial MIGS stent was simulated with a structural simulation, and then an FSI simulation was developed to simulate aqueous humor after surgery. In the future, the established methodology will allow designing new devices or analyzing the optimal implantation position of the device.

In summary, this doctoral thesis explored the fundamentals of corneal biomechanics through an in-silico model of the NCT procedure. Creating advanced methodologies for decoupling IOP estimates and corneal mechanical properties, and integrating high-fidelity modeling techniques and machine learning for creating predictive models of corneal tissue mechanical response are two of the main objectives of this thesis. The work carried out may therefore make a significant contribution to improving the treatment of ocular pathologies.

8.2 Future Lines

- Two uniformly distributed families of fibers have been considered in the model of the corneal tissue material properties: one in the nasal-temporal direction and another in the superior-inferior direction. Literature data (Meek and Boote, 2009; Pandolfi and Holzapfel, 2008) demonstrated that the distribution of collagen fibers vary in the thickness of the cornea. A study on the influence of the variability of the material properties of the corneal tissue in the thickness could be beneficial for this work.

- The new wIOP algorithm presented in chapter 4 is based on corneas with healthy geometries. Further studies should be conducted with the aim to study the air pressure distribution on the corneal surface in case of non-symmetric corneal geometries, for example in keratoconic patients. Or other studies should be conducted in analyzig the energy balance in case the air jet does not impact exactly the apex of the cornea.

- An in vitro validation of the procedure of chapter 4 should be performed. The problem with in vitro validation is that we should have a very sensitive sensor (with a sampling similar to the one of the camera) capable of measuring the IOP changes in the experimental set up during the air puff. To the best of our knowledge, some experimental set-up with Corvis ST have been proposed to

estimate the influence of the IOP on corneal deformation during the air puff (Kling and Marcos, 2013; Bekesi et al., 2016a,b, 2017; Eliasy et al., 2018). However, the pressure transducers used in these experiments does not capture the IOP change which occurs during the air puff.

- Regarding the results of chapter 6, more reliable experimental data about the mechanical stress-strain response of the keratoconic tissue could significantly enhance our ability to compare the mechanical model's performance against the real scenario. Notably, given that keratoconus initiates in the posterior corneal surface before extending to the anterior surface, investigating the influence of keratoconus progression could be a promising direction for further exploration in this study. Moreover, it could be beneficial to assess the indexes' capability to detect changes in material properties of the fellow eye of keratoconic patients, which may be at risk of developing the pathology. Furthermore, in a clinical context, it could be advantageous to perform multiple sectional analyses, considering the enhancement achieved in the numerical scenario.

8.3 Publications in peer-reviewed journals

The publications on international journals achieved during the thesis period are listed below:

- **E. Redaelli**, J. Grasa, B. Calvo, J. F. Rodriguez Matas, and G. Luraghi, *A detailed methodology to model the non contact tonometry: a fluid structure interaction study.* Frontiers in Bioengineering and Biotechnology, 10 (2022), 981665.
- **E. Redaelli**, M. Nana, B. Calvo, J. F. Rodriguez Matas, G. Luraghi, J. Rozema, and J. Grasa, *Improving early detection of keratoconus by non contact tonometry. a computational study and new biomarkers proposal.* Journal of the Mechanical Behavior of Biomedical Materials, 152 (2024), 106413.
- **E. Redaelli**, B. Calvo, J. F. Rodriguez Matas, G. Luraghi, and J. Grasa, *Non-Contact Tonometry: Predicting Intraocular Pressure Using a Material - Corneal Thickness - Independent Methodology.* Frontiers in Bioengineering and Biotechnology, 12 (2024), 1406870.
- **E. Redaelli**, B. Calvo, J. F. Rodriguez Matas, G. Luraghi, and J. Grasa, *A POD-NN model of the eye deformation during a Non Contact Tonometry to determine the mechanical properties of the corneal tissue.* Computer Methods in Applied Mechanics and Engineering, submitted.

8.4 Conference contributions

The present work has been presented to a total of 13 international and national conferences from which 10 were podium presentations and 3 posters.

- **E. Redaelli**, B. Fantaci, J. Grasa, G. Luraghi and J. F. Rodriguez Matas; *Non Contact Tonometry: a Fluid Structure Interaction study*; X Jornada de Jóvenes Investigadores del I3A; Poster presentation; Zaragoza; 21/10/2021.

- **E. Redaelli**, J. Grasa, B Calvo, J. F. Rodriguez Matas and G. Luraghi; *Corvis ST biomarkers in healthy and keratoconic eyes: clinical and numerical evaluation*; XI Jornada de Jóvenes Investigadores del I3A; Poster presentation; Zaragoza; 16/06/2022.

- **E. Redaelli**, J. Grasa, B. Calvo, J. F. Rodriguez Matas and G. Luraghi; *A detailed methodology to model the Non Contact Tonometry: a Fluid Structure Interaction study.*; 27th Congress of the European Society of Biomechanics; Podium presentation; Porto, Portugal; 27/06/2022.

- **E. Redaelli**, J. Grasa, B. Calvo, J. F. Rodriguez Matas and G. Luraghi; *A patient-specific fluid structure interaction simulation of the non-contact tonometry*; 11th meeting of the Italian chapter of the European Society of Biomechanics (ESB); Podium presentation; Marina di Massa, Italy; 06/10/2022.

- **E. Redaelli**, J. Grasa, B. Calvo, J. F. Rodriguez Matas and G. Luraghi; *Can Corvis ST detect the biomechanical properties of the corneal tissue?*; 11th meeting of the Spanish chapter of the European Society of Biomechanics (ESB); Podium presentation; Zaragoza; 25/10/2022.

- **E. Redaelli**, B. Calvo, G. Luraghi, J. F. Rodriguez Matas and J. Grasa; *A New Procedure to Estimate Patient-Specific Intraocular Pressure*; XII Jornada de Jóvenes Investigadores del I3A; Poster presentation; Zaragoza; 15/06/2023.

- **E. Redaelli**, B. Calvo, G. Luraghi, J. F. Rodriguez Matas and J. Grasa; *An energetic analysis of the Non-Contact Tonometry: combining numerical simulations and clinical images.*; 28th Congress of the European Society of Biomechanics; Podium presentation; Maastricht, Netherlands; 10/07/2023.

- **E. Redaelli**, B. Calvo, G. Luraghi, J. F. Rodriguez Matas and J. Grasa; *Analysis of the Influence of Keratoconus Mechanical Properties, Dimension and Position on the Outputs of Corvis*; 11th Meeting on Visual and Physiological Optics; Podium presentation; Antwerp, Belgium; 28/08/2023.

- **E. Redaelli**, B. Calvo, G. Luraghi, J. F. Rodriguez Matas and J. Grasa; *FSI simulations to study eye biomechanics.*; 14th European LS-DYNA Congress; Podium presentation; Baden Baden, Germany; 19/10/2023.

- **E. Redaelli**, B. Calvo, G. Luraghi, J. F. Rodriguez Matas and J. Grasa; *Decoupling Intraocular Pressure Measurement from Corneal Biomechanics*; 12th meeting of the Spanish chapter of the European Society of Biomechanics (ESB); Podium presentation; Malaga, Spain; 03/11/2023.

- **E. Redaelli**, P. Vitullio, S. Fresca, J. F. Rodriguez Matas, P. Zunino, G. Luraghi, B. Calvo, and J. Grasa; *A Novel Artificial Neural Network to determine the Mechanical properties of the Human Corneal Tissue.*; 2024 Annual Meeting of the Association for Research in Vision and Ophtalmology; Podium presentation; Seattle, USA; 05/05/2024.

- **E. Redaelli**, B. Calvo, G. Luraghi, J. F. Rodriguez Matas and J. Grasa; *Determining patient-specific corneal mechanical properties in real time using deep learning.*; 29th Congress of the European Society of Biomechanics; Podium presentation; Edimburgh, UK; 02/07/2024.

- **V. Tahsini**, E. Redaelli, M. Frigelli, M. Nambiar, P. Büchler and S. Kling; *Assessing corneal biomechanics by simultaneous uniaxial extensometry and optical coherence elastography.*; 29th Congress of the European Society of Biomechanics; Podium presentation; Edimburgh, UK; 02/07/2024.

8.5 Peer-review activity

During the phD, the author has peer-reviewed 5 papers in international scientific journals.

8.6 Co-Supervision M.Sc. Thesis

- **Nana Michael**, *Analysis of the influence of Keratoconus Mechanical Properties, Dimension and Position on the output of Corvis ST.* Politecnico di Milano, academic year 2021-2022. Advisor: Rodriguez Matas J. F.; Coadvisors: Grasa J., Redaelli E.

- **De Palma Cecilia**, *Modelling the aqueous and vitreous humors in a non-contact tonometry simulation.* Politecnico di Milano, academic year 2022-2023. Advisor: Luraghi G.; Coadvisors: Grasa J., Redaelli E.

- **Perri Letizia Maria**, *Development of a numerical methodology to model minimally-invasive glaucoma surgery implants.* Politecnico di Milano, academic year 2022-2023. Advisor: Luraghi G.; Coadvisors: Grasa J., Redaelli E.

- **Allievi Eleonora**, *Statistical analysis of Corvis ST biomarkers.* Politecnico di Milano, academic year 2023-2024. Advisor: Luraghi G.; Coadvisors: Grasa J., Redaelli E.

8.7 Teaching

The author has taught practical courses in Industrial Technologies Engineering Bachelor (Resistencia de Materiales).

8.8 Funding

This project has received funding from the European Union's Horizon 2020 research and innovation program under the Marie Skłodowska-Curie grant agreement No 956720, grant PID2020-113822RB-C21 funded by MCIN/AEI/ 10.13039/501100011033 and the Department of Industry and Innovation (Government of Aragon) through the research group Grant T24-20R (cofinanced with Feder 2014-2020: Construyendo Europa desde Aragon).

Part of the work was performed by the ICTS "NANBIOSIS" specifically by the High Performance Computing Unit (U27), of the CIBER in Bioengineering, Biomaterials & Nanomedicne (CIBER-BBN at the University of Zaragoza).

9

Conclusiones y líneas futuras

9.1 Principales conclusiones y aportaciones originales

El objetivo de esta tesis doctoral ha sido construir una metodología basada en simulaciones in-silico de alta fidelidad y técnicas de inteligencia artificial para estimar en tiempo real la presión intraocular (PIO) y las propiedades mecánicas del tejido corneal in vivo a partir de los resultados de una tonometría de no contacto (NCT), realizada específicamente por el dispositivo Corvis ST. La NCT evalúa la PIO y la biomecánica corneal deformando la superficie corneal con un chorro de aire durante 30 ms, y registrando la deformación con una cámara de alta velocidad.

Durante el desarrollo de esta metodología, se construye una simulación in-silico de Interacción Fluido-Estructura (FSI) del NCT para abordar la interacción entre el globo ocular - la estructura- y el chorro de aire - el fluido. El globo ocular incorpora los principales tejidos del ojo: córnea, esclera, cristalino y humores. En primer lugar demostramos que es esencial utilizar una herramienta FSI para simular el NCT. Las propiedades mecánicas de los tejidos influyen en la deformación de la córnea, que a su vez afecta a la presión del aire sobre ella, y viceversa la deformación de la córnea depende de la presión del aire. Por lo tanto, es crucial simular la NCT utilizando un enfoque FSI bidireccional. La presión del aire es mayor en el ápice corneal (con presiones máximas que oscilan entre 160 y 180 mmHg) y disminuye hacia la periferia del ojo. Sin embargo, la córnea se deforma creando dos picos de deformación, por encima de los cuales la presión del aire se vuelve negativa (hasta -20 mmHg) debido a cambios en la dirección del flujo. Este efecto de presión negativa no sería observable sin una simulación FSI adecuada.
Por primera vez, el tejido corneal se ha modelado como un material hiperelástico

anisotrópico cuasi-incompresible. Las constantes del modelo se estimaron inicialmente a partir de ensayos experimentales ex vivo documentados en la literatura. Mediante un estudio de "Full Factorial", se ha demostrado que los parámetros que describen la rigidez de las fibras contribuyen (con una contribución comparable a la matriz extracelular de la córnea) tanto a la amplitud de la deformación como a la distancia máxima entre los picos. Durante la deformación, la superficie anterior de la sección corneal experimenta compresión, mientras que la posterior experimenta tensión. En tensión, las fibras de colágeno se activan, lo que aumenta la rigidez y la capacidad de carga del tejido. No considerar la anisotropía del tejido resultaría en una córnea significativamente menos rígida y una estimación incorrecta de sus propiedades.
Se ha demostrado también que los fluidos intraoculares deben modelarse como fluidos y no como una presión estática homogénea actuando sobre la cara posterior de la córnea, ya que durante la simulación, el incremento de la PIO (de 2 a 3 veces el valor inicial de la presión) influye en la deformación corneal, es decir, el conjunto córnea más humores se rigidiza al aumentar la PIO. Si la PIO se mantiene constante a lo largo de la simulación, daría lugar a una respuesta mecánica más rígida del tejido corneal. Por último, se ha demostrado que la influencia del cristalino, la zónula ciliar y la membrana vítrea en la deformación corneal es inferior al 5%, lo que significa que podrían eliminarse del modelo mejorando la eficiencia computacional. La aportación original del modelo construido es que constituye el primer modelo de alta fidelidad de la NCT. Por primera vez se considera una simulación 3D, los fluidos intraoculares están modelados como fluido y el material de la córnea se considera anisótropo.

Para que la información proporcionada por la simulación sea confiable, el modelo in silico debe replicar lo más fielmente posible la respuesta del problema real. Se ha validado el modelo utilizando datos clínicos de 20 pacientes. Con el fin de aplicar esta metodología a la simulación de un gran número de pacientes, se ha desarrollado un algoritmo en Python que automatiza completamente la simulación del Corvis ST con diferentes parámetros de entrada (PIO, propiedades mecánicas y geometría de la córnea). El algoritmo automatizado construye un modelo geométrico de la córnea para cada paciente a partir de su topografía corneal. Los datos de elevación de la córnea obtenidos del topógrafo Pentacam se extienden utilizando la aproximación de polinomios de Zernike, y el modelo geométrico y de elementos finitos se construye basándose en estos datos. Cada modelo específico de la córnea del paciente se combina con modelos de limbo, esclera y humores con medidas promedio, y se realiza la simulación del Corvis ST ajustando las propiedades mecánicas y la PIO según sea necesario. El proceso de construcción del archivo de entrada y la selección aleatoria de parámetros está completamente automatizado y tarda unos pocos segundos. El tiempo de cómputo de cada simulación es de 24 horas en 16 CPUs. Lanzando 100 simulaciones para cada paciente, se ha verificado que la deformación de la córnea con un rango promedio de propiedades del tejido corneal reproduce las deformaciones y la presión del aire registradas por el Corvis ST. Para tejidos sanos, el desplazamiento máximo de la cara anterior es del orden de 0.9 mm. La simulación de la NTC con diferentes propiedades y PIO ha resaltado el fuerte acoplamiento entre la presión intraocular (PIO), el espesor corneal y la respuesta mecánica del tejido en el comportamiento biomecánico de la córnea. Se ha observado que es posible obtener la misma deformación corneal tanto

con propiedades mecánicas rígidas y baja PIO, como con propiedades mecánicas más blandas y alta PIO.

Una vez que la herramienta FSI se ha desarrollado y validado con éxito, se ha empleado para idear dos nuevas metodologías destinadas a desacoplar la medición de la PIO de la estimación de las propiedades mecánicas del tejido corneal. Actualmente en clínica, la PIO se estima en función del tiempo en el que se produce la primera aplanación de la córnea. El análisis energético del problema NTC nos ha permitido desacoplar el efecto de la respuesta del tejido de la córnea y a evaluar la PIO a partir del tiempo de máxima velocidad del ápex corneal. Al considerar el equilibrio entre el trabajo mecánico del fluido interno (PIO) y el trabajo mecánico del fluido externo (pulso de aire) en simulaciones con diferentes geometrias, propriedades mecanicas del tejido corneal y PIO, se ha observado que hay un punto de equilibrio entre trabajo externo y trabajo interno y este punto se corresponde al punto de máxima velocidad de la córnea. Numéricamente se ha demostrado que este punto no depende de las propriedades mecánicas de la córnea y del grosor corneal. La novedad de esta metodología aporta un nuevo algoritmo wIOP para estimar la PIO a partir de la relación entre el tiempo de velocidad máxima del ápice y la PIO inicial.

El modelo FSI propuesto, emplea 24 horas en 16 CPUs, para reproducir el test NTC, por lo que dificulta su utilización para estimar las propiedades del tejido utilizando por ejemplo un proceso de optimización cuyo función objetivo sería determinar las propiedades del tejido que hagan coincidir la deformación numérica con la registrada por el Corvis ST para un paciente. En esta tesis se ha propuesto un modelo reducido para estimar las propiedades mecánicas del tejido corneal. Se utiliza una metodología que integra los resultados de la simulación NTC, descomposición ortogonal (POD) y redes neuronales artificiales (RNA) para llegar a obtener los parámetros que describen las propiedades mecánicas del tejido corneal en tiempo real. Se han utilizado un gran conjunto de datos de simulaciones (581) para entrenar una RNA. Este enfoque totalmente basado en datos es prometedor para la implementación práctica dentro del software del dispositivo clínico, ofreciendo el potencial para la evaluación in vivo de la biomecánica de la córnea durante los exámenes o pruebas diagnósticas. Es la primera vez que un modelo de orden reducido ha sido utilizado en combinación con modelos de RNA para estimar en tiempo real y de manera paciente especifica las propredades mecánicas del tejido corneal.

El modelo numérico FSI desarrollado del globo ocular también se ha utilizado en el marco de esta tesis para simular otros dos problemas clínicos. Se ha estudiado la viabilidad del equipo Corvis ST para detectar la patología del queratocono. Se ha realizado la simulación FSI de la NCT con diferentes modelos de córnea que simulan distintos estadios del queratocono. Numéricamente se ha observado que, en casos de pacientes con queratocono que todavía no han desarrollado problemas evidentes en la topografía, la deformación de la córnea a lo largo del chorro de aire es diferente de la de un paciente sano. Los datos obtenidos de las simulaciones ponen de manifiesto las mejoras potenciales que se pueden conseguir ajustando el funcionamiento de Corvis ST. Una rotación de 90 grados de la cámara durante el procedimiento clínico puede mejorar

la capacidad del dispositivo para detectar la presencia de tejido enfermo y su posición relativa cuando se encuentra en la posición más típica en el cuadrante nasal inferior. Además, se proponen dos nuevos índices de asimetría. La adición de los ajustes propuestos en el dispositivo clínico puede ayudar en la detección del queratocono, incluso en los casos más difíciles en los que no se aprecian indicaciones a través del análisis topográfico. Al considerar las deformaciones corneales a lo largo de ambos meridianos e introducir índices basados en la asimetría, se ofrece una comprensión más completa del comportamiento corneal en el queratocono. Dado que la zona patológica suele aparecer en el cuadrante Temporal-Inferior del ojo, afectando más al plano Superior-Inferior (SI) respecto al plano NT, las deformaciones del plano SI son mayores que la deformación del NT durante la NCT.

Por último, por primera vez en literatura se ha simulado el flujo del humor acuoso tras la implantación de dispositivos MIGS, observando que numéricamente es necesario utilizar una simulación de acoplamiento fluido-estructura porque las propiedades del ojo influyen sobre la PIO y viceversa. En primer lugar, se ha simulado el implante de una endoprótesis MIGS comercial con una simulación estructural y, a continuación, se ha desarrollado una simulación FSI para simular el humor acuoso después de la cirugía. En el futuro, la metodología establecida permitirá diseñar nuevos dispositivos o analizar la posición óptima de implantación del dispositivo.

En resumen, esta tesis doctoral exploró los fundamentos de la biomecánica corneal mediante un modelo in-silico del procedimiento NCT. La creación de metodologías avanzadas para desacoplar las estimaciones de la PIO y las propiedades mecánicas corneales, y la integración de técnicas de modelado de alta fidelidad y aprendizaje automático para la creación de modelos predictivos de la respuesta mecánica del tejido corneal son dos de las principales aportaciones originales de esta tesis. El trabajo realizado puede suponer, por tanto, una contribución significativa a la mejora del tratamiento de patologías oculares.

9.2 Líneas futuras

- En el modelo de las propiedades materiales del tejido corneal se han considerado dos familias de fibras distribuidas uniformemente: una en la dirección nasal-temporal y otra en la dirección superior-inferior. Los datos de la literatura (Meek and Boote, 2009; Pandolfi and Holzapfel, 2008) demostraron que la distribución de las fibras de colágeno varía en el espesor de la córnea. Un estudio sobre la influencia de la variabilidad de las propiedades materiales del tejido corneal en el espesor podría ser beneficioso para este trabajo.
- El nuevo algoritmo wIOP presentado en el capítulo 4 se basa en córneas con geometrías sanas. Deberían realizarse más estudios con el fin de estudiar la distribución de la presión del aire en la superficie corneal en caso de geometrías corneales no simétricas, por ejemplo en pacientes queratocónicos. También deberían realizarse otros estudios para analizar el balance energético en caso de que el chorro de aire no impacte exactamente en el ápice de la córnea.

- Debería realizarse una validación in vitro del procedimiento del capítulo 4. El problema de la validación in vitro es que deberíamos disponer de un sensor muy sensible (con un muestreo similar al de la cámara) capaz de medir los cambios de la PIO en el montaje experimental durante el soplo de aire. Hasta donde sabemos, se han propuesto algunos montajes experimentales con Corvis ST para estimar la influencia de la PIO en la deformación corneal durante el soplo de aire (Kling and Marcos, 2013; Bekesi et al., 2016a,b, 2017; Eliasy et al., 2018). Sin embargo, los transductores de presión utilizados en estos experimentos no captan el cambio de PIO que se produce durante el soplo de aire.
- En cuanto a los resultados del capítulo 6, unos datos experimentales más fiables sobre la respuesta mecánica tensión-deformación del tejido queratocónico podrían mejorar significativamente nuestra capacidad para comparar el rendimiento del modelo mecánico con el escenario real. En particular, dado que el queratocono se inicia en la superficie posterior de la córnea antes de extenderse a la superficie anterior, investigar la influencia de la progresión del queratocono podría ser una dirección prometedora para seguir explorando en este estudio. Además, podría ser beneficioso evaluar la capacidad de los índices para detectar cambios en las propiedades materiales del ojo contralateral de los pacientes con queratocono, que pueden estar en riesgo de desarrollar la patología. Además, en un contexto clínico, podría ser ventajoso realizar análisis seccionales múltiples, teniendo en cuenta la mejora conseguida en el escenario numérico.

9.3 Publicaciones en revistas

La lista de publicaciones en revistas internacionales publicadas durante esta Tesis se enumera a continuación:

- **E. Redaelli**, J. Grasa, B. Calvo, J. F. Rodriguez Matas, and G. Luraghi, *A detailed methodology to model the non contact tonometry: a fluid structure interaction study.* Frontiers in Bioengineering and Biotechnology, 10 (2022), 981665.
- **E. Redaelli**, M. Nana, B. Calvo, J. F. Rodriguez Matas, G. Luraghi, J. Rozema, and J. Grasa, *Improving early detection of keratoconus by non contact tonometry. a computational study and new biomarkers proposal.* Journal of the Mechanical Behavior of Biomedical Materials, 152 (2024), 106413.
- **E. Redaelli**, B. Calvo, J. F. Rodriguez Matas, G. Luraghi, and J. Grasa, *Non-Contact Tonometry: Predicting Intraocular Pressure Using a Material - Corneal Thickness - Independent Methodology.* Frontiers in Bioengineering and Biotechnology, 12 (2024), 1406870.
- **E. Redaelli**, B. Calvo, J. F. Rodriguez Matas, G. Luraghi, and J. Grasa, *A POD-NN model of the eye deformation during a Non Contact Tonometry to determine the mechanical properties of the corneal tissue.* Computer Methods in Applied Mechanics and Engineering, submitted.

9.4 Contribuciones en congresos

El presente trabajo se ha presentado en un total de 13 congresos internacionales y nacionales, de los cuales 10 han sido comunicaciones orales y 3 en formato póster.

- **E. Redaelli**, B. Fantaci, J. Grasa, G. Luraghi and J. F. Rodriguez Matas; *Non Contact Tonometry: a Fluid Structure Interaction study*; X Jornada de Jóvenes Investigadores del I3A; Poster presentation; Zaragoza; 21/10/2021.

- **E. Redaelli**, J. Grasa, B Calvo, J. F. Rodriguez Matas and G. Luraghi; *Corvis ST biomarkers in healthy and keratoconic eyes: clinical and numerical evaluation*; XI Jornada de Jóvenes Investigadores del I3A; Poster presentation; Zaragoza; 16/06/2022.

- **E. Redaelli**, J. Grasa, B. Calvo, J. F. Rodriguez Matas and G. Luraghi; *A detailed methodology to model the Non Contact Tonometry: a Fluid Structure Interaction study.*; 27th Congress of the European Society of Biomechanics; Podium presentation; Porto, Portugal; 27/06/2022.

- **E. Redaelli**, J. Grasa, B. Calvo, J. F. Rodriguez Matas and G. Luraghi; *A patient-specific fluid structure interaction simulation of the non-contact tonometry*; 11th meeting of the Italian chapter of the European Society of Biomechanics (ESB); Podium presentation; Marina di Massa, Italy; 06/10/2022.

- **E. Redaelli**, J. Grasa, B. Calvo, J. F. Rodriguez Matas and G. Luraghi; *Can Corvis ST detect the biomechanical properties of the corneal tissue?*; 11th meeting of the Spanish chapter of the European Society of Biomechanics (ESB); Podium presentation; Zaragoza; 25/10/2022.

- **E. Redaelli**, B. Calvo, G. Luraghi, J. F. Rodriguez Matas and J. Grasa; *A New Procedure to Estimate Patient-Specific Intraocular Pressure*; XII Jornada de Jóvenes Investigadores del I3A; Poster presentation; Zaragoza; 15/06/2023.

- **E. Redaelli**, B. Calvo, G. Luraghi, J. F. Rodriguez Matas and J. Grasa; *An energetic analysis of the Non-Contact Tonometry: combining numerical simulations and clinical images.*; 28th Congress of the European Society of Biomechanics; Podium presentation; Maastricht, Netherlands; 10/07/2023.

- **E. Redaelli**, B. Calvo, G. Luraghi, J. F. Rodriguez Matas and J. Grasa; *Analysis of the Influence of Keratoconus Mechanical Properties, Dimension and Position on the Outputs of Corvis*; 11th Meeting on Visual and Physiological Optics; Podium presentation; Antwerp, Belgium; 28/08/2023.

- **E. Redaelli**, B. Calvo, G. Luraghi, J. F. Rodriguez Matas and J. Grasa; *FSI simulations to study eye biomechanics.*; 14th European LS-DYNA Congress; Podium presentation; Baden Baden, Germany; 19/10/2023.

- **E. Redaelli**, B. Calvo, G. Luraghi, J. F. Rodriguez Matas and J. Grasa; *Decoupling Intraocular Pressure Measurement from Corneal Biomechanics*; 12th meeting of the Spanish chapter of the European Society of Biomechanics (ESB); Podium presentation; Malaga, Spain; 03/11/2023.

- **E. Redaelli**, P. Vitullio, S. Fresca, J. F. Rodriguez Matas, P. Zunino, G. Luraghi, B. Calvo, and J. Grasa; *A Novel Artificial Neural Network to determine the Mechanical properties of the Human Corneal Tissue.*; 2024 Annual Meeting of the Association for Research in Vision and Ophtalmology; Podium presentation; Seattle, USA; 05/05/2024.

- **E. Redaelli**, B. Calvo, G. Luraghi, J. F. Rodriguez Matas and J. Grasa; *Determining patient-specific corneal mechanical properties in real time using deep learning.*; 29th Congress of the European Society of Biomechanics; Podium presentation; Edimburgh, UK; 02/07/2024.

- **V. Tahsini**, E. Redaelli, M. Frigelli, M. Nambiar, P. Büchler and S. Kling; *Assessing corneal biomechanics by simultaneous uniaxial extensometry and optical coherence elastography.*; 29th Congress of the European Society of Biomechanics; Podium presentation; Edimburgh, UK; 02/07/2024.

9.5 Revisión de artículos

Durante el curso del doctorado, la autora ha revisado cinco artículos de revistas internacionales.

9.6 Co-supervisión de Tesis de Master

- **Nana Michael**, *Analysis of the influence of Keratoconus Mechanical Properties, Dimension and Position on the output of Corvis ST.* Politecnico di Milano, academic year 2021-2022. Advisor: Rodriguez Matas J. F.; Coadvisors: Grasa J., Redaelli E.
- **De Palma Cecilia**, *Modelling the aqueous and vitreous humors in a non-contact tonometry simulation.* Politecnico di Milano, academic year 2022-2023. Advisor: Luraghi G.; Coadvisors: Grasa J., Redaelli E.
- **Perri Letizia Maria**, *Development of a numerical methodology to model minimally-invasive glaucoma surgery implants.* Politecnico di Milano, academic year 2022-2023. Advisor: Luraghi G.; Coadvisors: Grasa J., Redaelli E.

- **Allievi Eleonora**, *Statistical analysis of Corvis ST biomarkers.* Politecnico di Milano, academic year 2023-2024. Advisor: Luraghi G.; Coadvisors: Grasa J., Redaelli E.

9.7 Docencia

La autora ha impartido clases prácticas en el Grado de Tecnologías Industriales (Resistencia de Materiales).

9.8 Financiación

Este proyecto ha recibido financiación del programa de investigación e innovación Horizonte 2020 de la Unión Europea bajo el acuerdo de subvención Marie Skłodowska-Curie nº 956720, subvención PID2020-113822RB-C21 y del Departamento de Industria e Innovación (Gobierno de Aragón) a través del grupo de investigación Grant T24-20R (cofinanciado con Feder 2014-2020: Construyendo Europa desde Aragón).

Parte del trabajo ha sido realizado por la ICTS «NANBIOSIS» concretamente por la Unidad de Computación de Altas Prestaciones (U27), del CIBER en Bioingeniería, Biomateriales & Nanomedicne (CIBER-BBN de la Universidad de Zaragoza).

Appendices

A

Corvis ST biomarkers

The corneal deformation during the NCT is defined in the Corvis ST by means of some biomarkers. The Corvis ST manual (OCULUS, 2019a) provides the definition of the biomarkers given as output by the device.

- DEFLECTION AMPLITUDE: Shift of the corneal apex in the vertical direction. It depicts the movement of the corneal apex with reference to the superimposed cornea in its non-deformed state. The total movement of the eye is compensated and only the movement of the cornea is described.

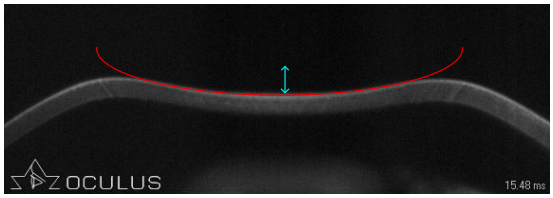

(a) Clinical definition.

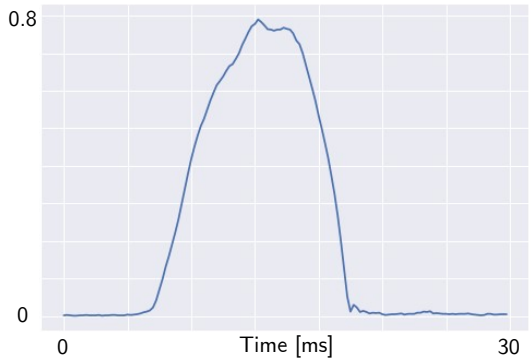

(b) Example of temporal evolution.

Figure A.1: Deflection Amplitude.

- EYE MOVEMENT: Describes the movement of the entire eye (determined by the movement of the edge points in the periphery).

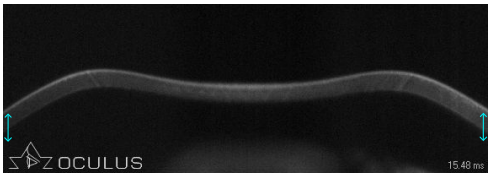

Figure A.2: Clinical definition of eye movement.

- DEFORMATION AMPLITUDE: Depicts the movement of the corneal apex in the vertical direction. It consists of the sum of the deflection amplitude and the total eye movement.

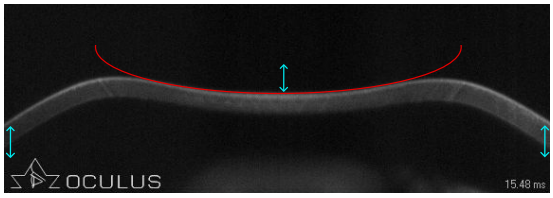

Figure A.3: Clinical definition of deformation amplitude.

- PEAK DISTANCE: Distance between the highest points of the undeformed areas of the cornea.

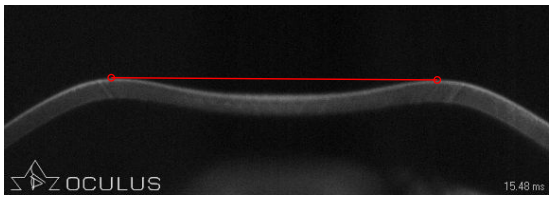

(a) Clinical definition.

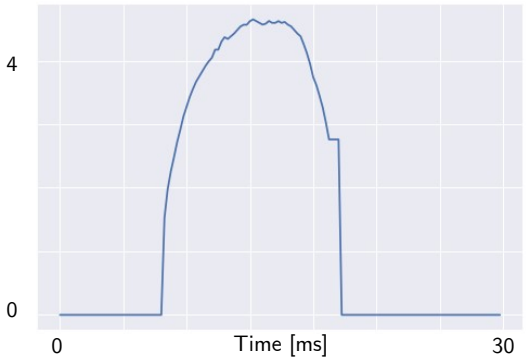

(b) Example of temporal evolution.

Figure A.4: Peak Distance.

- APPLANATION LENGTH: Length of the straight line which describes the applanated region of the cornea.
- APPLANATION TIME: The applanation shows the cornea at the time of transition from a convex shape to a concave shape in the central area of the cornea.
- CORNEAL VELOCITY: Speed of the corneal apex in the vertical direction.
- INVERSE RADIUS: inverse of the bend radius of the circle describing the anterior surface of the cornea in the concave shape.

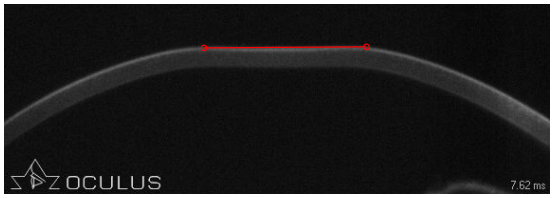

(a) Clinical definition.

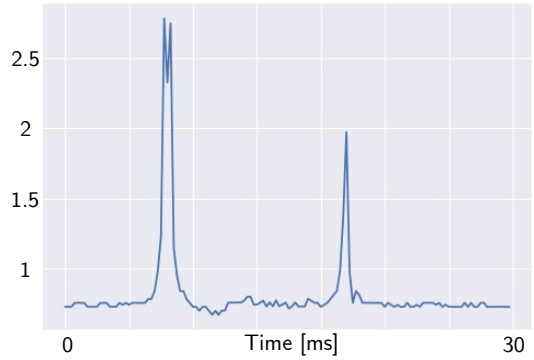

(b) Example of temporal evolution.

Figure A.5: Applanation Length.

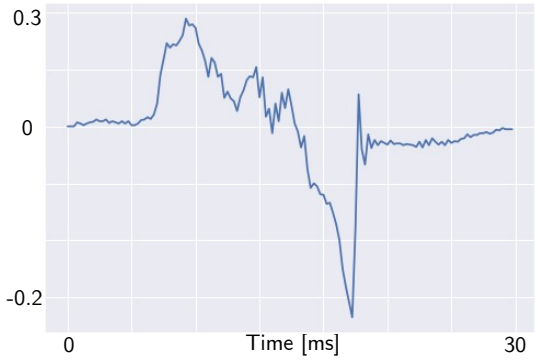

Figure A.6: Example of temporal evolution of corneal velocity.

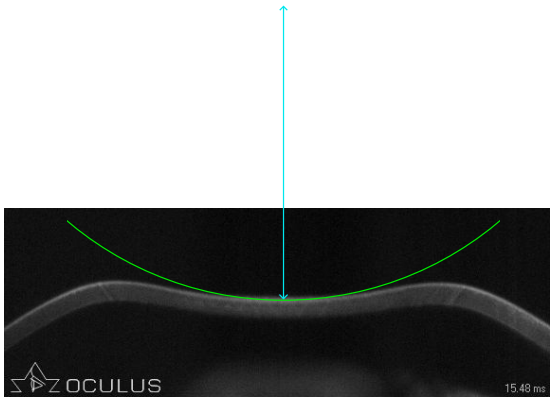

Figure A.7: Clinical definition of inverse radius.

- DELTA ARC LENGTH: reflects the arc length in a defined 7 mm zone. First, the absolute arc length in the non-deformed state is determined. The zone is set precisely at 3.5 mm from the apex in both directions. In precisely the same zone, the change in the arc length over time is measured.

- DA RATIO 2mm: Describes the relationship between the deformation amplitude at the apex and the deformation amplitude at 2mm. With softer tissues, the cornea starts to deform in the middle and only smaller movement in the paracentral region can be observed. As a result, the ratio is higher for softer corneas than for

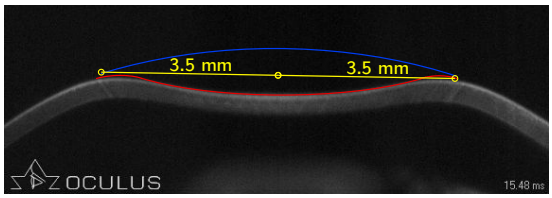

(a) Clinical definition.

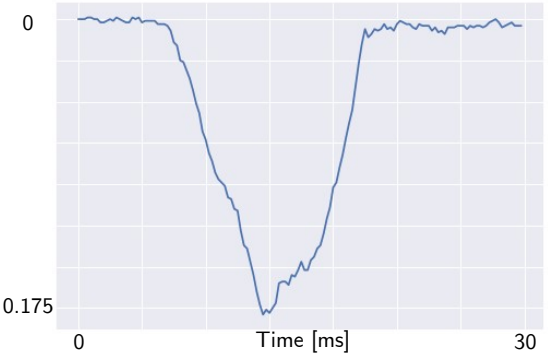

(b) Example of temporal evolution.

Figure A.8: Delta Arc Length.

more rigid corneas.

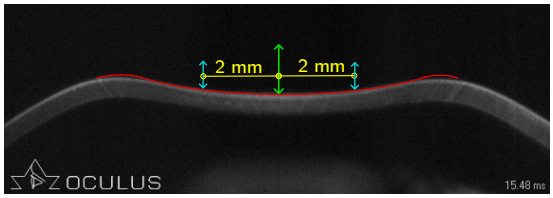

Figure A.9: Clinical definition of DA ratio 2 mm.

B

Zero-Pressure algorithm

The following is the Python algorithm code used to find the zero-pressure configuration of the eye, in case the simulations are run with LsDyna.

```
# -*- coding: utf-8 -*-
"""
Created on Mon Oct 25 09:56:28 2021

@author: Elena
"""
import os
import numpy as np
from qd.cae.dyna import *
from qd.cae.Binout import Binout
from qd.cae.KeyFile import KeyFile

#function to read the nodes of the eyeball from the results of the
    simulation
#input: working folder and the time step to be considered
#output: matrix with ids and coordinates of the eyeball nodes
def read_nodes (folder, step):
    file=os.path.join(folder,'binout*')
    binout = Binout(file)
    x=binout.read("nodout", 'x_coordinate')
    x=x[step][:]
    y=binout.read("nodout", 'y_coordinate')
    y=y[step][:]
    z=binout.read("nodout", 'z_coordinate')
```

```
    z=z[step][:]
    ids=binout.read("nodout", 'ids')
    return np.transpose(np.array([ids,x,y,z]))

#function for the zero-pressure algorithm
#input: working folder
#the function creates a new input file for each iteration and run
   the simulations
def zero_pressure (folder):
    #FIRST ITERATION
    print('ZERO PRESSURE ITERATION: 1')
    file=os.path.join(folder,'occhio.k')
    s = 'mpirun -np 8 /opt/LSTC/ls-dyna_F14_mpp I=occhio.k'
    os.system(s)
    #TARGET CONFIGURATION
    target=read_nodes(folder, 0)
    #UNDEFORMED CONFIGURATION: @ 1st iteration it is identical to
       the target one
    undeformed=read_nodes(folder, 0)
    #DEFORMED CONFIGURATION
    deformed=read_nodes(folder, -1)
    kf =  KeyFile(file, read_keywords=True, parse_mesh=True)
    membrane=kf.get_element_node_ids(Element.shell, 3)
    #ERROR @first iteration
    error = np.zeros((len(deformed),4))
    error[:,1:4]=deformed[:,1:4]-target[:,1:4]
    error[:,0]=target[:,0]
    emax=0
    for i in range(len(deformed)):
        e=np.sqrt((error[i,1]**2)+(error[i,2]**2)+(error[i,3]**2))
        if (error[i,0] != membrane).all():
            if e>emax:
                emax=e
    print('Error=%f',emax)
    #UNDEFORMED CONFIGURATION @ 2nd iteration
    undeformed[:,1:4]=undeformed[:,1:4]-error[:,1:4]
    #new input file
    kf = KeyFile(file, read_keywords=True)
    kf.remove_keyword("*NODE")
    kf.remove_keyword("*END")
    kf.save(str(folder)+"/occhio_it2.k")
    fid = open(str(folder)+"/occhio_it2.k","a")
    fid.write("*NODE\n")
    for i in range (len(undeformed)):
        fid.write("%8d%15.8f%15.8f%15.8f\n"%(undeformed[i,0],
           undeformed[i,1],undeformed[i,2],undeformed[i,3]))
    fid.write("*END\n")
    fid.close()
    #while loop zero pressure
```

```
    tol = 0.001
    itemax=10
    it=2
    while emax>tol and it<=itemax:
        print('ZERO PRESSURE ITERATION: ' + str(it))
        s = 'mpirun -np 8 /opt/LSTC/ls-dyna_F14_mpp I=occhio_it'+
           str(it)+'.k'
        os.system(s)
        #DEFORMED CONFIGURATION
        deformed=read_nodes(folder, -1)
        #ERROR
        error = np.zeros((len(deformed),4))
        error[:,1:4]=deformed[:,1:4]-target[:,1:4]
        error[:,0]=target[:,0]
        i=1
        emax=0
        for i in range(len(deformed)):
            e=np.sqrt(sum(pow(error[i,1:4], 2)))
            if (error[i,0] != membrane).all():
                if e>emax:
                    emax=e
        #UNDEFORMED CONFIGURATION next iteration
        undeformed[:,1:4]=undeformed[:,1:4]-error[:,1:4]
        #new input file
        kf =  KeyFile(str(folder)+"/occhio_it"+str(it)+".k",
           read_keywords=True)
        kf.remove_keyword("*NODE")
        kf.remove_keyword("*END")
        kf.save(str(folder)+"/occhio_it"+str(it+1)+".k")
        fid = open(str(folder)+"/occhio_it"+str(it+1)+".k","a")
        fid.write("*NODE\n")
        for i in range (len(undeformed)):
            fid.write("%8d%15.6f%15.6f%15.6f\n"%(undeformed[i,0],
               undeformed[i,1],undeformed[i,2],undeformed[i,3]))
        fid.write("*END\n")
        fid.close()
        #move to the next iteration
        it=it+1
        print('Error=%f',emax)
    return(it)


folder="/home/eredaelli/Documentos/zp"
#zero pressure configuration
it=zero_pressure(folder)
```

C

Ex-vivo characterization of corneal tissue

C.1 Introduction

To test the range of mechanical properties of the corneal tissue used in the simulations, some ex-vivo experiments are conducted in collaboration with Bern University (Bern, Switzerland). Samples of human and porcine corneas are test uniaxially and, simultaneously, the corneal thickness change is recorded with an OCT system.

C.2 Methods

In order to test the range of mechanical properties used in the simulation, uniaxial tensile tests, which are used to assess the response of materials to stretching or compression along a single axis, in conjunction with OCT scans, which provide high-resolution, non-invasive imaging of the corneal structure were conducted. The uniaxial tensile test device used (Ustretch, CellScale, Waterloo, Canada) and the OCT system (a custom-built system at the University of Bern) (Kling, 2020) were integrated with the same computer to facilitate simultaneous control. The experimental set up is presented in figure C.1. The primary goal was to achieve synchronization between the two machines, ensuring that the OCT images were recorded precisely at the initiation of the uniaxial test.

30 fresh porcine eyes were obtained from the local slaughterhouse. They were individually preserved, cut in laboratory and uniaxially tested at room temperature. The tissue was prestretched with a small force of 20 mN to ensure uniform tension across the samples. The samples were then loaded with 6 cycles at a strain rate of

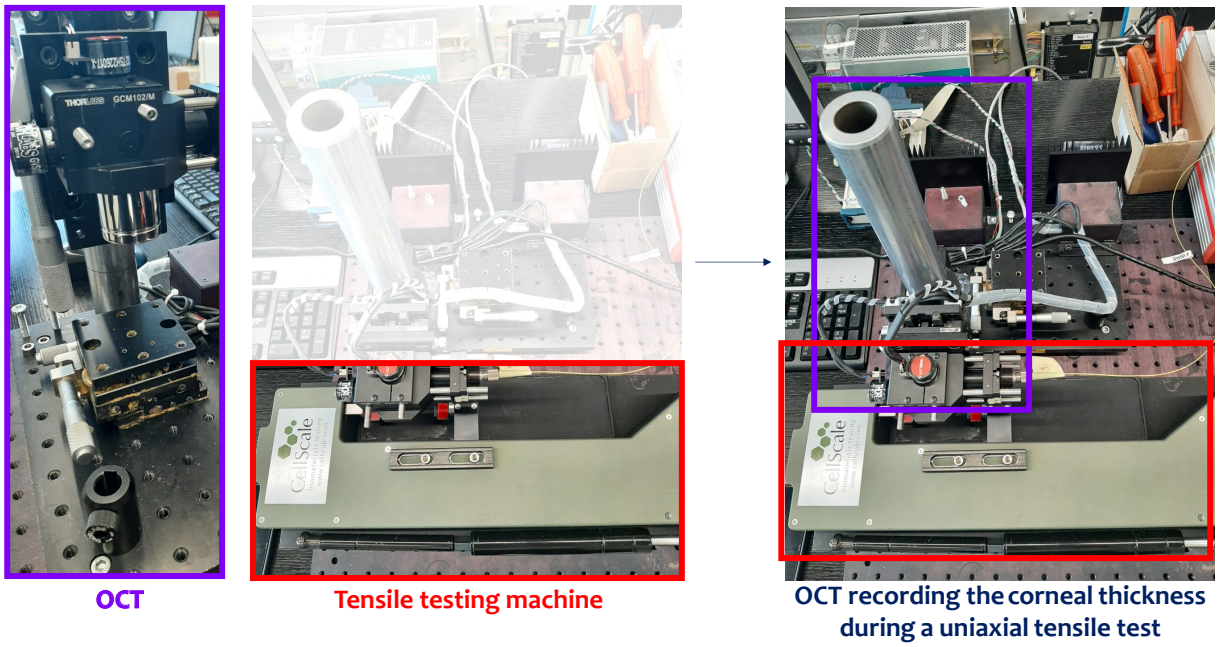

Figure C.1: Ex-vivo set up to characterize the corneal tissue. The OCT system and the uniaxial tensile test machine are syncronized in order to record the corneal thickness change during the test.

0.75%/s. The last cycle of force-displacement data was recorded for analysis; as the mechanical response of the tissue stabilized after the fifth cycle of preconditioning. The OCT recorded the last uniaxial cycle. This step was used to prove the effectiveness of the set-up rather than to estimate the mechanical properties of the corneal tissue. A code was written in Python to segment the images of the OCT device and calculate the change in the sample thickness during the uniaxial test.

10 fresh porcine eyes were obtained from the local slaughterhouse. Each porcine cornea was cut with the Femto LDV Z8 Ziemer femtosecond laser (Ziemer Ophthalmic Systems AG, Switzerland). For each eye, three strips 8 mm long and 3.5 mm wide were cut. These strips were cut at depths of alternating 100 μm and 150 μm. In this way, samples with a thickness of 150 μm were obtained at a depth of 100 μm (D1), 350 μm (D2) and 600 μm (D3), measured from the top surface of the strip. They were individually preserved in a hydration preserving culture media. For the first 5 porcine corneas, the media contained 5% Dextran, for the last 5 corneas it contained 15% Dextran. The strips were uniaxially tested in a bath containing the same culture media using the Ustretch device. Each sample was prestretched with a small force of 20 mN and then loaded with 6 cycles at a strain rate of 0.75%/s. The last cycle of force-displacement data was recorded for analysis and recorded by the OCT.

12 human donor eyes were tested. Each human cornea was cut with the Femto LDV Z8 Ziemer femtosecond laser (Ziemer Ophthalmic Systems AG, Switzerland). Each eye had undergone partial crosslinking previously. Only half of each eye was subjected to crosslinking. For each eye, four strips 6 mm long and 2 mm wide were cut. These strips were cut at depths of 100 μm. In this way, two crosslinked samples with a thickness of

100 μm and two not crosslinked samples with a thickness of 100 μm were obtained for each eye. They were individually preserved in a culture media containing 15% Dextran. The strips were uniaxially tested in a bath containing the same culture media using the Ustretch device. Each sample was prestretched with a force of 20 mN and then loaded with 6 cycles at a strain rate of 0.75%/s. The last cycle of force-displacement data was recorded for analysis and recorded by the OCT.

C.2.1 Results

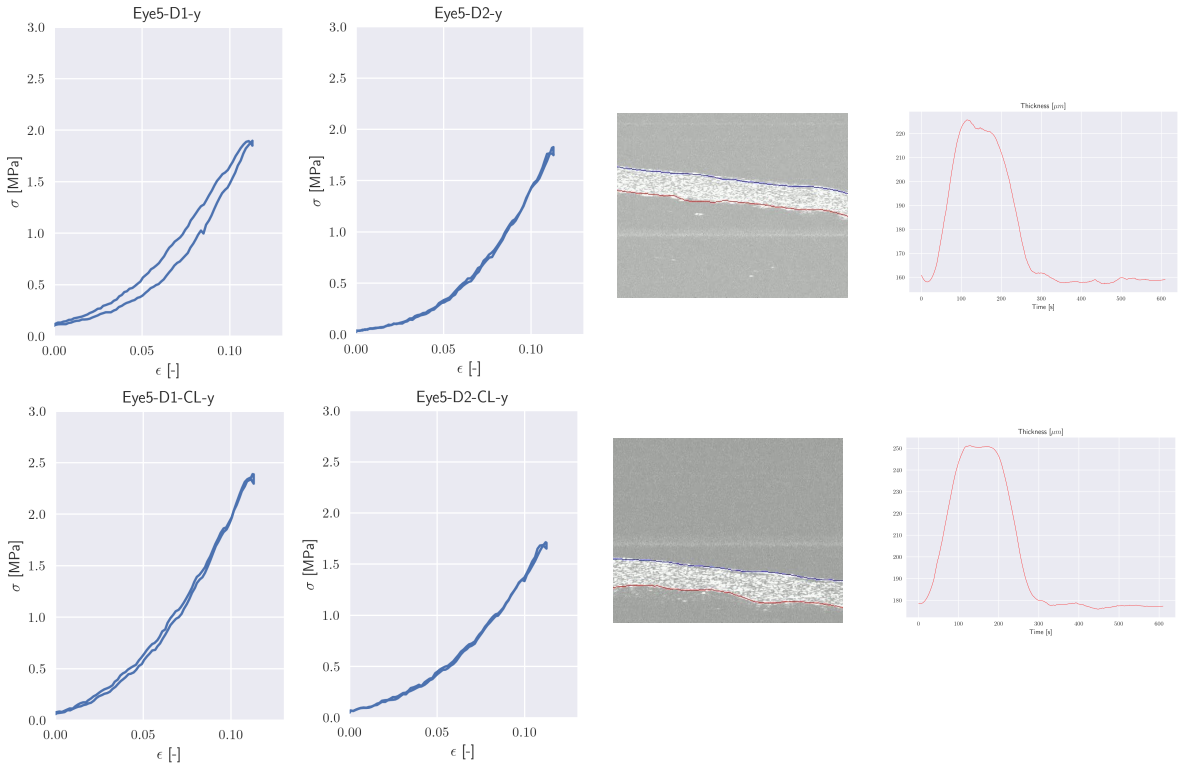

Figure C.2: Uniaxial tensile test and OCT results. The stress strain behaviour of different corneal samples of the same eye are reported on the left. On the right, an example of segmentation of sample thickness and the change of thickness in time are depicted.

Prior to testing, porcine corneal samples were analyzed to determine the effects of storage solutions on their mechanical properties. It was found that samples stored in a 5% dextran solution exhibited significant swelling due to the solution being too diluted. In contrast, samples stored in a 15% dextran solution maintained consistent thickness even after several days. Consequently, the corneas preserved in the 15% dextran solution were selected for further testing and the human samples were preserved in a solution of 15% dextran. The results of uniaxial tests on an example of human cornea are depicted in figure C.2. The engineering stress and strain data are depicted in the plot and they indicate that the corneal samples subjected to the crosslinking process exhibit increased stiffness compared to the untreated corneas. Furthermore, the samples taken from deeper layers of the cornea show higher deformability compared to the more superficial layers, a trend previously demonstrated in other works (Nambiar et al., 2023). The primary objective of the study, which was to determine the deformation range of

human corneas, has been successfully achieved. Although the samples were tested up to 13% strain, which is significantly higher than physiological levels, the mechanical response aligns well with the anisotropic model of Holzapfel Gasser Ogden used in our simulations. This model predicts isotropic deformation at low strains and stiffening due to fiber recruitment at higher strains.

Additionally, OCT was employed to measure the corneal thickness, with results illustrated in figure C.2. Surprisingly, contrary to expectations, the corneal thickness increased under tensile load and decreased during relaxation, as shown in figure C.2. This behavior is unexpected because the cornea, primarily composed of water, is generally considered an incompressible material. Thus, when it elongates in the planar directions, one would anticipate a reduction in thickness. This anomalous result challenges our understanding of the corneal mechanical response and suggests a complex interaction between the corneal structure and its constituent materials under varying stress conditions. It could be possible that the corneal samples need a slower strain rate in order to show the correct mechanical behavour or that the solution used does not prevent from swelling during the test.

C.3 Discussion

The main novelty of this study is the incorporation of OCT scans, which provide information on the thickness of the corneal tissue. This additional dimension adds depth to the analysis by allowing exploration not only of in-plane mechanical properties but also of out-of-plane behavior. Hoever, the OCT measurements revealed an unexpected phenomenon: the corneal thickness increased under tensile stress and decreased during relaxation, contrary to the anticipated behavior for an incompressible material like the cornea, which is predominantly composed of water. Normally, one would expect that elongation in the planar directions would result in a reduction in thickness. This finding challenges the traditional understanding of corneal biomechanics and suggests as a future line an in-depth exploration of the experimental set up.

The inclusion of corneal thickness as a constraint in the parameter estimation process for the mechanical behavior of corneal tissue serves to enhance the precision and applicability of the research findings. By incorporating OCT data, we should achieve a more comprehensive understanding of the corneal biomechanical response. This integration allows for the validation of the numerical model against experimental observations, strengthening the overall reliability of the simulation. For this reason this experimental set up should be investigated in detail.

Bibliography

Abadi, M., Agarwal, A., Barham, P., Brevdo, E., Chen, Z., Citro, C., Corrado, G. S., Davis, A., Dean, J., Devin, M., Ghemawat, S., Goodfellow, I., Harp, A., Irving, G., Isard, M., Jia, Y., Jozefowicz, R., Kaiser, L., Kudlur, M., Levenberg, J., Mané, D., Monga, R., Moore, S., Murray, D., Olah, C., Schuster, M., Shlens, J., Steiner, B., Sutskever, I., Talwar, K., Tucker, P., Vanhoucke, V., Vasudevan, V., Viégas, F., Vinyals, O., Warden, P., Wattenberg, M., Wicke, M., Yu, Y., and Zheng, X. (2015). TensorFlow: Large-scale machine learning on heterogeneous systems. Software available from tensorflow.org.

Abràmoff, M. D., Lou, Y., Erginay, A., Clarida, W., Amelon, R., Folk, J. C., and Niemeijer, M. (2016). Improved automated detection of diabetic retinopathy on a publicly available dataset through integration of deep learning. *Investigative ophthalmology & visual science*, 57(13):5200–5206.

Ajazaj, V., Kaçaniku, G., Asani, M., Shabani, A., and Dida, E. (2018). Intraocular pressure after corneal refractive surgery. *medical archives*, 72(5):341.

Ambekar, R., Toussaint Jr, K. C., and Johnson, A. W. (2011). The effect of keratoconus on the structural, mechanical, and optical properties of the cornea. *Journal of the mechanical behavior of biomedical materials*, 4(3):223–236.

Ambrósio Jr, R., Lopes, B. T., Faria-Correia, F., Salomão, M. Q., Bühren, J., Roberts, C. J., Elsheikh, A., Vinciguerra, R., and Vinciguerra, P. (2017). Integration of scheimpflug-based corneal tomography and biomechanical assessments for enhancing ectasia detection. *Journal of Refractive Surgery*, 33(7):434–443.

Anderson, K., El-Sheikh, A., and Newson, T. (2004). Application of structural analysis to the mechanical behaviour of the cornea. *Journal of the Royal Society Interface*, 1(1):3–15.

Andreassen, T. T., Simonsen, A. H., and Oxlund, H. (1980). Biomechanical properties of keratoconus and normal corneas. *Experimental eye research*, 31(4):435–441.

Aoki, S., Asaoka, R., Fujino, Y., Nakakura, S., Murata, H., and Kiuchi, Y. (2023). Comparing corneal biomechanic changes among solo cataract surgery, microhook ab interno trabeculotomy and istent implantation. *Scientific Reports*, 13(1):19148.

Arbelaez, M. C., Versaci, F., Vestri, G., Barboni, P., and Savini, G. (2012). Use of a support vector machine for keratoconus and subclinical keratoconus detection by topographic and tomographic data. *Ophthalmology*, 119(11):2231–2238.

Ariza-Gracia, M., Ortillés, Á., Cristóbal, J., Matas, J. R., and Calvo, B. (2017a). A numerical-experimental protocol to characterize corneal tissue with an application to predict astigmatic keratotomy surgery. *Journal of the Mechanical Behavior of Biomedical Materials*, 74:304–314.

Ariza-Gracia, M. Á., Flecha-Lescún, J., Büchler, P., and Calvo, B. (2020). Corneal biomechanics after intrastromal ring surgery: Optomechanical in silico assessment. *Translational vision science & technology*, 9(11):26–26.

Ariza-Gracia, M. Á., Redondo, S., Llorens, D. P., Calvo, B., and Matas, J. F. R. (2017b). A predictive tool for determining patient-specific mechanical properties of human corneal tissue. *Computer methods in applied mechanics and engineering*, 317:226–247.

Ariza-Gracia, M. Á., Wu, W., Calvo, B., Malvè, M., Büchler, P., and Matas, J. F. R. (2018). Fluid–structure simulation of a general non-contact tonometry. a required complexity? *Computer methods in applied mechanics and engineering*, 340:202–215.

Ariza-Gracia, M. Á., Zurita, J., Piñero, D. P., Calvo, B., and Rodríguez-Matas, J. F. (2016). Automatized patient-specific methodology for numerical determination of biomechanical corneal response. *Annals of biomedical engineering*, 44:1753–1772.

Ariza-Gracia, M. Á., Zurita, J. F., Piñero, D. P., Rodriguez-Matas, J. F., and Calvo, B. (2015). Coupled biomechanical response of the cornea assessed by non-contact tonometry. a simulation study. *PloS one*, 10(3):e0121486.

Asaoka, R., Nakakura, S., Tabuchi, H., Murata, H., Nakao, Y., Ihara, N., Rimayanti, U., Aihara, M., and Kiuchi, Y. (2015). The relationship between corvis st tonometry measured corneal parameters and intraocular pressure, corneal thickness and corneal curvature. *PloS one*, 10(10):e0140385.

Ashofteh Yazdi, A., Melchor, J., Torres, J., Faris, I., Callejas, A., Gonzalez-Andrades, M., and Rus, G. (2020). Characterization of non-linear mechanical behavior of the cornea. *Scientific reports*, 10(1):11549.

Ávila, F. J., Marcellán, M. C., and Remón, L. (2021). On the relationship between corneal biomechanics, macrostructure, and optical properties. *Journal of Imaging*, 7(12):280.

Bahler, C. K., Hann, C. R., Fjield, T., Haffner, D., Heitzmann, H., and Fautsch, M. P. (2012). Second-generation trabecular meshwork bypass stent (istent inject) increases outflow facility in cultured human anterior segments. *American journal of ophthalmology*, 153(6):1206–1213.

Bao, F., Jiang, L., Wang, X., Zhang, D., Wang, Q., and Zeng, Y. (2012). Assessment of the ex vivo biomechanical properties of porcine cornea with inflation test for corneal xenotransplantation. *Journal of medical engineering & technology*, 36(1):17–21.

Basson, N., Peng, C.-H. S., Geoghegan, P., van der Lecq, T., Steven, D., Williams, S., Lim, A. E., and Ho, W. H. (2024). A computational fluid dynamics investigation of endothelial cell damage from glaucoma drainage devices. *Scientific Reports*, 14(1):3777.

Bekesi, N., Dorronsoro, C., de la Hoz, A., and Marcos, S. (2016a). Material properties from air puff corneal deformation by numerical simulations on model corneas. *PLoS One*, 11(10):e0165669.

Bekesi, N., Gallego-Munoz, P., Ibarés-Frías, L., Perez-Merino, P., Martinez-Garcia, M. C., Kochevar, I. E., and Marcos, S. (2017). Biomechanical changes after in vivo collagen cross-linking with rose bengal–green light and riboflavin-uva. *Investigative Ophthalmology & Visual Science*, 58(3):1612–1620.

Bekesi, N., Kochevar, I. E., and Marcos, S. (2016b). Corneal biomechanical response following collagen cross-linking with rose bengal–green light and riboflavin-uva. *Investigative ophthalmology & visual science*, 57(3):992–1001.

Blackburn, B. J., Jenkins, M. W., Rollins, A. M., and Dupps, W. J. (2019). A review of structural and biomechanical changes in the cornea in aging, disease, and photochemical crosslinking. *Frontiers in bioengineering and biotechnology*, 7:66.

Boote, C., Sigal, I. A., Grytz, R., Hua, Y., Nguyen, T. D., and Girard, M. J. (2020). Scleral structure and biomechanics. *Progress in retinal and eye research*, 74:100773.

Boszczyk, A., Kasprzak, H., and Siedlecki, D. (2019). Non-contact tonometry using corvis st: analysis of corneal vibrations and their relation with intraocular pressure. *JOSA A*, 36(4):B28–B34.

Brown, J. M., Campbell, J. P., Beers, A., Chang, K., Ostmo, S., Chan, R. P., Dy, J., Erdogmus, D., Ioannidis, S., Kalpathy-Cramer, J., et al. (2018). Automated diagnosis of plus disease in retinopathy of prematurity using deep convolutional neural networks. *JAMA ophthalmology*, 136(7):803–810.

Brusini, P., Salvetat, M. L., and Zeppieri, M. (2021). How to measure intraocular pressure: an updated review of various tonometers. *Journal of clinical medicine*, 10(17):3860.

Brusini, P., Salvetat, M. L., and Zeppieri, M. (2022). *Intraocular Pressure and Ocular Hypertension*. MDPI Books.

Cabeza-Gil, I., Grasa, J., and Calvo, B. (2021). A validated finite element model to reproduce helmholtz's theory of accommodation: a powerful tool to investigate presbyopia. *Ophthalmic and Physiological Optics*, 41(6):1241–1253.

Cantor, L., Lindfield, D., Ghinelli, F., Świder, A. W., Torelli, F., Steeds, C., Dickerson Jr, J. E., and Nguyen, D. Q. (2023). Systematic literature review of clinical, economic, and humanistic outcomes following minimally invasive glaucoma surgery or selective

laser trabeculoplasty for the treatment of open-angle glaucoma with or without cataract extraction. *Clinical Ophthalmology*, pages 85–101.

Chen, L., Huang, Y., Zhang, X., Shi, Y., Gao, Z., Sun, B., Shen, Y., Sun, L., Cao, Y., Zhang, Q., et al. (2023). Corneal biomechanical properties demonstrate anisotropy and correlate with axial length in myopic eyes. *Investigative Ophthalmology & Visual Science*, 64(10):27–27.

Chong, J. and Dupps Jr, W. J. (2021). Corneal biomechanics: Measurement and structural correlations. *Experimental Eye Research*, 205:108508.

Corp, L. S. T. (2021). Ls-dyna. Computer Software.

Curatolo, A., Birkenfeld, J. S., Martinez-Enriquez, E., Germann, J. A., Muralidharan, G., Palací, J., Pascual, D., Eliasy, A., Abass, A., Solarski, J., et al. (2020). Multi-meridian corneal imaging of air-puff induced deformation for improved detection of biomechanical abnormalities. *Biomedical optics express*, 11(11):6337–6355.

Daxer, A. and Fratzl, P. (1997). Collagen fibril orientation in the human corneal stroma and its implication in keratoconus. *Investigative Ophthalmology and Visual Science*, 38(1):121–129.

del Barrio, J. L. A., Wilkins, M., Cochener, B., Ang, M., et al. (2019). Refractive surgery. *The Lancet*, 393(10185):2085–2098.

DelMonte, D. W. and Kim, T. (2011). Anatomy and physiology of the cornea. *Journal of Cataract & Refractive Surgery*, 37(3):588–598.

Eilaghi, A., Flanagan, J. G., Tertinegg, I., Simmons, C. A., Brodland, G. W., and Ethier, C. R. (2010). Biaxial mechanical testing of human sclera. *Journal of biomechanics*, 43(9):1696–1701.

Eliasy, A., Abass, A., Lopes, B. T., Vinciguerra, R., Zhang, H., Vinciguerra, P., Ambrosio Jr, R., Roberts, C. J., and Elsheikh, A. (2020). Characterization of cone size and centre in keratoconic corneas. *Journal of the Royal Society Interface*, 17(169):20200271.

Eliasy, A., Chen, K.-J., Vinciguerra, R., Lopes, B. T., Abass, A., Vinciguerra, P., Ambrósio Jr, R., Roberts, C. J., and Elsheikh, A. (2019). Determination of corneal biomechanical behavior in-vivo for healthy eyes using corvis st tonometry: stress-strain index. *Frontiers in bioengineering and biotechnology*, 7:105.

Eliasy, A., Chen, K.-J., Vinciguerra, R., Maklad, O., Vinciguerra, P., Ambrósio Jr, R., Roberts, C. J., and Elsheikh, A. (2018). Ex-vivo experimental validation of biomechanically-corrected intraocular pressure measurements on human eyes using the corvis st. *Experimental eye research*, 175:98–102.

Eliasy, A., Lopes, B. T., Wang, J., Abass, A., Vinciguerra, R., Vinciguerra, P., Bao, F.-j., and Elsheikh, A. (2022). Introduction and clinical validation of an updated biomechanically corrected intraocular pressure biop (v2). *Current eye research*, pages 1–10.

Eliasy, A., Lopes, B. T., Wang, J., Abass, A., Vinciguerra, R., Vinciguerra, P., Bao, F.-j., and Elsheikh, A. (2023). Introduction and clinical validation of an updated biomechanically corrected intraocular pressure biop (v2). *Current eye research*, 48(4):382–391.

Elsheikh, A. and Anderson, K. (2005). Comparative study of corneal strip extensometry and inflation tests. *Journal of the Royal Society Interface*, 2(3):177–185.

Elsheikh, A., Brown, M., Alhasso, D., Rama, P., Campanelli, M., Garway-Heath, D., et al. (2008). Experimental assessment of corneal anisotropy. *Journal of refractive surgery*, 24(2):178.

Elsheikh, A. and Wang, D. (2007). Numerical modelling of corneal biomechanical behaviour. *Computer methods in biomechanics and biomedical engineering*, 10(2):85–95.

Elsheikh, A., Wang, D., Brown, M., Rama, P., Campanelli, M., and Pye, D. (2007). Assessment of corneal biomechanical properties and their variation with age. *Current eye research*, 32(1):11–19.

Esporcatte, L. P. G., Salomão, M. Q., Lopes, B. T., Vinciguerra, P., Vinciguerra, R., Roberts, C., Elsheikh, A., Dawson, D. G., and Ambrósio, R. (2020). Biomechanical diagnostics of the cornea. *Eye and Vision*, 7(1):1–12.

Ferrari, G. and Rama, P. (2020). The keratoconus enigma: a review with emphasis on pathogenesis. *The Ocular Surface*, 18(3):363–373.

Fresca, S., Manzoni, A., Dedè, L., and Quarteroni, A. (2020). Deep learning-based reduced order models in cardiac electrophysiology. *PloS one*, 15(10):e0239416.

Frigelli, M., Büchler, P., and Kling, S. (2023). Optomechanical assessment of photorefractive corneal cross-linking via optical coherence elastography. *Frontiers in Bioengineering and Biotechnology*, 11.

Gefen, A., Shalom, R., Elad, D., and Mandel, Y. (2009). Biomechanical analysis of the keratoconic cornea. *Journal of the mechanical behavior of biomedical materials*, 2(3):224–236.

Giraudet, C., Diaz, J., Le Tallec, P., and Allain, J.-M. (2022). Multiscale mechanical model based on patient-specific geometry: application to early keratoconus development. *Journal of the mechanical behavior of biomedical materials*, 129:105121.

Glass, D. H., Roberts, C. J., Litsky, A. S., and Weber, P. A. (2008). A viscoelastic biomechanical model of the cornea describing the effect of viscosity and elasticity on hysteresis. *Investigative ophthalmology & visual science*, 49(9):3919–3926.

Goel, M., Picciani, R. G., Lee, R. K., and Bhattacharya, S. K. (2010). Aqueous humor dynamics: a review. *The open ophthalmology journal*, 4:52.

Goldmann, H. and Schmidt, T. (1957). Über applanationstonometrie. *Ophthalmologica*, 134(4):221–242.

Gonzalez Castro, G., Fitt, A. D., and Sweeney, J. (2016). On the validity of the imbert-fick law: mathematical modelling of eye pressure measurement. *World Journal of Mechanics*, 6:35–51.

Greene, P., Sergienko, N., and Wang, S. (2016). Review: Measurement techniques for intraocular pressure. *Optom Open Access*, 1(118):2476–2075.

Gulli, A. and Pal, S. (2017). *Deep learning with Keras*. Packt Publishing Ltd.

Hamilton, D. R., Manche, E. E., Rich, L. F., and Maloney, R. K. (2002). Steroid-induced glaucoma after laser in situ keratomileusis associated with interface fluid. *Ophthalmology*, 109(4):659–665.

Harris, C. R., Millman, K. J., van der Walt, S. J., Gommers, R., Virtanen, P., Cournapeau, D., Wieser, E., Taylor, J., Berg, S., Smith, N. J., Kern, R., Picus, M., Hoyer, S., van Kerkwijk, M. H., Brett, M., Haldane, A., del Río, J. F., Wiebe, M., Peterson, P., Gérard-Marchant, P., Sheppard, K., Reddy, T., Weckesser, W., Abbasi, H., Gohlke, C., and Oliphant, T. E. (2020). Array programming with NumPy. *Nature*, 585(7825):357–362.

Helmy, H. and Hashem, O. (2020). Intraocular pressure calculation in myopic patients after laser-assisted in situ keratomileusis. *Clinical Ophthalmology*, pages 509–516.

Hesthaven, J. S. and Ubbiali, S. (2018). Non-intrusive reduced order modeling of nonlinear problems using neural networks. *Journal of Computational Physics*, 363:55–78.

Hollingsworth, J. G., Bonshek, R. E., and Efron, N. (2005). Correlation of the appearance of the keratoconic cornea in vivo by confocal microscopy and in vitro by light microscopy. *Cornea*, 24(4):397–405.

Holzapfel, G. A., Gasser, T. C., and Ogden, R. W. (2000). A new constitutive framework for arterial wall mechanics and a comparative study of material models. *Journal of elasticity and the physical science of solids*, 61:1–48.

Hong, J., Xu, J., Wei, A., Deng, S. X., Cui, X., Yu, X., and Sun, X. (2013). A new tonometer—the corvis st tonometer: clinical comparison with noncontact and goldmann applanation tonometers. *Investigative ophthalmology & visual science*, 54(1):659–665.

Hsu, F. L.-T., Shih, P.-J., and Wang, I.-J. (2023). Development and validation of an intuitive biomechanics-based method for intraocular pressure measurement: a modal analysis approach. *BMC ophthalmology*, 23(1):124.

Huang, L., Shen, M., Liu, T., Zhang, Y., and Wang, Y. (2020). Inverse solution of corneal material parameters based on non-contact tonometry: A comparative study of different constitutive models. *Journal of Biomechanics*, 112:110055.

Imbert, D. A. (1885). *Théorie des ophtalmotonomètres,...* A. Davy.

Issarti, I., Koppen, C., and Rozema, J. J. (2021). Influence of the eye globe design on biomechanical analysis. *Computers in Biology and Medicine*, 135:104612.

Jan, N.-J. and Sigal, I. A. (2018). Collagen fiber recruitment: a microstructural basis for the nonlinear response of the posterior pole of the eye to increases in intraocular pressure. *Acta biomaterialia*, 72:295–305.

Jannesari, M., Kadkhodaei, M., Mosaddegh, P., Kasprzak, H., and Behrouz, M. J. (2018). Assessment of corneal and fatty tissues biomechanical response in dynamic tonometry tests by using inverse models. *Acta of bioengineering and biomechanics*, 20(1).

Joda, A. A., Shervin, M. M. S., Kook, D., and Elsheikh, A. (2016). Development and validation of a correction equation for corvis tonometry. *Computer methods in biomechanics and biomedical engineering*, 19(9):943–953.

Jongebloed, W. and Worst, J. (1987). The cisternal anatomy of the vitreous body. *Documenta ophthalmologica*, 67:183–196.

Jordanova, E., Hentova-Sencanic, P., Marjanović, I., Senčanin, I., Stefanović, I., and Baralić, M. (2022). The cornea and methods for measuring intraocular pressure. *Sanamed*, 17(3):167–173.

Kaushik, S., Pandav, S. S., Banger, A., Aggarwal, K., and Gupta, A. (2012). Relationship between corneal biomechanical properties, central corneal thickness, and intraocular pressure across the spectrum of glaucoma. *American journal of ophthalmology*, 153(5):840–849.

Kels, B. D., Grzybowski, A., and Grant-Kels, J. M. (2015). Human ocular anatomy. *Clinics in dermatology*, 33(2):140–146.

Kim, Y., Roy, S., Jung, G.-Y., Oh, J.-S., and Kim, G.-W. (2019). Dual optical signal-based intraocular pressure-sensing principle using pressure-sensitive mechanoluminescent zns: Cu/pdms soft composite. *Scientific Reports*, 9(1):15215.

Kingma, D. P. and Ba, J. (2014). Adam: A method for stochastic optimization. *arXiv preprint arXiv:1412.6980*.

Kling, S. (2020). Optical coherence elastography by ambient pressure modulation for high-resolution strain mapping applied to patterned cross-linking. *Journal of the Royal Society Interface*, 17(162):20190786.

Kling, S. and Hafezi, F. (2017). Corneal biomechanics–a review. *Ophthalmic and Physiological Optics*, 37(3):240–252.

Kling, S. and Marcos, S. (2013). Contributing factors to corneal deformation in air puff measurements. *Investigative ophthalmology & visual science*, 54(7):5078–5085.

Kohlhaas, M., Spoerl, E., Boehm, A. G., and Pollack, K. (2006). A correction formula for the real intraocular pressure after lasik for the correction of myopic astigmatism.

Krag, S. and Andreassen, T. T. (2003). Mechanical properties of the human lens capsule. *Progress in retinal and eye research*, 22(6):749–767.

Kudsieh, B., Fernández-Vigo, J. I., Agujetas, R., Montanero, J. M., Ruiz-Moreno, J. M., Fernández-Vigo, J. Á., and García-Feijóo, J. (2020). Numerical model to predict and compare the hypotensive efficacy and safety of minimally invasive glaucoma surgery devices. *Plos one*, 15(9):e0239324.

Lee, R. M., Bouremel, Y., Eames, I., Brocchini, S., and Khaw, P. T. (2020). Translating minimally invasive glaucoma surgery devices. *Clinical and translational science*, 13(1):14–25.

LeGrand, Y. and ElHage, S. G. (2013). *Physiological optics*, volume 13. Springer.

Li, X., Luo, S., Wang, Z., Miao, Y., Zhu, M., Zheng, X., Luo, G., Bao, F., Chen, S., and Wang, J. (2023). Dynamic topography analysis of the cornea and its application to the diagnosis of keratoconus. *Computers in Biology and Medicine*, 158:106800.

Liu, G., Rong, H., Zhang, P., Xue, Y., Du, B., Wang, B., Hu, J., Chen, Z., and Wei, R. (2021). The effect of axial length elongation on corneal biomechanical property. *Frontiers in Bioengineering and Biotechnology*, 9:777239.

Liu, J. and Roberts, C. J. (2005). Influence of corneal biomechanical properties on intraocular pressure measurement: quantitative analysis. *Journal of Cataract & Refractive Surgery*, 31(1):146–155.

Liu, T., Shen, M., Huang, L., Xiang, Y., Li, H., Zhang, Y., and Wang, Y. (2020). Characterization of hyperelastic mechanical properties for youth corneal anterior central stroma based on collagen fibril crimping constitutive model. *Journal of the Mechanical Behavior of Biomedical Materials*, 103:103575.

Lopes, B. T., Bao, F., Wang, J., Liu, X., Wang, L., Abass, A., Eliasy, A., and Elsheikh, A. (2021). Review of in-vivo characterisation of corneal biomechanics. *Medicine in Novel Technology and Devices*, 11:100073.

Lopes, B. T., Eliasy, A., and Ambrosio, R. (2019). Artificial intelligence in corneal diagnosis: where are we? *Current Ophthalmology Reports*, 7:204–211.

Lopes, B. T., Ramos, I. C., Salomão, M. Q., Guerra, F. P., Schallhorn, S. C., Schallhorn, J. M., Vinciguerra, R., Vinciguerra, P., Price Jr, F. W., Price, M. O., et al. (2018). Enhanced tomographic assessment to detect corneal ectasia based on artificial intelligence. *American journal of ophthalmology*, 195:223–232.

Luce, D. A. (2005). Determining in vivo biomechanical properties of the cornea with an ocular response analyzer. *Journal of Cataract & Refractive Surgery*, 31(1):156–162.

Mahdian, M., Seifzadeh, A., Mokhtarian, A., and Doroodgar, F. (2021). Characterization of the transient mechanical properties of human cornea tissue using the tensile test simulation. *Materials Today Communications*, 26:102122.

Maklad, O., Eliasy, A., Chen, K.-J., Theofilis, V., and Elsheikh, A. (2020a). Simulation of air puff tonometry test using arbitrary lagrangian–eulerian (ale) deforming mesh for corneal material characterisation. *International Journal of Environmental Research and Public Health*, 17(1):54.

Maklad, O., Eliasy, A., Chen, K.-J., Wang, J., Abass, A., Lopes, B. T., Theofilis, V., and Elsheikh, A. (2020b). Fluid-structure interaction based algorithms for iop and corneal material behavior. *Frontiers in bioengineering and biotechnology*, page 970.

Maklad, O. M. Y. (2019). *Influence of fluid-structure interaction on human eye biomechanics under air puff non-contact tonometry*. The University of Liverpool (United Kingdom).

Maklakoff, C. L. (1885). Ophthalmotonometrie. *Arch Ophthalmol (Paris)*, 5:159.

Mauro, A., Massarotti, N., Mohamed, S., Uña, I. R., Romano, M. R., and Romano, V. (2018). A novel patient-oriented numerical procedure for glaucoma drainage devices. *International Journal for Numerical Methods in Biomedical Engineering*, 34(12):e3141.

Meek, K. M., Blamires, T., Elliott, G. F., Gyi, T. J., and Nave, C. (1987). The organisation of collagen fibrils in the human corneal stroma: a synchrotron x-ray diffraction study. *Current eye research*, 6(7):841–846.

Meek, K. M. and Boote, C. (2009). The use of x-ray scattering techniques to quantify the orientation and distribution of collagen in the corneal stroma. *Progress in retinal and eye research*, 28(5):369–392.

Meek, K. M. and Knupp, C. (2015). Corneal structure and transparency. *Progress in retinal and eye research*, 49:1–16.

Meek, K. M., Knupp, C., Lewis, P. N., Morgan, S. R., and Hayes, S. (2024). Structural control of corneal transparency, refractive power and dynamics. *Eye*, pages 1–7.

Meek, K. M., Tuft, S. J., Huang, Y., Gill, P. S., Hayes, S., Newton, R. H., and Bron, A. J. (2005). Changes in collagen orientation and distribution in keratoconus corneas. *Investigative ophthalmology & visual science*, 46(6):1948–1956.

Meeney, A. and Mudhar, H. (2013). Histopathological reporting of corneal pathology by a biomedical scientist: the sheffield experience. *Eye*, 27(2):272–276.

Montanino, A., Angelillo, M., and Pandolfi, A. (2018). Modelling with a meshfree approach the cornea-aqueous humor interaction during the air puff test. *Journal of the Mechanical Behavior of Biomedical Materials*, 77:205–216.

Montanino, A., Angelillo, M., and Pandolfi, A. (2019). A 3d fluid-solid interaction model of the air puff test in the human cornea. *Journal of the Mechanical Behavior of Biomedical Materials*, 94:22–31.

Montanino, A., van Overbeeke, S., and Pandolfi, A. (2023). Modeling the biomechanics of laser corneal refractive surgery. *Journal of the Mechanical Behavior of Biomedical Materials*, 145:105998.

Morishige, N., Wahlert, A. J., Kenney, M. C., Brown, D. J., Kawamoto, K., Chikama, T.-i., Nishida, T., and Jester, J. V. (2007). Second-harmonic imaging microscopy of normal human and keratoconus cornea. *Investigative ophthalmology & visual science*, 48(3):1087–1094.

Morrison, J. C., Johnson, E. C., Cepurna, W., and Jia, L. (2005). Understanding mechanisms of pressure-induced optic nerve damage. *Progress in retinal and eye research*, 24(2):217–240.

Muench, S., Roellig, M., Spoerl, E., and Balzani, D. (2019). Numerical and experimental study of the spatial stress distribution on the cornea surface during a non-contact tonometry examination. *Experimental Mechanics*, 59(9):1285–1297.

Nambiar, M. H., Seiler, T. G., Senti, S., Liechti, L., Müller, F., Studer, H., Roy, A. S., and Büchler, P. (2023). Depth-dependent mechanical properties of the human cornea by uniaxial extension. *Experimental eye research*, 237:109718.

Nash, I. S., Greene, P. R., and Foster, C. S. (1982). Comparison of mechanical properties of keratoconus and normal corneas. *Experimental eye research*, 35(5):413–424.

Nguyen, B. A., Roberts, C. J., and Reilly, M. A. (2019). Biomechanical impact of the sclera on corneal deformation response to an air-puff: a finite-element study. *Frontiers in bioengineering and biotechnology*, 6:210.

OCULUS (2019a). Oculus corvis® corvis st® hr interpretation guide.

OCULUS (2019b). Oculus pentacam® pentacam® hr interpretation guide.

Oehring, D., Jenkins, D., Buckhurst, P. J., and Buckhurst, H. (2021). Experimental assessment of the spatial and temporal distribution of non-contact tonometer airflows. *Applied Sciences*, 11(6):2499.

Ortillés, Á., Rodríguez-Matas, J. F., Ariza-Gracia, M. Á., Pascual, G., and Calvo, B. (2017). Why non-contact tonometry tests cannot evaluate the effects of corneal collagen cross-linking. *Journal of Refractive Surgery*, 33(3):184–192.

Pandolfi, A. and Holzapfel, G. A. (2008). Three-dimensional modeling and computational analysis of the human cornea considering distributed collagen fibril orientations. *Journal of biomechanical engineering*, 130(6).

Pandolfi, A. and Manganiello, F. (2006). A model for the human cornea: constitutive formulation and numerical analysis. *Biomechanics and modeling in mechanobiology*, 5(4):237–246.

Popovic, M., Campos-Moller, X., Saheb, H., and Ahmed, I. I. K. (2018). Efficacy and adverse event profile of the istent and istent inject trabecular micro-bypass for open-angle glaucoma: a meta-analysis. *Journal of Current Glaucoma Practice*, 12(2):67.

Rahmati, S. M., Razaghi, R., and Karimi, A. (2021). Biomechanics of the keratoconic cornea: Theory, segmentation, pressure distribution, and coupled fe-optimization algorithm. *Journal of the Mechanical Behavior of Biomedical Materials*, 113:104155.

Rajabi, S., Asharlous, A., Riazi, A., Khabazkhoob, M., and Moalej, A. (2022). Differences and limits of agreement among pentacam, corvis-st, and iol-master 700 optical biometric devices regarding central corneal thickness measurements. *Journal of Current Ophthalmology*, 34(1):44.

Ramachandran, P., Zoph, B., and Le, Q. V. (2017). Searching for activation functions. *arXiv preprint arXiv:1710.05941*.

Redaelli, E., Grasa, J., Calvo, B., Rodriguez Matas, J. F., and Luraghi, G. (2022). A detailed methodology to model the non contact tonometry: a fluid structure interaction study. *Frontiers in Bioengineering and Biotechnology*, 10:981665.

Redaelli, E., Nana, M., Calvo, B., Matas, J. F. R., Luraghi, G., Rozema, J., and Grasa, J. (2024). Improving early detection of keratoconus by non contact tonometry. a computational study and new biomarkers proposal. *Journal of the Mechanical Behavior of Biomedical Materials*, 152:106413.

Remington, L. A. (2012). *Clinical Anatomy and Physiology of the Visual System*. Elsevier.

Roberts, C. J., Mahmoud, A. M., Bons, J. P., Hossain, A., Elsheikh, A., Vinciguerra, R., Vinciguerra, P., and Ambrósio Jr, R. (2017). Introduction of two novel stiffness parameters and interpretation of air puff–induced biomechanical deformation parameters with a dynamic scheimpflug analyzer. *Journal of refractive surgery*, 33(4):266–273.

Romero-Jiménez, M., Santodomingo-Rubido, J., and Wolffsohn, J. S. (2010). Keratoconus: a review. *Contact Lens and Anterior Eye*, 33(4):157–166.

Roy, A. S. and Dupps, W. J. (2011). Patient-specific computational modeling of keratoconus progression and differential responses to collagen cross-linking. *Investigative ophthalmology & visual science*, 52(12):9174–9187.

RStudio Team (2020). *RStudio: Integrated Development Environment for R*. RStudio, PBC., Boston, MA.

Rüfer, F., Schröder, A., and Erb, C. (2005). White-to-white corneal diameter: normal values in healthy humans obtained with the orbscan ii topography system. *Cornea*, 24(3):259–261.

Ruggeri, A. and Pajaro, S. (2002). Automatic recognition of cell layers in corneal confocal microscopy images. *Computer methods and programs in biomedicine*, 68(1):25–35.

Santodomingo-Rubido, J., Carracedo, G., Suzaki, A., Villa-Collar, C., Vincent, S. J., and Wolffsohn, J. S. (2022). Keratoconus: An updated review. *Contact Lens and Anterior Eye*, 45(3):101559.

Shalaby, W. S., Jia, J., Katz, L. J., and Lee, D. (2021). istent inject: comprehensive review. *Journal of Cataract & Refractive Surgery*, 47(3):385–399.

Sharma, H., Nainiwal, S. K., Sarraf, A., Porwal, R., and Sharma, V. (2020). Intraocular pressure measurement techniques: Current concepts and a review. *Indian Journal of Clinical and Experimental Ophthalmology*, 6(3):315–323.

Silva, F. and Lira, M. (2022). Intraocular pressure measurement: A review. *Survey of Ophthalmology*.

Simonini, I. and Pandolfi, A. (2016). The influence of intraocular pressure and air jet pressure on corneal contactless tonometry tests. *Journal of the mechanical behavior of biomedical materials*, 58:75–89.

Sng, C. C. and Barton, K. (2021). *Minimally invasive glaucoma surgery*. Springer Nature.

Sridhar, U. and Tripathy, K. (2022). Corneal topography.

Tan, D. T., Dart, J. K., Holland, E. J., and Kinoshita, S. (2012). Corneal transplantation. *The Lancet*, 379(9827):1749–1761.

Ting, D. S. W., Cheung, C. Y.-L., Lim, G., Tan, G. S. W., Quang, N. D., Gan, A., Hamzah, H., Garcia-Franco, R., San Yeo, I. Y., Lee, S. Y., et al. (2017). Development and validation of a deep learning system for diabetic retinopathy and related eye diseases using retinal images from multiethnic populations with diabetes. *Jama*, 318(22):2211–2223.

Ting, D. S. W., Pasquale, L. R., Peng, L., Campbell, J. P., Lee, A. Y., Raman, R., Tan, G. S. W., Schmetterer, L., Keane, P. A., and Wong, T. Y. (2019). Artificial intelligence and deep learning in ophthalmology. *British Journal of Ophthalmology*, 103(2):167–175.

Vellara, H. R. and Patel, D. V. (2015). Biomechanical properties of the keratoconic cornea: a review. *Clinical and Experimental Optometry*, 98(1):31–38.

Villamarin, A., Roy, S., Hasballa, R., Vardoulis, O., Reymond, P., and Stergiopulos, N. (2012). 3d simulation of the aqueous flow in the human eye. *Medical engineering & physics*, 34(10):1462–1470.

Vinciguerra, R., Ambrósio Jr, R., Elsheikh, A., Roberts, C. J., Lopes, B., Morenghi, E., Azzolini, C., and Vinciguerra, P. (2016). Detection of keratoconus with a new biomechanical index. *Journal of refractive surgery*, 32(12):803–810.

Vinciguerra, R., Ambrósio Jr, R., Roberts, C. J., Azzolini, C., and Vinciguerra, P. (2017). Biomechanical characterization of subclinical keratoconus without topographic or tomographic abnormalities. *Journal of Refractive Surgery*, 33(6):399–407.

Virtanen, P., Gommers, R., Oliphant, T. E., Haberland, M., Reddy, T., Cournapeau, D., Burovski, E., Peterson, P., Weckesser, W., Bright, J., van der Walt, S. J., Brett, M., Wilson, J., Millman, K. J., Mayorov, N., Nelson, A. R. J., Jones, E., Kern, R., Larson, E., Carey, C. J., Polat, İ., Feng, Y., Moore, E. W., VanderPlas, J., Laxalde, D., Perktold, J., Cimrman, R., Henriksen, I., Quintero, E. A., Harris, C. R., Archibald, A. M., Ribeiro, A. H., Pedregosa, F., van Mulbregt, P., and SciPy 1.0 Contributors (2020). SciPy 1.0: Fundamental Algorithms for Scientific Computing in Python. *Nature Methods*, 17:261–272.

Wang, J., Li, X., Wang, Z., Davey, P. G., Li, Y., Yang, L., Lin, M., Zheng, X., Bao, F., and Elsheikh, A. (2022). Accuracy and reliability of orthogonal polynomials in representing corneal topography. *Medicine in Novel Technology and Devices*, 15:100133.

Wang, J., Liu, X., Bao, F., Lopes, B. T., Wang, L., Eliasy, A., Abass, A., and Elsheikh, A. (2021). Review of ex-vivo characterisation of corneal biomechanics. *Medicine in Novel Technology and Devices*, 11:100074.

Wang, Q., Hesthaven, J. S., and Ray, D. (2019). Non-intrusive reduced order modeling of unsteady flows using artificial neural networks with application to a combustion problem. *Journal of computational physics*, 384:289–307.

Wang, Y. X., Xu, L., Wei, W. B., and Jonas, J. B. (2018). Intraocular pressure and its normal range adjusted for ocular and systemic parameters. the beijing eye study 2011. *PLoS One*, 13(5):e0196926.

Wei, Y., Lopes, B. T., Eliasy, A., Wu, R., Fathy, A., Elsheikh, A., and Abass, A. (2021). Performance of zernike polynomials in reconstructing raw-elevation data captured by pentacam hr, medmont e300 and eye surface profiler. *Heliyon*, 7(12).

Whitford, C., Joda, A., Jones, S., Bao, F., Rama, P., and Elsheikh, A. (2016). Ex vivo testing of intact eye globes under inflation conditions to determine regional variation of mechanical stiffness. *Eye and vision*, 3:1–12.

WHO (2019). World report on vision.

Wilde, G., Burd, H., and Judge, S. (2012). Shear modulus data for the human lens determined from a spinning lens test. *Experimental eye research*, 97(1):36–48.

Wollensak, G., Spoerl, E., and Seiler, T. (2003). Stress-strain measurements of human and porcine corneas after riboflavin–ultraviolet-a-induced cross-linking. *Journal of Cataract & Refractive Surgery*, 29(9):1780–1785.

Wu, Y., Luttrell, I., Feng, S., Chen, P. P., Spaide, T., Lee, A. Y., and Wen, J. C. (2020). Development and validation of a machine learning, smartphone-based tonometer. *British Journal of Ophthalmology*, 104(10):1394–1398.

Xiang, Y., Shen, M., Xue, C., Wu, D., and Wang, Y. (2018). Tensile biomechanical properties and constitutive parameters of human corneal stroma extracted by smile procedure. *Journal of the Mechanical Behavior of Biomedical Materials*, 85:102–108.

Xue, C., Xiang, Y., Shen, M., Wu, D., Wang, Y., et al. (2018). Preliminary investigation of the mechanical anisotropy of the normal human corneal stroma. *Journal of Ophthalmology*, 2018.

Yadav, K. S., Rajpurohit, R., and Sharma, S. (2019). Glaucoma: Current treatment and impact of advanced drug delivery systems. *Life sciences*, 221:362–376.

Zhang, D., Zhang, H., Tian, L., Zheng, Y., Fu, C., Zhai, C., and Li, L. (2021). Exploring the biomechanical properties of the human cornea in vivo based on corvis st. *Frontiers in Bioengineering and Biotechnology*, 9:771763.

Zhao, Y., Shen, Y., Yan, Z., Tian, M., Zhao, J., and Zhou, X. (2019). Relationship among corneal stiffness, thickness, and biomechanical parameters measured by corvis st, pentacam and ora in keratoconus. *Frontiers in physiology*, 10:740.